

CNT REINFORCED EPOXY FOAMED AND ELECTROSPUN NANO-FIBER
INTERLAYER SYSTEMS FOR MANUFACTURING LIGHTER AND
STRONGER FEATHERWEIGHT™ COMPOSITES

by

VASILEIOS M DRAKONAKIS

Presented to the Faculty of the Graduate School of
The University of Texas at Arlington in Partial Fulfillment
of the Requirements
for the Degree of

DOCTOR OF PHILOSOPHY

THE UNIVERSITY OF TEXAS AT ARLINGTON

August 2012

Copyright © by Vasileios M Drakonakis 2012

All Rights Reserved

DEDICATION

To Lina

ACKNOWLEDGMENTS

I am grateful to all the people who contributed toward the completion of this effort with endless support in various forms. First of all, my gratitude goes to Dr. John Priest for supervising me towards the completion of this work. In addition, special thanks go to Dr. Victoria Chen for her advice and direction in the realization of important sections of this dissertation. Many thanks also to Dr. Brian Huff and Dr. Erick Jones for their advice as committee members throughout this effort.

I would like to thank Dr. James Seferis who was one of my main financial and scientific supporters from the very beginning of this dissertation and for giving me the opportunity to work on an international level obtaining priceless academic, industrial, and cultural experiences and creating a global professional network. With my deepest gratitude, I would like to thank Dr. Haris Doumanidis for his consummate and technical guidance in the scientific paths that this effort has led me to during the last five years as well as for his inspirational paradigm of facing difficulties in life with moral force and quality.

Moreover, I would like to thank Dr. Brian Wardle for his guidance and support to specific parts of this work as well as to the NECST lab members for their help in the work that was held at MIT. Here, I would also like to thank especially Dr. George Papanicolaou, whose mentoring and great support five years ago inspired me to begin this adventurous journey toward attaining my doctorate, under the moral he has adopted: “you never fail until you stop trying”.

Additionally, my deepest gratitude goes to my spiritual father, Father Apostolos Sakelariou, who even though physically absent, through his prayers, encouragement, and advice spiritually protected me during all phases of this effort; to my beloved parents, Michail and Anneta, who were always at my side, patiently supporting me since the beginning of my life; to my brother and at the same time best friend Tassos; and to my son Michail, who was born in

February 2012 and who keeps reminding me daily the biggest happiness of life through his inimitable smile. Finally and most importantly, I thank from the deepest of my heart my biggest fan and supporter, my wife Lina; her unlimited encouragement, patience, and love pricelessly contributed to the completion of this effort.

July 12th, 2012

ABSTRACT

CNT REINFORCED EPOXY FOAMED AND ELECTROSPUN NANO-FIBER INTERLAYER SYSTEMS FOR MANUFACTURING LIGHTER AND STRONGER FEATHERWEIGHT™ COMPOSITES

Vasileios M Drakonakis, PhD

The University of Texas at Arlington, 2012

Supervising Professor: John W. Priest

Multiple works have been performed in improving carbon fiber reinforced polymer (CFRP) composites especially in terms of strength so delamination, which is the major defect in laminated composites, is prevented. Nevertheless, there is not much focus on improving conventional CFRP systems in terms of weight especially when these are used in primary structures. This work questions whether lighter and at the same time stronger CFRP composites can be manufactured in order to replace conventional CFRP systems in major applications. Under this perspective, this study demonstrates that inducing controlled porosity may offer a systemic approach for manufacturing light weight carbon fiber reinforced polymer (CFRP) matrix composites. Additionally, towards this scope, this work has focused on analyzing and describing the related matrix systems utilizing mostly classic viscoelastic theory. An in-depth characterization of the thermosetting matrix systems viscoelasticity kinetics as well as of the impregnation process towards its improvement in terms of lower cost is explored. Overall, this work makes an effort to establish the fundamentals for creating the next generation of light

weight structural composites, the featherweight composites, by introducing porosity through several controlled reinforcements in a systemic and reproducible manner at the macro-micro- and nano-scales in the interlayer. By extensively describing the matrix system and the manufacturing processes and focusing on analytically testing the interlayer reinforcement systems, it is expected that featherweight CFRP will achieve lighter weight and at the same time higher mechanical properties.

TABLE OF CONTENTS

ACKNOWLEDGEMENTS	iii
ABSTRACT	v
TABLE OF CONTENTS	vii
LIST OF ILLUSTRATIONS.....	xi
LIST OF TABLES	xix
Chapter	Page
1. INTRODUCTION	1
1.1 Problem Introduction	1
1.2 Scope of this Research - Featherweight Composites.....	2
1.3 The Interlayer Reinforcement – Critical Part of the Featherweights.....	3
1.4 Need for Research	4
1.5 Research Methodology Overview	5
1.6 Dissertation Outline	7
2. BACKGROUND	9
2.1 Matrix System Description and Analysis.....	9
2.1.1 Dynamic Mechanical Analysis	9
2.1.2 t - T Equivalence Principle and Master Curve	13
2.1.3 Viscoelastic Behavior	15
2.1.4 GSLS Model Assumptions	16
2.1.5 Master Curves for Tg and Degradation Processes.....	22
2.1.6 Model Approach	27
2.2 Differential Scanning Calorimetry	29

2.3 CFRP Impregnation and Manufacturing	30
2.3.1 Hot-melt impregnation.....	31
2.3.2 Prepreg Efficiency.....	35
2.4 Innovative Clave Manufacturing and Processing.....	37
2.4.1 Autoclaving.....	37
2.4.2 Pressurized Vessel	40
2.5 Processing of Multilayer Structured Laminates- Interlayer Introduction ...	42
2.5.1 Interlayer Processing and Fabrication	43
2.5.2 Toughening Mechanisms of Interlayer.....	50
2.6 Carbon Nanotubes in the Interlayer	54
2.6.1 Literature CNT and PNC Modulus Approaches.....	56
2.7 Porosity in Epoxy Matrix Interlayer Systems through Foaming Agents....	59
2.8 Electrospun Fibers in the Interlayer	62
2.9 Review Summary.....	65
3. RESEARCH METHODOLOGY	67
3.1 Objective #1	67
3.1.1 Rationale	67
3.1.2 Experimental Procedure	67
3.2 Objective #2	69
3.2.1 Rationale	69
3.2.2 Experimental Procedure	69
3.3 Objective #3	73
3.3.1 Rationale	73
3.3.2 Experimental Procedure	73
3.4 Objective #4	77
3.4.1 Rationale	77

3.4.2 Experimental Procedure	78
3.5 Objective #5	85
3.5.1 Rationale	85
3.5.2 Experimental Procedure	85
3.6 Objective #6	88
3.6.1 Rationale	89
3.6.2 Experimental Procedure	89
4. RESULTS AND DISCUSSION.....	92
4.1 Results for Specific Objective #1: Matrix System Description	92
4.2 Results for Specific Objective #2: Innovative Manufacturing Process.....	95
4.2.1 DSC Analysis Curing Evaluation.....	95
4.2.2 DMA for Viscoelastic Behaviour Evaluation.....	99
4.2.3 Flexural & Compression Mechanical Testing	102
4.2.4 SEM for Surface Micro-Characterization	107
4.2.5 Parametrical Prediction of Strength	110
4.3 Results for Specific Objective #3: Micro-Particle Reinforced Interlayer .	133
4.3.1 Fracture – Toughness Testing Evaluation	133
4.3.2 Toughness Improvement Evaluation	135
4.4 Results for Specific Objective #4: Carbon Nanotubes in the Interlayer..	136
4.4.1 CNT Density and Modulus Approach.....	139
4.4.2 Interlayer Zoom in – PNC	143
4.4.3 Modelling and Experimentation Results	145
4.5 Results for Specific Objective #5: Porosity in Epoxy Matrix Systems	157
4.5.1 CNT Fraction for Pore Surface Reinforcement.....	157
4.5.2 Montmorillonite Nanoclay Reinforced Polyurethane.....	161
4.5.3 CNT Reinforced Epoxy Foam Interlayered CFRP	163

4.5.4 DMA for Viscoelastic Behaviour Evaluation.....	164
4.5.5 Mechanical Testing for Interlayer Evaluation.....	166
4.5.6 SEM for Interlayer Micro-Characterization.....	172
4.5.7 Parametrical Prediction of Strength	178
4.6 Results for Specific Objective #6: CNT Electrospun Fiber Interlayer	208
4.6.1 CNT Reinforced Electrospun Fiber CFRP	208
4.6.2 DMA Viscoelastic Behaviour Evaluation	211
4.6.3 Mechanical Testing Interlayer Evaluation	212
4.6.4 SEM Interlayer Micro-Characterization	218
4.6.5 Parametrical Prediction of Strength	224
4.7 Comparison of the Three Different Interlayer Enabling Systems	244
5. CONCLUSIONS	249
5.1 Conclusions for Objective #1	249
5.2 Conclusions for Objective #2	250
5.3 Conclusions for Objective #3	252
5.4 Conclusions for Objective #4	252
5.5 Conclusions for Objective #5	253
5.6 Conclusions for Objective #6	256
5.7 Summary and Future Work.....	258
REFERENCES.....	260
BIOGRAPHICAL INFORMATION	274

LIST OF ILLUSTRATIONS

Figure	Page
2.1 Standard linear Solid (“SLS”) Model (23)- Two Elastic Springs and One Viscous Dashpot in Series-Parallel Sequence.....	19
2.2 Measured DMA Storage Modulus of Phenolic Resin/Carbon Fiber Composite vs. Temperature - Nine Different Frequencies: from 0.01 to 5 Hz in Nitrogen Atmosphere at 300 ml/min (1; 2)	21
2.3 Storage Modulus for Glass Transition vs. Inverse Frequency at Different Temperatures (1; 2).....	22
2.4 Shift Factors Compared with Arrhenius Type Equation Using $E=790.4\text{KJ/mol}$ and $T_0=277.50\text{C}$ for the Glass Transition (1; 2).....	23
2.5 Storage Modulus for Degradation Processes vs. Inverse Frequency at Different Temperatures (1; 2).....	24
2.6 Horizontal Shift Factor for Degradation Process (1; 2)	25
2.7 Vertical Shift Factor for Degradation Process (1; 2)	25
2.8 DMA Storage Modulus Master Curves for Glass Transition and Degradation Processes (1; 17; 22)	26
2.9 Typical Characteristic DSC Curve of a Semi-Crystallized Thermoplastic Polymer (29).....	30
2.10 Hotmelt Prepreg Process	31
2.11 Fibers Introduction to the Prepreger	33
2.12 Resin Viscosity vs. Temperature.....	33
2.13 Reverse Roll Coater Design.....	33
2.14 Prepreg Doctor Blade.....	33
2.15 Main Prepreg Heater	34
2.16 Chill Plate and Take-up Roller.	35
2.17 Overall Resin Distribution while Prepregging (3)	36

2.18 Autoclave Entire Lay-up (3).....	38
2.19 Typical Temperature and Pressure Profile for Curing in a Clave (3)	39
2.20 Heatcon Composite System - Repair Clave Model HCS3100 (46)	40
2.21 Development of Conventional and Multilayer Structured Composites (53).....	43
2.22 Second-Pass of Impregnation (5)	46
2.23 Two Different Ways for Applying the Homogeneous Interlayer: (a) applying half interlayer on each side of prepreg in the second-pass of the impregnation, (b) applying full interlayer on one side of the fiber bed in the second-pass of the impregnation.....	47
2.24 Schematic of Fiber-Packing Arrangements with the Homogeneous Interlayer Implemented. Maximum Packing Achieved at $\theta = 30^\circ$ (58).....	49
2.25 (a) Toughening Mechanisms Observed in Present Work, (b) Hackle Formation (5)	52
2.26 SEM at PCL - Mode II Fracture Surfaces of Non Interlayered Epoxy Laminates at a) Low and b) High Magnification (5; 48)	53
2.27 SEM at PCL - Mode II Fracture Surfaces of 25% Modifier Particles Interlayered Epoxy Laminate at a) Low and b) High Magnification (5; 48).....	53
2.28 SEM at PCL - Mode II Fracture Surfaces of 44% Modifier Particles Interlayered Epoxy Laminate at A) Low, B) High, and C) Higher Magnifications (5; 48)	54
2.29 Porous Nanocomposite Compared to Conventional Composite	60
2.30 Carbon Fiber Alignment at Surface of Foam	60
2.31 The Reinforcing Procedure of Foam Pores with Carbon Fibers (6).....	61
2.32 Scheme of Pore Reinforcement (109).....	62
2.33 Electrospinning Configuration at a Laboratory Scale (119)	63
2.34 Nanofibers Produced through Electrospinning (119)	63
3.1 Lay-up	70
3.2 Fracture-Toughness Configurations: (a) specimen dimensions, (b) Double Cantilever Beam testing and	

(c) End Notch Flexure testing (5; 53)	76
3.3 Fabrication of Variable Volume Fraction Aligned-CNT Nano-Composites. (a) process flow for fabricating nanocomposites, (b) optical images of 1% volume fraction RTM6 nano-composite specimens after fabrication (132)	82
3.4 Aligned CNT Volume Fraction from Mechanical Densification of CNT Forest. 1mm tall aligned-CNT forests at 1% (as-grown), 8% (uniaxially densified), and 20% (biaxially densified) volume fraction (132)	83
3.5 ASTM D638-03 Dimensions in cm	88
4.1 DMA Storage Modulus for the Glass Transition Compared to the Model (continuous line) vs. Temperature, at 0.01, 0.1 and 1 Hz (1; 2).	92
4.2 DMA Storage Modulus during Degradation Compared to the Model (continuous line), vs. Temperature, at 0.01, 0.1 and 1.0 Hz (1; 2).	93
4.3 DMA Storage Modulus for Both Glass Transition and Degradation Processes, Compared to the Model (continuous line), vs. Temperature, at 0.01, 0.1 and 1.0 Hz (1; 2).	94
4.4 Comparison of $\tan\delta$ with the Model (continuous line), vs. Temperature, at (a) 1.0 Hz and (b) 0.01 Hz (1; 2).	94
4.5 Uncured Samples, Heat of Cure Comparison (4)	96
4.6 DSC Dynamic Scans at 1 and 5 °C/min for Different Pressure Manufactured Samples (a) 0 psi, (b) 70 psi (485 kPa) (4)	97
4.7 8 Plies Samples Comparison for the Rate 5 °C/min at 0, 30, 50, 70 psi (0, 205, 345, and 485 kPa) (4)	98
4.8 Storage Modulus of Carbon Fiber Prepregs – 8 Plies Manufactured in 0, 30, 50 and 70 psi (0, 205, 345, and 485 kPa) in (a) 1 and (b) 5 °C/min heating rates (4)	99
4.9 Normalized Moduli Comparison of 0 psi, 70 psi (485 kPa) and 70 psi (485kPa) Annealed. Tg of the Annealed 70 psi Sample at 220 °C is Much Closer to the 0 psi Sample Tg (4).	100
4.10 $\tan\delta$ of Carbon Fiber Prepregs – 8 Plies Manufactured in 0, 30, 50 and 70 psi (0, 205, 345, and 485 kPa) in 1 and 5 °C/min (4).	101
4.11 Flexural Testing, Stress – Strain Curves for (a) 0 psi, (b) 30 psi (205 kPa), (c) 50 psi (345 kPa), and (d) 70 psi (485 kPa)	102
4.12 Stress-Strain Comparison of CFRP Specimens Manufactured under	

0, 30, 50, and 70 psi (0, 205, 345, and 485 kPa) Derived from Flexural Testing	103
4.13 Compression Testing, Stress - Strain Curves for (a) 0 psi, (b) 30 psi (205 kPa), (c) 50 psi (345 kPa), and (d) 70 psi (485 kPa)	104
4.14 Stress-Strain Comparison of CFRP Specimens Manufactured under 0, 30, 50, and 70 psi (0, 205, 345, and 485 kPa) Derived from Compression Testing	105
4.15 (SEM) Left: All Different Samples Manufactured in Different Pressures, Right: Samples Manufactured at 0 psi/kPa, Showing Increased Void Formation	107
4.16 (SEM) Left: The Entire Thickness Cross Section of a Sample Manufactured at 30 psi (205 kPa), Right: Void Formation at 30 psi (205 kPa) Sample.....	107
4.17 (SEM) Left: The Entire Thickness Cross Section of a Sample Manufactured at 50 psi (345 kPa), Right: Smaller Voids also Formed at 50 psi (345 kPa) Sample.....	108
4.18 (SEM) Left: The Entire Thickness Cross Section of a Sample Manufactured at 70 psi (485 kPa), Right: Even Smaller and Less Voids Formed at 70 psi (485 kPa) Sample	108
4.19 Scatter Plot- Manufacturing Pressure Variation	112
4.20 Residuals Analysis - Manufacturing Pressure Variation	115
4.21 Levene's Test Algorithm Developed in Microsoft XL (139) - Manufacturing Pressure Variation	116
4.22 Outliers and Influence- Manufacturing Pressure Variation	118
4.23 Influence on Parameters (DFBETAS) - Manufacturing Pressure Variation	119
4.24 Interactions - Manufacturing Pressure Variation	120
4.25 Pearson Correlation with Predictor Variables and Interactions - Manufacturing Pressure Variation	121
4.26 Pearson Correlation with Predictor Variables and Standardized Interactions- Manufacturing Pressure Variation.....	121
4.27 Best Subsets Regression for Evaluating the Different Predictor Variables Cases for Best Manufacturing Pressure Variation.....	122
4.28 Backward Elimination and Forward Stepwise Methods for Evaluating the Different Predictor Variables Cases for Best Manufacturing Pressure Variation	123

4.29 Model 1 Residuals Graphs – Manufacturing Pressure Variation	126
4.30 Model 2 Residuals Graphs – Manufacturing Pressure Variation	128
4.31 Mode I Interlaminar Fracture-Toughness (GIC) of Epoxy-Based Model System vs. Modifier Particle Concentration in Interlayer (5).....	134
4.32 Mode II Interlaminar Toughness (GIIC) of Epoxy-Based Model System vs. Modifier Particle Concentration in Interlayer (5).....	134
4.33 Percent Mode II Interlaminar Fracture-Toughness Improvement of Epoxy-Model System vs. Modifier Particle Concentration in Interlayer (5)	135
4.34 Carbon Atoms in a Hexagonal CNT Sheet	139
4.35 Section of Carbon Nanotube (Parallel to Base)	140
4.36 CNT Density vs. CNT External Radius and Number of Walls	146
4.37 PNC Density as a function of CNT volume fraction for different CNT	147
4.38 CNT Modulus vs. CNT External Radius and Number of Walls.....	148
4.39 PNC Modulus for Aligned, Aligned in Plane, and Randomly Oriented CNT of $R_{ext}=4\text{nm}$ and 3 Walls	149
4.40 PNC Modulus for Aligned, Aligned in Plane, and Randomly Oriented CNT of $R_{ext}=8-9\text{nm}$ and 5-6 Walls.....	149
4.41 PNC Modulus for Aligned CNT of $R_{ext}=4, 8, \text{ and } 12\text{nm}$ and 3, 6, and 6 Walls Respectively.....	150
4.42 PNC Modulus Comparison according to the Different Theories of CNT Modulus Described in Background.....	151
4.43 Material Modulus vs. Density	152
4.44 Comparison of Aligned CNT PNC (A-PNC) Results to Extant elastic modulus data of random CNT PNC (R-PNC) (88; 134).....	153
4.45 PNC Modulus vs. CNT Volume Fraction; Correlation of Experimental Findings with Theoretical Model	154
4.46 PNC Modulus vs. Density. Theoretical Results for Different Types of CNT and Experimental Results for CNT with 4nm External Radius and 3 Walls.	154
4.47 Experimental and Theoretical PNC Modulus vs. Density for CNT of 4m External Radius and 3 Walls.....	155

4.48 PNC Density vs. CNT Volume Fraction: (a) experimental approach 1, (b) experimental approach 2, (c) theoretical approach, (d) merge of a, b, and c graphs.....	156
4.49 Pore Tangential Nano-Reinforcement Mechanism	159
4.50 Polyurethane Reinforced with Montmorillonite Nano-Clays in Different Weight Fractions.....	162
4.51 Epoxy Foamed Interlayer System Scheme within CFRP.....	164
4.52 Control CFRP Flexural Testing	166
4.53 CFRP with Epoxy Foamed Interlayer Flexural Testing	167
4.54 CNT Reinforced Epoxy Foamed Interlayer CFRP Flexural Testing	167
4.55 Control CFRP Tensile Testing	169
4.56 CFRP with Epoxy Foamed Interlayer Tensile Testing	170
4.57 CNT Reinforced Epoxy Foamed Interlayer CFRP Tensile Testing.....	170
4.58 Stiffness Improvement of Epoxy Foamed Interlayer	172
4.59 Mode II Fracture Toughness Improvement of Epoxy Foamed Interlayer	172
4.60 (SEM) Control CFRP Fracture Surface at SEM.....	173
4.61 (SEM) Epoxy Foamed Interlayer within Carbon Fiber Plies.....	174
4.62 (SEM) CNT Reinforced Epoxy Foamed Interlayer within Carbon Fiber Plies	175
4.63 (SEM) CNT Reinforced Epoxy Foamed Interlayer within Carbon Fiber Plies	176
4.64 (SEM) (a) and (b): CNT Reinforced Epoxy Foamed Interlayer within Carbon Fiber Plies	177
4.65 Scatter Plot of Epoxy Foamed Interlayer CFRP	180
4.66 Residuals Analysis for Epoxy Foamed Interlayer CFRP Model.....	183
4.67 Residuals Analysis for Epoxy Foamed Interlayer CFRP Model with transformation.....	188
4.68 Microsoft XL (139) Algorithm for Levene's Test.....	189
4.69 Outliers and Influence on Preliminary Model of Epoxy Foamed Interlayer CFRP	191

4.70 Influence on parameters of on Preliminary Model of Epoxy Foamed Interlayer CFRP	191
4.71 Interactions of Epoxy Foamed Interlayer CFRP Preliminary Model	193
4.72 Pearson Correlation with Predictor Variables and Interactions – Epoxy Foamed Interlayer CFRP	194
4.73 Pearson Correlation with Predictor Variables and Standardized Interactions – Epoxy Foamed Interlayer CFRP	194
4.74 Best Subsets Regression of all Predictor Variables and Interactions for Both Cases for Epoxy Foamed Interlayer CFRP	195
4.75 Backward Elimination and Forward Stepwise Methods for evaluating all Predictor Variables and Interactions for Both Cases for Epoxy Foamed Interlayer CFRP	196
4.76 Model 1 Residuals Graphs – Epoxy Foamed Interlayer CFRP	199
4.77 Model 2 Residuals Graphs – Epoxy Foamed Interlayer CFRP	201
4.78 Model 3 Residuals Graphs – Epoxy Foamed Interlayer CFRP	203
4.79 Scheme of Electrospun Fiber Interlayer within CFRP Plies.....	210
4.80 Control CFRP Flexural Testing	212
4.81 CFRP with Electrospun Fiber Interlayer Flexural Testing	213
4.82 CFRP with CNT Reinforced Electrospun Fiber Interlayer Flexural Testing	213
4.83 Control CFRP Tensile Testing	215
4.84 CFRP with Electrospun Fiber Interlayer Tensile Testing	215
4.85 CFRP with CNT Reinforced Electrospun Fiber Interlayer Tensile Testing.....	216
4.86 Stiffness Improvement of Electrospun Fiber Interlayer	218
4.87 Mode II Fracture Toughness Improvement of Electrospun Fiber Interlayer.....	218
4.88 (SEM) Electrospun Fiber Interlayer within CFRP Plies.....	219
4.89 (SEM) Electrospun Fibers on Top of Fiber Bed prior to Polymerization	220
4.90 (SEM) Electrospun Fibers including CNT	221

4.91 (SEM) CNT Reinforced Electrospun Fiber Interlayer within CFRP Plies	223
4.92 (SEM) CNT Reinforced Electrospun Fiber Interlayer within CFRP Plies	223
4.93 Scatter Plot – Electrospun Fiber Interlayer CFRP	226
4.94 Residuals Analysis of the Preliminary Fitted Model – Electrospun Fiber Interlayer CFRP	229
4.95 Microsoft XL (139) Algorithm for Levene’s Test – Electrospun Fiber Interlayer CFRP	230
4.96 Outliers and Influence – Electrospun Fiber Interlayer CFRP	232
4.97 Influence on Parameters – Electrospun Fiber Interlayer CFRP	232
4.98 Interactions – Electrospun Fiber Interlayer CFRP	234
4.99 Pearson Correlation (predictor variables & interactions) – Electrospun Fiber Interlayer CFRP	235
4.100 Pearson Correlation (predictor variables & standardized interactions) – Electrospun Fiber Interlayer CFRP	235
4.101 Best Subsets Regression for Evaluating All Predictor Variables in the Two Cases for Electrospun Fiber Interlayered Composite	236
4.102 Backward Elimination and Forward Stepwise Methods for Evaluating All Predictor Variables in the Two Cases for Electrospun Fiber Interlayered Composite	237
4.103 Model Residuals graphs – Electrospun Fiber Interlayer CFRP	240
4.104 Flexural Strength Improvement Comparison between the Three Different Interlayer Systems	246
4.105 Mode II Fracture Toughness Improvement Comparison between the Three Different Interlayer Systems	247

LIST OF TABLES

Table	Page
2.1 GLSL Viscoelastic Model Parameters Explanation (9)	18
2.2 Repair Clave and Autoclave Advantages and Disadvantages (46; 47)	41
3.1 Experimental Parameters and Characteristics for DMA Evaluation	68
3.2 Lay-up Before Curing in Repair Clave (46)	70
4.1 Theoretical and Experimental Correlation of Storage Modulus and $\tan\delta$ at 0.01 and 1 Hz	95
4.2 Flexural and Compression Average Moduli and Strengths for the CFRP Panels Manufactured under 0, 30, 50, and 70 psi (0, 205, 345, and 485 kPa)	106
4.3 Comparison of Specimens Manufactured in Press Clave and Autoclave	109
4.4 Variables – Preliminary Fitted Model of Manufacturing Pressure Variation	110
4.5 Pearson Correlation Matrix- Manufacturing Pressure Variation	111
4.6 Model Data - Manufacturing Pressure Variation	112
4.7 Parameters of the Preliminary Fitted Model - Manufacturing Pressure Variation	113
4.8 ANOVA Table – Manufacturing Pressure Variation	113
4.9 Other Parameters of the Preliminary Model Regression - Manufacturing Pressure Variation	114
4.10 Model 1 Parameters – Manufacturing Pressure Variation	124
4.11 Model 1 ANOVA Table – Manufacturing Pressure Variation	125
4.12 Other Information of Model 1 – Manufacturing Pressure Variation	125
4.13 Model 2 Parameters – Manufacturing Pressure Variation	127
4.14 Model 2 ANOVA Table – Manufacturing Pressure Variation	127
4.15 Other Information of Model 2 – Manufacturing Pressure Variation	127

4.16 Model Assumption Comparison – Manufacturing Pressure Variation	129
4.17 Outliers and Influence - Manufacturing Pressure Variation	130
4.18 Observation Influence on Parameters - Manufacturing Pressure Variation.....	130
4.19 ANOVA Table of the Selected Model – Manufacturing Pressure Variation	130
4.20 More Information on the Selected Model – Manufacturing Pressure Variation.....	131
4.21 Selected Model Parameters and Covariance Table – Manufacturing Pressure Variation.....	132
4.22 PNC Theoretical and Experimental Approaches Correlation.....	157
4.23 Preliminary Foam System Morphology	158
4.24 Epoxy Foamed Interlayered CFRP DMA Characterization.....	165
4.25 Epoxy Foamed Interlayer CFRP Flexural Testing Summary.....	168
4.26 Epoxy Foamed Interlayer CFRP Tensile Testing Summary	171
4.27 Mode II Fracture Toughness Evaluation of Epoxy Foamed Interlayer CFRP	172
4.28 Variables – Epoxy Foamed Interlayer CFRP for Regression Analysis	178
4.29 Pearson Correlation Matrix – Epoxy Foamed Interlayer CFRP	178
4.30 Flexural Strength Model Data of Epoxy Foamed Interlayer CFRP	180
4.31 Parameters of the Preliminary Fitted Model – Epoxy Foam Interlayer CFRP	181
4.32 ANOVA Table – Epoxy Foam Interlayer CFRP	181
4.33 Other Parameters of the Preliminary Model Regression – Epoxy Foam Interlayer CFRP	182
4.34 Transformations Evaluations for Interlayer Improvement (x4 of the preliminary fitted model).....	185
4.35 Parameters of Preliminary Fitted Model Using Transformation	186
4.36 ANOVA Table of Preliminary Fitted Model Using Transformation	186
4.37 Other Parameters of Preliminary Fitted Model Using Transformation	187
4.38 Model 1 Parameters – Epoxy Foamed Interlayer CFRP.....	198
4.39 Model 1 ANOVA Table – Epoxy Foamed Interlayer CFRP.....	198

4.40 Other Information of Model 1 – Epoxy Foamed Interlayer CFRP	198
4.41 Model 2 Parameters – Epoxy Foamed Interlayer CFRP.....	200
4.42 Model 2 ANOVA Table – Epoxy Foamed Interlayer CFRP.....	200
4.43 Other information of Model 2 – Epoxy Foamed Interlayer CFRP	200
4.44 Model 3 Parameters – Epoxy Foamed Interlayer CFRP.....	202
4.45 Model 3 ANOVA Table – Epoxy Foamed Interlayer CFRP.....	202
4.46 Other information of Model 3 – Epoxy Foamed Interlayer CFRP	202
4.47 Model Assumptions Comparison – Epoxy Foamed Interlayer CFRP	204
4.48 Outliers and Influence - Epoxy Foamed Interlayer CFRP.....	205
4.49 Observation Influence on Parameters - Epoxy Foamed Interlayer CFRP	205
4.50 Selected Model ANOVA Table – Epoxy Foamed Interlayer CFRP	205
4.51 Other Information on Selected Model – Epoxy Foamed Interlayer CFRP	206
4.52 Selected Model Parameters and Covariance Table – Epoxy Foamed Interlayer CFRP	207
4.53 Dynamic Mechanical Analysis of Electrospun Fiber Interlayer CFRP	211
4.54 Flexural Testing Summary of CFRP Composites with CNT Electrospun Fibers	214
4.55 Tensile Testing Summary of CFRP Composites with CNT Electrospun Fibers	216
4.56 Mode II Fracture Toughness Improvement of CFRP with Electrospun Fiber Interlayer	217
4.57 Preliminary Model Variables – Electrospun Fiber Interlayer CFRP	224
4.58 Pearson Correlation Matrix – Electrospun Fiber Interlayer CFRP	224
4.59 Model Data – Electrospun Fiber Interlayer CFRP.....	226
4.60 Parameters of the Preliminary Fitted Model – Electrospun Fiber Interlayer CFRP	227
4.61 ANOVA Table – Electrospun Fiber Interlayer CFRP	227
4.62 Other Parameters of the Preliminary Model Regression – Electrospun Fiber Interlayer CFRP	228

4.63 Model 1 Parameters – Electrospun Fiber Interlayer CFRP.....	239
4.64 Model 1 ANOVA Table – Electrospun Fiber Interlayer CFRP	239
4.65 Other information of Model 1 – Electrospun Fiber Interlayer CFRP	240
4.66 Model Assumptions Fulfillment – Electrospun Fiber Interlayer CFRP	241
4.67 Variance Inflation – Electrospun Fiber Interlayer CFRP	241
4.68 Outliers and Influence– Electrospun Fiber Interlayer CFRP	242
4.69 Observation Influence on Parameters – DFBETAS – Electrospun Fiber Interlayer CFRP	242
4.70 Selected Model Parameters and Covariance Table – Epoxy Foamed Interlayer CFRP	243
4.71 List of Interlayer Types	245
4.72 Average Densities of CFRP with All Interlayer Cases	248

CHAPTER 1

INTRODUCTION

1.1 Problem Introduction

The quest for lighter but stronger composites for use in aviation is a never ending one. With the increase in fuel prices, increased pressure can be expected for the development and use of lighter structural materials. One way of achieving this goal is to induce porosity into the system without sacrificing strength. For many years, honeycomb construction has been a key to making lightweight efficient sandwich structures. Notably, structural foams have met with limited acceptance, due to variations in properties and durability issues. This work over the past four years has demonstrated that controlled induced porosity, especially at the nano-scale, where it is likely connected to the free volume of the polymer matrix, can potentially have a major impact.

The focus of the present work is to create a unique framework for creating the next generation composite technology that can achieve significantly lighter structures, while maintaining its load bearing structure characteristics such as strength. Although the introduction of classic continuous fiber reinforced composites promised a nominal 40% reduction in weight over aluminum, its inherent anisotropy and heterogeneity as well as imperfect interface adhesions reduced the effectiveness to less than 20%. However, the introduction of porosity in continuous fiber reinforced composites promises similar game changing potential. Even though the special location and structure of porosity and its transparency to the environment, such as open pores versus closed pores (i.e. Sponges whose pores diffuse the light and make it opaque), promises similar challenges. Nonetheless, even if only a 20% further reduction in weight is achieved by controlling porosity at different scales (macro, micro, and nano) without reduction in strength, it may be viewed as the only way for CFRP to achieve their full potential of producing the promised 40% weight reduction over

traditional aluminum structures. At the moment, no one can refute that for the past 30+ years, the aviation designers and engineers have been caught in a paradigm where design of load bearing structures in commercial and military aircraft has been that of “black aluminum,” that is, no order of magnitude changes over aluminum have been realized.

The recent experience of the Boeing 787 is demonstrating this analogy beyond preliminary design, where changes even at this late stage are taking place by substituting aluminum for composite load bearing structures. Especially when one considers utilization of CFRP in smaller aircraft that are prone to damage, such as military, next generation of commercial narrow body aircraft, and general aviation aircraft, the long established metal-repair procedures that are used for larger commercial aircraft, such as the Boeing 777 and the Boeing 787, will not be acceptable. Studies are currently underway where materials that may be considered as a special form of structural foam have been evaluated for primary aircraft structures.

1.2 Scope of this Research - Featherweight Composites

Featherweight composites have been inspired by flying structures and architectures found in nature for millions of years now. These structures, which can be shown from a micro-, nano- and macro-structural (MNM) aspect, constitute the feathers that have been reliably serving flying members of the animal kingdom. Taking into account the harmony that feather structures present in nature, this work makes an effort to include their micro- and nano-design in a new class of materials which will serve technological applications with similar reliability.

The feathers structural beauty and optimization may be attributed to their scalable hollowness and porosity from the macro- to nano-scale. The hollowness of a feather reduces weight systematically within its parts from the rachis to the barb and to the hamuli. Feathers are not only hollow, but fractal. This means they use self similarity across many scales to optimize lift (bending moments), drag (shear stress), thermal conduction, radiation reflection, convective

boundary layer, electrical dissipation and wetting properties, among other things. Overall, this configuration comprises a neat fractal structure which contributes to the high strength as well as to the reduction of weight while independently controls loft (bulk).

Inspired by the feathers unique role in nature, a new class of materials is introduced, the featherweight composites, which consists of hollow parts from a macro- to micro- and nano-scales structured in a fractal configuration. Featherweight composites aim to replace conventional carbon fiber reinforced composites (CFRP) in applications where material properties, density, and bulk must be independently controlled. This goal can be achieved by inducing porosity into the system without sacrificing strength.

The main focus of this is to present an ideal framework for creating and introducing the next generation of polymer composite materials technology that is dramatically lighter than conventional CFRP, while maintaining its load bearing structure characteristics such as strength.

Featherweight composites have an optimal functionality in structures where the strength over weight ratio needs to be maximized for energy savings at a first glance, but for other reasons as well. Aviation, automotive industries, sporting goods, marine industries, etc., will derive tremendous benefits from such material system designs. This concept is expected to make a significant impact on energy versus material focused utilization.

1.3 The Interlayer Reinforcement – Critical Part of the Featherweights

Even though polymeric composite layered structures and processes have been established and widely used in aviation and in other high tech industries, from an analytical as well as from a manufacturing perspective, laminates are expected to behave as homogeneous structures with uniform stress through the material thickness.

The laminate interlayer (the region between two successive laminates/pplies) is an extensively investigated part of the carbon fiber reinforced composite mainly due to its tendency to delamination. Numerous works around the world have been performed in order to reinforce the interlayer of a multi-lamina (carbon) fiber reinforced composite and significantly increase its

strength. The interlayer and as a result the entire composite properties enhancement has been several times improved through micro and/or nano reinforcements. Furthermore, the interlayer property enhancement is a matter of manufacturing; this work as such supports the impregnation of the interlayer micro- and/or nano- modifications together with the carbon fiber bed under the method of double pass impregnation that will be extensively discussed later on.

The work performed with prepreps that modify the interlayer while maintaining an overall high level of fiber content throughout the laminate is extended and exploited to provide nano-, micro-, and macro-cellular interlayer structures which will result in a light-weight configuration. The advantage of the interlayered structures is that they are able to use nano-structured architectures, such as nano foam, random and oriented nanotubes, electrospun nanofibers etc, in order to create a new generation of polymer matrix composites that can make an impact on the lightness of aircraft structures, by decreasing the weight of conventional composite structures nominally, by more than 20% without affecting strength.

1.4 Need for Research

There is a continuous need, mainly in the aerospace industry as well as in other industries such as automotive, marine, etc, for lighter structures in order to achieve lower energy consumption. The latter will benefit industries from an economic and an ecological point of view as well as from a business growing point of view due to longer travel distances with the same fuel amount. This research will contribute in establishing much lighter materials in primary structures without sacrificing the strength and thus, essentially contribute to more energy efficient structures. Furthermore, the need for this research is critical in order to overcome the “black aluminum” paradigm that was previously described and manage to fully offer the theoretical weight benefits the conventional CFRP promised when initially utilized in high tech applications. The philosophy of this research work is to create new composite structures which will constitute materials that can be even lighter and theoretically result in additional weight reduction of more than 20% without sacrificing strength.

1.5 Research Methodology Overview

In order to work towards covering the needs of this research such as the tremendous energy savings and the lighter primary structures in high tech application to fully exploit CFRP theoretical benefits, particular steps have to be followed in the design and built of the featherweight composites. Initially, the matrix system and the manufacturing methods have to be extensively described and analyzed, and then the interlayer systems have to be designed, analyzed, and tested for evaluating their contribution to the scope of featherweight composites. At first, an effort is made to assess the Dynamic Mechanical Analysis (DMA) technique as the main one for describing and analyzing the kinetics and the viscoelastic behavior of the matrix systems used in featherweights, furthermore, an investigation on the high tech manufacturing methods for carbon fiber reinforced composites is performed. The steps on the prepregging-layup-autoclaving procedure are described in a distinguishable and appropriate manner followed by a new clave method that separates the heat from the pressure providing cost effective manufacturing. Moreover, all the technologies utilized in the interlayer, both the ones that reduce the weight by creating nano free volume and the ones that increase the strength and the toughness of the composite, are investigated separately at first followed by their integration in specific engineered material models. Based on an extensively investigated interlayer system that is currently in use in aviation, technologies such as randomly oriented carbon nanotubes, aligned carbon nanotubes, controlled polymeric foams reinforced with nano inclusions and electrospun nano-fibers, are presented in this work as critical interlayer reinforcements resulting in integrating methods for featherweight composites design and engineering.

The main objective of this work is to basically improve current Carbon Fiber Reinforced Polymer Composites in terms of light weight and high strength. The key part of investigation for achieving such a goal is the introduction and the reinforcement of the interlayer – the area between two successive plies. Working towards this objective, a detailed literature review on the

technologies involved to the featherweights is given, an analytical examination of all the phases of the entire composite as well as of the manufacturing processes that take place is needed. As a result, the resin matrix system, the entire manufacturing process (prepreg, lay-up, and autoclaving), and the interlayer itself are extensively analyzed and described in order to exhibit new ways of introducing higher strength, and lower weight to CFRP. This work consists of a well-complimented effort from the basis of the composites theory to the nanotechnology trying to establish a new era of lighter and stronger polymer composite structures in aerospace and other technological fields.

Having extensively analyzed the featherweight composites manufacturing process, several technologies are separately utilized for the interlayer reinforcement in order to address the potential of several choices available to the engineer, which will offer him/her the ease to design the appropriate material for a particular application. The systems designed for the interlayer aim to be fractal structures from the macro to micro and to nano sizes giving to the overall material a strength and weight combination similar to the real feathers met in nature.

Eventually, the Interlayer Enabling Systems (IES) under investigation focus on lighter weight and multi-functionality utilizing nanotechnology in order to introduce scaled porosity down to nano-porosity and to at least maintain if not improve the material system strength. For this purpose the following more specific objectives have been assessed:

Preliminary, Interlayer Building Objectives

- Objective #1: Viscoelastic Analysis and Description Technique – Suitability for the Matrix System Characterization (1; 2)
- Objective #2: Exploration of Manufacturing Process and Evaluation of Innovative Clave Manufacturing (3; 4).
- Objective #3: Micro-spherical Particles (Modifier Particles) Reinforced Interlayer (5) – The Base on Which New Interlayer Structures are Introduced to the Composite to Form the Featherweights.

New Interlayers Investigation Objectives

- Objective #4: Carbon Nanotube in Detail Density and Modulus Analysis (6; 7) – Smallest Part of the Fractal Structure within the Interlayer and Mean of Introducing Nano-Porosity.
- Objective #5: CNT Controlled Nano-porosity Reinforced Interlayer – Strength, and Light Weight Improvements
- Objective #6: CNT Electrospun Fibers Reinforced Interlayer – Strength, and Light Weight Improvements

Objectives 1 to 3 introduce the basic processes of experimentally analyzing an interlayer system, the dynamic behaviour characterization, the composite manufacturing, and the main process of interlayer introduction. After that, objectives 4 to 6 are set for the new interlayers investigation, design, manufacturing, and evaluation for meeting the specifics for featherweight composites.

1.6 Dissertation Outline

The dissertation thesis includes two main parts which are specifically connected to each other. First part is the matrix system viscoelastic description and analysis through both modeling and experimental results with main focus on evaluating the technique (Dynamic Mechanical Analysis – DMA) used to describe the viscoelastic behaviour of the epoxy resin matrix system. The first part also describes the manufacturing process of composites introducing and evaluating an innovative technique for processing composites of equal properties with dramatically reduced cost. Furthermore, the first part is introducing the concept of interlayer reinforcement, together with its processing starting from a micro-sphere interlayer system that has already been manufactured in Polymeric Composites Laboratory. The second part includes design, manufacturing, and evaluation of new interlayer systems with ultimate goal to establish lighter composites with higher strength. Two new interlayer systems, the controlled epoxy foamed, and the electrospun nano-fiber interlayer system are introduced and extensively investigated. The introduction of carbon nanotubes in those two latter interlayers is examined as

well. The interlayer systems are compared in the end of the analysis in terms of flexural strength and fracture toughness improvement.

The main body of the dissertation thesis discusses in-detail the previously mentioned two parts and focuses firstly on the technological background which starts in chapter two giving information on matrix system viscoelastic analysis in order to address the suitability of the experimental process viscoelastic characterization, on prepreg and final composite structures manufacturing, and on the interlayer systems that will be investigated. The micro-spherical particles as an established interlayer system is used as the base on which the new interlayer systems will be introduced. Thus, the characterization of micro-spherical particles interlayer is also included in chapter two. Background on epoxy foaming and electrospun techniques is also mentioned towards the end of chapter two. Furthermore, the third chapter with the rationale for experimental procedure for each objective proceeds giving the actual tasks that are performed for accomplishing each objective. In other words, chapter three presents the research methodology that is followed to meet each of the six objectives. After that, the fourth chapter presents the results derived from each research task as these have been mentioned in chapter three. Finally, the conclusions of all the modeling and experimental work are in chapter five where the results are summarized. An overall summary with hints of future research to be performed is following in chapter five and the dissertation ends followed by a references list. Overall, general background, research methodology, results and discussion, and conclusions are presented within four chapters respectively, for all objectives addressed in section 1.5.

Working towards the main objective of this research, completion of the specific objectives addressed in section 1.5 through the tasks mentioned in research methodology, and exploration, analysis, and interpretation of the collected results, are performed. The main scope of this research is accomplished through the theoretical and experimental proof that featherweight composites can be manufactured to be lighter than conventional CFRP and at the same time not only to maintain their properties, but also to be stronger.

CHAPTER 2

BACKGROUND

2.1 Matrix System Description and Analysis

Starting with the matrix system, it is very critical to describe the composite resin system viscoelastic characterization technique in order to understand and address its suitability for utilization in the viscoelastic characterization that is performed in matrix system. This technique is called dynamic mechanical analysis (DMA) and it has to be explained in detail. In this section, the Generalized Standard Linear Solid (GSLs) model developed by Seferis and co-workers (1; 2; 8; 9) is extensively described as well in order to demonstrate the potential of dynamic mechanical analysis to describe the viscoelastic behavior of composites. GSLs is based on classic viscoelastic theory, as a consequence the potential DMA correlation with the model justifies the DMA experimentation as the major technique for accurately describe the viscoelastic behaviour of polymer composites. This potential is later on proved in the results and discussion section, where DMA results are correlated with the model.

2.1.1 Dynamic Mechanical Analysis

Dynamic Mechanical Analysis (“DMA”) and the properties measured by this technique are widely used to study the behavior of viscoelastic materials. DMA is a very useful method for quality control and for correlations between structure and properties of polymeric composite materials. Furthermore, testing polymeric composites with DMA is complex as their dynamic mechanical properties are sensitive to fiber orientation as well as inhomogeneities in thermoset matrix cross-linking (10). Dynamic mechanical measurements are also able to detect the presence of the interphase in glass- and carbon-fiber reinforced polymers (10; 11; 12). Utilizing frequency multiplexing, calculation of apparent activation energies from relaxation spectra and correlation with rheological models is possible.

DMA shows high potential as an experimental technique for composite degradation studies due to its ability to show in situ viscoelastic characteristics of degrading composites over a wide range of temperatures and times or frequencies.

For viscoelastic materials, strain is not in phase with displacement stress, when a sinusoidal stress is applied. The dynamic modulus, M^* , is defined as the ratio of an applied sinusoidal stress, σ^* , to the resulting sinusoidal strain, ε^* . In the case that the sample is linearly viscoelastic, the frequency of the strain will be the same as the frequency of the applied stress, but will lag the stress by an angle δ , which is called the phase lag. In the non – linear viscoelastic region, which is met at higher stress levels, the strain is no longer sinusoidal and no longer proportional to the stress. The applied sinusoidal stress and the corresponding strain for the linear viscoelastic region are given through (13; 14):

$$\sigma^* = \sigma_0 \cdot e^{i \cdot \omega \cdot t} \quad 1$$

$$\varepsilon^* = \varepsilon_0 \cdot e^{i \cdot \omega \cdot t - i \cdot \delta} \quad 2$$

Where:

σ_0 = sinusoidal stress amplitude (MPa)

ω = stress angular frequency (s^{-1})

t = time (s)

ε_0 = sinusoidal strain amplitude

δ = phase lag between stress and strain (angle degrees)

The dynamic mechanical modulus M^* is the one of the most common concepts to express dynamic mechanical data acquired during the experiment. It is defined as the ratio of an applied sinusoidal stress to the resulting sinusoidal strain in the material being tested. M^* can be expressed as follows:

$$M^* = \frac{\sigma^*}{\varepsilon^*} = |M^*| \cdot e^{i\delta} = M' + i \cdot M'' \quad 3.1$$

$$|M^*|^2 = (M')^2 + (M'')^2 \quad 3.2$$

$$\tan \delta = \frac{M''}{M'} \quad 3.3$$

Where:

M' = storage modulus (MPa)

M'' = loss modulus (MPa)

$|M^*|$ = magnitude of dynamic mechanical modulus (MPa)

δ = phase lag between the applied stress and the strain response (angle degrees)

Dynamic mechanical data may also be expressed in the form of complex compliance,

J^* defined as the reciprocal of complex modulus (14):

$$J^* = J' - i \cdot J'' = |J^*| \cdot e^{-i\delta} = \frac{1}{M^*} \quad 4.1$$

$$J' = \frac{M'}{|M^*|^2} \quad 4.2$$

$$J'' = \frac{M''}{|M^*|^2} \quad 4.3$$

Where:

J' = storage compliance (MPa⁻¹)

J'' = loss compliance (MPa⁻¹)

$|J^*|$ = magnitude of complex compliance (MPa⁻¹)

Finally, dynamic mechanical data may also be expressed in the form of complex dynamic viscosity, μ^* , most commonly in the case of liquid systems:

$$\mu^* = \mu' + i \cdot \mu'' = |\mu^*| \cdot e^{i\left(\delta - \frac{\pi}{2}\right)} = \frac{M^*}{i \cdot \omega} \quad 5.1$$

$$\mu' = \frac{M''}{\omega} \quad 5.2$$

$$\mu'' = \frac{M'}{\omega} \quad 5.3$$

$$|\mu^*| = \frac{|M^*|}{\omega} \quad 5.4$$

Where:

μ' = viscous (or in-phase) component (Pa*s)

μ'' = elastic (or out-of-phase) component (Pa*s)

$|\mu^*|$ = magnitude of complex viscosity (Pa*s)

The viscous parameter is in-phase when speaking for complex viscosity. However the material is not only viscous and it also tends to partly restore some of the obtained deformation (elastic parameter). This restoration occurs with retardation, and thus it is out-of-phase. Nevertheless, it should be noted that all of these methods of reporting data are equivalent. Knowing any two parameters, the rest can be defined by using the equations 1 through 5.4 (8; 9; 15; 16; 17).

In the transition zones of a polymer during the experiment, the dynamic modulus is strongly dependent on temperature, and frequency, ω . Studying E' (Storage Modulus) (or G' (Shear Storage Modulus)) and $\tan\delta$ by changing frequency at constant temperature, and by changing temperature at constant frequency, is of high interest. DMA investigations of E^* (or G^*) versus T and ω can give information about relaxation processes such as the main chain relaxation from glass to rubber state related to the glass-transition process, and secondary transitions associated with movements of side chains or with motions of small parts of the main chain (10). In addition, dynamic mechanical properties associated with structural changes due to chemical reactions may be studied as well, for instance, during thermoset crosslinking reactions and during phase transformation from an organic to an inorganic material system, because of the degradation process.

2.1.2 *t-T Equivalence Principle and Master Curve*

When external parameters (e.g. temperature, pressure, mechanical, electrical or magnetic fields, etc) affect the internal parameters of a system (volume, strain, electrical or magnetic polarization), the polymeric system then passes from the equilibrium state into a stable “excited” state. The process of spontaneous return of a microscopic system into a thermodynamically stable state is termed relaxation (18)

In order to describe the viscoelasticity temperature dependence in terms of relaxation time, α_T coefficient was introduced (19):

$$\alpha_T = \frac{\tau(T)}{\tau(T_g)} \quad 6$$

Where:

α_T = shift factor

$\tau(T)$ and $\tau(T_g)$ are the relaxation times at T and T_g temperature respectively. Apparently $\alpha_T = 1$ at T_g .

The shift factor, α_T , has been determined by using the time-temperature superposition principle, an essentially empirical principle which has been verified by extensive experimental and theoretical studies. Among several analytical expressions of α_T , the expression proposed by (20) is the most well-known equation.

The simplest application of time-temperature superposition is to build a master curve by selecting a particular temperature and applying only a horizontal shift on a logarithmic time scale in order to make the curve for other temperatures join as continuously as possible to the curve at this particular temperature. Thus, mathematically a modulus can be expressed as:

$$M(T_1, t) = M\left(T_2, \frac{t}{\alpha_T}\right) \quad 7.1$$

$$M(T_1, t) = M(T_2, \omega \cdot \alpha_T) \quad 7.2$$

Even though the success and the general application to amorphous polymers of this superposition principle have been proven, one additional correction is required. The molecular theories of viscoelasticity suggest that there must be an extra small vertical shift factor changing from the actual temperature T (at a density ρ) to the reference temperature T_o (at a density ρ_o). Consequently, the mathematical expression for the correction becomes:

$$\frac{M(T_1, t)}{\rho \cdot (T_1) \cdot T_1} = \frac{M\left(T_2, \frac{t}{\alpha_T}\right)}{\rho \cdot (T_2) \cdot T_2} \quad 8.1$$

$$\frac{M(T_1, t)}{\rho \cdot (T_1) \cdot T_1} = \frac{M(T_2, \omega \cdot \alpha_T)}{\rho \cdot (T_2) \cdot T_2} \quad 8.2$$

The above method gives the modulus or compliance over time (or frequency) over a quite wide range. Hence, calculation of the relaxation (or retardation) time spectrum, and comparison of results with theoretical models is possible. One equation that describes the relaxation time is the Williams, Landel and Ferry equation known as "WLF equation" (20):

$$\log(\alpha_T) = \frac{C_1 \cdot (T - T_R)}{C_2 + (T - T_R)} \quad 9$$

Where C_1 and C_2 are constants and T_R is a reference temperature. The WLF equation covers the temperature range $T = T_R \pm 50$ °C for most of the amorphous polymers.

It is significant for the shift time to shorten in order to simulate (at the reference temperature T_R) a low-temperature property, while for the relative time to lengthen in order to simulate (at the T_R) a high-temperature property (17).

Furthermore, expressing the activation energy (E) dependence is possible, based on kinetic theory. Using the activation energy, the Arrhenius shift factor can then be expressed as:

$$\log(\alpha_T) = \left(\frac{E}{2.303 \cdot R}\right) \cdot \left(\frac{1}{T} - \frac{1}{T_R}\right) \quad 10$$

With regards to the glass transition process, the activation energy is in the range of 400-1000 KJ/mol. In the WLF equation, the activation energy at the reference temperature can be expressed by the constants C_1 and C_2 as:

$$E = 2.303 \cdot R \cdot (T_R^2) \cdot \left(\frac{C_1}{C_2} \right) \quad 11$$

Based on shift factors form, the relaxation time can be described as a function of temperature in two forms: the Arrhenius-type equation, and the WLF equation. The Arrhenius-type equation is mostly used below T_g while the WLF equation is usually used above T_g (9; 16; 17).

2.1.3 Viscoelastic Behavior

Generally, the composite materials are assumed to be invariant during viscoelastic analysis of polymers. Nevertheless, for the situations that viscoelastic characterization is of the most use, the structure is likely to be changing while the experiment is in progress. For those systems that materials undergo significant chemical or physical alteration, the retardation or relaxation time increases during the experiment (19). Viscoelasticity of epoxy curing reactions, where the reaction kinetics is successfully described by the changing retardation time, has been analyzed by (8; 21).

During carbonization processing of carbon carbon composites, the viscoelastic properties change due to degradation reactions which affect the final structure and performance of the composite. In such systems, a polymer matrix pre-form is degraded in an inert gaseous atmosphere, transitioning the organic resin of the composite to a carbon matrix. Therefore, the viscoelastic polymeric matrix composite most likely converts to an elastic carbon matrix composite. Being coupled with shrinkage and gasification during degradation, this transition is considered significant processing step due to the fact that it can be related to micro-cracking initiation and laminate delamination in the manufacturing processing of CCC (22). Moreover, the polymer matrix modulus at the rubber state may begin to increase due to further crosslinking

reactions at high temperatures. In addition, chain-scission reactions, which comprise typical degradation reactions for thermosetting matrix systems, can simultaneously occur resulting in modulus reduction. Understanding of these related structural changes is critical in order to control the CCC final performance.

Additionally, composite materials thermo-oxidative stability (TOS) is of primary technological concern in projects such as supersonic transport airplane development and in aircraft engine applications. In such high temperature load bearing applications, the degrading composites viscoelastic properties reflect the stiffness variation as a function of time and temperature. For quality assurance specifications and control tests in elevated temperature applications, degrading composites viscoelastic characteristics must be identified in the form of modulus and/or compliance. Consequently, the viscoelastic properties may be correlated with oven aging or weight-loss measurements, which comprise other conventional TOS techniques.

For the purpose of analyzing the matrix system of this study, a dynamic mechanical time-temperature multiplexing method is utilized to research the glass transition temperature and the initial degradation processes of a phenolic resin / carbon fiber composite system, which has been used as a pre-form of CCC. Modulus master curves for the two processes, have been created by a horizontal and vertical shift method. Based on the master curves results, the generalized standard linear solid model extensively utilized by (1; 2; 17), is developed in order to describe the dynamic mechanical properties of the model composite systems as a function of frequency and temperature during degradation.

2.1.4 GSLM Model Assumptions

The assumptions of the Generalized Standard Linear Solid Model are as following:

- I. Opposite to most studies assumptions, the relaxation time is not invariant as temperature varies.

- II. It is assumed that there are non-zero constants in the general form of linear viscoelasticity and thus, the form can be reduced to four non-zero constants which can describe both stress relaxation and creep.
- III. A mechanical analogous model is assumed to describe the viscoelastic behaviour of the composite, which has two elastic springs and one viscous dashpot in a series-parallel sequence.
- IV. The analogy to dielectric analysis has been demonstrated and utilized for the analysis of dynamic mechanical experiments
- V. The relaxation time can be described by the Arrhenius-type equation below T_g and by the WLF equation above T_g.

Based on the assumptions described above, the generalized standard linear solid model proposed by Dillman and Seferis is defined as (8):

$$G^* = G' + G'' = G_u - \frac{G_u - G_r}{(1 + i \cdot \tau \cdot \omega^\beta)^\alpha} \quad 12$$

Where G' and G'' have been previously defined and α, and β are parameters ranging from 0 to 1 which account for an asymmetric relaxation time distribution.

The real and imaginary components of the complex modulus can be derived by equations 3.1 through 3.3 as it is clearly described in the Dillman – Seferis model (8). According to the same model, the compliance form of the model J* can also be described (8; 9).

The characteristic feature of α and β in the model has been investigated in terms of J' and J'' in the τω axis (22). The empirical parameters α and β account for the non-ideality of the system when the distribution of the relaxation time is considered. As utilized in this study, the relaxation time may be described by the Arrhenius-type equation as:

$$\tau = \tau_0 \cdot e^{\left(\frac{E}{R}\right) \cdot \left(\frac{1}{T} - \frac{1}{T_0}\right)} \quad 13$$

Subsequently, the model consists of four parameters that need to be determined: τ₀, E, α, and β (R = gas constant). The effect of these parameters on the normalized G' and G'' curves in the

temperature axis can be derived by curves that have been expressed in (8; 9). It is important to note that α may be accounted by the combined effects of β and τ_0 . The activation energy, E, of the relaxation time is considered as a unique value that represents the characteristics of the nature of a polymer in the same way that the universal constants represent in the WLF equation (20). In this study, the activation energy is determined by the superposition principle, resulting in a temperature – dependent relaxation time. The other parameters of τ_0 and β are appropriately determined to fit the experimental data. Table 2.1 summarizes information about the variables.

Table 2.1 GLSL Viscoelastic Model Parameters Explanation (9)

Variable	Range
T	$T_{\text{Reference}} \pm 50 \text{ } ^\circ\text{C}$
E	$400 \text{ kJ} < E < 1000 \text{ kJ}$
τ_0	$\tau_0 > 0$
α	$0 < \alpha < 1$
β	$0 < \beta < 1$

The general form of linear viscoelasticity is generally described by the equation (13):

$$\alpha_0 \cdot \sigma + \alpha_1 \cdot \left(\frac{d\sigma}{dt} \right) + \alpha_2 \cdot \left(\frac{d^2\sigma}{dt^2} \right) + \dots = b_0 \cdot \varepsilon + b_1 \cdot \left(\frac{d\varepsilon}{dt} \right) + b_2 \cdot \left(\frac{d^2\varepsilon}{dt^2} \right) + \dots \quad 14$$

Assuming non-zero constants in equation 14, four non-zero constants can describe the characteristic features of both stress relaxation and creep. Then, the model equation will be formed as:

$$\alpha_0 \cdot \sigma + \alpha_1 \cdot \left(\frac{d\sigma}{dt} \right) = b_0 \cdot \varepsilon + b_1 \cdot \left(\frac{d\varepsilon}{dt} \right) \quad 15$$

The mechanical model, whose viscoelastic behaviour is described by two elastic springs and one viscous dashpot in a series-parallel sequence (Figure 2.1), has the following form of differential equation:

$$\sigma + \tau \cdot \left(\frac{d\sigma}{dt} \right) = G_r \cdot \varepsilon + G_u \cdot \tau \cdot \left(\frac{d\varepsilon}{dt} \right) \quad 16$$

Where

G_r : relaxed modulus (GPa),

G_u : unrelaxed modulus (GPa), and

τ : relaxation time (s).

The latter is defined as:

$$\tau = \left(\frac{\mu}{G_u - G_r} \right) \quad 17$$

This model is known as Standard linear Solid (“SLS”) model (23).

In DMA experiments with an oscillating stress of frequency ω , the complex modulus can be derived as:

$$G^* = G' + i \cdot G'' = G_u - \frac{G_u - G_r}{1 + i \cdot \tau \cdot \omega} \quad 18$$

The complex modulus G^* consists of

G' : storage modulus (GPa), and

G'' : loss modulus (GPa).

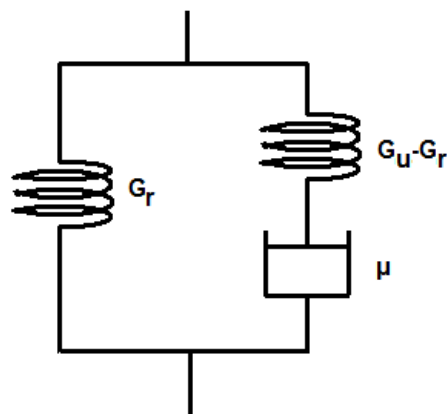


Figure 2.1 Standard linear Solid (“SLS”) Model (23)- Two Elastic Springs and One Viscous Dashpot in Series-Parallel Sequence

Successful efforts to monitor the polymers dynamic behavior have also been made through dielectric analyses and studies. The analogy of viscoelastic characterization to dielectric analysis has been demonstrated and utilized for the analysis of dynamic mechanical experiments (8; 24; 25; 26). Based on this analogy, a generalized standard linear solid model proposed by (8) is defined as:

$$G^* = G' + i \cdot G'' = G_u - \frac{G_u - G_r}{(1 + i \cdot \tau \cdot \omega^\beta)^\alpha} \quad 19$$

Where α and β are parameters ranging from 0 to 1 which account for an asymmetric relaxation time distribution.

The real and imaginary components of the complex modulus can be derived by equations 16 through 19 as it is clearly described in (8). According to the same model, the compliance form of the model J^* can also be described (8; 9).

The characteristic feature of α and β in the model has been described and investigated through J' and J'' in the $\tau\omega$ axis (22). The system's non-ideality is explained by the empirical parameters α and β , which take into consideration the relaxation time distribution. As utilized in this study, the relaxation time may be described by the Arrhenius-type equation as:

$$\tau = \tau_0 \cdot e^{\left(\frac{E}{R}\right) \left(\frac{1}{T} - \frac{1}{T_0}\right)} \quad 20$$

Subsequently, the model includes four parameters that need to be determined: τ_0 , E , α , and β . The influence of these parameters on the normalized G' and G'' curves in the temperature axis can be derived by curves that have been expressed in (8) model. The relaxation time activation energy E , is considered as a unique value which represents the characteristics of the polymer nature in the same way that the universal constants represent in

the WLF equation (20). In this work, the activation energy is derived by the superposition process, resulting in a temperature dependent relaxation time. The rest parameters, τ_0 and β are appropriately determined to fit the experimental data, and analyzed in the following sections.

Figure 2.2 presents the storage modulus of the composite at nine different frequencies as a function of temperature. The higher modulus at higher frequencies shows typical viscoelastic behavior, as it was expected. The glass transition process is observed between 220°C and 300°C, identified by the decreasing modulus. Following the glass transition, a modulus increase is observed between 320°C and 350°C because of the thermal degradation process and the high temperature crosslinking reactions. Above 350°C, the modulus decreases and its dependence on frequency disappears, showing an elastic behavior. Additionally, the increasing and decreasing modulus between 320°C and 400°C may be justified by the coupled structural changes due to random chain scission and additional crosslinking reactions.

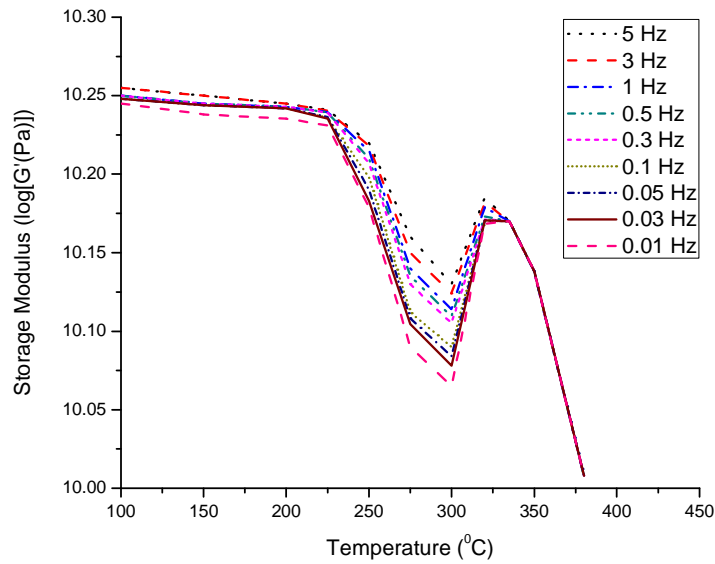


Figure 2.2 Measured DMA Storage Modulus of Phenolic Resin/Carbon Fiber Composite vs. Temperature - Nine Different Frequencies: from 0.01 to 5 Hz in Nitrogen Atmosphere at 300 ml/min (1; 2)

2.1.5 Master Curves for Tg and Degradation Processes

By analyzing the master curve of glass transition, the high modulus portion is given by low-temperature experiments and the low modulus portion by high-temperature experiments (1; 2; 17). The storage modulus dependence on temperature and frequency is demonstrated in Figure 2.3 for the glass transition between 230 and 295⁰C. As it can be observed, there is an overall change in the shape of the modulus-frequency curve as the temperature varies.

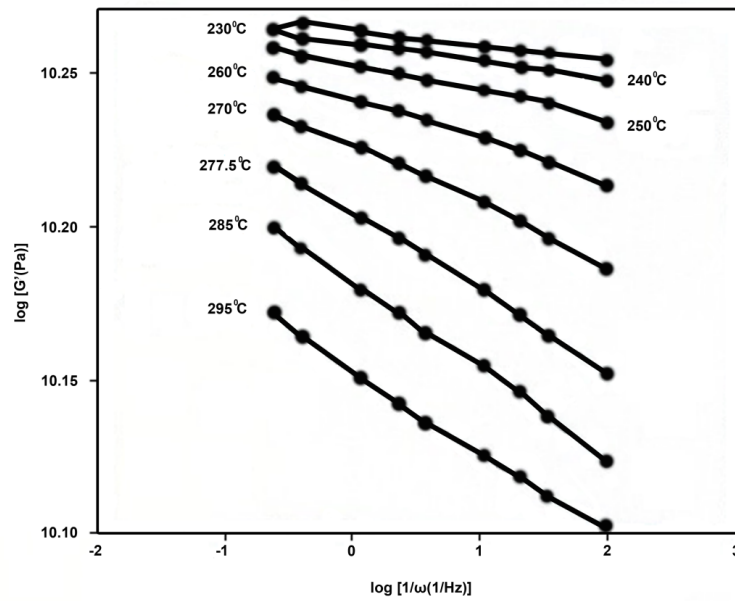


Figure 2.3 Storage Modulus for Glass Transition vs. Inverse Frequency at Different Temperatures (1; 2)

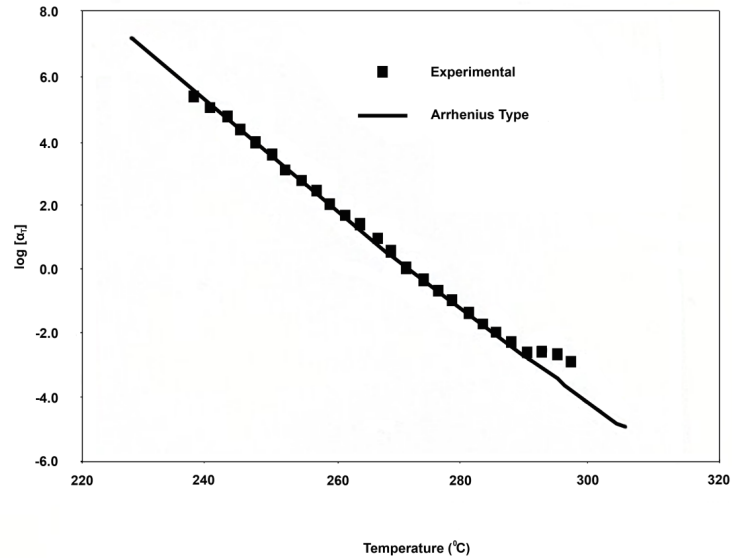


Figure 2.4 Shift Factors Compared with Arrhenius Type Equation Using $E=790.4\text{KJ/mol}$ and $T_0=277.50\text{C}$ for the Glass Transition (1; 2)

Note that the time dependent modulus is quite similar in form to the storage modulus plotted versus inverse frequency. Dynamic results found in the literature are sometimes plotted versus frequency and sometimes versus inverse frequency (27).

Moreover, in Figure 2.4 the shift factors temperature dependence, which was empirically constructed, is compared to the Arrhenius-type equation 10 with $E=2766.2\text{ KJ/mol}$ and $T_0=277.5^{\circ}\text{C}$. This equation fits the shift factor up to 290°C with a correlation of more than 99% (End of glass transition region), but beyond 290°C , it seems that equation 10 does not fit the shift factor anymore because degradation begins to occur.

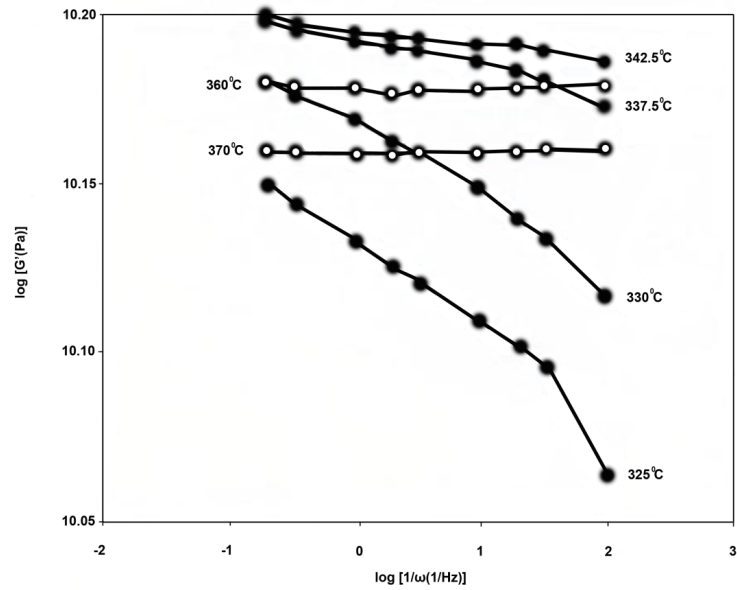


Figure 2.5 Storage Modulus for Degradation Processes vs. Inverse Frequency at Different Temperatures (1; 2)

As far as the degradation process is concerned, the storage modulus dependence on temperature and frequency is presented in Figure 2.5 between 320 and 370⁰C. It can be observed that overall shape of the modulus-frequency curve changes as the temperature varies. At low temperatures the frequency-dependent viscoelastic storage modulus rapidly changes with regards to frequency, on the other hand, at high temperatures, the modulus is almost constant with regards to frequency.

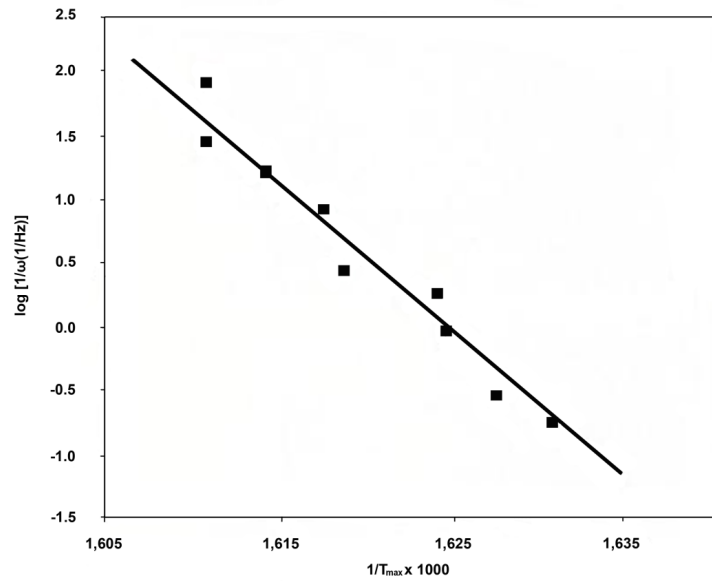


Figure 2.6 Horizontal Shift Factor for Degradation Process (1; 2)

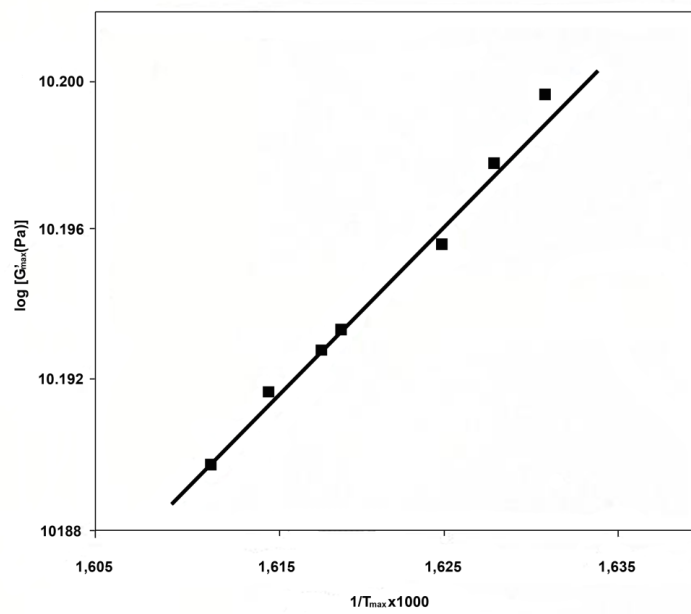


Figure 2.7 Vertical Shift Factor for Degradation Process (1; 2)

Furthermore, the modulus and frequency logarithmic values at the maximum peaks due to the high frequency dependence of the modulus in those areas are presented in Figure 2.6 and Figure 2.7, as a function of maximum temperature (T_{max}). Logarithmic values of frequency and G'_{max} exhibited linear relations with respect $1/T_{max}$, giving activation energies for the shift factors as -2461.3 KJ/mol and 8.782 KJ/mole in the horizontal and vertical directions, respectively, with a reference temperature of 342.5⁰C.

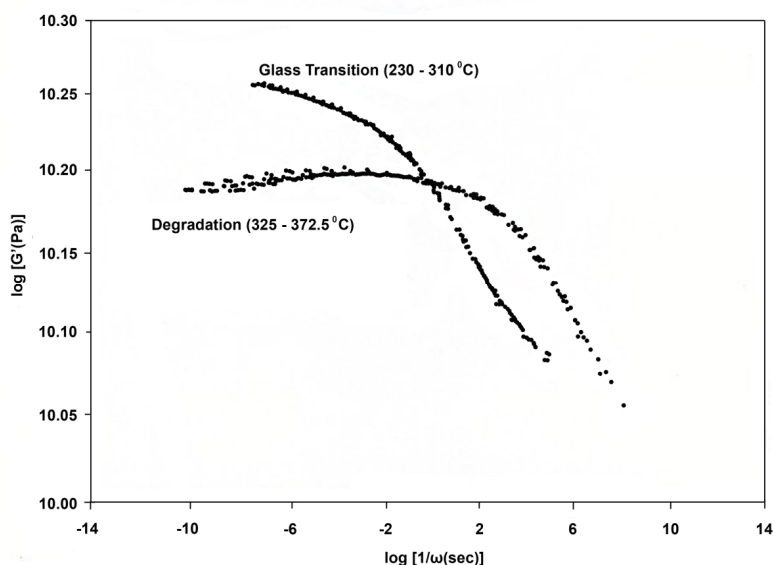


Figure 2.8 DMA Storage Modulus Master Curves for Glass Transition and Degradation Processes (1; 17; 22)

Consequently, through the utilization of these shift factors, the degradation master curve can be built as demonstrated in Figure 2.8 (1; 17; 22). A considerable conclusion is that at a specific time and temperature, the polymer property during degradation is comparable with the polymer property before degradation. The degradation process provides a favorably comparable storage modulus, demonstrating the possibility to improve or change the polymer modulus by controlled degradation processing. Considering the degradation process from a CCC point of view, the initial degradation step, which has been investigated in this study up to

400°C, is an outstanding processing stage revealing a significant change of polymer modulus from a rubbery to an elastic state.

2.1.6 Model Approach

From equation 19 the real and imaginary components of the complex modulus can be derived as (1; 2):

$$G' = G_u - \frac{(G_u - G_r) \cdot \cos(\alpha \cdot \theta)}{\left[1 + 2 \cdot (\tau \cdot \omega)^\beta \cdot \cos\left(\frac{\beta \cdot \pi}{2}\right) + (\tau \cdot \omega)^{2\beta}\right]^{\frac{\alpha}{2}}} \quad 21$$

$$G'' = \frac{(G_u - G_r) \cdot \sin(\alpha \cdot \theta)}{\left[1 + 2 \cdot (\tau \cdot \omega)^\beta \cdot \cos\left(\frac{\beta \cdot \pi}{2}\right) + (\tau \cdot \omega)^{2\beta}\right]^{\frac{\alpha}{2}}} \quad 22$$

$$\tan\theta = \frac{(\tau \cdot \omega)^\beta \cdot \sin\left(\frac{\beta \cdot \pi}{2}\right)}{1 + (\tau \cdot \omega)^\beta \cdot \cos\left(\frac{\beta \cdot \pi}{2}\right)} \quad 23$$

By equations 21 through 23 the relaxation times as well as the activation energies can be extracted for both the glass transition and the degradation processes independently through equations 24 and 25 (1; 2):

For the glass transition, ν is equal to 1.7611 and this value is taken from master curve in Figure 2.8. Consequently, the relaxation time can be expressed as a function of temperature via:

$$\tau_g = 10^{1.7611} \cdot \exp\left[\frac{E_g}{R} \cdot \left(\frac{1}{T} - \frac{1}{T_g}\right)\right] \quad 24$$

Where $E_g = 766.2$ KJ/mol and $T_g = 277.5^\circ\text{C}$. The same procedure was performed for the degradation process, providing the following relaxation time:

$$\tau_g = 10^{6.492} \cdot \exp\left[\frac{E_d}{R} \cdot \left(\frac{1}{T} - \frac{1}{T_d}\right)\right] \quad 25$$

Where $E_d = -2461.3 \text{ KJ/mol}$ and $T_d = 342.5^\circ\text{C}$.

The relaxed and unrelaxed moduli in the degradation processes were also derived by the master curve. Since the relaxation time was already determined, the other two parameters of G_u and G_r could be determined by rearranging equation 21:

$$G' = G_u - (G_u - G_r) \cdot h(\alpha_T \cdot \omega, \beta) \quad 26$$

Where

$$h(\alpha_T \cdot \omega, \beta) = \frac{\cos(\alpha \cdot \theta)}{\left[1 + 2 \cdot (\alpha_T \cdot \omega)^\beta \cdot \cos\left(\frac{\beta \cdot \pi}{2}\right) + (\alpha_T \cdot \omega)^{2\beta} \right]^{\frac{\alpha}{2}}}$$

Based on these equations (1; 2), when the storage modulus master curve is plotted over $h(\alpha_T \omega, \beta)$ for a certain value of β , G_u , and G_r can be determined by the intercept and slope of the line, respectively.

The relaxed and unrelaxed moduli for the degradation process may be described by the temperature-dependent shift factor in the vertical direction, as:

$$G_u = G_u^0 \cdot \exp\left[\frac{E_v}{R} \cdot \left(\frac{1}{T} - \frac{1}{T_d}\right)\right] \quad 27$$

$$G_r = G_r^0 \cdot \exp\left[\frac{E_v}{R} \cdot \left(\frac{1}{T} - \frac{1}{T_d}\right)\right] \quad 28$$

Where $E_v = 8.782 \text{ KJ/mol}$, $T_d = 342.5^\circ\text{C}$, and G_u^0 and G_r^0 are 16.02 and 9.313 GPa, respectively.

As it has already been stated, DMA experimental results, presented later in chapter 4, correlate with the GSLS model. The experimental process that was followed for DMA experimentation is explained in chapter 3 as well.

2.2 Differential Scanning Calorimetry

The differential scanning calorimetry uses the difference in heat flow through a sample, when it is heated at a constant rate and through a range of temperatures, to measure crystallinity for thermoplastic matrices and crosslinking for thermoset matrices. Since each material has a finite heat capacity, a specific amount of heat is absorbed or liberated at each of its transitions, which results to heat flow in and out of sample. A small amount of sample is heated at a constant rate along with a standard reference sample. At the beginning, constant heat flows through the reference sample using it as a reference line to monitor transitions of the actual sample heat flow. During transitions, the amount of heat flowing to the sample will increase or decrease depending on whether the transition is endothermic or exothermic. This difference in heat flow is monitored against temperature continuously (28).

From the plot of differential energy of heat flow versus the temperature, the area under or over a curve representing the energy transition is calculated. This area is directly proportional to the heat of fusion of the sample. Then the crystallinity or the crosslinking can be calculated from equation 29 (28; 29):

$$X_c = \frac{\Delta H_f}{\Delta H_0} \quad 29$$

Where:

ΔH_f is the heat of fusion for the sample (J/g), and

ΔH_0 is the theoretical heat of fusion for the fully crystalline or crosslinked material (J/g)

The transitions which can be seen to the DSC curves as endothermic or exothermic peaks are classified as 1st class transitions. In addition, the change as a discontinuity to the DSC curve, which remains flat and it is only transferred to the right when the specific heat of the sample changes, represents the glass transition temperature area of the sample and is

classified as 2nd class transition. The graph in Figure 2.9 presents a typical characteristic example of a semi-crystallized thermoplastic polymer which has been scanned in DSC.

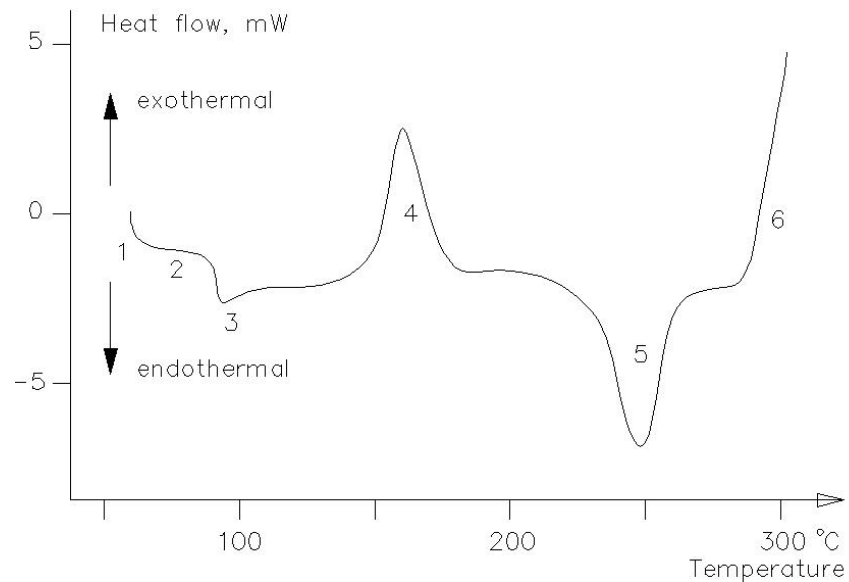


Figure 2.9 Typical Characteristic DSC Curve of a Semi-Crystallized Thermoplastic Polymer (29)

Where:

1. Initial deviation which depends on sample thermal capacity
2. DSC curve without thermal results (Baseline)
3. Glass Transition Temperature (2nd Class Transition)
4. Exothermic Peak of Remaining Crystallization (1st Class Transition) – Material is already semi-crystallized
5. Endothermic Peak of Sample Melting Point (1st Class Transition)
6. Oxidized Degradation Initiation

2.3 CFRP Impregnation and Manufacturing

As it has already been stated there is a three step process for achieving high quality composites and this is prepregging – lay-up – autoclaving. At this part the impregnation process

(prepregging) is in-detail described. In the prepregging of thermosetting resins, two main processes dominate the market: solution-dip impregnation and hot-melt impregnation. Some other processes, such as powder impregnation, which were originally developed for thermoplastics, have been applied to some thermosets but their use remains marginal and confined to experimental laboratory scale machines (30). In the present work hot melt impregnation is extensively described as the one mainly utilized in aerospace structures (3).

2.3.1 Hot-melt impregnation

A typical hot-melt prepregger comprises various components which are shown schematically in Figure 2.10 (3). These components can vary from one machine to another; the description given here is that of a “typical” prepregger. The prepregging process can be divided into three areas: the preimpregnation zone, where the fibers are aligned and the resin is `filmed (either on-line or separately); the impregnation zone per se, where the resin is forced into the fiber bed; and the postimpregnation zone, where the product is treated for storage and handling. In the preimpregnation zone, spools of fiber are placed on a creel and each tow is threaded into the machine.

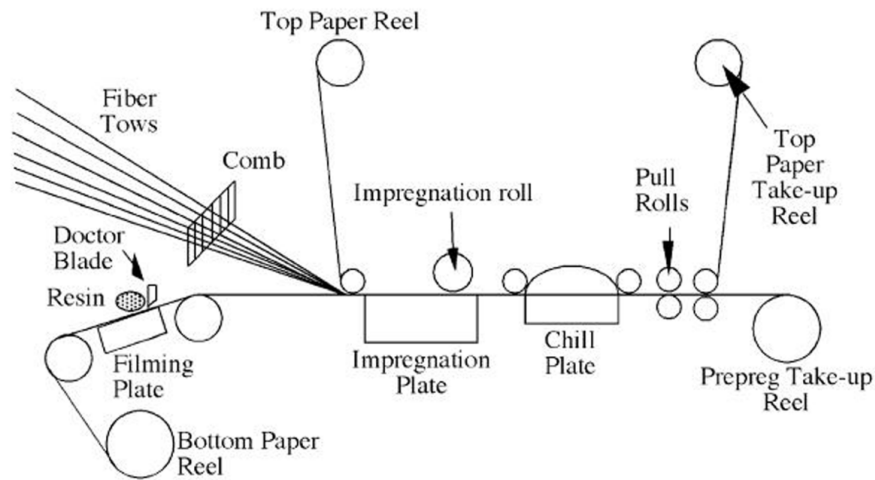


Figure 2.10 Hotmelt Prepreg Process

Located in front of the fiber reel is a comb through which the fibers are aligned in a systematic manner in order to prevent tow crossing and fiber damage; this is also when the areal weight is set. Once the tows have been aligned by the comb, they are threaded over a series of horizontal bars to provide adequate tension, as shown in Figure 2.11 (3). The amount of tension can be regulated by adjusting the tilt angle of the tension bars. Other ways to supply tension involve tension on the fiber spools themselves as well as sophisticated feedback control systems (31). Traditionally, a reverse roll coater or a doctor blade is used to prepare films onto release paper for hot-melt resin systems. The filming process is controlled by the coater temperature and the clearance between the doctor blade and the coating plate. A resin viscosity of 20 Pa*s is desired for filming, as suggested by Figure 2.12 (32). Resin is sheared spread on to the paper surface as the paper travels between the applicator and metering roll (reverse roll coater design, Figure 2.13 (3)) or between the filming plate and the blade (doctor blade design, Figure 2.14 (3)). Filming can take place on-line, just before the impregnation step, or it can take place off-line. While the advantages of on-line filming are evident, off-line filming might be used for economic or practical reasons. For example, some specific resin systems require a solvent evaporation step between filming and hot-melt impregnation. This may require a solvent recovery system. In such a case, filming off-line on a single station will be selected, despite the additional manipulations that it implies. Moreover, off-line filming operation can take place at a faster rate since it is not limited by the slower impregnation rate. Finally, a last advantage to off-line filming is that in case of fiber or paper breakage during impregnation, the filming operation is unaffected.



Figure 2.11 Fibers Introduction to the Prepreger

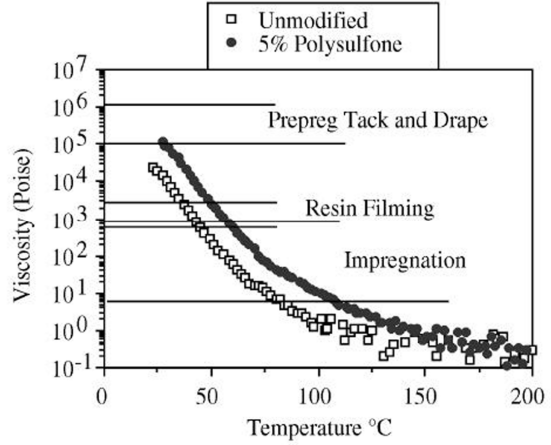


Figure 2.12 Resin Viscosity vs. Temperature

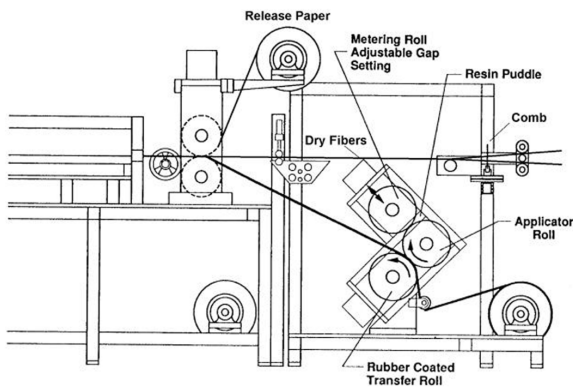


Figure 2.13 Reverse Roll Coater Design

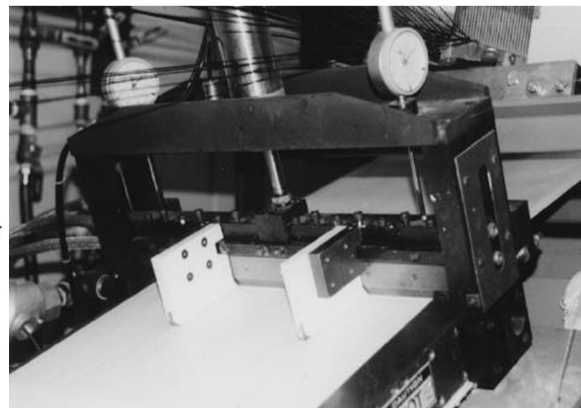


Figure 2.14 Prepreg Doctor Blade

The resin film resulting from the coating process is then brought into contact with the dry fiber web at the first roller station where the resin is released from the paper and impregnated into the fiber bed, as shown in Figure 2.15 (3) where it is seen that the fiber bed is sandwiched between two papers. The upper layer of release paper, which may or may not be film-coated, is used to prevent the rollers from contact with the resin and avoid resin build-up. Usually, the impregnation zone consists of a heated impregnation plate and one or more impregnation rollers. Generally, a set of nip-rollers follows the heated plate in order to control

the prepreg thickness (Figure 2.10). Often the impregnation rollers are heated to provide increased control of resin viscosity. Obtaining the desired areal weight and resin content, while maintaining fiber uniformity across the width (no splits or gaps within the fiber web), is an important aspect of product quality. The accurate control of tow spreading and resin flow is achieved by monitoring and carefully adjusting the impregnation temperature, impregnation gap, or pressure, as well as fiber tension and web speed. The impregnation zone is typically heated, either electrically or by hot oil, to a temperature where the resin viscosity is in a range close to 10 Pa*s (Figure 2.12). The impregnation rollers can be controlled by two different methods: gap control or pressure control (33). Gap control consists of setting a constant gap between the roll and the impregnation plate (or the second roll in the case of a nip-roller station). The pressure control method consists of applying a constant force on the roll, hence providing a constant pressure application on the prepreg. Note that the relationship between the applied force and the effective pressure experienced by the prepreg is not a simple direct relationship as the area of contact between the prepreg and the roll is not well defined. In commercial prepregers, a combination of gap and pressure control may be used.

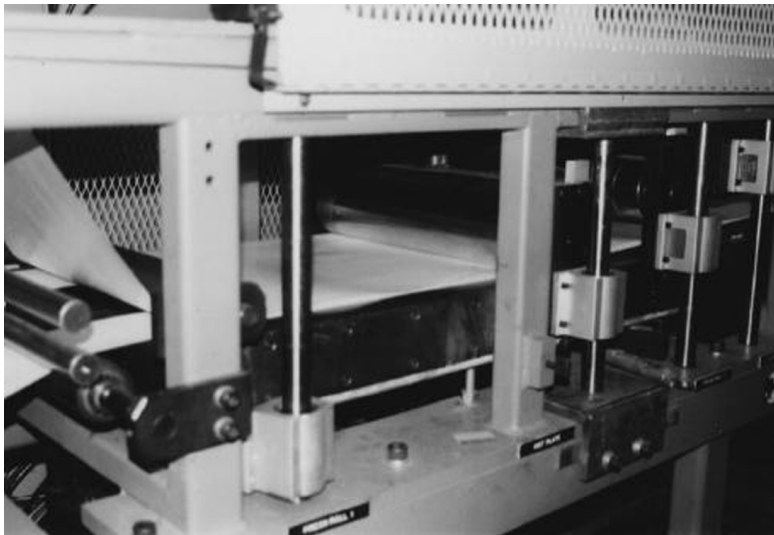


Figure 2.15 Main Prepreg Heater

Located after the impregnation zone are a chill plate and a pull-roll station, as seen in Figure 2.16 (3). Most chill plates are water-cooled and their role is to quickly decrease the prepreg temperature in order to quench any chemical reaction and also maintain uniform spreading of the fiber tows by sharply increasing resin viscosity. Positioned after the chill plate, the pull-roll station usually consists of a set of rubber nip-rollers which pull the fibers and paper through the process. Finally, the upper release paper is generally separated from the prepreg which is wound around the take-up roller with the lower release paper (Figure 2.16). In most commercial prepregging processes, a cutter is used to trim the prepreg edges before winding.

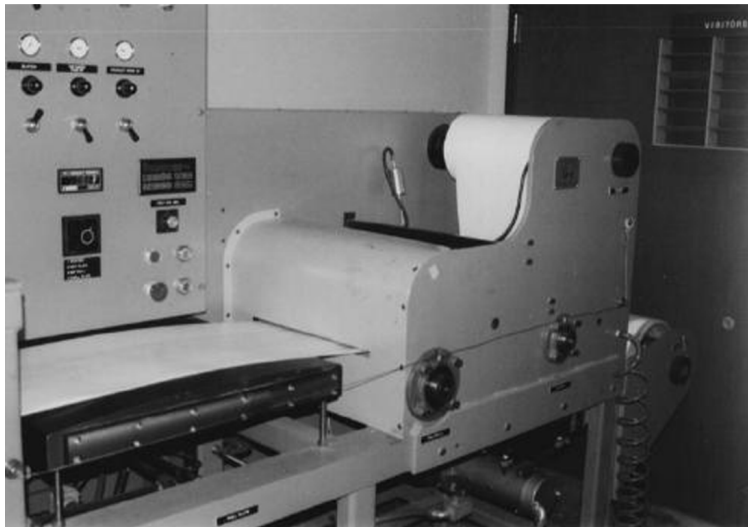


Figure 2.16 Chill Plate and Take-up Roller.

2.3.2 Prepreg Efficiency

For an optimum prepregging process, both the fractional resin uptake (f) and the fractional width change (e) must be as close to one as possible.

Fractional Resin Uptake:

$$f = \frac{B}{A+B+C}$$

30

Resin Distribution Function:

$$f^* = \frac{A+B}{A+B+C}$$

31

Where (Figure 2.17)

A= resin areal weight remaining on the collimated fiber tows (kg/m²);

B= resin areal weight penetrated into the collimated fiber tows (kg/m²); and

C= resin areal weight squeezed out of the fiber bed during impregnation (kg/m²).

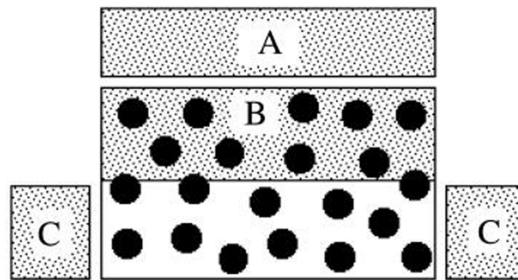


Figure 2.17 Overall Resin Distribution while Prepregging (3)

Fractional Width Change:

$$e = \frac{\text{width_of_fiber_tows_before_impregnation_}(m)}{\text{width_of_fiber_tows_after_impregnation_}(m)} = \frac{W_i}{W_f} \quad 32$$

If the fractional resin uptake (f) is high and the fractional width change (e) is low, resin impregnation becomes easier, but controlling the prepreg quality becomes difficult due to increased tow spreading. Accordingly, the prepregging efficiency (E_g) may be defined as the product of the fractional resin uptake and the fractional width change, via (34):

$$E_g = f \cdot e \quad 33$$

Using a more traditional descriptor (i.e., areal weight), the prepregging efficiency may be described as the areal weight of resin impregnated into the collimated fiber tows divided by the areal weight of resin used. For the production of large-width prepregs, the resin waste as well as the tow spreading can be neglected (i.e., $f^*=1$ and $e=1$), and thus the prepregging

efficiency may be approximately equal to one if the prepreg flow number and the initial thickness of the resin film are properly selected. In contrast, the prepregging efficiency is usually low in the manufacture of small-width prepregs (35). Collectively, prepregging can be viewed as a fundamental unit operation in which reinforcing fibers and matrix resin are brought together. This unit operation produces an intermediate product in the chain of composite manufacturing. This intermediate is then to be further processed by batch operation through bagging and autoclaving techniques. Deeper analysis in prepreg manufacturing process can be found in Seferis, Velisaris, and Drakonakis et.al. (3)

2.4 Innovative Clave Manufacturing and Processing

Before going through the interlayer technology and process, the rest steps in high quality composites manufacturing have to be described. More specifically, the last part of CFRP manufacturing, which is considered highly critical, is also the most expensive one. There has been extensive investigation in order to achieve high quality CFRP composites manufactured out of autoclave. This section makes an introduction on a new clave process which reduces the cost of the process by separating heat from pressure. First, a description of the autoclave is required in order to be able to compare and understand the benefits of the press clave.

2.4.1 Autoclaving

High quality polymeric composites manufacturing requires high pressure procedures of 70 to 100 psi (485 to 690 kPa) such as autoclaving which is used in high tech applications and mainly in aviation. The autoclave is a device that can generate a controlled pressure and temperature environment. While several autoclave types are available, all consist primarily of three units: a pressure vessel, a heating/cooling system, and a control unit. When prepreg based composites are processed using autoclaves, they undergo several steps prior to the actual autoclaving. These steps usually follow a strict procedure because they have been found to affect the final properties of the composite (36). Similar to other composite manufacturing techniques, the prepreg materials are stacked or laid-up to yield a laminate of the required

dimensions. The entire lay-up including prepreg plies, release film, and breather cloth is then covered with a vacuum bag as shown in Figure 2.18. Since the pressure in the bag and autoclave are different, a compacting force that corresponds to this pressure difference is exerted on the laminate. Through this feature and the flexible characteristics of the vacuum bag, the pressure is always acting normally to the laminate surface, which leads to a uniform pressure distribution. This uniform pressure distribution, which is applied continuously throughout cure, reduces the risk of void formation, especially when dealing with thermosetting prepreg materials (37; 38; 39; 40; 41; 42).

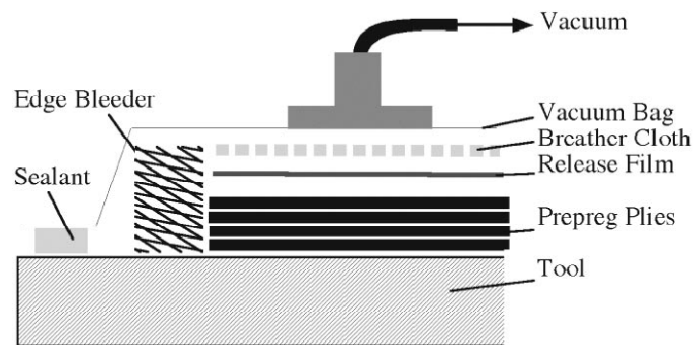


Figure 2.18 Autoclave Entire Lay-up (3)

After completion of the vacuum bag, the laminate can be autoclaved using a certain temperature and pressure profile. In composite fabrication the autoclave is usually pressurized with nitrogen so that fire hazards imposed by the exothermic prepreg materials are reduced (43). Heat is applied using heat exchangers in conjunction with fans that assist heat transfer (3; 44; 45).

Generally for autoclaves, the usual processing procedure for thermosetting prepreg curing is to firstly increase pressure and right after, heating the autoclave at a chosen heating rate to the desired temperature. According to most fluids behaviour, the viscosity of the matrix will decrease with this temperature rise. As a result, at elevated temperature the resin will freely flow, facilitating the consolidation process until eventually the chemical cross-linking starts

occurring, and forming gelation. At this point, the resin will soon change from a liquid into a solid and it will start preventing viscous flow. It is, therefore, important that the prepreg resins chemorheology is known in order to complete consolidation and volatile removal prior to resin gelation. A typical autoclave cycle containing two isothermal dwells is shown in Figure 2.19. The first dwell is performed to prolong the time range for consolidation and eventually to prereact the matrix to reduce the risks of large exotherms. The second dwell is the actual cure step. Most commercial epoxy based prepreg systems require cure temperatures of 121 °C or 178 °C. The application of pressure assists the consolidation and helps suppress voids in the laminates.

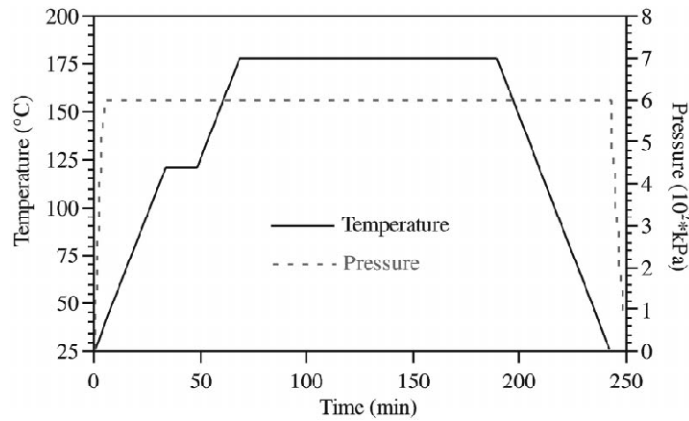


Figure 2.19 Typical Temperature and Pressure Profile for Curing in a Clave (3)

Nevertheless, high pressures might eventually drive too much resin out of the fiber bed leading again to void formation, resulted by resin starvation this time. Even though much research has focused on the autoclave consolidation and processing optimization, the developed models are of limited use. So many variables such as prepreg type, part dimensions, vacuum bag materials, lay-up, and processing conditions influence the consolidation that the composites industry has determined almost all operating conditions by trial and error. Consequently, the aerospace industry has tried to employ standardized procedures. For instance, the majority of these parts are cured using 121 °C or 178 °C standard cure cycles and they are also distinguished by using prepreg systems of high, intermediate, and low flow.

Considering this information the lay-up can be adjusted such that the optimum part qualities can be accomplished (3; 36; 39; 40; 44; 45).

2.4.2 Pressurized Vessel

The Repair Clave (Figure 2.20) is a semi-portable, pressure vessel, designed to provide controlled temperature, vacuum and pressure for repair of composite and metal-bonded parts that require higher pressures than can be achieved by vacuum only. Unlike a conventional autoclave, there are no internal heating elements in the vessel, so the heat for curing is derived from heat blankets or other heating elements.



Figure 2.20 Heatcon Composite System - Repair Clave Model HCS3100 (46)

Although, the main difference between a Repair Clave and an Autoclave comes from the fact that one is mainly dedicated to repairs of composite parts, while the other for manufacturing, it is believed that a Repair Clave could become a useful tool in manufacturing simple parts at a much more affordable cost. Currently autoclaves could be used for repairs also, if extensive re-build of a part is needed. The Repair Clave can be referred to as an affordable autoclave; as it reaches almost the same pressures, but it permits the use of localized heat which results in much more economical cures. However, one needs to investigate if the quality of a part manufactured in a Repair Clave can be maintained at the standards of a part manufactured through an Autoclave.

There are of course many differences that put the 2 claves apart, but by understanding these differences one can see at which common point the Repair Clave might be used as a possible future Autoclave for manufacturing simple composite parts, Table 2.2.

Table 2.2 Repair Clave and Autoclave Advantages and Disadvantages (46; 47)

	Repair Clave	Autoclave
Qualification	Qualified for repairing composite parts	Qualified for manufacturing and repair of composite parts
Design Considerations	For a vessel of 4 m (12 ft) length and 0.9 m (3 ft) diameter less than 2 cm thickness needed.	Thickness of vessel has to be large, as when pressure and temperature are applied together the deformation of the vessel is bigger. (e.g. for a 3m (9 ft) autoclave, 0.6 m (2ft) diameter, temperature < 343 C (650 F), a minimum 4.5 cm thickness is needed)
General Installation	The only extra it needs, is a commercially available air compressor	Installation is an important consideration: foundation, cooling water supply, electrical supply, gas (if used for heating), and pressurization medium supply and exhaust arrangements.
Operating Pressure	Max to 517 kPa (75 PSI)	Max operating Pressure to 586 kPa (85 PSI)
Pressurizing System	Through an external air compressor	Three pressurization gases are typically used for autoclaves: air, nitrogen, and carbon dioxide.
Heating System	Through heat blankets ; Heat blanket thermal uniformity is essential for the curing quality; If the heat-up rates for the heat blankets are not respected, cracks can appear in the structures.	Gas heating is regularly used in autoclaves with maximum operating temperatures of 450 to 540 °C (850 to 1000 °F). Steam heating is often used for autoclaves operating in the 150 to 175 °C (300 to 350 °F) range. Most small autoclaves (under 2 m, or 6 ft in diameter) are electrically heated. Gas circulation provides mass flow for temperature uniformity and heat transfer to the part load. However, gas stream can cause thermal or mechanical shock on the manufactured parts.
Electrical System	“Plug-in wall” (e.g. electrical supply: 90 Volts ac to 264 Volts ac 47 Hz to 63 Hz, 0.15 Amps; Power 50 Watts)	Even small autoclaves are not designed to just plug in and run. (e.g. electrical Supply: 230 Volts AC / 50 Hz (110 Volts on request) ; Power: 450 Watts)
Vacuum system	Similar System	Similar System
Control system	Similar System	The cure cycle is controlled by feedback from thermocouples, transducers, and advanced dielectric and ultrasonic sensors. Computer controlled systems are used but they are far more complex.
Loading system	Similar System	Similar System
Safety	Has a pressure relief valve in case of over-pressure; Because the temperature is separated from the pressure there is a decreased risk possibility	Use of pressurized gas to cure has redundant safety features on any autoclave because of the potential seriousness of any malfunction
Affordability	The electrical system, reduced need for safety features, reduced thickness of vessel and therefore decreased manufacturing costs	Big costs can come from various factors: electrical consuming system, gas used for pressurization (nitrogen can be very expensive and air is very dangerous), requires redundant safety features,
Repaired/ Manufactured Parts	Limited geometries that can be created / repaired due to the 2D heat blanket geometry; Also usage of heat blankets limits the number of plies that can be completely cured	Theoretically any 3D geometry can be manufactured; Higher number of prepreg plies can be processed at the same time; However, when used for repair, areas not being repaired are subject to high temperatures which may cause deterioration to existing bonds and finishes.

2.5 Processing of Multilayer Structured Laminates- Interlayer Introduction

In this section an introduction to the interlayer technology is made from the process description but also in interlayer systems that have already been described and evaluated in Polymeric Composites Laboratory (PCL) (48). Both thermosets and thermoplastics are considered as potential materials used in matrices for advanced polymeric composites. Thermosetting systems are generally more preferable than thermoplastic ones, due to their advantageous processing which consists of prepreg tack and lower viscosity during the process (49). Nevertheless, the thermosets used as matrices in polymeric composites were not able to provide the appropriate toughness capabilities in order to fulfill primary-structure applications requirements. The need for expanding the use of polymeric composites to commercial-aircraft primary structures has led to the toughening of thermosetting-resin systems as one of the most important objectives and has motivated essential research efforts. Many of those efforts are responsible for the development of a successful toughening technique suitable for primary structure applications that is based on layering concepts to form final multilayer laminate structures (50; 51).

Ply delamination is the most serious damage within the laminate structure occurring when a composite material is tested for impact. Delamination causes increased degradation in the resulting composite mechanical properties (52). In an attempt to impede delamination occurring during impact, a successful toughening technique for thermosetting-matrix composite systems, commercialized and qualified for use in primary structures, was developed (50; 51). This toughening technique establishes an engineering approach to the toughness issue by using layering concepts for toughening the highly stressed interlaminar regions within the composite. Laminating is attained by using a tough resin-rich layer between the plies of the composite structure which eventually results to a multilayer laminate structure. These lamination techniques can be implemented as heterogeneous or homogeneous modification, as schematically presented in Figure 2.21 (53; 54).

2.5.1 Interlayer Processing and Fabrication

This section focuses on the modeling of the interlayer-toughening concept with a second impregnation phase, double pass impregnation process. This second impregnation phase can be accomplished either through the development of a model multilayer composite structure containing a heterogeneous resin interlayer with rigid modifier particles or with a second-pass of resin only, developing a model multilayer structure containing a homogeneous resin interlayer.

In general as it has already been stated, the manufacture of conventional high quality composites consists of three main steps: prepreg processing, lay-up and autoclave processing. Trying to get a clear view of the multilayer structured composite process, its development is compared to the development of a conventional structure at each processing step as it is presented in Figure 2.21(5).

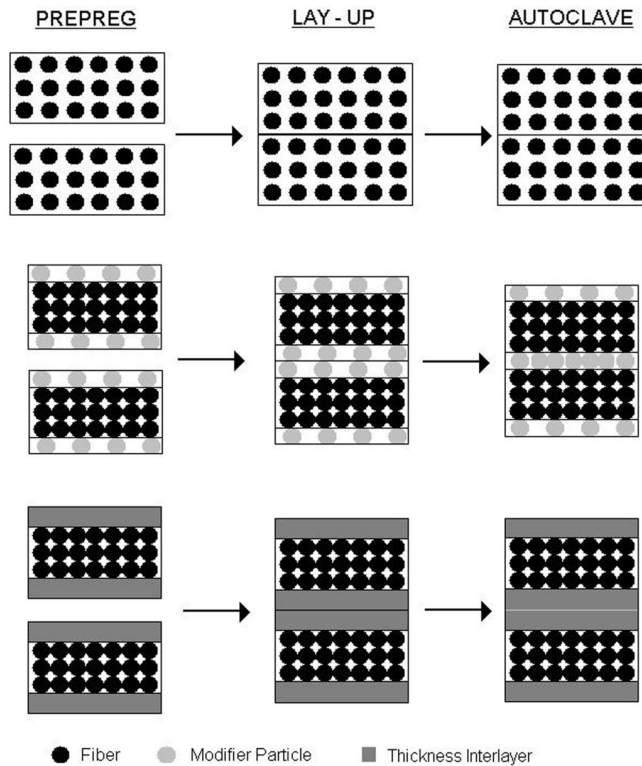


Figure 2.21 Development of Conventional and Multilayer Structured Composites (53)

2.5.1.1 Double Pass Impregnation

The difference between conventional prepreg and multilayer prepreg structures, either homogeneous or heterogeneous is shown schematically in Figure 2.21. The conventional prepreg has equally distributed reinforcing fibers within a matrix resin. Ideally, the prepreg has a constant thickness and the fibers have completely been wetted by the matrix resin. On the contrary, multilayer prepreg is generated by using a third component, the interleaf or the interlayer, which must be placed between each ply. Specific packing of the fibers must be performed to the toughened prepreg in order to accumulate the same resin as a conventional prepreg. The tighter fiber-packing accumulates less resin between fibers and allows for excess resin to remain on the prepreg surfaces. Acquiring a fully impregnated structure with low resin content within fibers is another difficulty of the prepreg processing.

In processing of this multilayer prepreg structure, different techniques can be used depending on the kind of multilayer (heterogeneous or homogeneous).

Heterogeneous Multilayer Structure

There are two techniques that can be used in performing heterogeneous multilayer structures: sprinkling modifier particles on the prepreg surface or premixing modifier particles with resin to be applied during the prepreg process (55; 56; 57). Consequently, a two-step prepreg process is developed, referred to as double impregnation, which is utilized to develop a model multilayer prepreg. In this double-pass impregnation step, the modifier particles are premixed with the same matrix resin that has been applied during the first-pass impregnation step (58).

The purpose of conventional prepregging is to impregnate collimated fiber tows with a desired amount of matrix resin at elevated temperature and pressure in order to create a uniform, partially reacted lamina structure (50; 51). Prepregging is a continuous process that consists of four basic operations. Firstly, the matrix-resin-film is created, then the coating, after

that the impregnation zone, where heat and pressure are applied to the ply, and finally the prepreg, which is collected on a take-up reel (59; 60).

In heterogeneous structure, the modifier particle diameter is the factor that controls the amount of resin that will be applied during each impregnation step. The maximum diameter of the modifier particles can also be calculated, however more details on the calculation of the modifier particle diameter are given in the autoclave process, which is one of the following units. During the second impregnation, the thickness of the resin film is equal to the average modifier-particle diameter and thus, an almost monolayer particle distribution is obtained on the prepreg surfaces. Therefore, if the final prepreg fiber areal weight and resin content desired are known, the amount of resin that may be applied during the first impregnation can be given via (53):

$$W_{r1st} = \frac{\left(\frac{A_f}{(1-W_r)} - A_f\right) - 2D_p p_r}{A_f + \left(\frac{A_f}{(1-W_r)} - A_f\right) - 2D_p p_r} \quad 34$$

Where

W_{r1st} = first-pass weight resin fraction

W_r = final desired resin weight fraction

A_f = areal weight, fibers (g/m^2)

D_p = average diameter of modifier particles (m)

P_r = density of resin (g/m^3)

Homogeneous Multilayer Structure

As far as the double-pass impregnation in the homogeneous multilayer structure is concerned, a first-pass resin-starved step should be applied for pressing and packing the fiber bed. During the second-pass impregnation, the full thickness of the resin interlayer is applied creating a prepreg with overall normal desired resin content. However, the application of the interlayer is not the same as in the heterogeneous structure. In the heterogeneous structure the

modifier particles of both surfaces of two different laminas that touch are intermingled and compressed with the final thickness of the interlayer equal to the diameter of the modifier particles. On the contrary, in a homogeneous prepreg structure, applying an additional interlayer and then laminating will result in surplus overall resin content, thus reducing strength and stiffness.

As it is obvious from Figure 2.22, if the full thickness is applied to both sides of the fiber bed, more resin than the desired will be accumulated in the final matrix system. There are two possible methods of applying the interlayer and avoiding accumulation of more than the desired resin. First, by applying half the thickness of the resin in the second-pass of the impregnation, a multilayer structure is achieved with the desired thickness of the interlayer without having more than the planned resin in the final matrix system. The second way of applying the interlayer is to enable it through one-sided impregnation. However, this may complicate the lay-up. Both techniques are schematically shown in Figure 2.23.

The amount of resin that may be applied during each impregnation step will be controlled by the maximum-thickness interlayer which can be determined. Its determination, however, is given in detail in the section of autoclave processing, which follows further below. If the final prepreg fiber areal weight and resin content desired are known, the amount of resin that may be applied during the first impregnation can be given by the formula 34 (53), if the D_p is replaced by the maximum-thickness of the interlayer (T_i).

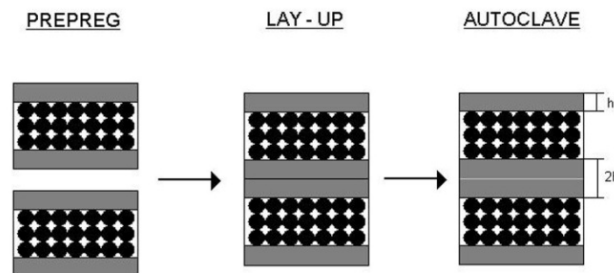


Figure 2.22 Second-Pass of Impregnation (5)

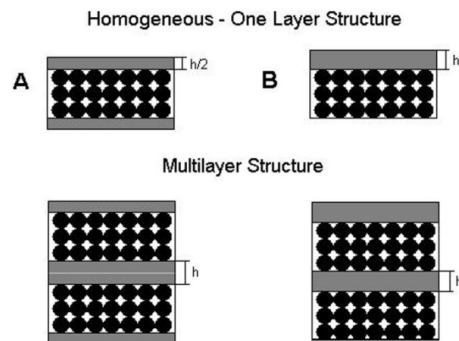


Figure 2.23 Two Different Ways for Applying the Homogeneous Interlayer: (a) applying half interlayer on each side of prepreg in the second-pass of the impregnation, (b) applying full interlayer on one side of the fiber bed in the second-pass of the impregnation

Although heterogeneous multilayer structure can be used in composites in order to give a higher toughness between each ply, the homogeneous structure can be described as not so efficient for toughness improvement in composites. However, it can offer great toughness and high tack in hybrid materials, where a metal or other foil can be used instead of a single ply. The use of either a metal foil or any other ply as a single laminate to a composite material can be adjusted in a multilayer structure through homogeneous interlayers, by implementing to each ply the impregnation and setting the interlayer thickness, either half from both sides or full from one side. The layered structure can be further processed by traditional lay-up and autoclaving.

2.5.1.2 LAY – UP

Lay-up follows the impregnation steps, where the desired shape is given and the anisotropic nature of each ply is taken into consideration. During the lay-up, prepreg tack comprises the overriding factor in prepreg performance. Prepreg must strictly have the appropriate tack to consolidate each ply together; over-tacking can easily damage the prepreg in the case that a ply has to be removed. Comparing the lay-up of a multilayer prepreg to a conventional one, a major difference can easily be observed as it is presented in Figure 2.21. In a conventional prepreg lay-up, only a small amount of resin separates the two plies. On the

contrary, the toughened prepreg lay-up consists of two heterogeneous or two half homogeneous layers which include in between the ply fiber bed. The amount of resin located between the plies will directly affect the resulting prepreg tack. It is important for the multilayer prepreg structure that resin is accumulated on the prepreg surface (53). If all the matrix resin has penetrated into the fiber bed, either modifier particles or nothing – depending if it is heterogeneous or homogeneous structure – will remain on the prepreg surface, which could create low-tack prepregs (61).

2.5.1.3 Autoclave Processing

The last step in CFRP manufacturing is the autoclave. During this step, heat and pressure are applied in order to cure the laminate with a homeomorphous fiber distribution. In the case of a multilayer structured composite, the influence of autoclave on resin distribution can be in detail described by Figure 2.21. The curing of a conventional composite causes resin flux, which develops a homeomorphous fiber with no distinct interface between the plies. On the contrary, the curing of the multilayer composite, although it also causes resin flux, it forms distinct layers as the modifier particles in the heterogeneous case and the second resin film in the homogeneous case are unable to penetrate into the fiber bed – due to the first-pass impregnation – and they are trapped between each ply. Eventually, the morphology contains layers of reinforcing fibers embedded in a matrix resin separated by resin – rich layers with a thickness that can be calculated. In the heterogeneous case, this interlayer contains twice the concentration of modifier particles that are initially placed on the prepreg surfaces. On the other hand, in the homogeneous case the desired resin is accumulated by placing only half of the resin thickness to each surface or full of it to one of the prepreg surfaces during the second impregnation step.

At this point, it should be mentioned that there are limitations of the maximum-thickness interlayer that can be used in processing. It is vital for manufacture to be able to calculate the thickness of the interlayer so that the resin content in total remains constant as in a single pass

of a conventional prepreg. The maximum-thickness interlayer can be calculated as a function of the fiber areal weight, the final resin content and the maximum fiber-packing arrangement. As the fiber-packing becomes closer, the amount of resin required within each ply decreases and the amount of resin available for the interlaminar region increases. For the assumption that the maximum fiber-packing arrangement is assumed to be between a square array and a hexagonal-packed structure, as shown in Figure 2.24, the maximum-thickness interlayer can be given via:

$$T_I = \frac{A_f \left(\left(1 + \left(\frac{V_r}{V_f} \right) \right) \pi - 2(1 + \cos(\theta)) \right)}{\rho_f \pi} \quad 35$$

Where

A_f = fiber areal, weight (g/m^2)

T_I = maximum-thickness interlayer (m)

V_r = resin volume fraction

V_f = fibers volume fraction

ρ_f = fiber density (g/m^3)

θ = shift angle as defined in Figure 2.24 (for maximum effect $\theta = 30^\circ$)

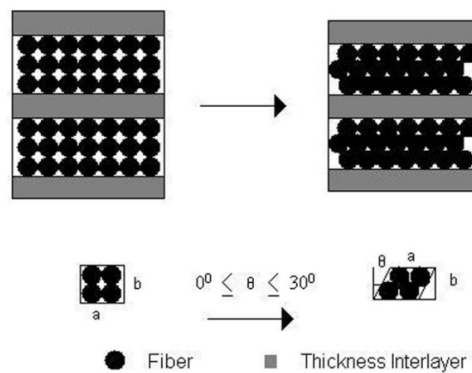


Figure 2.24 Schematic of Fiber-Packing Arrangements with the Homogeneous Interlayer Implemented. Maximum Packing Achieved at $\theta = 30^\circ$ (58)

As far as the heterogeneous case is concerned, the thickness T_1 can be replaced by the maximum modifier particles diameter D_{pmax} (53). Thus, the maximum modifier particle diameter that can be used in the interlayer is defined. As for the homogeneous case, the maximum-thickness interlayer derives directly by formula (44).

2.5.2 Toughening Mechanisms of Interlayer

Initial approaches to improve the toughness of thermosetting-resin systems comprised the blending of elastomers and/or thermoplastics to create a complete multiphase morphology. Firstly, significant improvements in toughness, by blending elastomers with epoxy, were demonstrated by (62), and (63). In this latter approach, the final morphology of the cured resin consisted of continuous epoxy-rich phase surrounding discrete second-phase particles.

Toughness improvements up to a certain order of magnitude were acquired and assigned to the second-phase particles strengthening the epoxies ability to yield and flow locally. Consequently, research carried on even further toughness improvements through the blending of elastomers with thermosetting matrices (64; 65; 66; 67). These investigations focused on the toughness improvement mechanisms in the elastomers-modified thermosetting systems.

Furthermore, toughness improvements are achieved by increasing the energy amount released during crack propagation. The need to meet the mechanical and temperature performance requirements of advanced polymer composites, researches changed over to the use of multipurpose epoxies blended with advanced thermoplastics such as polysulfones, polyethersulfones, and polyetherimides (68; 69; 70; 71).

Regarding heterogeneous multilayer toughened laminates, modifier particles are constrained between the prepreg plies and are not derived by phase separation. Modifier particles consist of a separate phase throughout the entire laminate processing, even though their surface interaction may play a significant role in toughness enhancement. Additionally, due to their thermoplastic nature, modifier particles crystallize upon thermal processing over their glass transition temperature and thus, they possess a relatively high modulus. This section

focuses on investigating the fracture surfaces of model heterogeneous multilayer laminates in order to comprehend their toughening mechanisms from the matrix point of view.

Working towards the examination of the modifier particle toughening mechanism, the effect of this interlayer in the fracture toughness improvement is evaluated. This is very critical in order to verify the toughening mechanisms on which the new interlayers will be based on. For this reason, the experimental fracture toughness testing of this model is performed in order to work as a reference to the other interlayer systems and is presented in the methodology and results of the present document.

Furthermore, the toughening mechanisms occurring in the interlayer systems of epoxy resins have already been described in PCL (5; 53). As a result there is no need to repeat the SEM characterization for this system. These SEM graphs are presented in this section in order to be able to explain the fracture toughness behaviour of the epoxy system with modifier particles that is presented later on.

The big difference of Mode II compared to Mode I fracture surfaces can be easily observed in traditional thermosetting matrices by the large difference in fracture surface roughness due to hackle formation, which are formed by the shear stresses acting on the resin system (Figure 2.25 (b)). The toughening mechanisms observed in epoxy resin systems are also presented schematically in Figure 2.25 (a). Tougher resin systems, such as Dicyanate and Epoxy, reveal particle stretching and then matrix yielding as toughening mechanisms due to particle good adhesion. On the other hand, the more brittle resin systems, such as BMI matrices, demonstrate crack deflection mechanism as there is no good adhesion with modifier particles. Thus, the more brittle the resin system is the less strong toughening mechanism utilizes (5; 53).

Determining a baseline Mode II fracture surface, an unmodified epoxy laminate with a conventional final morphology was examined in SEM. Figure 2.26 (a) and (b) presents the fracture surfaces in both low and high magnification respectively. The rough surface acquired by the Mode II testing is demonstrated in the low-magnification Figure 2.26 (b), while the high-

magnification Figure 2.26 (a) clearly demonstrates the hackle formation. In Mode II, as resin toughness increases hackle spacing decreases. The Mode II fracture surface of an epoxy multilayer laminate with 25% modifier particles by volume is presented in Figure 2.27 (a) and (b) in both low and high magnification respectively. As the magnification increases, hackles can be observed, however the surface is partly dominated by a considerable amount of highly deformed matrix. At low-magnification, holes also appear in the resin system, where modifier particles may have de-bonded during the fracture testing. The additional deformation in the resin system must occur due to the modifier particles incorporation and it appears to be yielding of the actual modifier particles.

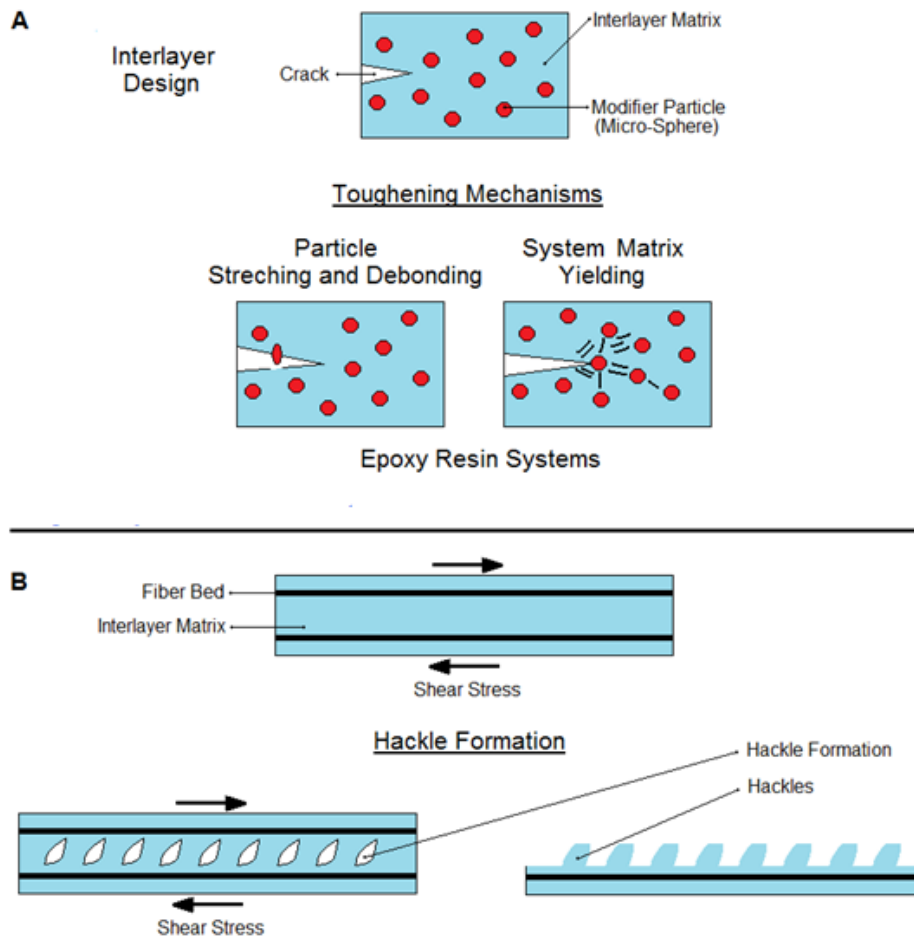


Figure 2.25 (a) Toughening Mechanisms Observed in Present Work, (b) Hackle Formation (5)



Figure 2.26 SEM at PCL - Mode II Fracture Surfaces of Non Interlayered Epoxy Laminates at a) Low and b) High Magnification (5; 48)

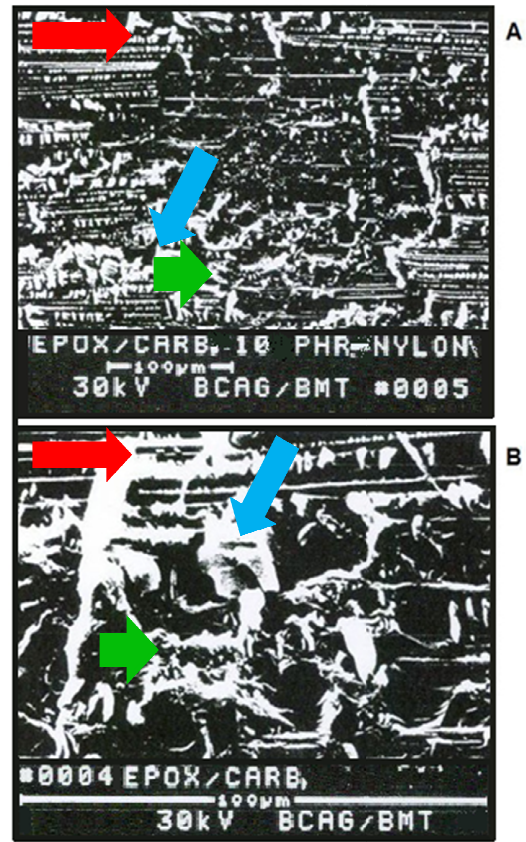





Figure 2.27 SEM at PCL - Mode II Fracture Surfaces of 25% Modifier Particles Interlayered Epoxy Laminate at a) Low and b) High Magnification (5; 48)

-  Stress Direction
-  Pointing Modifier Particles
-  Pointing Hackles

The epoxy heterogeneous multilayer laminates at a higher volume content of modifier particles (44%) is presented in Figure 2.28 in different magnifications. The matrix resin presents an overall rougher morphology. Nevertheless, at higher magnifications (Figure 2.28 (b)), the larger amount of matrix deformation occurring between the hackles with the modifier particles

concentration increase is easier to be detected. This deformation occurs at the modifier particle surface suggesting good bonding between the particles and the matrix system forming a modifier particle yielding and debonding failure mechanism. Further magnification increase (Figure 2.28 (c)), demonstrates the rough modifier particle surface between hackles.

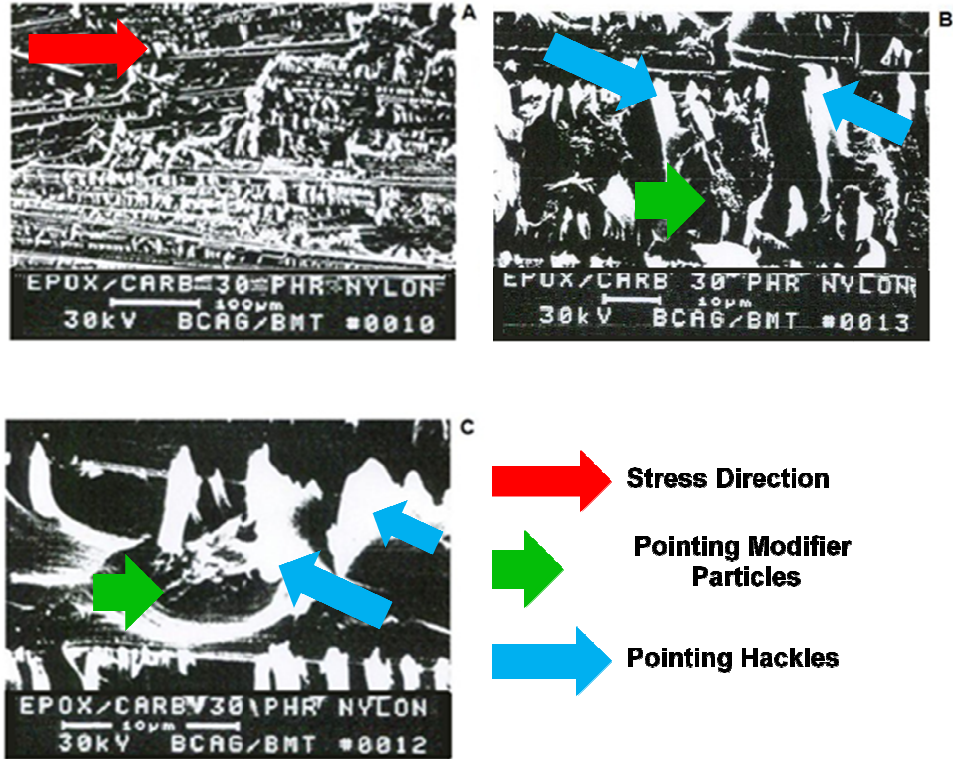


Figure 2.28 SEM at PCL - Mode II Fracture Surfaces of 44% Modifier Particles Interlayered Epoxy Laminate at A) Low, B) High, and C) Higher Magnifications (5; 48)

2.6 Carbon Nanotubes in the Interlayer

The laminate interlayer is an extensively investigated part of the carbon fiber reinforced composite mainly due to its tendency to delamination. Numerous works around the world have been performed in order to reinforce the interlayer of a multi-lamina (carbon) fiber reinforced composite and significantly increase its fracture toughness in different modes its electrical properties, its thermal conductivity, its strength etc. The interlayer and as a result the entire

composite properties enhancement has been achieved through micro and/or nano reinforcements. Furthermore, the interlayer property enhancement is a matter of manufacturing; this work as such supports the impregnation of the interlayer micro- and/or nano- modifications together with the carbon fiber bed under the method of double pass impregnation that was extensively discussed in section 2.5. However, at this point a focus on the interlayer is placed, which is examined extensively as a separate material made out of the same epoxy resin with the one that the CFRP is made in order to address the benefits that a CNT reinforced interlayer adds to the overall material.

As it has already been mentioned there is much work that has made successful efforts to enhance the properties of the interlayer utilizing several manufacturing methods of polymer composites. Significant increase in fracture toughness modes I and II has been observed in CFRP composites by using micro-particles made out of nylon (5; 72) or other kind of plastics that assist mainly to the toughness improvement (73; 74). Moreover, successful interlayer reinforcements have been done through the use of vapor grown carbon fibers (VGCF) (75; 76) or by utilizing carbon nanofibers that are introduced within the interlayer in different ways (77; 78).

Another important work on the interlayer improvement is the layers stitching or better known the nano-stitching (79; 80). NECST team (81) at the Massachusetts Institute of Technology (MIT) is developing a technology for reinforcing and strengthening critical areas of a composite laminate (interlaminar matrix regions) with aligned carbon nanotubes (CNT) in the z-axis, to enhance strength, toughness, and to introduce electrical and thermal tailoring opportunities using nano- and micro-engineering. Additionally, the CNT grown on z-axis in the interlayer will increase the load transfer between fibers. It is also possible that these entangled CNT would bridge matrix cracks (80; 81).

In addition, there are other groups that succeeded in reinforcing the CFRP interlayer with nanoclays (82) and particularly montmorillonite nanoclays (83). The findings of these

projects yield again a significant enhancement in composites fracture toughness and especially mode I (82; 83). Other projects, which focused on the multifunctionality of composites, examined CFRP samples that contain either piezoelectric devices (84) or shape memory alloy wires (SMA) (85). In both cases the increase of electrical and thermal conductivity as well as the censoring of the material was significantly important in contributing to material multifunctionality. The mechanical strength of the materials was increased up to a point as well.

Finally, the nano-additive that has been investigated the most in the area of the interlayer as well as throughout the entire matrix system of the CFRP is the carbon nanotubes (CNT). CNT have been used in so many ways by many groups which are trying to exploit their spectacular mechanical and thermoelectrical properties to the highest level (75; 86; 87; 88; 89; 90). Additionally, previous work shows growing CNT on the surface of filler fibers dramatically increases the surface area over which to transfer load, thus increasing the interface shear strength (75). NECST team work has demonstrated how significantly and positively the aligned CNT in the interlayer of a CFRP affect the toughness of the composite material. This team's work has referenced previous work on randomly oriented CNT and emphasizes the generic role of CNT in the composite interlayer.

Consequently, CNT have been utilized through many ways to benefit several material designs; nevertheless, they have never combined their outstanding mechanical and thermoelectrical properties with the characteristic of introducing nanoporosity. CNT in this work are used in the interlayer as an introduction of controlled nanoporosity as well and they consist of the smallest structural part of the fractal architecture of the interlayer.

2.6.1 Literature CNT and PNC Modulus Approaches

In the literature, there are different ways and approaches for calculating the modulus of CNT, and even more for calculating the modulus of CNT reinforced polymers. Some of the most common methods are presented in this section. Some approaches use the rule of mixtures for randomly oriented short fibers (88); however, the latter assumes in most cases that the CNT are

bulk cylindrical configurations, without taking into account the number of the CNT walls and the amount of the carbon atom hexagonal sheets included in the CNT.

Furthermore, when considering aligned carbon nanotubes, existing research considers the waviness of the CNT, and then calculates the effective modulus of the PNC (91; 92). This is a finite element method (FEM) approach where the effective modulus of a polymeric cell reinforced with a wavy, sinusoidal CNT is calculated. This modulus is given by equation 36 (91):

$$E_{cell} = \frac{F_{tot} \cdot \lambda}{2 \cdot A \cdot \Delta} \quad 36$$

Where:

E_{cell} = effective modulus of the Cell (GPa)

F_{tot} = the sum of all nodal resultant forces on the displaced plane (N)

A = the cross sectional area of the cell (mm^2)

Δ = axial displacement (mm)

λ = the wave length (mm)

Taking into account the waviness and the wavelength ratios, the effective reinforcing modulus

E_{ERM} is then calculated through equation 37 (91):

$$E_{ERM} = \frac{E_{cell} - (1 - V_{CNT}) \cdot E_{matrix}}{V_{CNT}} \quad 37$$

Where:

V_{CNT} = CNT volume fraction

E_{matrix} = Polymer modulus (GPa)

Although this approach has a better agreement with experimental results, it still treats the CNT modulus as graphene modulus, since $E_{matrix} = E_{CNT} / E_{ratio}$.

A similar approach in calculating a FEM cell modulus has been taken in another modulus prediction model for aligned CNT (93), without taking into account the CNT waviness. The difference here is that an effort to calculate the modulus of a single wall nanotube is made first, and then the rule of mixtures is simply applied. Even though this approach takes into account the hollowness of the CNT, it is limited to a single wall nanotube.

Moreover, there is an approach that firstly calculates the multi wall CNT (MWNT) modulus (89), using, however, as a reference the single wall CNT (SWNT) modulus, which is considered again as a bulk cylinder. This may complicate the calculation, since the modulus of a single wall nanotube varies according to its diameter. This approach calculates the MWNT modulus through equation 38 (89):

$$E_{MWNT} = \frac{N}{N-1+R} \cdot E_{SWNT} \cdot R \quad 38$$

Where:

E_{MWNT} = MWNT Modulus (GPa)

N = Number of Walls

R = Average Thickness of Wall / Average Distance between walls (These dimensions are considered about the same) (nm)

E_{SWNT} = SWNT Modulus (GPa)

Finally, there are also models for calculating the modulus of continuous CNT fabricated through the unification of CNT forests (86; 94). This approach considers again CNT as bulk cylindrical configurations and gives values from 12 to 15 GPa for CNT volume fractions varying from 0 to 10%.

Most approaches for calculating carbon nanotube modulus do not take into account the number of the CNT walls and the amount of the graphene sheets included in the CNT. Thus, at this section it is proposed to avoid restricting the graphene modulus value between 1 and 4 TPa, as is typically found in literature for the CNT modulus in the rule of mixtures equations, but

rather first to try to find the CNT modulus in a manner that the carbon atom hexagonal sheets fraction over the CNT volume is taken into account, and then calculate the PNC modulus.

2.7 Porosity in Epoxy Matrix Interlayer Systems through Foaming Agents

Under the effort of making lighter CFRP composites an extensive investigation of foam processing and properties, especially during the last two decades is being performed. In general, foams can be categorized in two groups: expanded ones, such as polystyrene foams, and the porous ones, such as epoxy foams.

As they exhibit high adherent strength, low water absorption, good dimensional stability, good heat resistance and generally good resistance to chemical attack, epoxy foams have gained special attention in the composites industry. Additionally, a particular advantage of epoxy foams, very important in this work, is their tendency to inhibit crack propagation in composite materials. Thus, they are of particular interest of being introduced as part of an interlayer system. Even though epoxy foams as matrices are not very popular in mechanical applications, as they are considered weak, it is possible to improve the properties of foams, if the size of the pores is reduced by ultimately introducing them at the nano-scale. Polynanomeric concept, where the uniqueness of polymers, metals, and ceramic distributions vanish, has been defined by (95). Research work performed at Polymeric Composites Laboratory (PCL) facilities in collaboration with Department of Polymer Science and Engineering at Sung Kyun Kwan University, which utilizes nano-foams as matrices in interlayer structures demonstrates the importance of reinforcing the porous or cellular structure with nanosized additives (95; 96; 97; 98; 99; 100).

The comparison of a property between a conventional composite and the porous structured nanocomposite can be very beneficial for the latter material as it gives higher properties in lower weight fraction or other processing conditions. The purpose of this structure is to be able not only to create cells within the matrix in order to lighten the whole material, but

also to control the size and reinforce the pores that are created in order to support the material nano-, micro- cellular structure.

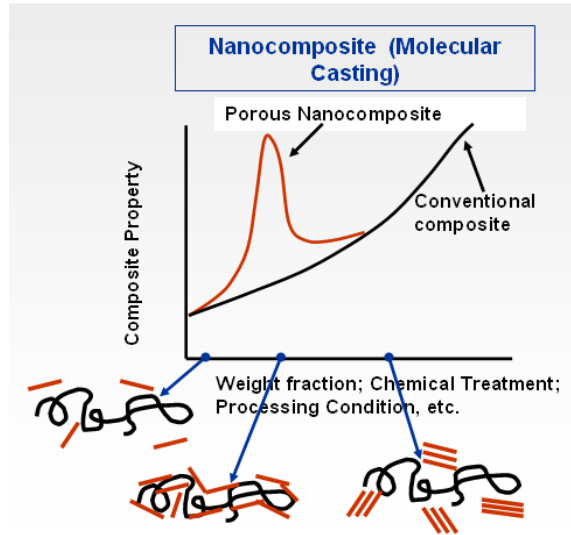


Figure 2.29 Porous Nanocomposite Compared to Conventional Composite (101)

According to work that has been done (101; 102; 103; 104; 105; 106; 107; 108; 109; 110), it is possible to reinforce the pores and control their size. Figure 2.30 shows how the pore surface of foam structured materials can be reinforced.

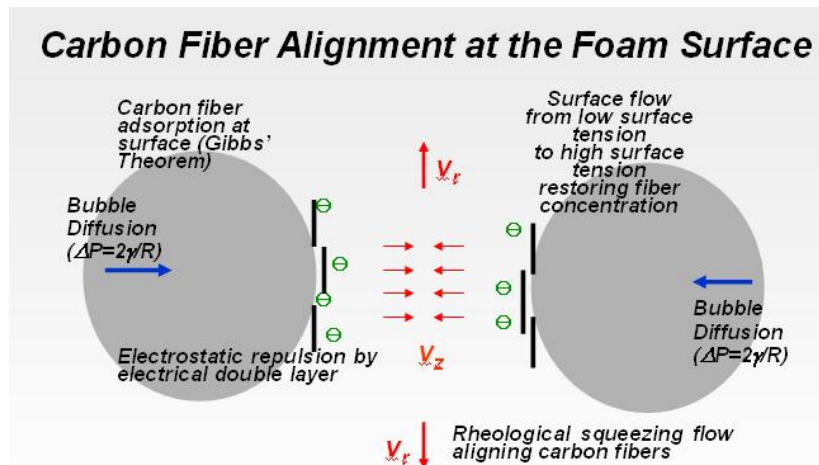


Figure 2.30 Carbon Fiber Alignment at Surface of Foam (101), (110)

As schematically shown in the Figure 2.30, and Figure 2.31, when the nano-sized reinforcement is incorporated during the bubble formation, it tends to be placed on the bubble surface, due to the surface free energy of the bubble, complying with the Gibb's Theorem. In addition, since the nano-sized entities are usually electrically-charged due to the isomorphic substitution, the bubble surface becomes charged, and electrical double layers are formed around the bubble, generating electrostatic repulsive forces. As a result, the reinforced bubbles are desirably stabilized mechanically as well as electrically, to give a light-weighted high performance composite foam structures (101; 102; 103; 104; 105; 106; 107; 108; 109; 110).

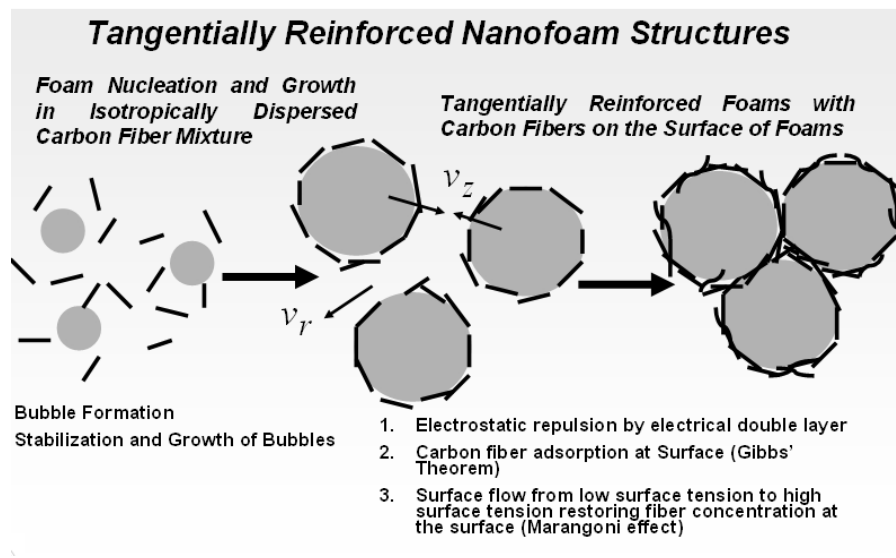


Figure 2.31 The Reinforcing Procedure of Foam Pores with Carbon Fibers (6)

Figure 2.31 illustrates the procedure of reinforcing nano-foam structures as described before. In this manner, both light weight and high strength can be achieved.

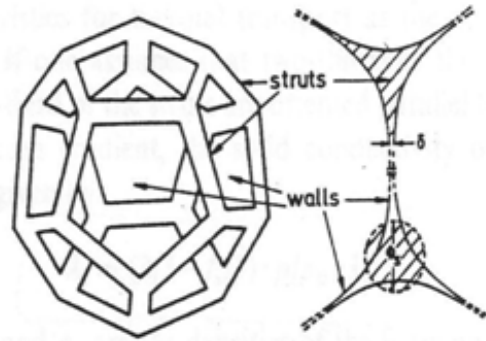


Figure 2.32 Scheme of Pore Reinforcement (109)

Figure 2.32, as a continuation to pore reinforcement, shows a schematic of polymeric foams, which are composed of cell walls and struts. The reinforcing entities are placed at the wall in an anisotropic fashion and at the struts are placed in a semi-anisotropic fashion. The key issue in foam reinforcement is the anisotropic alignment control of the nano- and micro-sized reinforcing entities at the cell walls.

2.8 Electrospun Fibers in the Interlayer

Having already mentioned that electrospun fibers are utilized as another interlayer reinforcement, the use of these fibers in featherweight composite materials primarily assists the consistency of the fractal architecture. Such a structure decreases the weight, and at the same time increases even more the stiffness, of the carbon fiber reinforced prepregs. These fibers are formed as polymer-based fibers manufactured by electrospinning.

More specifically, the electrospinning method that will be mainly utilized in this research work provides a unique way for the creation of continuous ultra fine to micron-sized fibers (diameters from less than 3nm to several micrometers) (111; 112). The formation of nano-fibers through electrospinning is based on the uniaxial stretching of a viscoelastic solution (113; 114). During this process the fluid solution, ejected through a metallic needle (spinneret), solidifies into fibers having a smaller diameter by several magnitude orders. The fundamental principle underlying the electrospinning method is the use of a high voltage electrostatic field to charge a

polymer solution, and thus induce the ejection of a liquid jet through the spinneret towards a metallic collector (115; 116). Electrospinning can be utilized for a very broad range of materials, including polymers, composites, ceramics and metals, processed into highly porous structures composed of nano-scale to micron-scale diameter fibers (117).

Figure 2.33 and

Figure 2.34 illustrate a basic electrospinning configuration utilizing a simple syringe-like apparatus. At the laboratory level, this apparatus consists of three main devices: 1) a capillary tube (syringe) with a metallic needle of small diameter filled with the fluid solution or melt, 2) a high voltage power supply, and 3) a conductive collecting device. Both direct and alternating current (DC and AC) power supplies can be used for electrospinning, with DC being the most common (118).

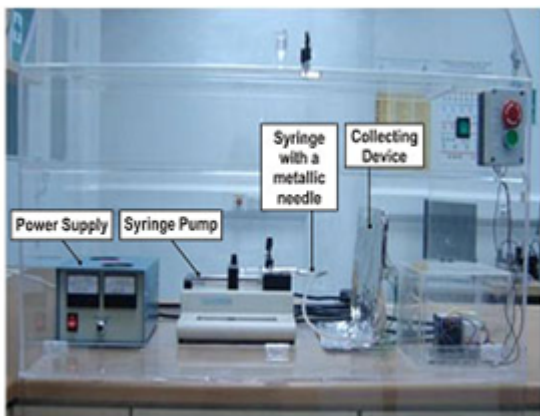


Figure 2.33 Electrospinning Configuration at a Laboratory Scale (119)

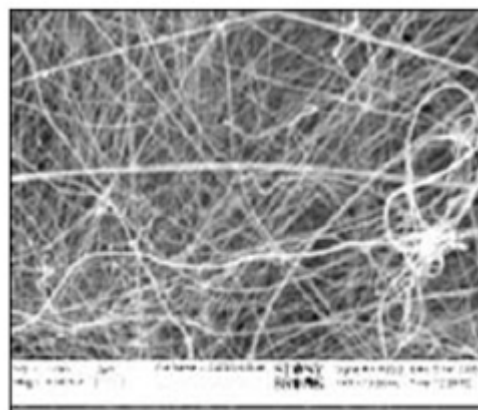


Figure 2.34 Nanofibers Produced through Electrospinning (119)

In a typical electrospinning set-up, a polymer is dissolved in a solvent or molten and placed in a syringe. With the use of a syringe pump, the solution or melt is fed through the needle tip at a constant and controllable rate. The one electrode of the voltage source is placed

either into the fluid or attached onto the metal needle of the syringe. The other one is connected to the grounded collector. Thus, an electric field is formed between a droplet of the solution held by its surface tension at the end of syringe needle tip and the metallic collection target (120; 121).

When the high voltage is applied, the pendent solution drop at the end of the needle tip becomes electrically charged and the high induced charges are distributed over the liquid surface. As the intensity of the electric field is sufficiently high, the quasispherical surface of the solution at the tip of the capillary tube elongates forming a conical shape, commonly known as the Taylor cone (122) There is a threshold value of the applied electric field at which the electrostatic force acting on the suspended surface of the cone overcomes the surface tension force of the deformed drop of the solution. When the applied electric field surpasses this critical value, a single charged jet is ejected from the cone tip (113; 121). Prior to deposition on the collector, the discharged jet undergoes a chaotic motion due to an electrically induced bending instability, during its transit to the collecting device (112; 114). The simultaneous effect of the jet stretching and the solvent evaporation (or melt solidification) leads to the formation of long and ultrathin fibers. As the jet travels through the atmosphere, the solvent gradually evaporates, leaving behind dry, meters-long fibers accumulating randomly on a collecting device.

The electrospinning from molten polymers has to be performed in vacuum conditions (123). For low viscosity solutions, the jet breaks up into drops, while for solutions with sufficient high viscosity it travels to the collector as fiber jets (117). The fibers are collected as a nonwoven or directionally oriented web of fibers on the surface of a grounded collector. The electrospinning process could be carried out at room temperature unless heat is required to keep the polymer in the liquid state. The most common form of collecting fibers is in the form of 2-D fibrous non-woven mats.

Alternatively, single fibers or linear fiber assemblies (yarns) can be produced. Ultra-thin web-like, circular, spring-like, beaded, flat ribbon-like, branching and splitting fibers have been

observed, demonstrating the variety of morphological features produced from different polymer solutions during electrospinning (124). The final fiber assemblies and properties depend on the polymer type and operating conditions (117; 119; 120; 125).

2.9 Review Summary

Summarizing the background, the first part gave information on how a matrix system is analyzed from a viscoelastic point of view. Information on an established viscoelastic model for polymer matrix systems and how the dynamic mechanical analysis can prove that a composite follows the viscoelastic behaviour was given. Differential scanning calorimetry technique was also investigated. Later on the manufacturing processes were in detail described showing how normal CFRP are manufactured. Furthermore, a newclave utilized separating heat from pressure while CFRP processing was introduced. The Repair Clave raises the need for evaluation of the CFRP parts manufactured through its process to justify in terms of quality its advantages over the expensive conventional autoclave. The multilayer structures introduction and the examination of the toughening mechanisms through modifier particles interlayer were given in order to show the technology background on which the new interlayer systems will be based on. The role of carbon nanotubes within a thermosetting matrix and their suitability in assisting the interlayer systems was also discussed. Finally, the descriptions of technologies, such as epoxy foams and electrospun fibers, which are used as interlayer reinforcements in multilayer structures, were provided.

This research work describes the manufacturing processes for CFRP giving the place for process innovation in order to apply the interlayer and to cure the composite. Additionally, new carbon nanotube models describing the density and the modulus can be introduced within the composites for material properties improvement if the geometry of the CNT is taken into account. This is necessary in order to describe CNT effects and understand their importance in the interlayer as the smallest part of the fractal structure within the featherweight composites materials. Finally, controlled epoxy foams and electrospun fibers have not been used as

interlayer reinforcements so far and thus, their incorporation with CNT within the interlayer systems forms layer by layer fractal structures, which make CFRP lighter and stronger than the conventional composite structures.

CHAPTER 3
RESEARCH METHODOLOGY

3.1 Objective #1

*Viscoelastic Analysis and Description Technique Suitability for the Matrix System
Characterization (1; 2)*

3.1.1 Rationale

The major experimental process for analyzing the dynamic behaviour of a polymer composite is dynamic mechanical analysis. In this approach, based on the generalized standard linear solid viscoelastic model (GSLs), which according to literature is the most appropriate to describe linear viscoelastic processes, extensive DMA analysis was performed on the manufactured samples to correlate the model findings and verify the viscoelastic nature of the matrix and its suitability for featherweight composites. Based on the agreement of DMA results with the model, DMA can be assessed as the suitable experimental process for describing the viscoelastic behaviour of Featherweight composites. The latter require matrix systems with in-detail described viscoelastic characteristics in order to be able to predict the behaviour of the overall material under the application conditions.

3.1.2 Experimental Procedure

Based on the generalized standard linear solid model that has been presented in background section 2.1, the dynamic mechanical properties of phenolic composite systems as a function of frequency and temperature during glass transition and degradation (126; 127), are investigated. DMA experimental results of the phenolic resin system are also presented in order to address the correlation of the experimental process with the theoretical model for viscoelastic behaviour description. A phenolic resin system is used for its distinct separation of glass

transition and degradation processes. As a result the agreement with experimental results is more obvious.

3.1.2.1 Materials

Phenolic resin (SC-1008), which is commercially available, is impregnated into the 8H woven T-300 carbon fiber bed provided by the Toray Company. The materials are cured by elevating temperature up to 135°C using controlled heating rates and postcured at 250°C for 5 hours. This thermal treatment fully cured the phenolic resin (12). Also, during the curing process the laminates are pressurized at 586 kPa in the autoclave, having been laid up under vacuum first. The phenolic resin used for this investigation of addressing DMA suitability for the matrix system characterization is selected over other thermosetting systems due to the fact that it distinctively demonstrates the two main processes of the polymers viscoelastic behaviour – glass transition and degradation processes – and thus, the agreement of the theoretical model with the experimental technique is more apparent.

3.1.2.2 Task 1&2: Implementation of the Generalized Standard Linear Solid Model and Correlation with Dynamic Mechanical Analysis Experimentation

A TA Instruments DMA 2980 is used for performing the dynamic mechanical experiments. The DMA measurements are performed in regular serrated clamps, which are utilized in the horizontal set-up. Following, a detailed description of the experimental description is given in Table 3.1.

Table 3.1 Experimental Parameters and Characteristics for DMA Evaluation

Shape	rectangular – shape composite sample
Dimension	24x12x1.5 mm ³
Oscillation Amplitude	0.2 mm
Atmosphere	Nitrogen
Nitrogen Flow Rate	300 ml/min
Nine Different Frequent	0.01, 0.1, and 1 Hz
Temperature Increase	2.5°C steps from 100°C to 450°C
Heating Rate	~1°C between steps

The Storage and Loss moduli are measured while the temperature is elevating. Due to requirements from the aerospace industry, a correlation of more than 95% is required for acceptable experimental results, so they can be within acceptable design tolerance.

3.2 Objective #2

Exploration of Manufacturing Process and Evaluation of Innovative Clave Manufacturing (3; 4).

3.2.1 Rationale

An extensive description of the manufacturing process is required in order to understand the current process and its weaknesses to implement the interlayer. This way, the modified process of double pass impregnation for implementing the interlayer and the analytic work to calculate the amount of desired resin per pass in order to maintain resin volume fraction at the same level can be justified. In aviation, there is a requirement of controlling the resin volume fraction so the fiber volume fraction is maintained in values above 60%. This particular volume fraction does not allow strength and other critical properties of the composite to get reduced.

Furthermore, an evaluation of the repair clave is performed. The need for such an evaluation is that if the repair clave is appropriate, then featherweights – conventional CFRP as well – could be manufactured at a much lower cost. The evaluation is performed by manufacturing samples at different pressures, then testing if their percentage of curing is above the limits, and eventually testing their mechanical properties to see if they are at the same levels as the traditional autoclave samples.

3.2.2 Experimental Procedure

3.2.2.1 Impregnation Process and Materials to Be Tested

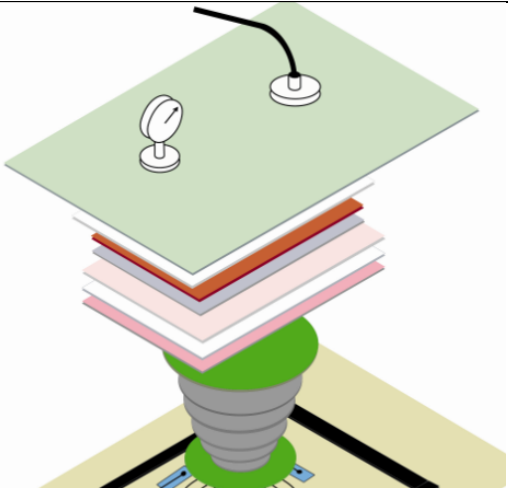
In order to investigate the role of pressure during clave manufacturing and its effect on the final material product when pressure is applied separately from heat, four different plates are manufactured under four different process pressures (4). The four different pressures are 0,

30, 50 and 70 psi (0, 205, 345, and 485 kPa). Each panel had eight plies of woven carbon fiber prepreg (type: Cytec Engineered Materials BMS 8-297, HMF 934 Carbon Prepreg-fiberite 934, resin density 1.3 g/cm³). The configuration of the plies is (0, 90, +/-45)s. Dimensions of the panels are 400x200 mm² with an approximate thickness of 1.5 mm. After manufactured the panels are cut to appropriate samples for Differential Scanning Calorimetry (DSC), Dynamic Mechanical Analysis (DMA) - 3 point bending clamps, Flexural Mechanical Strength, and Compression Mechanical Strength tests.

3.2.2.2 Task 1: Materials Processing and Fabrication

The prepreg plies are stored in a refrigerator in temperature below 0°F or -17.7°C. When ready for process, they are cut in the desired dimensions and orientation. After that the lay-up takes place. The plies are placed in the desired configuration, and on top of them all the layers described in Table 3.2 are applied.

Table 3.2 Lay-up Before Curing in Repair Clave (46)

Bagging material <hr/> 2 layers of 4oz breather <hr/> Heat blanket [in all tests presented the heat blanket used is: 120 V, 1125 W and 15*15 inch(38*38 cm)] <hr/> Thermocouples <hr/> 1 layer Solid release film <hr/> 1 layer Bleeder (style 120 glass) <hr/> 1 layer Perforated release film <hr/> Carbon prepreg plies	 <p>Figure 3.1 Lay-up</p>
---	---

The vacuum has to be at least 500 mm Hg 0°C. When the desired vacuum is accomplished, the laid-up panel is placed into the vessel. The vessel is sealed and the pressure

can be adjusted to the desired level. Since the pressure is in the level required by the experiment, the temperature profile by controlling the heat blanket initiates curing. All the measurement parameters can be controlled by a data acquisition system attached to the vessel. The processing/claving lasts about 4 hours. The first step elevates the temperature up to 350 °F or 177 °C with a rate 2.5 °C /min, and then it goes through an isothermal period of two hours at 177 °C. After two hours in the isothermal phase the temperature starts reducing with a rate of 2.5 °C per minute. The pressure is released and the panel is ready after removing all the lay-up extra layers.

3.2.2.3 Task 2: Differential Scanning Calorimetry Analysis for Evaluating Curing

The Differential Scanning Calorimetry used for these experiments is a 29 series DSC of TA Instruments, model 2910. Three different temperature elevating rates are used, 0.5, 1 and 5 °C/ min. For all of those three different rates the samples are elevated up to 400 °C. Taking the panels manufactured in the pressurized vessel “repair clave” small samples of 5 to 20 mg weight are cut for all the four different panels. Hence, eventually experiments of the 4 different panels manufactured at 0, 30, 50 and 70 psi (0, 205, 345, and 485 kPa) are tested in 3 different temperature rates, i.e. 0.5, 1 and 5 °C/min. More than three experiments are performed for each temperature rate in order to verify repeatable results on repair clave curing efficiency.

3.2.2.4 Task 3: Dynamic Mechanical Analysis for Evaluating Viscoelastic Behaviour

The Dynamic Mechanical Analyzer used for this study is a Triton DMA. Two different temperature elevating rates are used, 1 and 5 °C/min. For both of these two different rates the samples are elevated up to 300 °C. The samples are tested in 3-point bending experiments. Taking the panels manufactured in the pressurized vessel “repair clave”, samples of approximately 50x12 mm² (l x w) are cut from all four different panels, and are tested in the DMA. The thickness is approximately 1.65mm for the 0 psi, 1.58mm for the 30 psi (205 kPa), 1.51mm for the 50 psi (345 kPa), and 1.47mm for the 70psi (485 kPa). Thus, eventually

experiments of the 4 different panels manufactured at 0, 30, 50 and 70 psi (0, 205, 345, and 485 kPa) are tested in 2 different rates 1 and 5 °C/min under 3-point bending loading. More than three experiments are performed for each temperature rate in order to verify the results. The storage and loss moduli are measured while the temperature is increasing.

3.2.2.5 Task 4: Samples Flexural Mechanical Testing for Evaluating CFRP properties

The specimens are tested in a screw Instron machine (model 4505). More than five specimens are tested for each of the four different CFRP panels of 0, 30, 50, and 70 psi (0, 205, 345, and 485 kPa) manufactured. Specimens of 135x12 mm² (l x w) are cut from the CFRP panels (The length mentioned is the gauge length). The thickness is approximately 1.65mm for the 0 psi, 1.58mm for the 30 psi (205 kPa), 1.51mm for the 50 psi (345 kPa), and 1.47mm for the 70psi (485 kPa). The crosshead of the machine in the three point bending test had a speed of 5mm/min and the test is performed from no loading state to failure. The flexural strength is measured while deformation is increasing. Mode II fracture toughness is also measured.

3.2.2.6 Task 5: Samples Compression Testing for Evaluating CFRP properties

Furthermore, specimens from the panels are also tested under compression testing in the same Instron machine that flexural testing took place. More than five specimens are tested for each of the four different CFRP panels of 0, 30, 50, and 70 psi (0, 205, 345, and 485 kPa) manufactured. Specimens of 50x12 mm² (l x w) are cut from the CFRP panels (The length mentioned is the gauge length). The thickness is again proportional to the pressure that the CFRP panel has been manufactured with. The crosshead of the machine in the compression test had a speed of 1.5mm/min and the test is performed from no loading state to failure. The compression strength is measured while deformation is increasing.

3.2.2.7 Task 6: Scanning Electron Microscopy for Surface Characterization

The manufactured samples are also observed in scanning electron microscope characterization for visual explanation of the mechanical analysis. Samples were cut in

dimensions of $10 \times 5 \times 1.5 \text{ mm}^3$ so the cross section ($5 \times 1.5 \text{ mm}^2$) can be observed in the microscope. Although carbon fibers are conductive, the matrix reduces the conductivity for SEM observation, thus, higher conductivity was achieved through gold low-vacuum sputter coating. The SEM utilized was a VEGA TESCAN 3SB microscope. Samples are exposed to an electron beam which comes through a tungsten heated filament electron gun. Finally, resolution of the SEM utilized as high as 3nm at 30kV and as low as 8nm at 3kV. Particularly the Press Clave manufactured samples were tested at 30kV.

3.2.2.8 Task 7: Statistical Regression Model for Parametrical Prediction of Strength

A multiple regression statistical model is developed based on the experimental results for prediction of the material strength as a function of manufacturing pressure, flex strength, compression strength, and glass transition temperature.

3.3 Objective #3

Micro-spherical Particles (Modifier Particles) Reinforced Interlayer (5) – The Base New Interlayers.

3.3.1 Rationale

Micro-spherical particles reinforced interlayer is a first attempt to reinforce the interlayer and initially examine the efficiency of the double pass impregnation manufacturing process. This interlayer has already been introduced in composite systems at PCL. However, the main focus on this effort is to see how - as a first step - the interlayer is reinforced, and improves the fracture toughness, and to understand the mechanisms on which the new interlayers will be based.

3.3.2 Experimental Procedure

The experimental part of this interlayer is verified and further investigated in order to use it as a base for comparison with the new interlayer systems manufactured out of controlled epoxy foam and CNT reinforced electrospun nano-fibers.

3.3.2.1 Materials

The resin system tested with modifier particles interlayer is an epoxy-based resin system composed by: 60% tetraglycidyl-diaminodiphenylmethane (TGDDM) or MY – 720, 40% diglycidylether of bisphenol A (DGEBA) or Epon 828, 10 parts per hundred parts epoxy (phr) polyethersulfone (PES) or Victrex 5003P, and 42 phr diaminodiphenylsulfone (DDS) curing agent as HT 976 Hardener. The described materials are now available by Huntsman.

The epoxy, resin system is chosen due to the fact that it represents the temperature and the toughness capabilities for the most of the applications in aviation. As far as the heterogeneous structure is concerned, a model system of semi-crystalline Nylon 6 modifier particles, now available from Toray, is used. The Nylon 6 modifier particles had an average particle diameter of 20 μm or 40 μm . The modifier particles are mixed with the base resin system and applied during the impregnation processing (double-pass impregnation).

3.3.2.2 Task 1: Materials Processing and Fabrication

The prepreg samples during the process had a fiber areal weight of 255 g/m^2 and final resin contents of 35% resin by weight. The reinforcing carbon fibers for all prepreps came in 12K tows Toray T800HB. The areal weights of the modifier particles that are applied during the second impregnation to the prepreg surfaces are measured with an acetone extraction procedure. According to this procedure, the resin films produced during the second impregnation process are washed with acetone through a vacuum-filtration apparatus. The base resin is soluble in the acetone and passed through the filter paper, while the modifier particles are not soluble in the acetone and is filtered out. Filter paper weight increase is close to the particles weight applied to the prepreg surfaces. Then, the modifier particle areal weight can be given by dividing it by the length and width of the resin film via (53):

$$A_p = \frac{W_p}{L_f W_f} \quad 39$$

Where:

A_p = modifier particle areal, weight (g/m^2)

W_p = modifier particle weight in resin film (g)

L_f = resin film, length (m)

W_f = resin film, width (m)

The double pass impregnation process is used for applying the modifier particles into the interlayer. The areal weight calculation of modifier particles assists in defining the resin content required for first and second impregnation passes. This way the overall resin volume fraction of the composite can be controlled and remain in the same level as the one of the conventional CFRP.

3.3.2.3 Task 2: Fracture – Toughness Testing for Evaluating the Interlayer

The following fracture toughness testing methodology description is the same followed by the Mode II fracture toughness testing of CNT epoxy foamed and CNT electrospun interlayers. In order to perform the fracture-toughness testing, a screw-operated Instron mechanical testing machine, Model 4505, is utilized. Mode I interlaminar fracture-toughness testing is performed through Double Cantilever Beam (DCB) testing (B) and Mode II interlaminar fracture-toughness testing through End Notch Flexure (ENF) testing (C) as schematically presented in Figure 3.2.

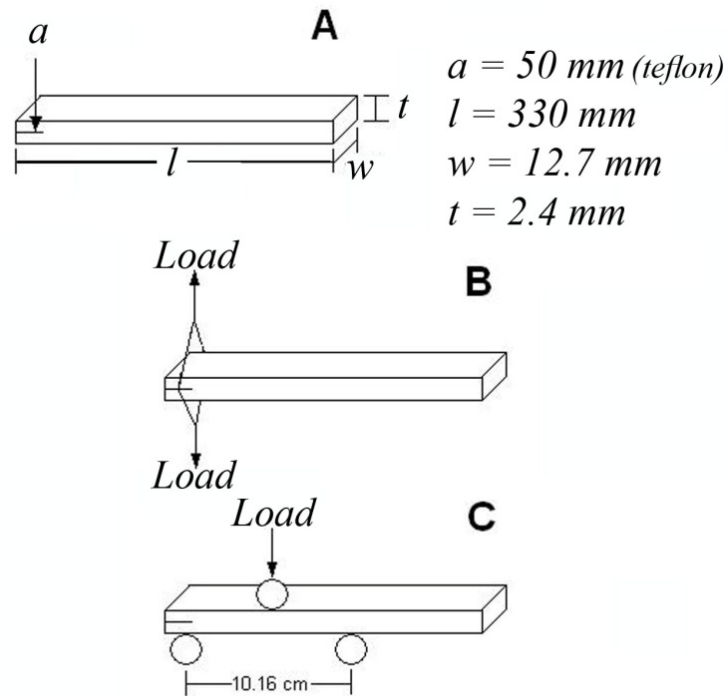


Figure 3.2 Fracture-Toughness Configurations: (a) specimen dimensions, (b) Double Cantilever Beam testing and c) End Notch Flexure testing (5; 53)

The Mode I fracture-toughness is given through (58):

$$G_{IC} = \frac{\Delta A}{w\Delta a}$$

40

Where:

G_{IC} = Mode I critical strain energy-release rate (J/m^2)

ΔA = difference in area under adjacent load/displacement curves (J)

w = width of fracture sample (m)

Δa = increase in crack length (m)

The Mode II fracture-toughness is given through (58):

$$G_{IIC} = \frac{9a^2 P^2 C}{2w(3a^3 + 2L^3)}$$

41

Where:

G_{IIC} = Mode II energy-release rate (J/m²)

a = crack length (m)

P = maximum load (N)

C = sample compliance (Pa⁻¹)

w = sample width (m)

L = distance between central load and support (m)

The micro-sphere interlayer manufactured samples are extensively described in order to understand how the micro-sphere reinforcement impedes the crack propagation in loads developed during Mode II fracture toughness test. The observed behaviour has to be in accordance with scanning electron microscope characterization that has been performed in Polymeric Composites Laboratory (5; 53; 48), for the specific micro-sphere multilayer structures. The understanding of the micro-sphere heterogeneous interlayer is the base for introducing the controlled epoxy foamed and CNT electrospun fibers interlayers.

3.4 Objective #4

Carbon Nanotube in Detail Density and Modulus Analysis (6; 7) – Smallest Part of Fractal

Structure

3.4.1 Rationale

As the smallest part of the featherweight fractal structures carbon nanotubes need to be analyzed in an extensive way in order to find out how they can assist in reducing the overall material weight. This is first approached theoretically and then experimentally. Theoretically, the density and the modulus of the CNT are approached based on their geometry and not on bulk material properties. This way, the experimental results are expected to have a much better

correlation than with other models as the CNT structure plays significant role to its properties. Nobody would expect that a nanotube with 14 nm diameter and 3 walls would have as a tube the same density and modulus with a nanotube with 7nm diameter and 10 walls. For this reason, the approach in analyzing CNT was based on its geometrical characteristics.

3.4.2 Experimental Procedure

3.4.2.1 Task 1: CNT Density and Modulus Approach

Carbon nanotubes have to be extensively analyzed in order to explore their potential for lower density introduction and strength improvement. Based on the existing literature an effort is made to provide an approach of calculating the carbon nanotube density and modulus as well as the polymer nanocomposite (CNT reinforced polymer) density and modulus (6). Specific experimental procedures are also followed in order to correlate the models with experimental results. The correlation of theoretical and experimental results is tested through Pearson correlation and is expected to be above 0.95 in order to have acceptable results for describing the PNC density and modulus. If Pearson correlation is above 0.95, then the experimental and theoretical results are within such limits that PNC density and modulus present correlated significant improvements.

Furthermore, summarizing the approaches of calculating the CNT and the PNC modulus available in literature, it is of high interest to investigate how the CNT modulus would behave considering the real geometry of the CNT, as this approach has been followed in the density calculation model as well. For this reason, the model that is proposed has a strong relation with the CNT density approach.

It is assumed that the CNT layers are modeled as concentric parallel springs with simply added stiffnesses. As a result, it is also assumed that the CNT layers take the same displacement during deformation of the CNT and thus their loadings can be considered to be added (119; 125; 128).

3.4.2.2 Task 2: Interlayer Zoom in – Polymer Nanocomposite (PNC) Approaches

Considering a featherweight composite as a multilayer structure and by zooming in to the interlayer region, the latter can be considered as a polymer nanocomposite (PNC). The case of simply reinforcing the interlayer with carbon nanotubes for reducing the weight and improving the properties is examined.

PNC Density Approach

The density of a polymeric nano-composite reinforced with CNT is calculated through the rule of mixtures for a given value of epoxy density (1.2 or 1.4 g/cm³). The epoxy value can vary according to the desired matrix system. Several combinations of CNT external radius and number of walls have been tried.

PNC Modulus Approach

Having calculated the CNT modulus through the model according to the given number of walls and external radius, the rule of mixtures modified with certain parameters depending on the CNT orientation (129) is used for the PNC modulus calculation. Using this method for short fibers with length smaller than the critical (length where the stress transferred is large enough to break the fiber), the PNC modulus can be calculated through equation 42 (130):

$$E_{comp} = n \cdot z \cdot E_{NT} \cdot v_{CNT} + E_m \cdot (1 - v_{CNT}) \quad 42$$

Where:

E_{comp} : Modulus of the composite (GPa)

E_{NT} : Nanotube modulus (GPa)

E_m : Matrix modulus (GPa)

v_{CNT} : CNT volume fraction

$n =$ **1/5** for randomly oriented CNT,
 3/8 for aligned in plane CNT, and
 1 for aligned CNT

$$z = 1 - \frac{\tanh(\beta \cdot \frac{l}{2})}{(\beta \cdot \frac{l}{2})}$$

z , β , l values are related to nanotube critical length and are analytically discussed in section 4.4.

3.4.2.3 Task 3: Experimental Correlation of Density and Modulus Predictions through Thermo-Gravimetric Analysis (TGA) and Nano-Indentation Testing

In order to correlate the density and elastic modulus calculations, polymeric nanocomposites samples are manufactured and tested first in thermogravimetric analysis (TGA) in order to extract the density data of the samples, and second in nano-indentation testing for measuring the values of the elastic modulus. The polymeric nanocomposites are manufactured at NECST Laboratory at MIT. So at first the CNT are grown through a CVD process at a volume fraction of 1%. Then, the CNT forests are squeezed in order to get higher volume fractions and compare the differences in density and elastic modulus. In total, around eighty samples of aligned CNT in volume fractions from 1 – 30 % are prepared, from which around fifty are infiltrated with RTM6 Hexcel epoxy resin of 1.4 g/cm^3 in order to be tested in TGA and nano-indentation as PNC, while the rest are plainly tested in TGA. Samples of plain resin are also tested in TGA. The thermogravimetric testing of plain CNT forests in different volume fractions and plain resin samples is performed in order to verify the PNC pure experimental density calculations by using the separate densities of CNT forests and plain epoxy resin in the rule of mixtures and actually compose the density of the PNC.

Polymer nanocomposite fabrication

At first, continuous and aligned CNT are grown for fabricating the aligned PNC samples. Multi-walled Nanotubes (MWNT) are grown using the thermal chemical vapor deposition (CVD) method on silicon wafers with a thin catalyst layers of Fe(catalyst)/ Al_2O_3 (diffusion barrier)(1/10 nm) deposited by electron beam evaporation. CNT growth is performed in a (22 mm ID) quartz

tube furnace (G. Finkenbeiner, Inc.) at atmospheric pressure using reactant gases of C₂H₄, H₂ and He (Airgas, 75/400/125 sccm) (131). Typical growth temperature is 750 °C, and average CNT growth rate is 2 μm/s. CNT forests are grown on 1 x 1 cm silicon wafers with coverage of well aligned 10⁹–10¹⁰ CNT. Growth time is 10 min with a typical forest height (continuous CNT length) of 1 mm.

The as-grown (1% volume fraction) CNT forests are released from the growth substrate and the free standing forests are compressed using a mechanical biaxial densification instrument to desired volume fractions (1%, 8%, and 20% Vf) (132). The compressed forests (surfaces unmodified, non-functionalized) are then transferred to a z-stage and lowered into an uncured epoxy pool just touching the top surface of epoxy. An aerospace-grade epoxy, RTM 6 (Hexcel), having viscosity of approximately 80 cP at 90 °C is used for this study. Infiltration of polymer into CNT forest is driven by capillary action which is strongly affected by inter-CNT spacing (volume fraction effect) and polymer viscosity.

CNT preserve their alignment during polymer infiltration to forest, and the epoxy is cured following the recommended procedure from the manufacturer as 1 hour at 160 °C and 2 hours at 180 °C, yielding the desired nanocomposites. The cured samples are machined and mechanically polished to achieve a smooth surface for characterization. As a result of the polishing and base-growth CNT processes, no Fe catalyst is present in the specimens. Thermogravimetric analysis (TGA) indicates the forests contain less than 10% amorphous carbon, which is deposited on the CNT sidewalls from the hydrocarbon atmosphere during growth (133). Volume fractions for all samples are assessed by volumetric calculations. The aligned PNC samples fabricated for the nano-indentation testing are at ~1%, 8%, and 20% volume fractions (134). More aligned PNC samples are fabricated used in TGA testing with volume fractions from 1 to 30 %.

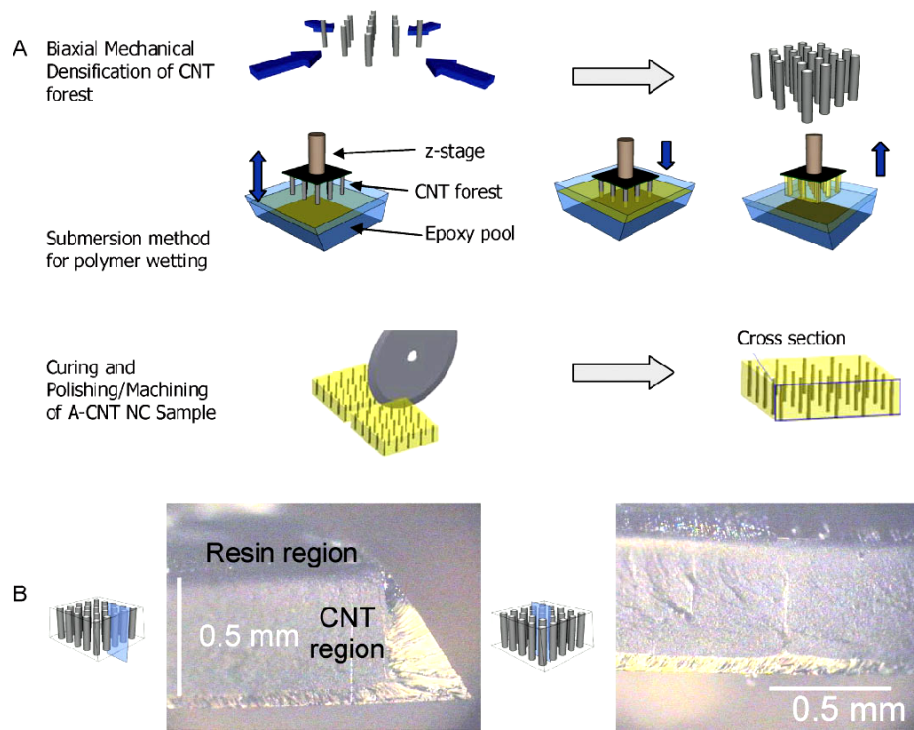


Figure 3.3 Fabrication of Variable Volume Fraction Aligned-CNT Nano-Composites. (a) process flow for fabricating nanocomposites, (b) optical images of 1% volume fraction RTM6 nano-composite specimens after fabrication (132)

In Figure 3.3 the flow of the PNC fabrication procedure is presented. The CNT forest is subtracted from the wafer and mechanically squeezed to higher volume fractions. The squeezed forest is attached on an adhesive tape and then deepened in the epoxy bath where it is infiltrated with resin. Afterwards, the sample is machined and polished to the desired shape for testing.

Following, in Figure 3.4, the densification of CNT forests from volume fraction of 1% as grown to 20 % is illustrated. By utilizing this method, samples of different volume fractions are also manufactured and tested in as far as the PNC density is concerned.

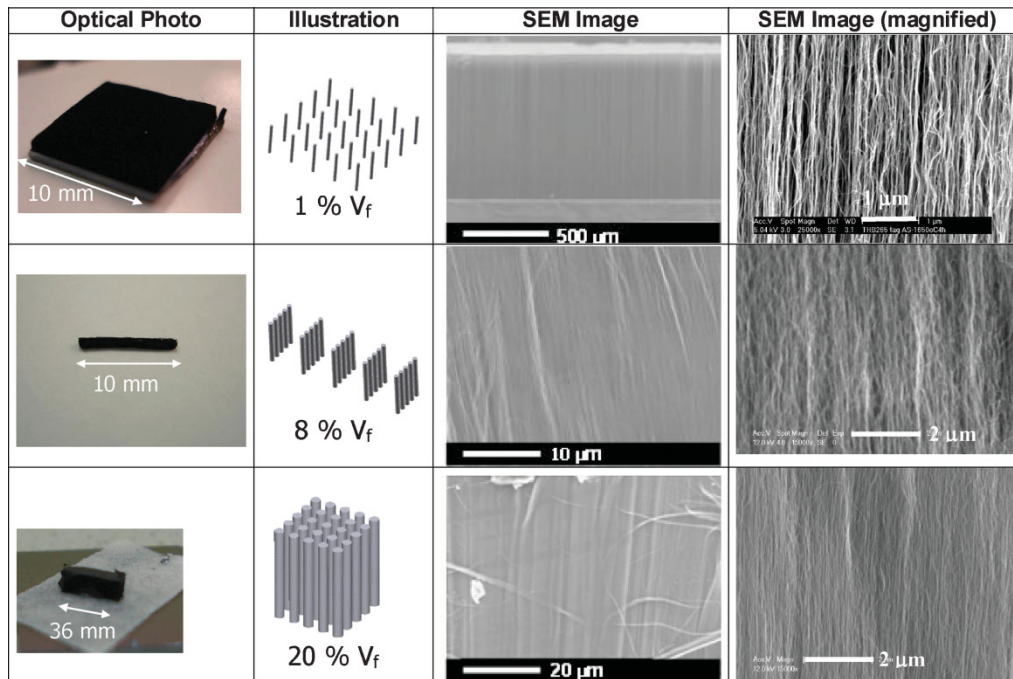


Figure 3.4 Aligned CNT Volume Fraction from Mechanical Densification of CNT Forest. 1mm tall aligned-CNT forests at 1% (as-grown), 8% (uniaxially densified), and 20% (biaxially densified) volume fraction (132)

Task 3A: Nano-indentation testing

The aligned PNC samples are tested via standard nano-indentation methods for modulus extraction. To achieve consistent results, the surfaces are mechanically polished in three steps with particle roughness ranging from 5 μm down to 0.005 μm . Surfaces are inspected under optical microscope before testing. The tests are performed using a Nanotest 600 nano-mechanical testing system (Micro Materials, UK). The nano-indenter monitors and records the load and displacement, which is capable of measuring and applying loads and depths ranging from 10 mN to 20 N (resolution ~ 100 nN) and up to 50 μm (resolution ~ 0.1 nm). Tests are performed inside the thermally insulated environmental chamber of the nano-indenter ($25\text{ }^\circ\text{C} \pm 0.5\text{ }^\circ\text{C}$) and relative humidity ($45\% \pm 2\%$) with a Berkovich-type indenter. In order to compare the results obtained for the unreinforced epoxy matrix and the nanocomposites, the

test parameters are held constant, including importantly for polymers loading and unloading rates (100 mN/s respectively). Depending on the sample sizes, 12–16 indents are applied over the surface of each sample with a spacing of 350 μm . The samples are mounted on an aluminum stub and indented to 30 μm . Good surface quality via the three step polishing method yields highly repeatable (overlapping indentation curves) results. The load–displacement curves are analyzed to determine modulus using the (135) theory where the unloading curve is used to obtain the reduced modulus (E_r). The reduced modulus is related to the specimen modulus through equation 43 for isotropic materials:

$$\frac{1}{E_r} = \frac{1-\nu^2}{E} + \frac{1-\nu_i^2}{E_i} \quad 43$$

Where E is the modulus of the sample, ν is the Poisson's ratio normal to loading of the sample, E_i is the indenter modulus, and ν_i is the indenter Poisson's ratio. The indenter is diamond with $E_i = 1141$ GPa and $\nu_i = 0.07$, ν is assumed as 0.3 due to the matrix (polymer) dominated response in this direction, and because this yields the most conservative (lowest) calculation of modulus. Due to the aligned nature of the CNT in most of the samples tested, the material is not isotropic and therefore when using equation 43, the extracted modulus is referred to here as an effective modulus (136).

Task 3B: Thermogravimetric Analysis (TGA)

The density is measured at 100 $^{\circ}\text{C}$ by dividing the accurate weight measured in the TGA experiment at this temperature with the volume measured by the sample prior to TGA experiment. In the experiment, the sample is heated to 100 $^{\circ}\text{C}$ and kept there for 5 minutes in order to evaporate any possible absorbed moisture. The volume of the sample is not affected at this temperature and as a result the initial volume is taken account. In general after the 5 minute isothermal at 100 $^{\circ}\text{C}$ the weight of the sample is 2 to 5 % lower than the initial weight and this reduction happened due to absorbed moisture evaporation. It has to be mentioned that the TGA experimentation of PNC is performed in two approaches. First, PNC samples are tested in TGA

measuring the thermogravimetric behavior of the PNC as a single body. Second, pure resin samples and pure CNT samples in different volume fractions are tested separately and the findings are combined in the rule of mixtures. As it is presented in results and discussion there is a good agreement between those two PNC thermogravimetric experimentation approaches.

3.5 Objective #5

CNT Controlled Nano-porosity Reinforced Interlayer

3.5.1 Rationale

This is the major step to establish a new interlayer that implemented within the CFRP plies constitutes a featherweight composite. Following specific steps to calculate the interlayer characteristics of epoxy foam and CNT, manufacturing takes place. After that, the final material is tested in a series of experiments to find out the viscoelastic, thermal, and mechanical properties as well as to observe and verify its final structure through microscopy. Through these tests, the epoxy foam interlayered composite is continuously compared with conventional CFRP to verify the overall density reduction and the strength enhancement.

3.5.2 Experimental Procedure

3.5.2.1 Task 1: Desired Pore Size Formula Calculation Development

At this level a formula is developed which is able to calculate the desired pore size in the epoxy matrix system. This way the CNT reinforced epoxy foamed interlayer is explored. Depending on the structure, the pore size may vary; however, in order to be able to use the final material - CFRP with CNT reinforced epoxy foamed interlayer - within primary structures of high tech applications, the pore size has to remain in the nano level and not exceed approximately 400 to 500 nm. This way stress concentration and crack initiation is avoided.

Stiffness calculations of the new materials are provided in order to compare the nano-foamed material with conventional CFRP. Also, a formula is developed for measuring the void content within the material, which is used in the calculation of the desired pore size.

Task 2: Formula for Calculating the Desired CNT volume fraction for pore surface reinforcement

The nanopores surface is reinforced with CNT. The desired CNT volume fraction is determined through specific formulas that contain the pores volume fraction. Additionally, the formula is going further into analyzing the pore surface reinforcement phenomenon. High stiffness of CNT, and thus high CNT resistance to bending, is taken into account. As a result, not the entire CNT length can be attached to the surface but only a part of it.

3.5.2.2 Task 3: Fabrication of Montmorillonite Nanoclay Reinforced Polyurethane samples

In order to easily explore the neat distribution of the nano-inclusion on the pore surface an experiment is conducted which simply uses nanoclays of montmorillonite within a polyurethane matrix system. This system can be clearly observed with scanning electron microscope due to bigger sizes of nano-clays compared to CNT. The montmorillonite reinforced polyurethane is done in three different nanoclay concentrations of 1, 3, and 5% manufacturing samples with and without nucleating agent. The samples are then characterized in scanning electron microscopy in order to observe the theoretical phenomenon explain how the nano-inclusions tend to reinforce the void surface during the formation of the voids

3.5.2.3 Task 4: Design and Manufacturing Epoxy foam samples reinforced with CNT-Interlayer

Samples are manufactured with epoxy (Epoxy 921 similar system to EPON 828) within the fiber bed adding an interlayer between the plies with epoxy foam and carbon nanotubes in the desired volume fractions that derive from the analysis described in section 3.5.2.1. In order to be able to assess the property contribution of both the epoxy foam and the CNT to the overall material three different groups of samples are manufactured with 4 plies of woven carbon fiber reinforced epoxy each at a fiber volume fraction of 60%.

A) Conventional CFRP control samples

B) CFRP with epoxy foamed interlayer

C) CFRP with CNT reinforced epoxy foamed interlayer

All the samples are then tested in DMA, Flexural and Tension Mechanical testing, and Scanning Electron Microscopy Characterization.

3.5.2.4 Task 5: Dynamic Mechanical Analysis for Evaluating Viscoelastic Behaviour

The Dynamic Mechanical Analyzer used for this study is a Triton DMA. The temperature elevating rate used is 2 °C/min. For this rate the samples are elevated up to 120 °C. The samples are tested in 3-point bending experiments. Taking the three different groups of samples manufactured with the CNT epoxy foamed interlayer, samples of approximately 40x10 mm² (l x w) are cut and tested in the DMA. The thickness is approximately 1 mm. More than three experiments are performed for each group of samples in order to verify the repeatability of the results.

3.5.2.5 Task 6: Mechanical Testing for Evaluating the Interlayer

Task 6A: Flexural Mechanical Testing

The specimens are tested in a screw Instron machine (model 4505). More than five specimens are tested for each of the three different CFRP sample groups manufactured. Specimens of 130x20 mm² (l x w) are taken for each of the CFRP group of samples (The length mentioned is the gauge length). The thickness is approximately 1 mm. The crosshead of the machine in the three point bending test had a speed of 5mm/min and the test is performed from no loading state to failure. Mode II fracture toughness is also measured with the characteristics described in section 3.3.2.3.

Task 6B: Tension Testing

Furthermore, specimens are also tested under tension testing in the same Instron machine that flexural testing took place. Specimens are prepared according to ASTM D638-03

(Figure 3.5). The thickness is again approximately 1 mm. The crosshead of the machine in the tensile test has a speed of 1mm/min and the test is performed from no loading state to failure.

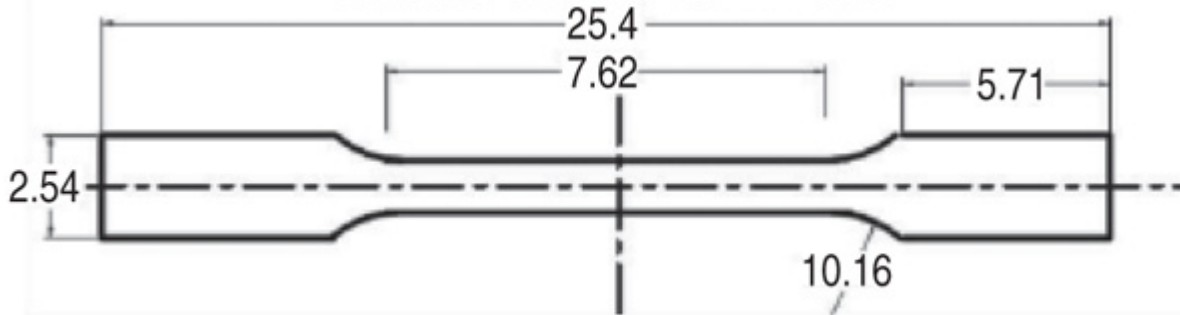


Figure 3.5 ASTM D638-03 Dimensions in cm

3.5.2.6 Task 7: Scanning Electron Microscope for Interlayer Characterization

The manufactured samples are also observed in scanning electron microscope characterization for visual explanation of the mechanical analysis. Samples were cut in dimensions of $10 \times 5 \times 1.5 \text{ mm}^3$ so the cross section ($5 \times 1.5 \text{ mm}^2$) can be observed in the microscope. Although carbon fibers are conductive, the matrix reduces the conductivity for SEM observation, thus, higher conductivity was achieved through gold low-vacuum sputter coating. The SEM utilized was a VEGA TESCAN 3SB microscope. Samples are exposed to an electron beam which comes through a tungsten heated filament electron gun. Finally, resolution of the SEM utilized as high as 3nm at 30kV and as low as 8nm at 3kV. Particularly, the epoxy foamed interlayered samples were tested at 20kV and 30kV.

3.5.2.7 Task 8: Statistical Regression Model for Parametrical Prediction of Strength

A multiple regression statistical model is also developed based on the experimental results for prediction of the material flexural strength as a function of interlayer improvement, flexural modulus, tensile strength, and glass transition temperature.

3.6 Objective #6

CNT Electrospun Fibers Reinforced Interlayer

3.6.1 Rationale

At this final objective, another technique for establishing a new interlayer for featherweight composites is evaluated. Following similar steps with those at objective #5 to calculate the electrospun fiber interlayer characteristics, manufacturing takes place. After that, the final material is tested in a series of experiments to find out the viscoelastic, thermal, and mechanical properties as well as to observe and verify its final structure through microscopy. Through these tests, the electrospun interlayered composite is continuously compared with conventional CFRP to verify the overall density reduction and the strength enhancement.

3.6.2 Experimental Procedure

3.6.2.1 Interlayer set up

The carbon fiber bed is placed within the electrospinning configuration and the electrospinning takes place on the fiber bed surface. The epoxy resin is then applied to the other surface of the fiber bed. This happens for 4 different plies which finally are consolidated together. The size restrictions of the electrospinning set up let us manufacture a panel of 200x400 mm². The cellulose acetate solution prepared for electrospinning on each layer is 20ml. The CNT are mixed with the cellulose acetate solution on a volume fraction of 1% and then spun onto the fiber bed. Furthermore, stiffness calculations of the new materials are provided in order to compare the electrospun material with conventional CFRP.

3.6.2.2 Task 1: Design and Manufacturing of Electrospun Fibers reinforced with CNT Interlayer

Samples are manufactured with epoxy (Epoxy 921 similar system to EPON 828) within the fiber bed adding an interlayer between the plies with electrospun fibers out of cellulose acetate and carbon nanotubes in specific volume fractions. In order to be able to assess the property contribution of both the polymeric electrospun fibers and the CNT to the overall

material three different groups of samples will be manufactured with 4 plies of woven carbon fiber reinforced epoxy each at a fiber volume fraction of 0.6.

- A) Conventional CFRP control samples
- B) CFRP with electrospun fibers in the interlayer
- C) CFRP with CNT reinforced electrospun fibers interlayer (1-2%)

All the samples are then tested in DMA, Flexural and Tension Mechanical testing, and Scanning Electron Microscopy Characterization.

3.6.2.3 Task 2: Dynamic Mechanical Analysis for Evaluating Viscoelastic Behaviour

The Dynamic Mechanical Analyzer used for this study is a Triton DMA. The temperature elevating rate used is 2 °C/min. For this rate the samples are elevated up to 120 °C. The samples are tested in 3-point bending experiments. Taking the three different groups of samples manufactured with the CNT epoxy foamed interlayer, samples of approximately 40x10 mm² (l x w) are cut and tested in the DMA. The thickness is approximately 1 mm. More than three experiments are performed for each group of samples in order to verify the repeatability of the results.

3.6.2.4 Task 3: Mechanical Testing for Evaluating the Interlayer

Task 3A: Flexural Mechanical Testing

The specimens are tested in a screw Instron machine (model 4505). More than five specimens are tested for each of the three different CFRP sample groups manufactured. Specimens of 130x20 mm² (l x w) are taken for each of the CFRP group of samples (The length mentioned is the gauge length). The thickness is approximately 1 mm. The crosshead of the machine in the three point bending test had a speed of 5mm/min and the test is performed from no loading state to failure. Mode II fracture toughness is also measured as described in section 3.3.2.3.

Task 3B: Tension Testing

Furthermore, specimens are also tested under tension testing in the same Instron machine that flexural testing took place. Specimens are prepared according to ASTM D638-03 (Figure 3.5). The thickness is again approximately 1 mm. The crosshead of the machine in the tensile test has a speed of 1mm/min and the test is performed from no loading state to failure.

3.6.2.5 Task 4: Scanning Electron Microscope Interlayer Characterization

The manufactured samples are also observed in scanning electron microscope characterization for visual explanation of the mechanical analysis. Samples were cut in dimensions of 10x5x1.5 mm³ so the cross section (5x1.5 mm²) can be observed in the microscope. Although carbon fibers are conductive, the matrix reduces the conductivity for SEM observation, thus, higher conductivity was achieved through gold low-vacuum sputter coating. The SEM utilized was a VEGA TESCAN 3SB microscope. Samples are exposed to an electron beam which comes through a tungsten heated filament electron gun. Finally, resolution of the SEM utilized as high as 3nm at 30kV and as low as 8nm at 3kV. Particularly, the electrospun fiber interlayered samples were tested at 20kV and 30kV.

3.6.2.6 Task 5: Statistical Regression Model for Parametrical Prediction of Strength

A multiple regression statistical model is also developed based on the experimental results for prediction of the material flexural strength as a function of interlayer improvement, flexural modulus, tension strength, and glass transition temperature.

CHAPTER 4
RESULTS AND DISCUSSION

4.1 Results for Specific Objective #1: Matrix System Description

Extracting the relaxation times, the activation energies and the relaxed and unrelaxed moduli from equations 21 through 24 leads to results, illustrated from Figure 4.1 to Figure 4.3, which fit the experimental results that were performed according to the process described in methodology section 3.1.

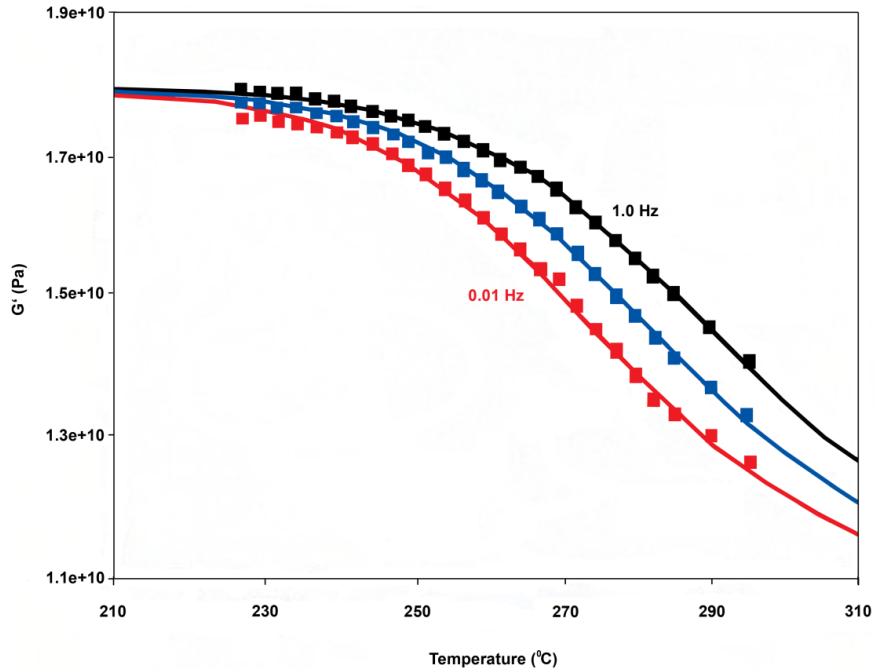


Figure 4.1 DMA Storage Modulus for the Glass Transition Compared to the Model (continuous line) vs. Temperature, at 0.01, 0.1 and 1 Hz (1; 2).

Figure 4.1 presents the comparison between the experimental (DMA) storage modulus data and the model prediction in the glass transition as a function of temperature for three

different frequencies: 0.01, 0.1, 1 Hz. The model is in excellent agreement with the experiment up to 290 °C.

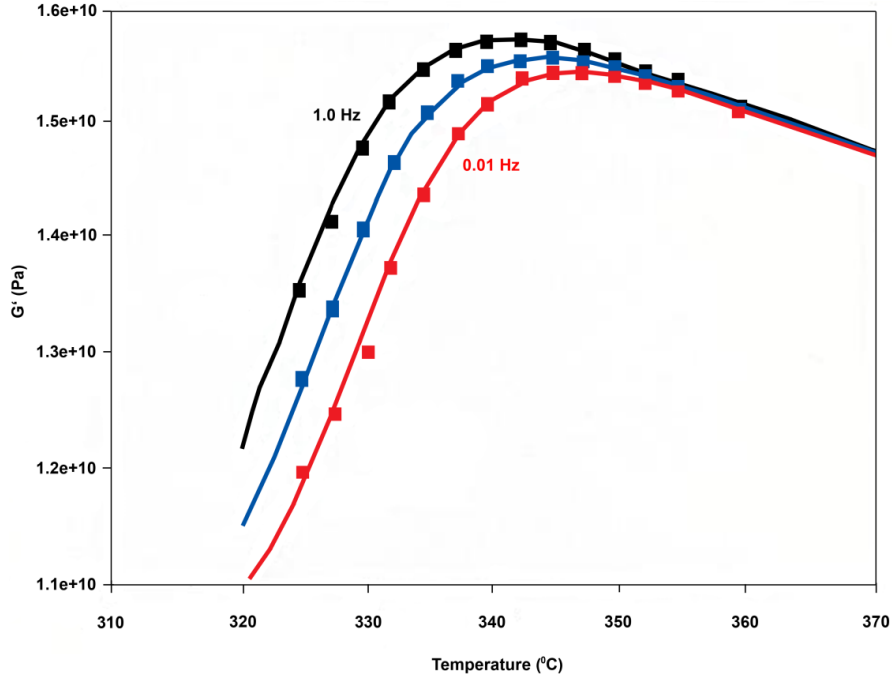


Figure 4.2 DMA Storage Modulus during Degradation Compared to the Model (continuous line), vs. Temperature, at 0.01, 0.1 and 1.0 Hz (1; 2).

Moreover, Figure 4.2 presents the comparison of DMA storage modulus with model prediction under the degradation process between 290°C and 360°C for three frequencies of 0.01, 0.1, 1 Hz. They are in good agreement as well, revealing the viscoelastic analysis methodology validity for the degradation process. Relaxation time and relaxed/unrelaxed modulus are the two temperature-dependent parameters involved in this model.

Additionally, as presented in Figure 4.3, the GSLS model describes the intermediate region between glass transition and degradation processes very well for different frequencies as well.

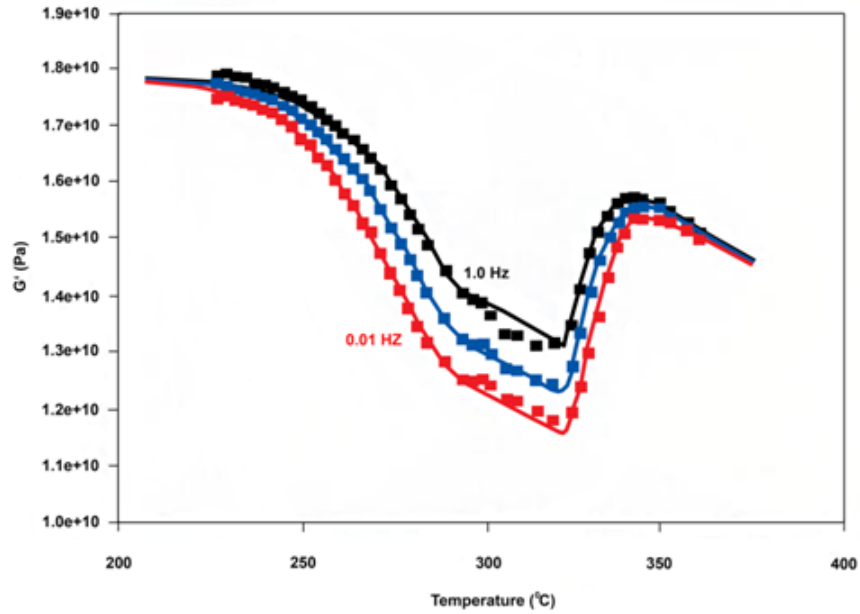


Figure 4.3 DMA Storage Modulus for Both Glass Transition and Degradation Processes, Compared to the Model (continuous line), vs. Temperature, at 0.01, 0.1 and 1.0 Hz (1; 2).

Finally, Figure 4.4 presents $\tan\delta$ value predicted by the model. Two peaks of $\tan\delta$ for 0.01 Hz and one broad peak for 1 Hz are predicted by the model. However, the correlation between experimental results and the GSL model present lower correlation compared to the storage modulus.

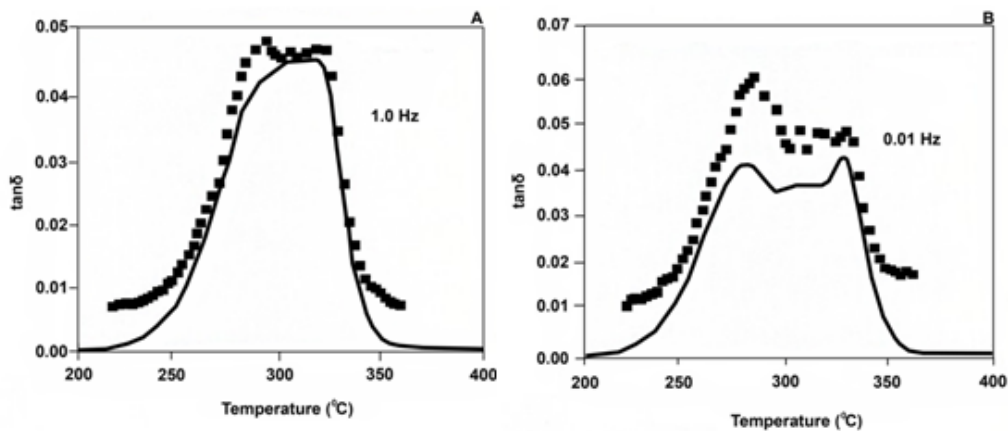


Figure 4.4 Comparison of $\tan\delta$ with the Model (continuous line), vs. Temperature, at (a) 1.0 Hz and (b) 0.01 Hz (1; 2).

The correlation between theoretical and experimental results is presented in Table 4.1. Correlation values must be higher than 0.95.

Table 4.1 Theoretical and Experimental Correlation of Storage Modulus and $\tan\delta$ at 0.01 and 1 Hz.

	Storage Modulus Experimental (1Hz)	Storage Modulus Experimental (0.01Hz)	$\tan\delta$ Experimental (1Hz)	Tanδ Experimental (0.01Hz)
Storage Modulus Theoretical (1Hz)	0.9984			
Storage Modulus Theoretical (0.01Hz)		0.9997		
$\tan\delta$ Theoretical (1Hz)			0.9929	
$\tan\delta$ Theoretical (0.01Hz)				0.9571

The good agreement of the phenolic dynamic mechanical analysis results with the generalized standard linear model, an established model for viscoelastic behaviour characterization, reveals the potential of dynamic mechanical analysis technique to explore and describe the viscoelastic characteristics of matrix resin systems and more specifically to give detailed information on the glass transition and degradation processes, which are of particular interest in aviation.

4.2 Results for Specific Objective #2: Innovative Manufacturing Process

This section mainly focuses on evaluating the thermosetting matrix systems that have been manufactured through the Repair Clave and compare the quality standards with those of the autoclave process.

4.2.1 DSC Analysis Curing Evaluation

At first, uncured samples of the prepreg, with which the panels were manufactured, were tested in DSC. Figure 4.5 shows the DSC scans for all uncured samples at 0.5, 1 and 5 °C/min heating rate. It can be easily noticed that with an increasing heating rate the area under

the peaks, which by integral represents the heat of the exothermic reaction needed for the cure, is increasing as well. Thus the higher the heating rate, the higher the heat of cure. This may happen due to the fact that the macromolecules of the polymer need more time to respond to the temperature elevation when the latter increases rapidly, due to the curing kinetics of the thermoset. Because of this time lag in the curing response, the material appears to extend and increase the exothermic heat of the polymerization reaction.

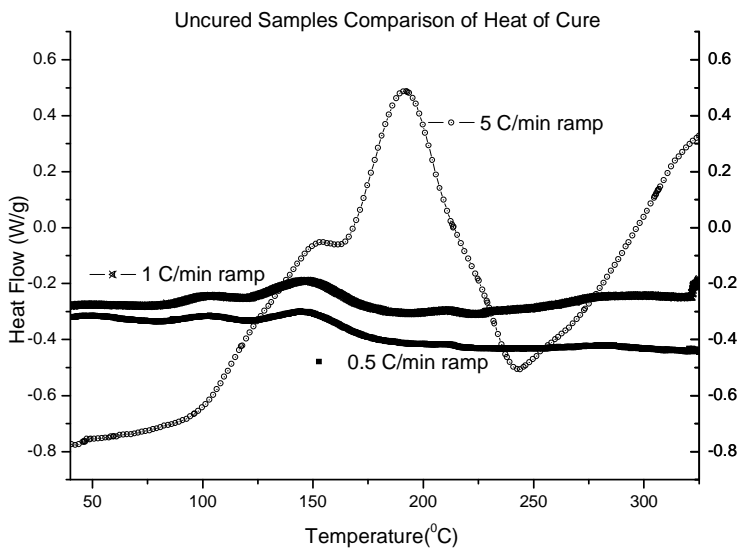
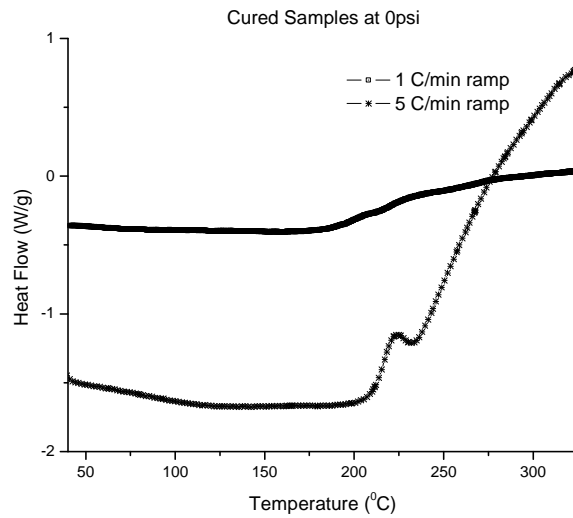


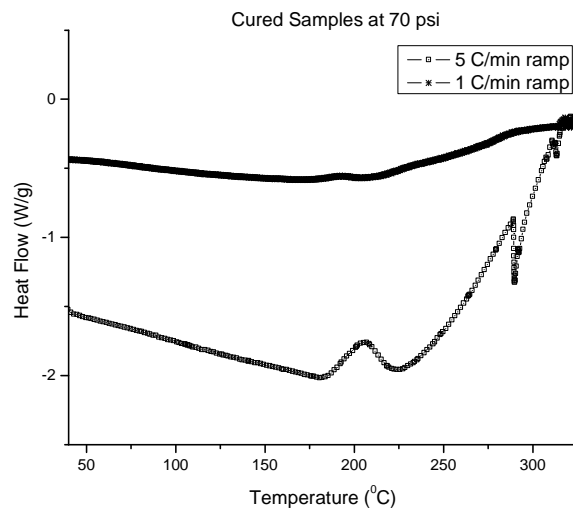
Figure 4.5 Uncured Samples, Heat of Cure Comparison (4)

Secondly, dynamic scans from 0 to 400 °C, at heating rates of 0.5 °C/min, 1°C/min, 5°C/min, were carried through for all different samples manufactured under the pressure of 0 to 70 psi (0 to 485 kPa). The sample weight varied from 3mg to 20mg, and generally two samples were collected for each of the pressure cases in each of the heating rates, in order to verify the results.

Figure 4.6 gives an indication of the samples evaluation in DSC based on the exothermic peak.



(a)



(b)

Figure 4.6 DSC Dynamic Scans at 1 and 5 °C/min for Different Pressure Manufactured Samples (a) 0 psi, (b) 70 psi (485 kPa) (4)

In Figure 4.6, the comparison between the two cases 0 psi/kPa and 70 psi (485 kPa) can be observed. For the rate of 1 °C/min the 0 psi samples still exhibit small exothermic peaks,

while the 70 psi does not show any peaks. This could be an indication that the 70 psi samples were better cured than the 0 psi ones. However, by checking the 5 °C/min rates this behavior is not repeated. This leads to the conclusion that pressure during manufacturing may not really affect the percentage of curing.

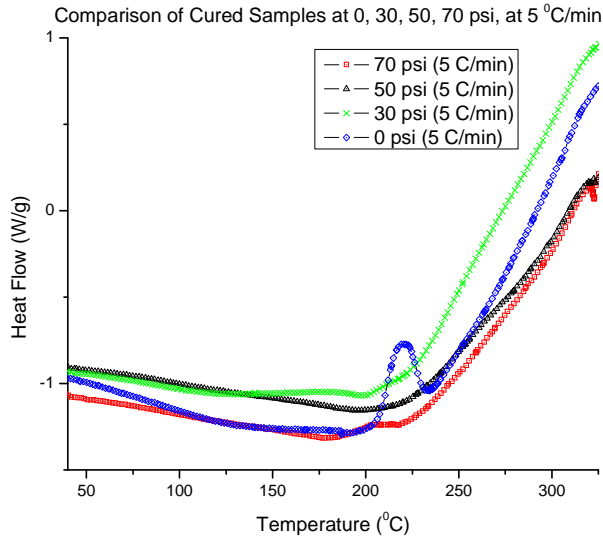


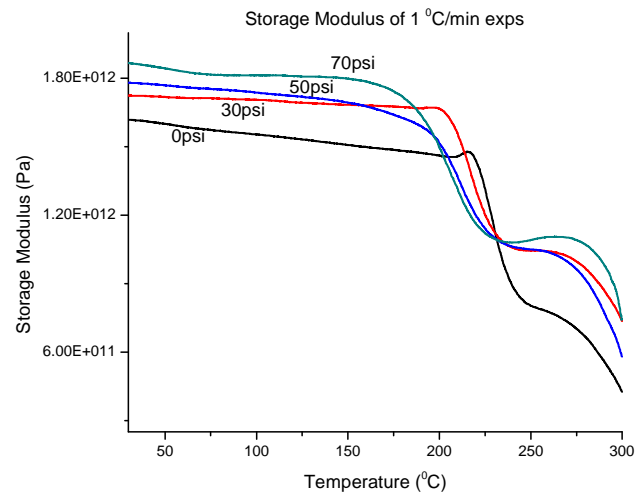
Figure 4.7 8 Plies Samples Comparison for the Rate 5 °C/min at 0, 30, 50, 70 psi (0, 205, 345, and 485 kPa) (4)

Figure 4.7 illustrates the curves for all the 8 ply-samples analyzed at a rate of 5 °C/min. As it can be seen, there is no consistent pattern of behavior for all pressure cases. The two exothermic peaks are noticed for 0 psi and 70 psi (485 kPa), the two extreme pressure cases. However, for the cases in between (30 and 50 psi (205 and 345 kPa)) there are no peaks, fact that shows that these were better cured than the rest of the samples. This observation can partly verify the conclusion that was made above, regarding the pressure non-monotonic effect on the curing percentage. Furthermore, it has also to be mentioned that the correlation of the DSC experiments of cured samples with the uncured ones gave a percentage of curing

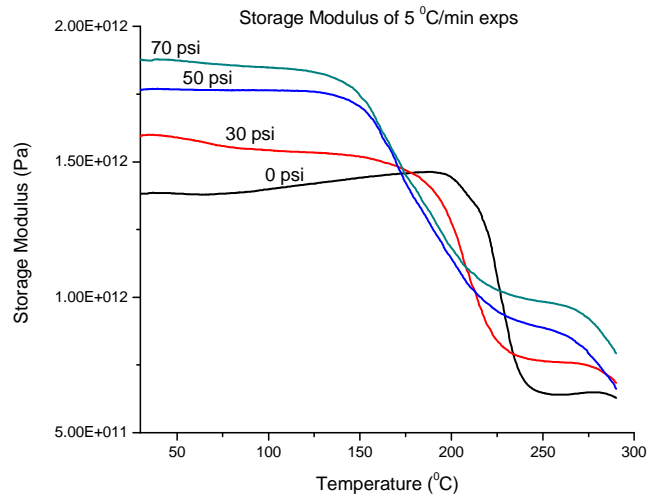
between 93 to 99%, not consistently distributed from 0 to 70 psi, which can also be concluded from the DSC graphs.

4.2.2 DMA for Viscoelastic Behaviour Evaluation

The following graphs present the storage modulus of the samples manufactured in 0, 30, 50 and 70 psi (0, 205, 345, and 485 kPa) in 1 and 5 °C/min heating rates.



(a)



(b)

Figure 4.8 Storage Modulus of Carbon Fiber Prepregs – 8 Plies Manufactured in 0, 30, 50 and 70 psi (0, 205, 345, and 485 kPa) in (a) 1 and (b) 5 °C/min heating rates (4)

It can be seen that there is an increase of the modulus while the manufacturing pressure increases, which is expected as the higher the pressure during manufacturing is, the less void formation within the composite is established. However, it is observed that glass transition temperature decreases while the pressure increases up to 50 °C from 70 to 0 psi. The glass transition reduction in 1 °C/min heating rate is in the order of around 30 °C ($T_g = 206$ °C at 70 psi (485 kPa) and $T_g = 228$ °C at 0 psi/kPa). This difference expands when the heating rate increases to 5 °C/min in the order of around 50 °C ($T_g = 180$ °C at 70 psi (485 kPa) and $T_g = 225$ °C at 0 psi/kPa).

This can be explained due to internal stresses (137) that the higher pressure imparts into the composite. Thus, the temperature increase relieves the stresses and the material softens, leading to an apparent decrease of the glass transition temperature. This was verified by annealing the 70 psi (485 kPa) manufactured samples at 220 °C for an hour, and then performing DMA at the 5 °C / min heating rate. The T_g value was increased from 180 °C to 214 °C, which is a value very close to the 0 psi manufactured sample, Figure 4.9.

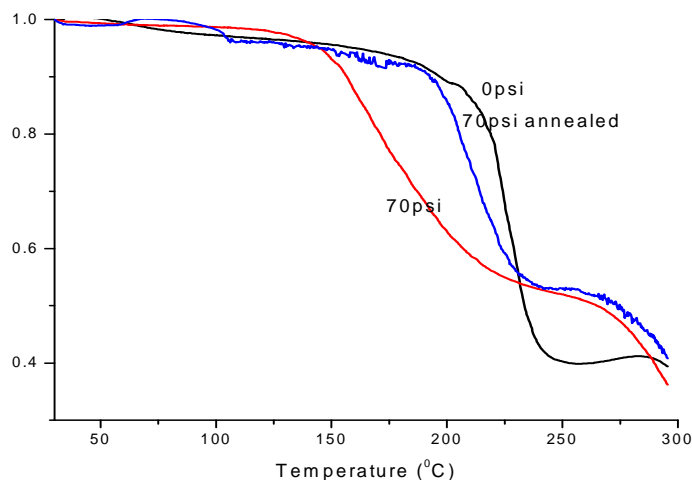
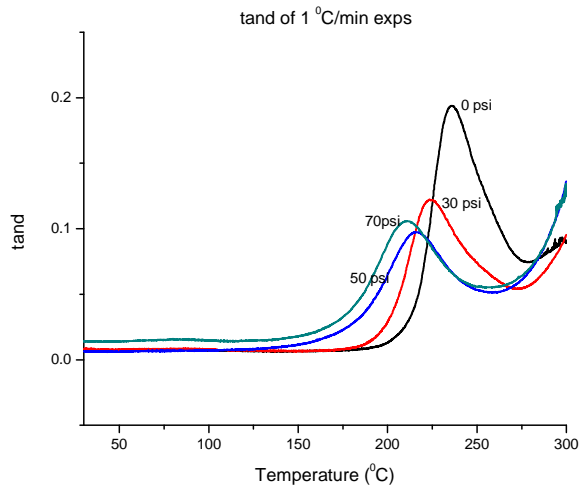
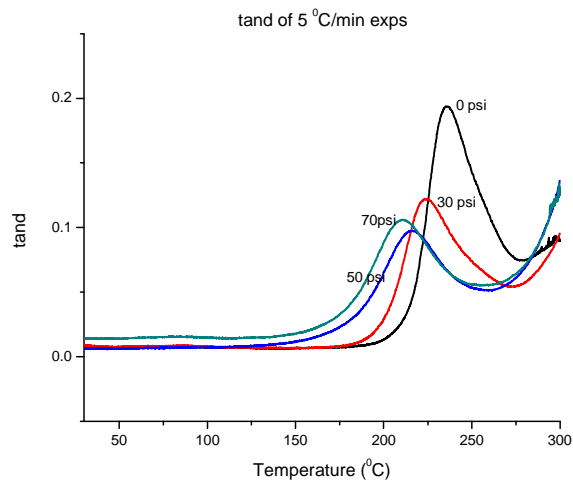


Figure 4.9 Normalized Moduli Comparison of 0 psi, 70 psi (485 kPa) and 70 psi (485kPa) Annealed. T_g of the Annealed 70 psi Sample at 220 °C is Much Closer to the 0 psi Sample T_g (4).

Finally, the $\tan\delta$ of different manufacturing pressures in 1 and 5 °C/min heating rate is presented in Figure 4.10. The glass transition temperature presents similar behavior as in the storage modulus. Also, the damping from the 0 psi to 70 psi (485 kPa) decreases for both heating rates, which correlates with the storage modulus slight increase while the manufacturing pressure increases.



(a)



(b)

Figure 4.10 $\tan\delta$ of Carbon Fiber Prepregs – 8 Plies Manufactured in 0, 30, 50 and 70 psi (0, 205, 345, and 485 kPa) in 1 and 5 °C/min (4)

4.2.3 Flexural & Compression Mechanical Testing

Two different tests were performed for the CFRP specimens manufactured under 0, 30, 50, and 70 psi (0, 205, 345, and 485 kPa). As stated in the experimental description, the first testing was flexural mechanical testing (three point bending). Figure 4.11 presents average specimens tested in each of the manufacturing pressures.

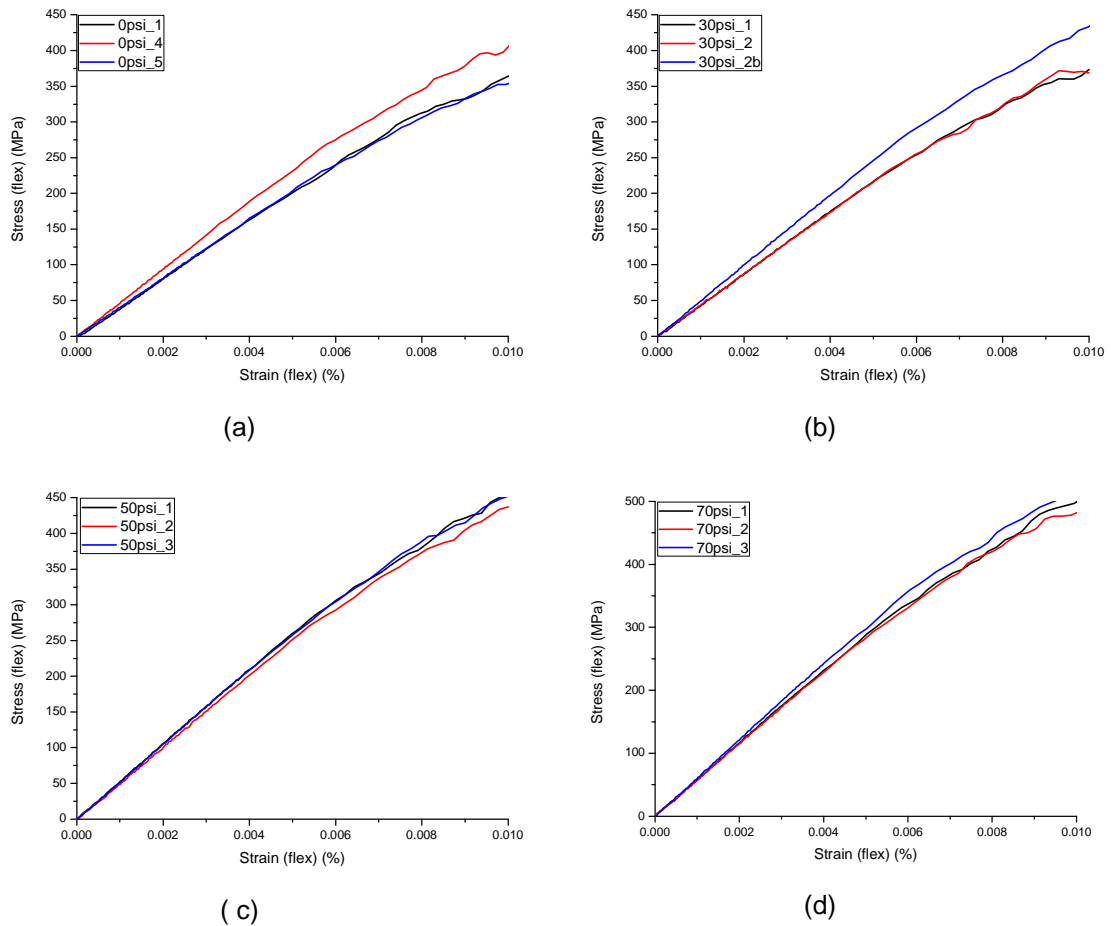


Figure 4.11 Flexural Testing, Stress – Strain Curves for (a) 0 psi, (b) 30 psi (205 kPa), (c) 50 psi (345 kPa), and (d) 70 psi (485 kPa)

Following, in Figure 4.12, a comparison of the four different panels manufactured under 0, 30, 50, and 70 psi (0, 205, 345, and 485 kPa) in flexural mechanical testing is presented

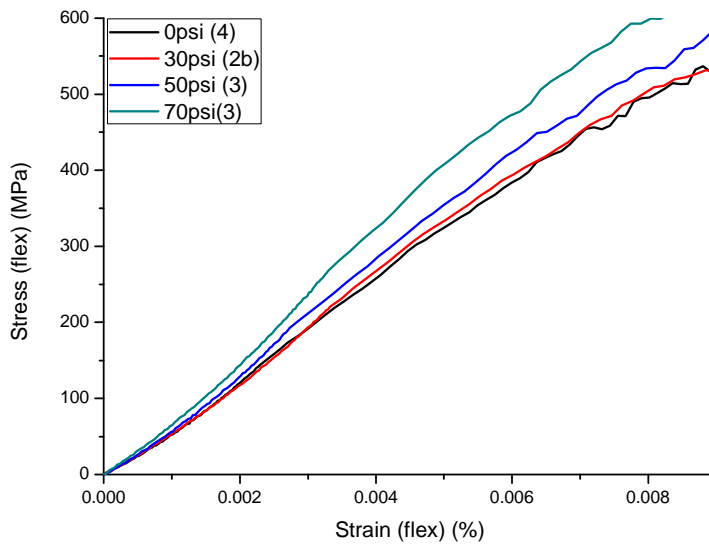


Figure 4.12 Stress-Strain Comparison of CFRP Specimens Manufactured under 0, 30, 50, and 70 psi (0, 205, 345, and 485 kPa) Derived from Flexural Testing

It can be seen that the specimens manufactured in 70 psi (485 kPa) have a larger inclination than the specimens manufactured under 0 psi/kPa in relation to the strain axis, which is translated to a higher modulus.

The flexural modulus is calculated by equation 44:

$$E_f = \frac{L^3 \cdot F}{4 \cdot w \cdot h^3 \cdot d} \quad 44$$

Where

E_f : Flexural Modulus (MPa)

L: Gauge length (mm)

w: specimen cross section width (mm)

h: specimen cross section height (mm)

F: Load (N)

d: the deflection due to load F (mm)

By calculating the flexural modulus through equation 45 applied for the elastic region of the stress-strain curve, the values of the flexural modulus are similar to the ones calculated by equation 44.

$$E_f = \frac{\sigma_2 - \sigma_1}{\epsilon_2 - \epsilon_1} \tag{45}$$

Where

σ_1, σ_2 : two random stress values on the stress-strain elastic region ($\sigma_2 > \sigma_1$)

ϵ_1, ϵ_2 : two random strain values on the stress-strain elastic region ($\epsilon_2 > \epsilon_1$)

Equation 45 actually gives the direction coefficient of the stress-strain curve elastic region which represents the flexural modulus.

Regarding the compression testing that was performed; Figure 4.13 presents the average specimens tested in each of the manufacturing pressures

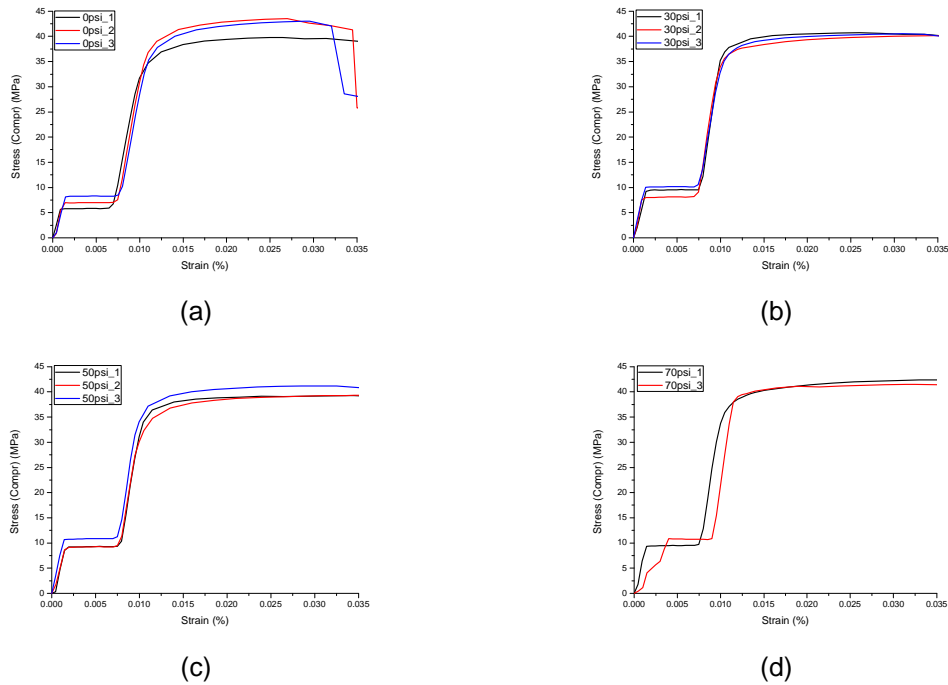


Figure 4.13 Compression Testing, Stress - Strain Curves for (a) 0 psi, (b) 30 psi (205 kPa), (c) 50 psi (345 kPa), and (d) 70 psi (485 kPa)

Following, in Figure 4.14, a comparison of the four different panels manufactured under 0, 30, 50, and 70 psi (0, 205, 345, and 485 kPa) in compression mechanical testing is presented

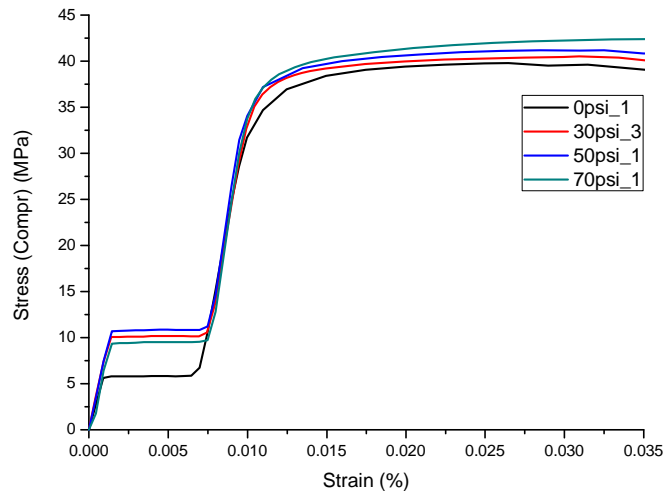


Figure 4.14 Stress-Strain Comparison of CFRP Specimens Manufactured under 0, 30, 50, and 70 psi (0, 205, 345, and 485 kPa) Derived from Compression Testing

It can be seen that there are no big differences in the inclination of the stress-strain curves at the elastic region. This means that the modulus of CFRP composites manufactured under different pressures does not present significant changes in compression loads from low to higher pressures while manufacturing. The compression modulus is derived from equation 45 applied for the elastic region of the compression testing stress-strain curve.

A plateau is also seen at around 10 MPa stress for all the tested samples. This plateau physically means that when the stress gets to the level of 10 MPa, an internal mechanism does not allow the stress to increase although strain increases. Potential material defects may collapse and as a result, the load does not increase. Furthermore, another scenario would be that at this load ply delamination may initiate resulting in a larger cross section and thus, in maintaining stress constant for a while. Finally, while the sample is under compression,

suddenly a slight bending starts occurring for 4 to 6 seconds along the sample due to the nature of the composite. Thus, another explanation could be that the material load does not evolve while this sudden bending is occurring and as a result the load presents a lag with regards to the strain increase. However, as it can be seen through the compression test results, the material modulus is not affected by this load lag as the inclination before and after the plateau has the same value for each of the experiments. At the second plateau, crack propagation has initiated.

The moduli and strength behaviour can also be seen in Table 4.2, where the average flexural and compression moduli and strengths for each of the CFRP panels are presented.

Table 4.2 Flexural and Compression Average Moduli and Strengths for the CFRP Panels Manufactured under 0, 30, 50, and 70 psi (0, 205, 345, and 485 kPa)

	0 psi (0 kPa)	30 psi (205 kPa)	50 psi (345 kPa)	70 psi (485 kPa)
Flexural modulus (GPa)	41.8±6.08	47±4.7	51.67±1.53	58.67±1.16
Flexural Strength (MPa)	448.8±40.4	522.46±42.35	547.9±6.35	613.4±21.8
Compression modulus (GPa)	8.88±0.311	9.96±0.38	9.29±1.1	9.02±2.22
Compression Strength (MPa)	42.1±2	40.47±0.25	39.97±1.07	43.13±2.17

4.2.4 SEM for Surface Micro-Characterization

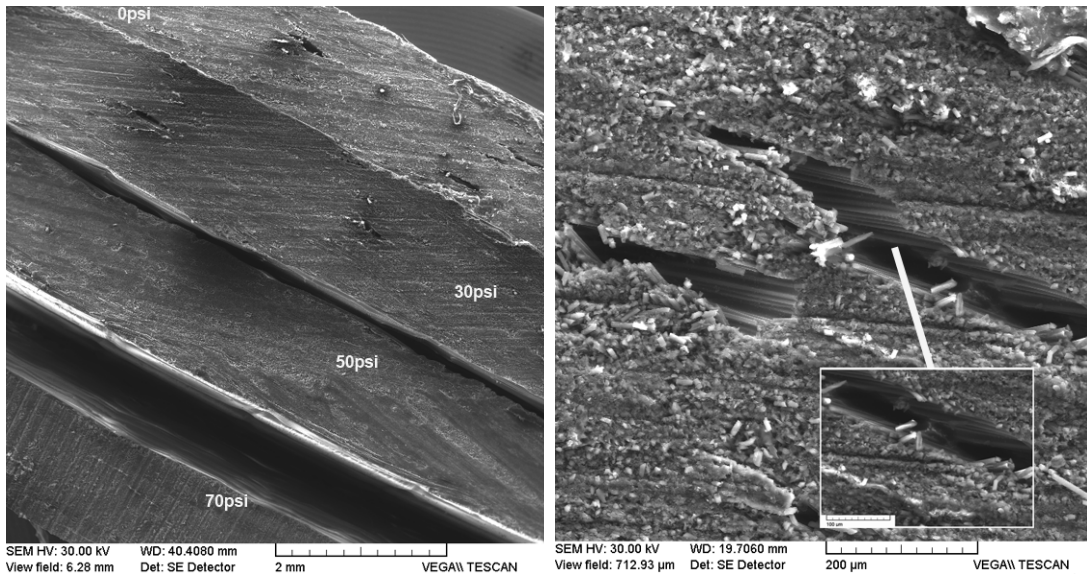


Figure 4.15 (SEM) Left: All Different Samples Manufactured in Different Pressures, Right: Samples Manufactured at 0 psi/kPa, Showing Increased Void Formation

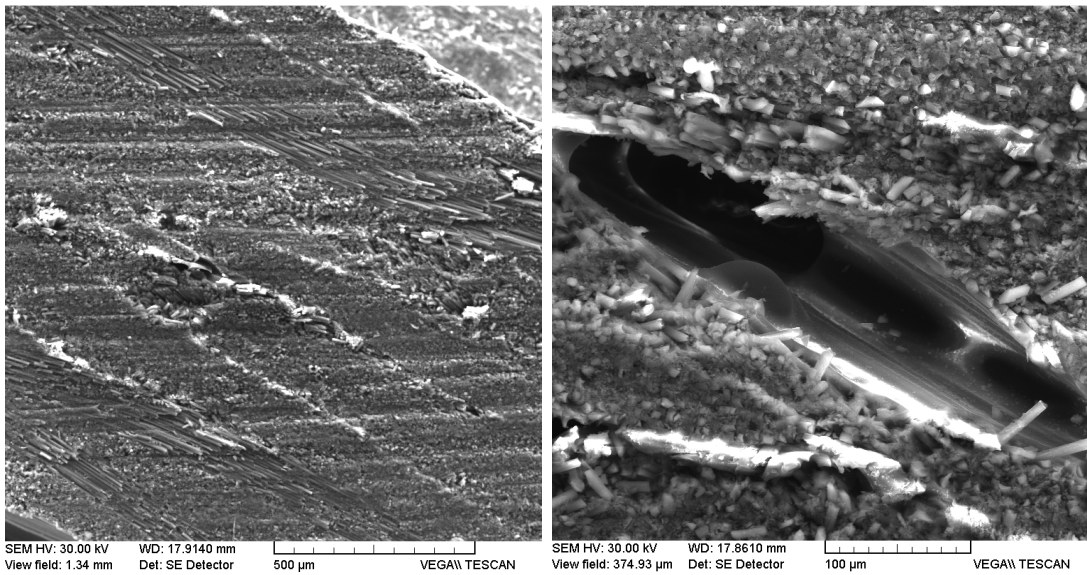


Figure 4.16 (SEM) Left: The Entire Thickness Cross Section of a Sample Manufactured at 30 psi (205 kPa), Right: Void Formation at 30 psi (205 kPa) Sample

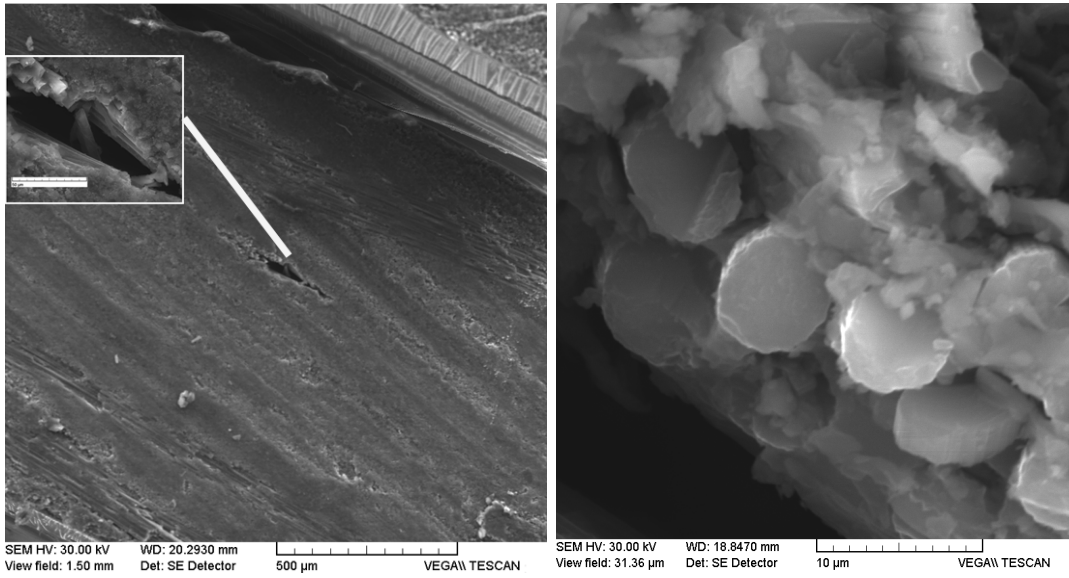


Figure 4.17 (SEM) Left: The Entire Thickness Cross Section of a Sample Manufactured at 50 psi (345 kPa), Right: Smaller Voids also Formed at 50 psi (345 kPa) Sample

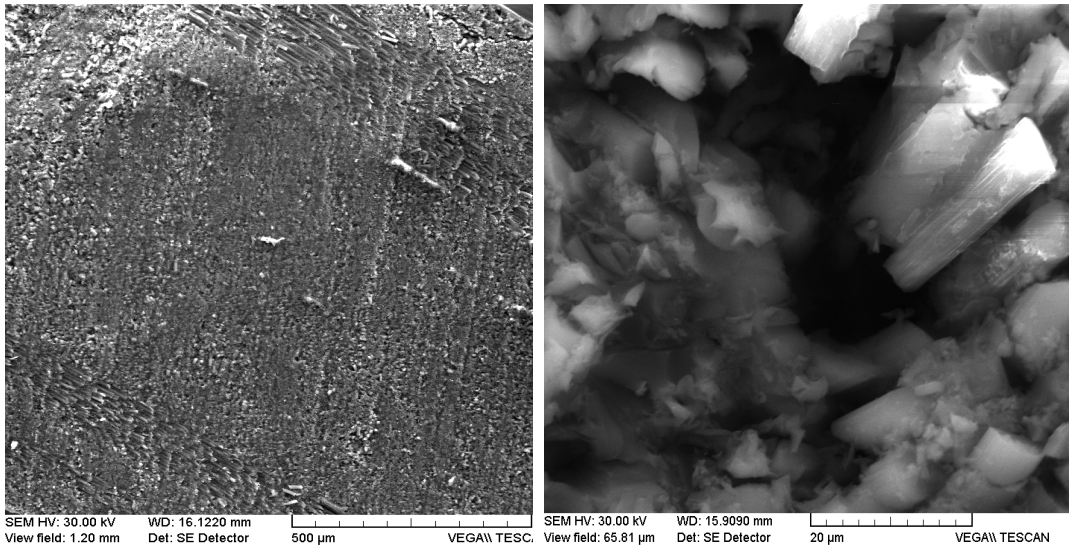


Figure 4.18 (SEM) Left: The Entire Thickness Cross Section of a Sample Manufactured at 70 psi (485 kPa), Right: Even Smaller and Less Voids Formed at 70 psi (485 kPa) Sample

Scanning electron microscope Figures from Figure 4.15 to Figure 4.18 clearly present void formation reduction in number and size as the manufacturing pressure increases. Table 4.3

illustrates mechanical testing results of specimens manufactured through conventional autoclave compared with those manufactured through the Press Clave. It can be seen that the high pressure - 70 psi (485 kPa) - specimens present mechanical properties very similar to the autoclaved ones.

Table 4.3 Comparison of Specimens Manufactured in Press Clave and Autoclave

	0 psi (0 kPa)	30 psi (205 kPa)	50 psi (345 kPa)	70 psi (485 kPa)	85 psi (586 kPa) Autoclave Processing
Flexural modulus (GPa)	41.8±6.08	47±4.7	51.67±1.53	58.67±1.16	60±2.3
Flexural Strength (MPa)	448.8±40.4	522.46±42.35	547.9±6.35	613.4±21.8	618±15.4
Compression modulus (GPa)	8.88±0.311	9.96±0.38	9.29±1.1	9.02±2.22	10.4±1.2
Compression Strength (MPa)	42.1±2	40.47±0.25	39.97±1.07	43.13±2.17	44.5±1.05

The analysis made throughout this section of innovative manufacturing with DSC, DMA, flexural and compression, and SEM characterizations gives the picture of the quality of composites manufactured through the press clave. DSC testing assures that composites are properly cured; DMA examines the viscoelastic behaviour of composites; flexural testing exhibits the stiffness improvement analogously with the higher manufacturing pressure; and SEM gives information on the surface quality of the samples manufactured under different pressures. Furthermore, compression tests show that both modulus and strength under compression do not vary, as a result they are not affected by the different manufacturing pressure. Consequently, the well cured specimens under the press clave, the acceptable surface that they present in SEM characterization and most importantly the slight differences in

flexural strength and modulus under high pressure manufacturing demonstrate that the press
 clave can be utilized as a descent alternative manufacturing process of the extremely expensive
 autoclave. Of course this high quality manufacturing through the press clave is achieved by the
 use of heat blankets, which are necessary for achieving the appropriate curing temperature
 profile while manufacturing and the thermal uniformity within the part while curing. The latter is
 very accurate in conventional autoclaves as it is very important for high quality CFRP parts.
 Thus, the heat blanket is a mandatory tool in press clave manufacturing for accurate thermal
 uniformity within the part that is manufactured. Nevertheless, besides the obvious financial and
 not only benefits of heat blankets utilization, their limitation compared to the heating system of
 an autoclave is the three dimensional and the complex geometry manufacturing of composite
 parts.

4.2.5 Parametrical Prediction of Strength

In this section an effort is made to predict the material flexural strength through given
 properties of the material, such as the moduli and the glass transition temperature, and through
 the manufacturing pressure. As a result, a linear regression model will be constructed using
 variables presented in Table 4.4.

Table 4.4 Variables – Preliminary Fitted Model of Manufacturing Pressure Variation

Random Variable (y)	Flexural Strength (MPa)
Predictor Variable (x1)	Flexural Modulus (GPa)
Predictor Variable (x2)	Manufacturing Pressure (PSI)
Predictor Variable (x3)	Compression Modulus (GPa)
Predictor Variable (x4)	Glass Transition Temperature (^o C), through tanδ

Next, the Pearson pairwise correlations followed by a scatter plot matrix of the variables from
 Table 4.4 are presented (Table 4.5 and Figure 4.19).

Table 4.5 Pearson Correlation Matrix- Manufacturing Pressure Variation

	Flexural Strength (MPa)	Flexural Modulus (GPa)	Manufacturing Pressure (PSI)	Compression Modulus (GPa)	Glass Transition Temperature ($^{\circ}$ C)
Flexural Strength (MPa)	1	0.960733	0.904119	0.157228	-0.83992
Flexural Modulus (GPa)	0.960733	1	0.854142	0.033783	-0.84134
Manufacturing Pressure (PSI)	0.904119	0.854142	1	0.102093	-0.88564
Compression Modulus (GPa)	0.157228	0.033783	0.102093	1	-0.05803
Glass Transition Temperature ($^{\circ}$ C)	-0.83992	-0.84134	-0.88564	-0.05803	1

In Table 4.5 and Figure 4.19, it can be seen that there is good correlation between the Flexural Strength with all predictor variables apart from compression modulus, which seems not to contribute in estimating the flexural strength. Compression modulus was expected to increase while the flexural strength increases as the material internal mechanisms get stronger and, thus, was expected to resist in compression loads. Nevertheless, it seems that the anisotropy of the composite dominates and the compressive loads resistance drops. As a result the compression modulus does not present the expected correlation with the response variable – flexural strength. The nonzero correlations between the predictor variables indicate the presence of multicollinearity. However, concern is raised for high correlations (above 0.7) of glass transition with flexural modulus and with manufacturing pressure, and manufacturing pressure with flexural modulus. High multicollinearity can result in high variance (low precision) in the estimated coefficients. However, this matter will be examined later through the variance inflation diagnostics.

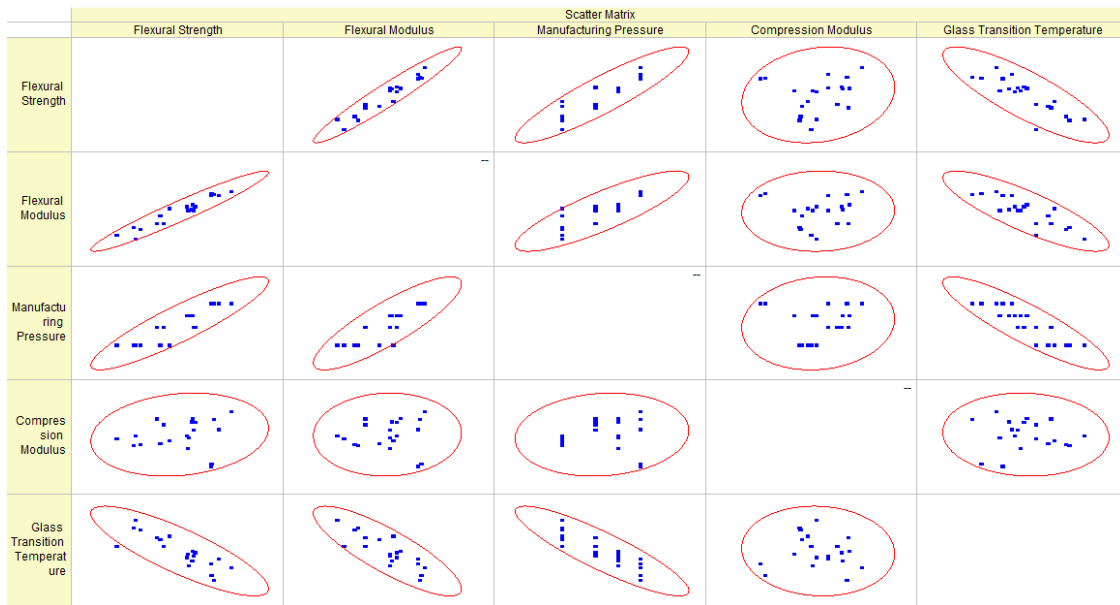


Figure 4.19 Scatter Plot- Manufacturing Pressure Variation

Table 4.6 Model Data - Manufacturing Pressure Variation

Flexural Strength (MPa)	X1-Flexural Modulus (GPa)	X2-Manufacturing Pressure (PSI)	X3-Compression Modulus (GPa)	X4-Glass Transition Temperature ($^{\circ}$ C)
444.5	40	0	8.54	229
433.3	35	0	9.15	235
393.9	37	0	8.95	219
485.6	47	0	8.6	223
429.8	41	0	8.51	230
505.05	51	0	8.82	225
479.2	43	30	10.35	224
493.05	43	30	9.94	219
557.5	50	30	9.58	213
560	52	30	10.1	215
555	53	50	10.4	216
545	50	50	8.3	214
543	52	50	9.15	212
547	50	50	9.01	207
554	50.5	50	10.15	210

Table 4.6 Continued

Flexural Strength (MPa)	X1-Flexural Modulus (GPa)	X2-Manufacturing Pressure (PSI)	X3-Compression Modulus (GPa)	X4-Glass Transition Temperature (^o C)
610	58	70	9.6	211
593.5	58	70	7.03	208
636.76	60	70	10.87	206
600	58.5	70	10.3	198
595	59	70	7.2	201

Table 4.6 presents the data used for the preliminary fitted model. Utilizing origin lab software, version 8 (138), the linear regression analysis is done. Following, Table 4.7 gives the parameters and

Table 4.8 the ANOVA Table of the preliminary fitted model.

Table 4.9 gives additional information for the regression of the preliminary fitted model.

Table 4.7 Parameters of the Preliminary Fitted Model - Manufacturing Pressure Variation

	Value	Standard Error	t-Value	Prob> t	Variance Inflation
Intercept	-38.3725	201.2253	-0.19069	0.85132	0
Flexural Modulus	6.69733	0.93852	7.13603	3.41E-06	4.24881
Manufacturing Pressure	0.82613	0.29719	2.77982	0.01402	5.821738
Compression Modulus	6.68964	3.34569	1.99948	0.06401	1.022777
Glass Transition Modulus	0.66796	0.80478	0.82999	0.41956	5.298013

Table 4.8 ANOVA Table – Manufacturing Pressure Variation

	DF	Sum of Squares	Mean Square	F Value	Prob>F
Model	4	82843.28	20710.82	92.99368	2.13E-10
Error	15	3340.682	222.7121		
Total	19	86183.97			

Table 4.9 Other Parameters of the Preliminary Model Regression - Manufacturing Pressure Variation

Number of Points	20
Degrees of Freedom	15
Residual Sum of Squares	3340.682
R Value	0.98043
R Square	0.96124
Adj. R Square	0.9509
Root MSE	14.92354

Through the analysis, it can be seen that the regression is significant since the p-value for the F-test on the regression is much smaller than a significance level of $\alpha = 0.1$. Furthermore, the high R^2 value shows that 96% of the variability in flexural strength is explained by this current model. With regard to multicollinearity, two variance inflation factors are above 5.0, and one is near 5.0. This indicates an inflation of the variance for these estimated coefficients is about a factor of 5, which is considered to be too high. Alternative models will have to be explored.

Additional to the above tables, Figure 4.20 contains several figures with information about the residuals of the model. Residuals are plotted versus each predictor variable and versus the fitted values obtained from the current model. A normal probability plot of the residuals is presented to assess the probability distribution of the residuals. Finally, in the bottom plot the residuals over the time order are plotted.

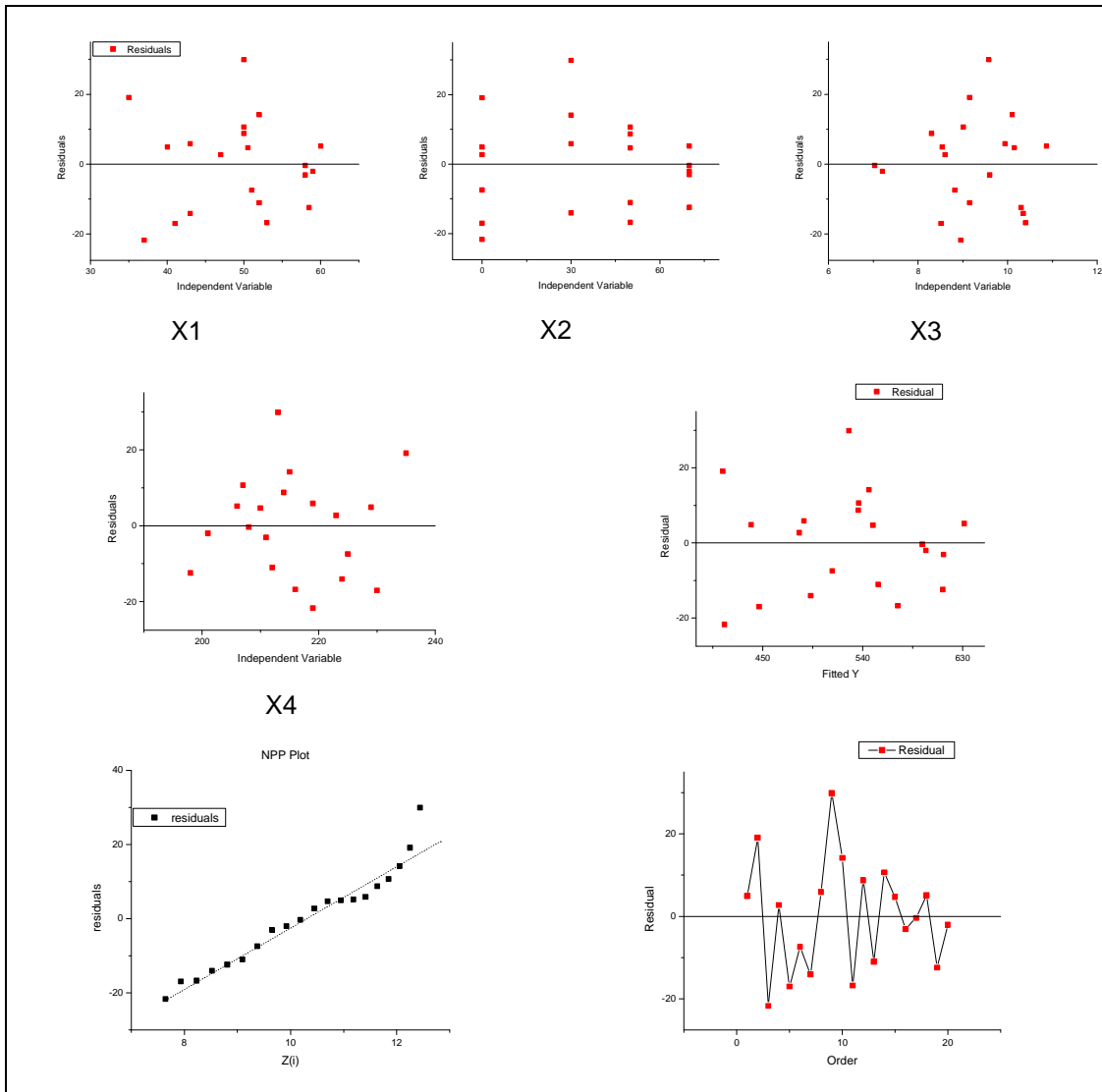


Figure 4.20 Residuals Analysis - Manufacturing Pressure Variation

Before going into the interpretation of the residual analysis, the model assumptions have to be clearly stated.

Assumptions:

Model Assumptions:

1. *MLR model form is reasonable.*
2. *Residuals have constant variance.*

The second assumption is that the errors have constant variance. This can be seen from the residuals versus the fitted values. In this case, there is no funnel shape, so constant error variance is reasonable. However, there is a constant variance test (Levene's test Figure 4.21) that will be performed to validate the constant error variance conclusion.

Hypothesis:

$$H_0: \text{Error Variance is Constant } (H_0 : \sigma_{d1} = \sigma_{d2})$$

$$H_1: \text{Error Variance is Not Constant } (H_1 : \sigma_{d1} \neq \sigma_{d2})$$

$$t^* = 0.212237 < t(0.95;15) = 1.753$$

The t-test conducted with the t-value derived from Levene's test (Figure 4.21) fails to reject H_0 , thus, constant error variance is verified to be a reasonable assumption.

The normal probability plot within Figure 4.20 exhibits a mostly straight line with a curve at the right. This indicates that the distribution of the residuals is similar to a normal distribution, except that it has a longer right tail. However, normality is not a required assumption. A normality test will be performed to assess if normality is violated.

Hypothesis:

$$H_0: \text{Normality Reasonable}$$

$$H_1: \text{Normality Violated}$$

$$\rho = 0.9713 > C(0.1, 20) = 0.96$$

The test fails to reject H_0 , thus, it does not detect the slight non-normality seen in the plot.

Finally, the time plot in Figure 4.20 appears to show a random jagged pattern. This indicates that correlation over time is not a problem.

Diagnostics

The variance inflation factors are higher than desired for manufacturing pressure and glass transition temperature. More specifically, VIF_2 and VIF_4 are too high as they inflate the error variance more than 5 times. Also, VIF_1 is close to 5 as well. When VIF values are below 5 or even better below 2, they are more preferable as the variance is not inflated. As a result, the issue of variance inflation will continue to be monitored, due to multicollinearity. Following, Figure 4.22 and Figure 4.23 show the results from the outlier analysis as well as their influences. In Figure 4.22, the Bonferroni outlier test and the x-outlier diagnostic do not detect any outliers.

yhat	e	tres	cookdi	hii	ti	dffitsi	x-outlier - hii 2*p/n	Bonferonni - ti t(1-.1/2(20);n-p-1)	DFFITs	COOKDi
							0.5	3.483	1	1
439.61	4.8862	0.34812	0.005171	0.1673	0.348121468	0.15601	ok	ok	ok	ok
414.22	19.084	1.6886	0.28025	0.3557	1.688587951	1.2547	ok	ok	y-outlier	ok
415.58	-21.685	-2.2428	0.69611	0.4675	-2.24279458	-2.1014	ok	ok	y-outlier	ok
482.89	2.7113	0.20587	0.003365	0.271	0.205874988	0.12551	ok	ok	ok	ok
446.78	-16.978	-1.2856	0.070873	0.1828	-1.285595458	-0.6081	ok	ok	ok	ok
512.49	-7.4357	-0.6848	0.093178	0.4894	-0.684793848	-0.6704	ok	ok	ok	ok
493.26	-14.058	-1.0877	0.074149	0.2408	-1.087701451	-0.6126	ok	ok	ok	ok
487.18	5.8744	0.41717	0.006947	0.1587	0.417165338	0.18116	ok	ok	ok	ok
527.64	29.859	2.4665	0.12269	0.119	2.466468591	0.90629	ok	ok	ok	ok
545.85	14.15	1.0382	0.041309	0.1615	1.038148935	0.45565	ok	ok	ok	ok
571.74	-16.745	-1.2715	0.072499	0.1893	-1.271513235	-0.6143	ok	ok	ok	ok
536.27	8.7314	0.62195	0.014373	0.1512	0.621949491	0.26254	ok	ok	ok	ok
554.01	-11.014	-0.75262	0.008278	0.0663	-0.752645297	-0.2005	ok	ok	ok	ok
536.34	10.657	0.77729	0.026905	0.1782	0.777249102	0.3619	ok	ok	ok	ok
549.32	4.6787	0.32567	0.003326	0.1285	0.325670287	0.12506	ok	ok	ok	ok
613.06	-3.0625	-0.22831	0.003575	0.2431	-0.228304681	-0.1294	ok	ok	ok	ok
593.87	-0.36627	-0.0315	0.000163	0.4335	-0.031504014	-0.0276	ok	ok	ok	ok
631.61	5.1468	0.39765	0.013686	0.29	0.39764475	0.25414	ok	ok	ok	ok
612.41	-12.41	-1.0057	0.093269	0.3157	-1.005662967	-0.6832	ok	ok	ok	ok
597.03	-2.0251	-0.16812	0.003876	0.3907	-0.168116575	-0.1346	ok	ok	ok	ok

Figure 4.22 Outliers and Influence- Manufacturing Pressure Variation

Intercept	Downloads	Page loads	Funding	First_time_Visitors		x0	x1	x2	x3	x4
-0.016513	-0.01551	-0.004565	-0.051	0.034231		ok	ok	ok	ok	ok
-0.44565	-0.48669	0.63105	-0.073	0.62952		ok	ok	ok	ok	ok
-1.7358	1.256	0.80294	0.1153	1.593	FLAG	FLAG	ok	ok	FLAG	FLAG
0.0095909	0.069548	-0.096333	-0.017	-0.019676		ok	ok	ok	ok	ok
0.18102	-0.05741	0.0096	0.1942	-0.23568		ok	ok	ok	ok	ok
0.19353	-0.55732	0.43405	0.0041	-0.10707		ok	ok	ok	ok	ok
0.24864	0.21767	-0.35914	-0.272	-0.28118		ok	ok	ok	ok	ok
0.033832	-0.12536	0.063729	0.0617	-0.018672		ok	ok	ok	ok	ok
0.44697	0.11966	-0.61683	0.2725	-0.54911		ok	ok	ok	ok	ok
-0.017409	0.24777	-0.27419	0.2573	-0.069968		ok	ok	ok	ok	ok
0.40346	-0.18425	-0.21418	-0.344	-0.35003		ok	ok	ok	ok	ok
-0.013523	-0.0913	0.15814	-0.161	0.061889		ok	ok	ok	ok	ok
0.0050225	0.024016	-0.069464	0.0264	-0.015992		ok	ok	ok	ok	ok
0.27805	-0.21675	-0.009586	-0.057	-0.25002		ok	ok	ok	ok	ok
0.040786	-0.05014	0.012726	0.065	-0.044721		ok	ok	ok	ok	ok
0.089254	-0.04224	-0.072367	-0.012	-0.086636		ok	ok	ok	ok	ok
0.004437	-0.00236	-0.010779	0.0219	-0.0079228		ok	ok	ok	ok	ok
-0.0861	0.10248	0.010388	0.1662	0.044261		ok	ok	ok	ok	ok
-0.36674	0.045705	0.21297	-0.282	0.44463		ok	ok	ok	ok	ok
-0.047796	0.001837	-0.000157	0.1004	0.036134		ok	ok	ok	ok	ok

Figure 4.23 Influence on Parameters (DFBETAS) - Manufacturing Pressure Variation

4.2.5.1 Interactions Analysis and Best Model Exploration

Interactions between the predictor variables are investigated to allow for modeling more complex relationships. Following, interactions x_1x_2 , x_1x_4 , and x_2x_4 are presented in Figure 4.24 as they are the ones that they present some trend which can possibly benefit the model. For each interaction the residuals are plotted against the interaction, the standardized interaction and the interaction regression on all predictor variables.

In Figure 4.24, residuals are also plotted against the standardized forms of the interactions. These standardized variables are calculated by first centering the mean of predictor variables to zero and by scaling the variance to one. Now the values approximately lie in $(-1, 1)$. Centering the predictor variables is of significant importance for multiplying them afterwards as interactions. Scaling the variance is important as well, for numerical stability. As a result, the standardized forms assist in overcoming high multicollinearity that the non standardized interactions present.

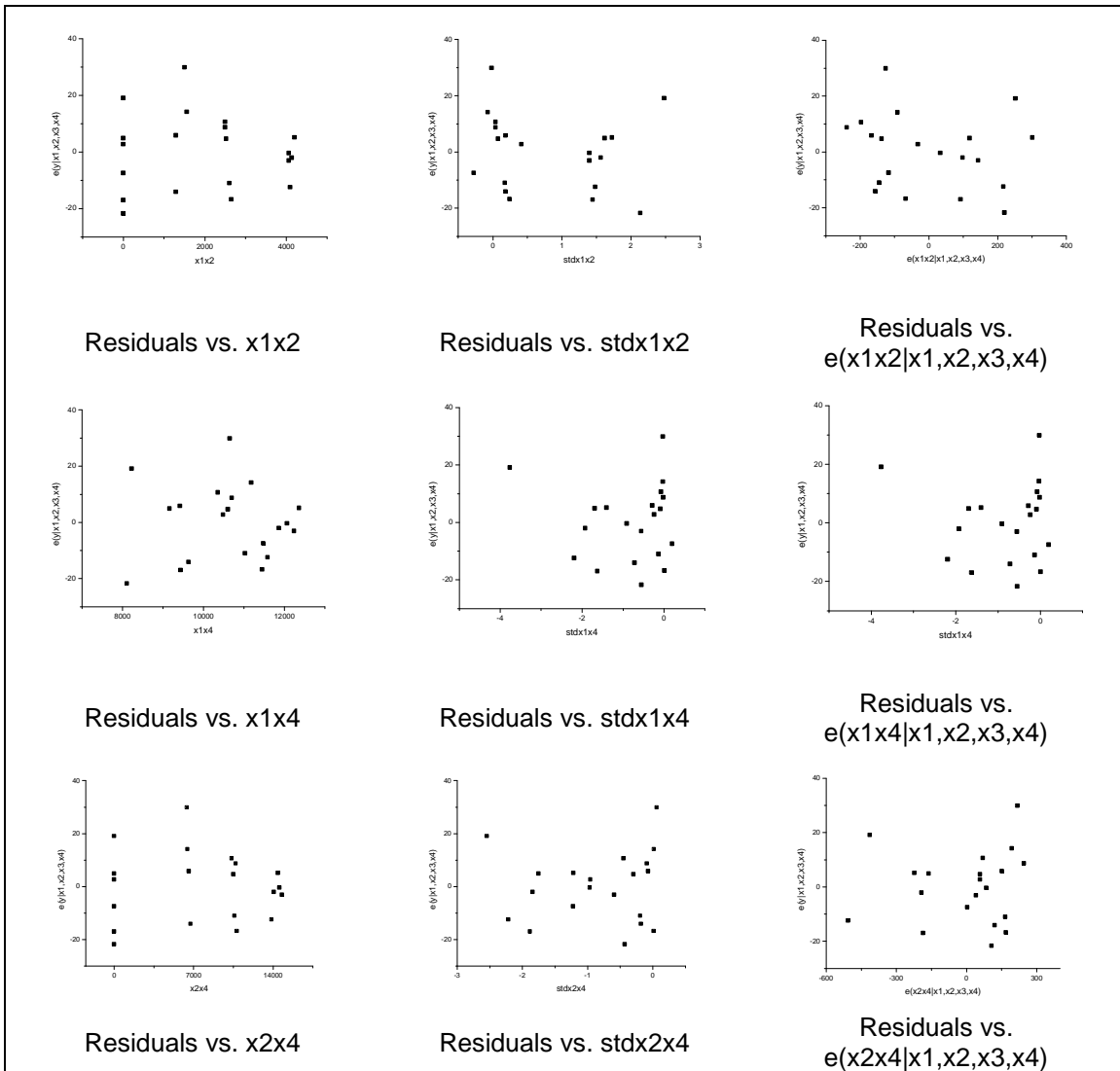


Figure 4.24 Interactions - Manufacturing Pressure Variation

Complementing the interactions graphs is the correlation matrix in Figure 4.25, which includes all variables and interactions. It seems that the interactions are highly correlated (above 0.7) with all predictor variables and other interactions apart from variable $x3$. This is a common phenomenon because interaction terms are composed from the original predictors. To overcome this high multicollinearity, the standardized form is employed. Figure 4.26 shows the

correlation with the standardized interactions, where it can be seen that standardized interactions overall have lower correlation with the other predictor variables.

	y	x1	x2	x3	x4	x1x2	x1x4	x2x4
Flexural Strength (MPa)	1	0.960733	0.904119	0.157228	-0.83992	0.91157	0.924236	0.901083
X1-Flexural Modulus (GPa)	0.960733	1	0.854142	0.033783	-0.84134	0.877619	0.976529	0.846189
X2-Manufacturing Pressure (PSI)	0.904119	0.854142	1	0.102093	-0.88564	0.992477	0.763564	0.99889
X3-Compression Modulus (GPa)	0.157228	0.033783	0.102093	1	-0.05803	0.067524	0.029514	0.1153
X4-Glass Transition Temperature (OC)	-0.83992	-0.84134	-0.88564	-0.05803	1	-0.88714	-0.70944	-0.87223
x1x2	0.91157	0.877619	0.992477	0.067524	-0.88714	1	0.789219	0.987428
x1x4	0.924236	0.976529	0.763564	0.029514	-0.70944	0.789219	1	0.760066
x2x4	0.901083	0.846189	0.99889	0.1153	-0.87223	0.987428	0.760066	1

Figure 4.25 Pearson Correlation with Predictor Variables and Interactions - Manufacturing Pressure Variation

	y	x1	x2	x3	x4	stdx1x2	stdx1x4	stdx2x4
Flexural Strength (MPa)	1	0.960733	0.904119	0.157228	-0.83992	-0.19114	0.177873	0.156427
X1-Flexural Modulus (GPa)	0.960733	1	0.854142	0.033783	-0.84134	-0.17256	0.217147	0.09335
X2-Manufacturing Pressure (PSI)	0.904119	0.854142	1	0.102093	-0.88564	-0.03945	0.076194	0.16233
X3-Compression Modulus (GPa)	0.157228	0.033783	0.102093	1	-0.05803	-0.2251	0.140433	0.304625
X4-Glass Transition Temperature (OC)	-0.83992	-0.84134	-0.88564	-0.05803	1	0.089379	-0.18106	-0.16509
stdx1x2	-0.19114	-0.17256	-0.03945	-0.2251	0.089379	1	-0.82306	-0.71888
stdx1x4	0.177873	0.217147	0.076194	0.140433	-0.18106	-0.82306	1	0.874245
stdx2x4	0.156427	0.09335	0.16233	0.304625	-0.16509	-0.71888	0.874245	1

Figure 4.26 Pearson Correlation with Predictor Variables and Standardized Interactions- Manufacturing Pressure Variation

At this point, a search for the best model that explains flexural strength will be performed. Figure 4.26 shows that there is high correlation between the standardized interactions. As a result, these should not be included together in the same model. Three different model searches will be performed which will include the four main predictor variables and each time one of the interactions. The first step is to do the three best subset regressions, which include all predictor variables and the standardized interaction stdx1x2, then all predictor variables and stdx1x4, and finally all predictor variables and stdx2x4 respectively (Figure 4.27). The best subset regression is performed with the Minitab software(140). Backward elimination

and stepwise methods are also performed to compare with the best subset results and are also presented in Figure 4.28.

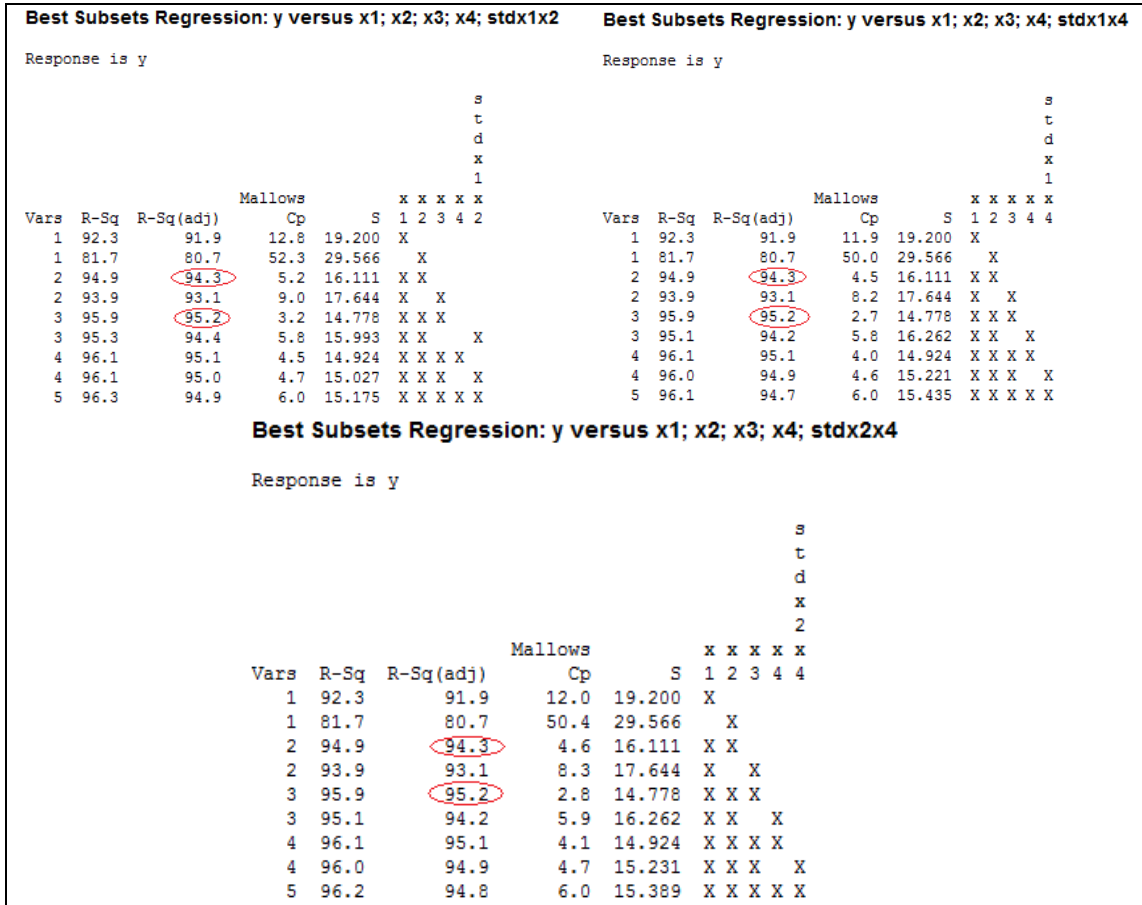


Figure 4.27 Best Subsets Regression for Evaluating the Different Predictor Variables Cases for Best Manufacturing Pressure Variation

Forward Selection												
Stepwise Regression: y versus x1; x2; x3; x4				Stepwise Regression: y versus x1; x2; x3; x4; stdx1x2				Stepwise Regression: y versus x1; x2; x3; x4; stdx1x2; stdx1x4				
Forward selection. Alpha-to-Enter: 0.1				Forward selection. Alpha-to-Enter: 0.1				Forward selection. Alpha-to-Enter: 0.1				
Response is y on 5 predictors, with N = 20				Response is y on 5 predictors, with N = 20				Response is y on 5 predictors, with N = 20				
Step	1	2	3	Step	1	2	3	Step	1	2	3	
Constant	103.0	192.7	123.4	Constant	103.0	192.7	123.4	Constant	103.0	192.7	123.4	
x1	8.61	6.24	6.43	x1	8.61	6.24	6.43	x1	8.61	6.24	6.43	
T-Value	14.69	6.60	7.37	T-Value	14.69	6.60	7.37	T-Value	14.69	6.60	7.37	
P-Value	0.000	0.000	0.000	P-Value	0.000	0.000	0.000	P-Value	0.000	0.000	0.000	
x2		0.75	0.68	x2		0.75	0.68	x2		0.75	0.68	
T-Value		2.93	2.87	T-Value		2.93	2.87	T-Value		2.93	2.87	
P-Value		0.009	0.011	P-Value		0.009	0.011	P-Value		0.009	0.011	
x3			6.8	x3			6.8	x3			6.8	
T-Value			2.05	T-Value			2.05	T-Value			2.05	
P-Value			0.057	P-Value			0.057	P-Value			0.057	
S	19.2	16.1	14.8	S	19.2	16.1	14.8	S	19.2	16.1	14.8	
R-Sq	92.30	94.88	95.95	R-Sq	92.30	94.88	95.95	R-Sq	92.30	94.88	95.95	
R-Sq(adj)	91.87	94.28	95.19	R-Sq(adj)	91.87	94.28	95.19	R-Sq(adj)	91.87	94.28	95.19	
Mallows Cp	12.8	5.2	3.2	Mallows Cp	11.9	4.5	2.7	Mallows Cp	12.0	4.6	2.8	
Backward Elimination												
Stepwise Regression: y versus x1; x2; x3; x4				Stepwise Regression: y versus x1; x2; x3; x4; stdx1x2				Stepwise Regression: y versus x1; x2; x3; x4; stdx1x2; stdx1x4				
Backward elimination. Alpha-to-Remove: 0.1				Backward elimination. Alpha-to-Remove: 0.1				Backward elimination. Alpha-to-Remove: 0.1				
Response is y on 5 predictors, with N = 20				Response is y on 5 predictors, with N = 20				Response is y on 5 predictors, with N = 20				
Step	1	2	3	Step	1	2	3	Step	1	2	3	
Constant	-26.75	-38.37	123.43	Constant	-36.43	-38.37	123.43	Constant	-40.97	-38.37	123.43	
x1	6.51	6.70	6.43	x1	6.73	6.70	6.43	x1	6.73	6.70	6.43	
T-Value	6.56	7.14	7.37	T-Value	6.73	7.14	7.37	T-Value	6.92	7.14	7.37	
P-Value	0.000	0.000	0.000	P-Value	0.000	0.000	0.000	P-Value	0.000	0.000	0.000	
x2	0.88	0.83	0.68	x2	0.81	0.83	0.68	x2	0.82	0.83	0.68	
T-Value	2.82	2.78	2.87	T-Value	2.53	2.78	2.87	T-Value	2.68	2.78	2.87	
P-Value	0.014	0.014	0.011	P-Value	0.024	0.014	0.011	P-Value	0.018	0.014	0.011	
x3	6.0	6.7	6.8	x3	6.8	6.7	6.8	x3	6.3	6.7	6.8	
T-Value	1.71	2.00	2.05	T-Value	1.93	2.00	2.05	T-Value	1.76	2.00	2.05	
P-Value	0.109	0.064	0.057	P-Value	0.074	0.064	0.057	P-Value	0.100	0.064	0.057	
x4	0.69	0.67		x4	0.65	0.67		x4	0.69	0.67		
T-Value	0.84	0.83		T-Value	0.77	0.83		T-Value	0.83	0.83		
P-Value	0.414	0.420		P-Value	0.456	0.420		P-Value	0.419	0.420		
stdx1x2	-3.1			stdx1x4	-0.6			stdx2x4	1.5			
T-Value	-0.71			T-Value	-0.15			T-Value	0.33			
P-Value	0.488			P-Value	0.882			P-Value	0.749			
S	15.2	14.9	14.8	S	15.4	14.9	14.8	S	15.4	14.9	14.8	
R-Sq	96.26	96.12	95.95	R-Sq	96.13	96.12	95.95	R-Sq	96.15	96.12	95.95	
R-Sq(adj)	94.92	95.09	95.19	R-Sq(adj)	94.75	95.09	95.19	R-Sq(adj)	94.78	95.09	95.19	
Mallows Cp	6.0	4.5	3.2	Mallows Cp	6.0	4.0	2.7	Mallows Cp	6.0	4.1	2.8	

Figure 4.28 Backward Elimination and Forward Stepwise Methods for Evaluating the Different Predictor Variables Cases for Best Manufacturing Pressure Variation

Taking into account the results from Figure 4.27, and Figure 4.28, the best subset regression analysis demonstrates that the best model with the highest adjusted R^2 and the lowest Mallows Cp coefficient is the one which includes flexural modulus, manufacturing pressure, and compression modulus predictor variables. Additionally, backward elimination and forward selection regression methods verify this finding as their best model for predicting

flexural strength is again the one containing the flexural modulus (x1), manufacturing pressure (x2), and compression modulus (x3) predictor variables. However, due to the fact that compression modulus is not contributing enough to the flexural strength prediction, as seen in correlation matrix in Table 4.5, the model with only two predictor variables flexural modulus (x1), and manufacturing pressure (x2) is also considered as it has pretty low Mallows Cp coefficient and high adjusted R^2 as well.

Furthermore, the analysis in Figure 4.28 shows that all the p-values for both models (with two predictor variables and with three predictor variables) are significant for $\alpha = 0.1$. The variance inflations are also measured for the two models and they are:

- For the two predictor variable model: $VIF_1=3.69$, $VIF_2=3.69$
- For the three predictor variable model: $VIF_1=3.74$, $VIF_2=3.77$, $VIF_3=1.02$

Variance inflations are relatively low, so they do not indicate high multicollinearity. As a result, the best two models selected (from the best subset analysis) are:

Model 1: Variables=x1, x2, / $R(\text{adj})^2 = 94.3$ / $C_p = 4.6$

Model 2: Variables=x1, x2, x3, / $R(\text{adj})^2 = 95.2$ / $C_p = 2.8$

The next step will be to evaluate and compare the two selected models and choose the best one to keep for predicting the flexural strength of the featherweights.

Model 1:

Parameters, ANOVA Table and other information on Model 1 are presented from Table 4.10 to Table 4.12.

Table 4.10 Model 1 Parameters – Manufacturing Pressure Variation

	Value	Standard Error	t-Value	Prob> t	VIF
Intercept	192.742	39.2906	4.90554	0.000	
X1-Flexural Modulus	6.242	0.9452	6.60431	0.000	3.69
X2-Manufacturing Pressure	0.748	0.2557	2.92631	0.009	3.69

Thus, model 1 can be written as:

$$\hat{y} = 192.742 + 6.24249 \cdot x_1 + 0.748256 \cdot x_2$$

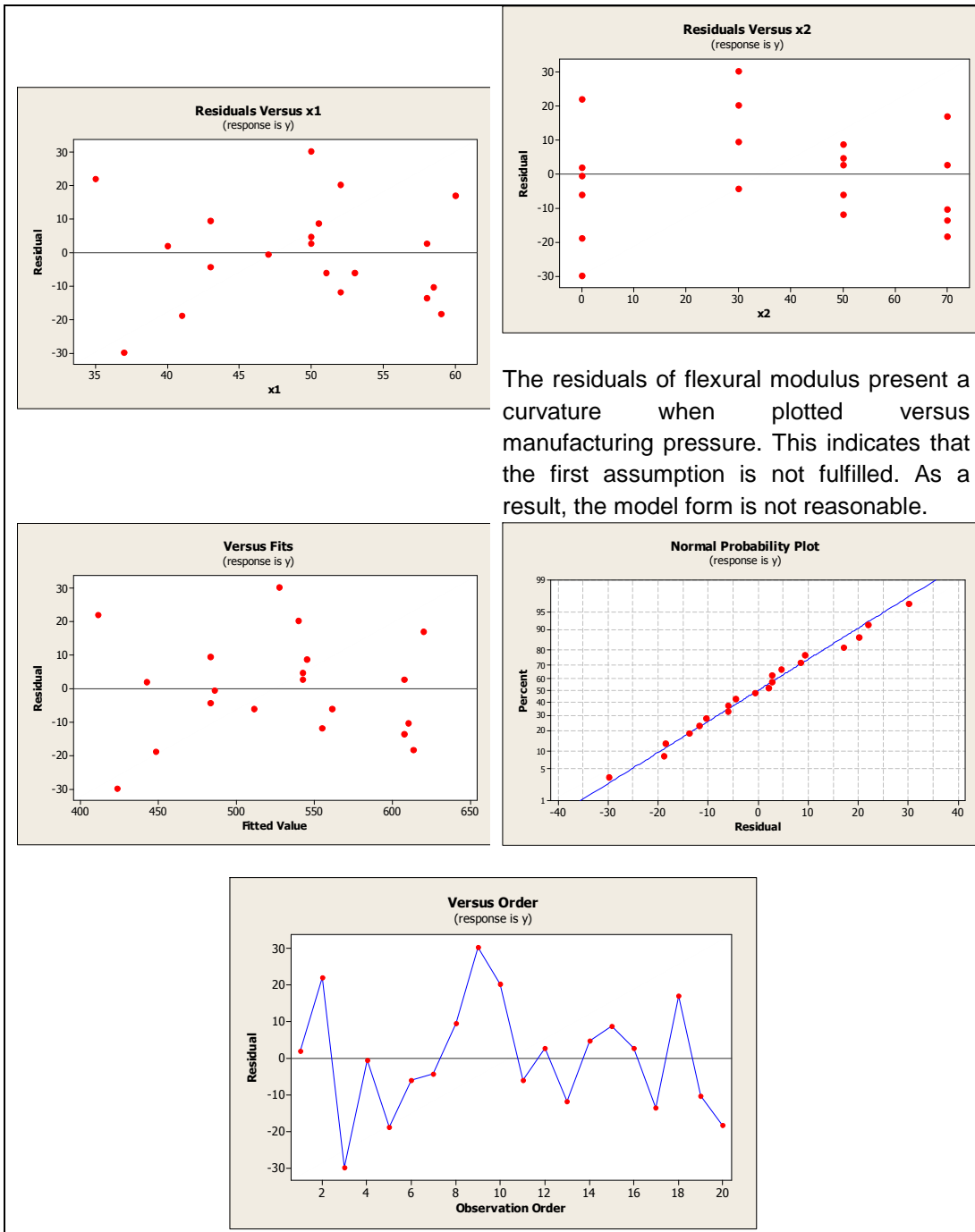
Table 4.11 Model 1 ANOVA Table – Manufacturing Pressure Variation

	DF	Sum of Squares	Mean Square	F Value	Prob>F
Model	2	81771.2	40885.6	157.11	0.000000
Error	17	4412.8	259.6		
Total	19	86184			

Table 4.12 Other Information of Model 1 – Manufacturing Pressure Variation

Number of Points	20
Degrees of Freedom	17
Residual Sum of Squares	4412.8
R Square	0.9488
Adj. R Square	0.9428
Root MSE	16.11211

Figure 4.29 presents the analysis of the residuals over the predictor variables, the fitted values, the time order, and the NPP plot for model 1.



The residuals of flexural modulus present a curvature when plotted versus manufacturing pressure. This indicates that the first assumption is not fulfilled. As a result, the model form is not reasonable.

Figure 4.29 Model 1 Residuals Graphs – Manufacturing Pressure Variation

Model 2:

Parameters, ANOVA Table and other information on Model 2 are presented from Table 4.13 to Table 4.15.

Table 4.13 Model 2 Parameters – Manufacturing Pressure Variation

	Value	Standard Error	t-Value	Prob> t	VIF
Intercept	123.428	49.4053	2.4983	0,024	
X1-Flexural Modulus	6.427	0.8716	7.3736	0.000	3.74
X2-Manufacturing Pressure	0.68	0.2369	2.8695	0.011	3.77
X3-Compression Modulus	6.791	3.3108	2.051	0.057	1.0214

Thus, model 2 can be written as:

$$\hat{y} = 123.428 + 6.4271 \cdot x_1 + 0.67979 \cdot x_2 + 6.79051 \cdot x_3$$

Table 4.14 Model 2 ANOVA Table – Manufacturing Pressure Variation

	DF	Sum of Squares	Mean Square	F Value	Prob>F
Model	3	82689.9	27563.3	126.216	0.0000000
Error	16	3494.1	218.4		
Total	19	86184			

Table 4.15 Other Information of Model 2 – Manufacturing Pressure Variation

Number of Points	20
Degrees of Freedom	16
Residual Sum of Squares	3494.1
R Square	0.9595
Adj. R Square	0.9519
Root MSE	14.78

Figure 4.30 presents the analysis of the residuals over the predictor variables, the fitted values, the time order, and the NPP plot for model 2.

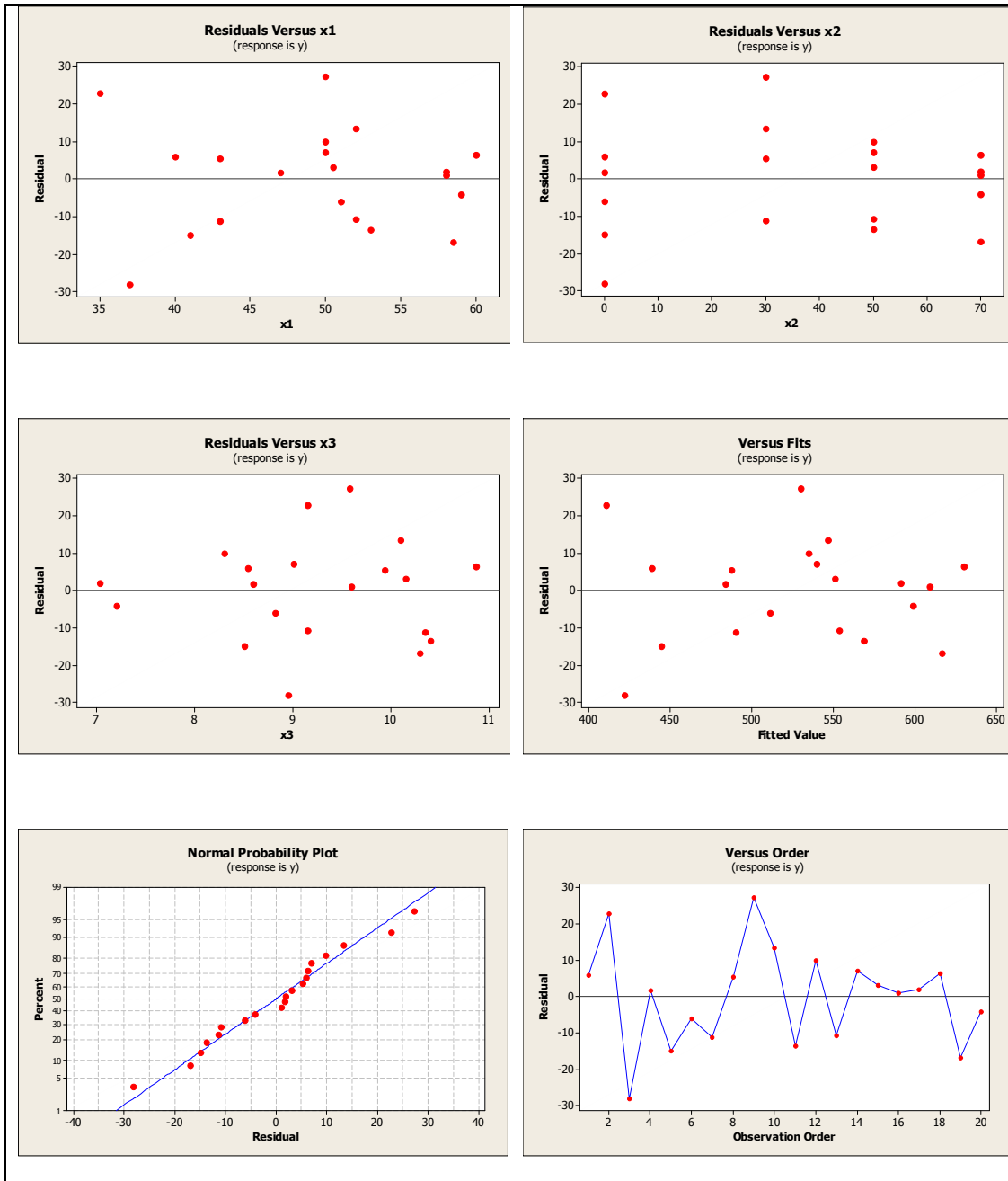


Figure 4.30 Model 2 Residuals Graphs – Manufacturing Pressure Variation

Having presented the parameters and the analysis of each of the two best models then a comparison among their assumptions is performed (Table 4.16).

Table 4.16 Model Assumption Comparison – Manufacturing Pressure Variation

	Model1	Model 2
ASSUMPT. 1	Slight Curvature in Residuals over the predictor variables → Model Form Not Reasonable	No curvature → Model Form Reasonable
ASSUMPT.2	No Funnel Shape → Const Error Variance	No Funnel Shape → Const Error Variance
ASSUMPT. 3	Normal Probability Plot → Normality Reasonable	Normal Probability Plot → Normality Reasonable
ASSUMPT. 4	No trend - No serial correlation	No trend – No serial correlation
Adjusted R ² Mallow Cp (x1-x4 & Std _{x1x2})	Adjusted R ² = 94.3% Cp = 5.2	Adjusted R ² = 95.2% Cp = 3.2
Adjusted R ² Mallow Cp (x1-x4 & Std _{x1x4})	Adjusted R ² = 94.3% Cp = 4.5	Adjusted R ² = 95.2% Cp = 2.7
Adjusted R ² Mallow Cp (x1-x4 & Std _{x1x4})	Adjusted R ² = 94.3% Cp = 4.6	Adjusted R ² = 95.2% Cp = 2.8

The first model fails to fulfill the first assumption, so the model form is not reasonable due to the curvature present in the plots of residuals versus the flexural modulus and manufacturing pressure. As a consequence, model 1 is not considered capable to predict flexural strength and it is not included in the model comparison in Table 4.17, and Table 4.18.

Variance inflations are considered low as variance is inflated almost four times for flexural modulus and manufacturing pressure predictor variables, while it is near to 1 for compression modulus

Table 4.17 presents the x and y outliers along with their influence to the fitted model for model 2. The model has neither x nor y outliers according to the leverage test and to the Bonferroni test, respectively. Concluding, there are no y and x outliers that influence model 2.

Table 4.17 Outliers and Influence - Manufacturing Pressure Variation

	Model 2
X - Outlier	0
Y - Outlier through Bonferonni test	0
Y - Outlier through DFFITS	Observations 3
Y - Outlier through COOKDi	0

Finally, the parameters influence of model 2 is presented in Table 4.18.

Table 4.18 Observation Influence on Parameters - Manufacturing Pressure Variation

Influence On	Model 2
Intercept	0
X1	Observation 3
X2	Observation 3
X3	0

Model Selection:

Model 2 is selected over model 1 for the main reason that assumption 1 is not fulfilled for model 1 form and thus the latter is not reasonable. Furthermore, model 2 has diagnostics capable for reasonably predicting the flexural strength.

The ANOVA Table as well as certain parameters of the selected model is presented in Table 4.19 and

Table 4.20 respectively.

Table 4.19 ANOVA Table of the Selected Model – Manufacturing Pressure Variation

	DF	Sum of Squares	Mean Square	F Value	Prob>F
Model	3	82689.9	27563.3	126.216	0.0000000
Error	16	3494.1	218.4		
Total	19	86184			

Table 4.20 More Information on the Selected Model – Manufacturing Pressure Variation

Number of Points	20
Degrees of Freedom	16
Residual Sum of Squares	3494.1
R Square	0.9595
Adj. R Square	0.9519
Root MSE	14.78

Thus, the selected model can be written as:

$$\hat{y} = 123.428 + 6.4271 \cdot x_1 + 0.67979 \cdot x_2 + 6.79051 \cdot x_3$$

Parameters Interpretation:

- 1) Regarding β_0 , for $x_1 = x_2 = x_3 = 0$, the value of $y_{\text{hat}} = 123.428$. Nevertheless, the point $[0, 0, 0]$ is not included in all x ranges.
- 2) The estimator for β_1 is $b_1 = 6.4271$ and it means that the estimated change of the flexural strength when the flexural modulus increases by 1 is 6.4271 MPa, assuming that the Manufacturing Pressure and the Compression Modulus remain constant.
- 3) The estimator for β_2 is $b_2 = 0.67979$ and it means that the change of the estimated flexural strength when the manufacturing pressure increases by 1 is 0.67979 MPa, assuming that the flexural modulus and the compression remain constant.
- 4) The estimator for β_3 is $b_3 = 6.79051$ and it means that the change of the estimated flexural strength when the compression modulus increases by 1 is 6.79051 MPa, assuming that the flexural modulus and the manufacturing pressure remain constant.

Inferences for the selected model parameters are presented through Bonferroni joint t-interval.

Table 4.21 Selected Model Parameters and Covariance Table – Manufacturing Pressure Variation

S(b) ²				b
2440.9	-33.921	7.7276	-111.89	123.428
-33.921	0.75975	-0.17668	0.29799	6.427
7.7276	-0.17668	0.056121	-0.11052	0.68
-111.89	0.29799	-0.11052	10.962	6.791

The Bonferroni joint t-interval for $\alpha = 0.03$ is conducted as following:

$$B = t\left(1 - \frac{\alpha}{2 \cdot g}; n - p\right) = t(1 - 0.005; 17) = t(0.995; 17) = 2.898$$

$$S\{b_1\} = \sqrt{0.75975} = 0.87164 \rightarrow \text{Interval: } \beta_1 = 6.427 \pm 2.898 \cdot 0.87164 \Rightarrow \beta_1 : (3.901, 8.953)$$

$$S\{b_2\} = \sqrt{0.056121} = 0.237 \rightarrow \text{Interval: } \beta_2 = 0.68 \pm 2.898 \cdot 0.237 \Rightarrow \beta_2 : (-0.007, 1.367)$$

$$S\{b_3\} = \sqrt{10.962} = 3.31 \rightarrow \text{Interval: } \beta_3 = 6.791 \pm 2.898 \cdot 3.31 \Rightarrow \beta_3 : (-2.8014, 16.3834)$$

We are 97% confident that β_1 is contained in (3.901, 8.953), β_2 is contained in (-0.007, 1.367), and β_3 is contained in (-2.814, 16.3834) simultaneously.

Individually for each parameter:

For β_1 , we are 99% confident that β_1 is contained in (3.901, 8.953).

For β_2 , we are 99% confident that β_2 is contained in (-0.007, 1.367).

Finally, for β_3 , we are 99% confident that β_3 is contained in (-2.814, 16.3834).

Summarizing, the best model for predicting flexural strength of composites when manufacturing pressure alters from specimen to specimen manufacturing is:

$$\hat{y} = 123.428 + 6.4271 \cdot x_1 + 0.67979 \cdot x_2 + 6.79051 \cdot x_3$$

The model uses as predictor variables flexural modulus (x_1), manufacturing pressure (x_2), and compression modulus (x_3). Flexural modulus and compression modulus are given material

properties, also, manufacturing pressure is a characteristic defined by the manufacturer. As a result, the developed statistical model assists the engineer to design a composite with a desired flexural strength by introducing to the model, the two moduli and the desired manufacturing pressure. This helps the engineer to avoid performing time-consuming experimental mechanical testing. Finally, it can be seen through the model equation that higher flexural and compression moduli contribute to a higher flexural strength as expected since material stiffness is enhanced. This is correlated by the experimental results where a 40% flexural modulus increase corresponds to an almost same (37%) flexural strength increase. Similar is the behaviour of the pressure while manufacturing. However, the rate of this change is different as the pressure has a smaller multiplier factor within the model. Thus, much bigger pressure is needed for similar (37%) flexural strength improvement. In fact the pressure increase is 500% (0 to 485 kPa).

4.3 Results for Specific Objective #3: Micro-Particle Reinforced Interlayer

4.3.1 Fracture – Toughness Testing Evaluation

Figure 4.31 presents Mode I interlaminar fracture-toughness of epoxy model system. The epoxy system structured laminates with the 0% modifier particles in the interlayer gives a G_{IC} of 300J/m^2 . After the multilayer structure creation, the epoxy system shows a slight decrease in G_{IC} values.

Figure 4.32 presents Mode II interlaminar fracture-toughness in epoxy resin system. Conventional epoxy structure laminate results demonstrate that G_{IIC} value is 500kJ/m^2 . The matrix system shows dramatic improvements in G_{IIC} with a maximum occurring towards higher concentrations. When crack propagation moves from the interlaminar region to the intralaminar region, a maximum G_{IIC} occurs.

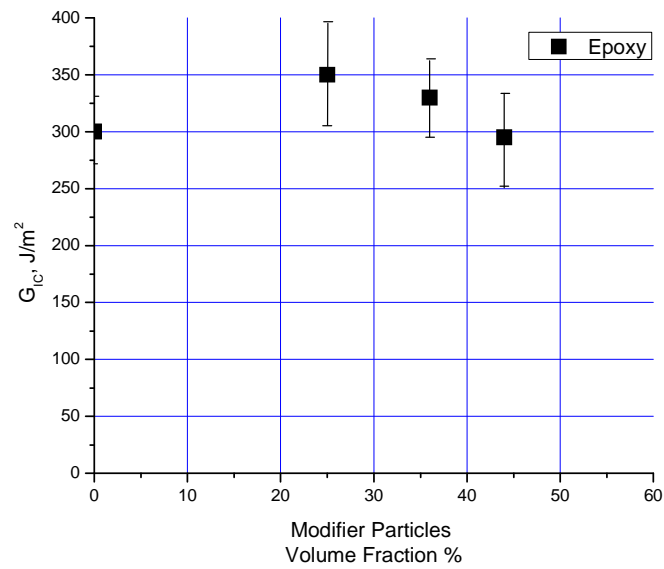


Figure 4.31 Mode I Interlaminar Fracture-Toughness (GIC) of Epoxy-Based Model System vs. Modifier Particle Concentration in Interlayer (5)

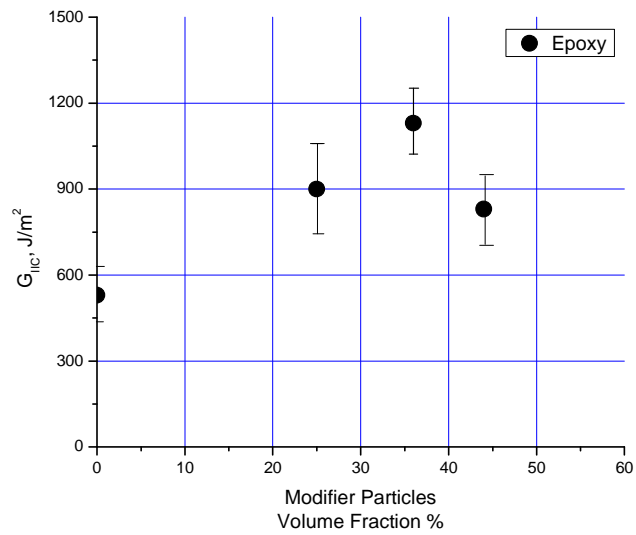


Figure 4.32 Mode II Interlaminar Toughness (GIIC) of Epoxy-Based Model System vs. Modifier Particle Concentration in Interlayer (5)

4.3.2 Toughness Improvement Evaluation

The ENF results taken from this model system combined with other resin systems (5) demonstrate that the host resin base toughness plays an important factor in the final layered structure toughness. Tougher resin systems have the toughest multilayer laminate, whereas more brittle resin systems have the least tough multilayer laminate. By plotting the ENF results as a percent G_{IIC} improvement in Figure 4.33, it is interesting to mention that epoxy produced an improvement of 118%. Other resin systems of different toughness are not investigated here due to the focus on epoxy systems later on when the new interlayers are introduced. The epoxy maximum improvement occurs at 36% modifier particles as presented in Figure 4.33. If compared to different toughness resin systems, it is derived that the more brittle the resin system is, the lower the maximum concentration of modifier particles is required to obtain similar toughness improvement.

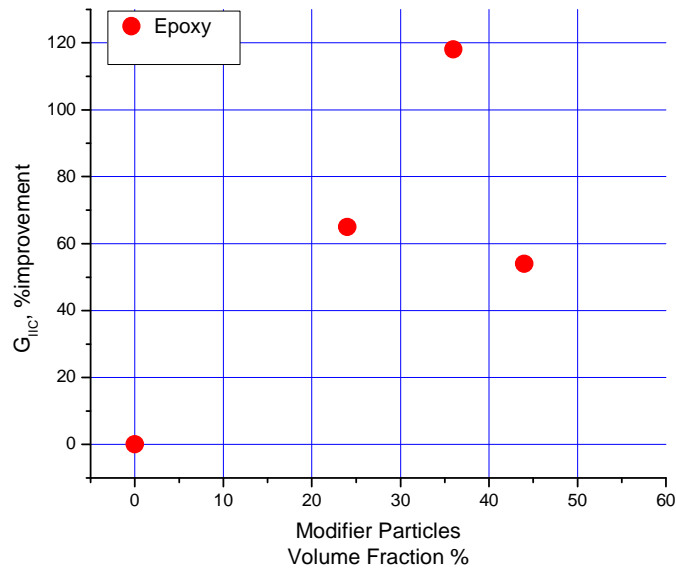


Figure 4.33 Percent Mode II Interlaminar Fracture-Toughness Improvement of Epoxy-Model System vs. Modifier Particle Concentration in Interlayer (5)

Figure 4.33, it can be seen that there is a maximum ratio of interlaminar fracture-toughness to intralaminar fracture-toughness that cannot be exceeded. If the interlaminar fracture-toughness is too high, crack propagation moves from a high toughness interlaminar region to a low toughness intralaminar region. Therefore, if the conventional Mode II fracture-toughness of a thermosetting matrix composite is known, the maximum toughness capability of that system can be predicted by defining a toughness capability ratio via (5):

$$T_c = \frac{G_{IICml}}{G_{IICcon}} = 2 \quad 46$$

Where:

T_c = toughness capability

G_{IICml} = maximum G_{IIC} of multilayer laminate (J/m^2)

G_{IICcon} = G_{IIC} of conventional laminate (J/m^2)

This toughness capability of 2 may only be valid for the modifier particles used in this section. The other toughness resin systems give similar improvement as well. Higher toughness capability ratios may be obtained through the optimization of modifier particle shape, size distribution, and interaction with the host resin matrix system, which involve their material and mechanical properties.

4.4 Results for Specific Objective #4: Carbon Nanotubes in the Interlayer

Having created a distinct interlayer within the CFRP plies and having proved its contribution to the fracture toughness improvement, the next step is to introduce new interlayer systems that involve the fractal architectures of the Featherweight composites. As it has already been stated this architecture is achieved through scalable structures from the macro (fiber tows) to micro (epoxy foam or electrospun fibers) and to nano (carbon nanotubes) sizes. It is considered critical to first investigate the role of the nano-structure of the fractal architecture (CNT) in order to understand how it behaves within the polymeric matrix. Obtaining knowledge

on the main nano-structure that is involved in the featherweight interlayers, it is then easier to understand and analyze the entire interlayer systems of epoxy foam and electrospun fibers.

Featherweight carbon fiber reinforced composites ultimately will introduce nano-free volume both within the matrix and the fibers in order to lighten the composite, without giving up mechanical strength. The polymer composite layer layout and bonding have become an important process used in modern applications. Nevertheless, from both an analysis as well as a manufacturing point of view, the lamination process is expected to yield an apparently homogeneous structure with a uniform nano-free volume distribution through the thickness of the material. This section describes the results of an effort to develop a controlled nano-free volume within the matrix system of a composite. Carbon nanotubes, which can be considered as hollow multilayered tubes, are introduced within the matrix creating nanoporosity. CNT are selected over other nanotubes such as alumina nanotubes etc, due to their nano-hollowness which is combined with high thermoelectrical transport and mechanical properties and can play major role in better load transfer and laminate bridging. Therefore, an analysis of the matrix system and the carbon nanotube density as well as their relation to the carbon nanotube number of walls and external radius is presented. Finally, the effect of nanotubes on the composite modulus and strength is analytically investigated as well.

Since 1990's Carbon Nanotubes (CNT) have stimulated the scientists' and engineers' interest due to their outstanding physical properties. The special physical properties of CNT are derived from the neat nano-structure of carbon atoms hexagonal sheets (graphene) folded in coaxial manner, showing strengths 20 times higher than steel, thermal properties double the pure diamond conductivity, and electrical properties with current carrying capacity that is 1000 times higher than copper (91). A huge variety of applications has been proposed for CNT, in order to take advantage of this unique ratio of size and properties. Chemical and biomedical probes, MEMS, ion storage devices, fuel cells, microscope and emission tips, structural

materials reinforcements, and thermoelectrical materials with property enhancement are some of those applications of nanotubes (91; 92).

This section focuses on the CNT structure and its influence to the density and modulus. Considering carbon nanotubes as hollow nano-structures, one can think that a CNT can be a cylindrical nano-pore when introduced into a matrix. The carbon atom hexagonal sheets contained over the total CNT volume can give a significantly reduced equivalent CNT density due to the influence of the CNT enclosed hollowness, which constitutes the nano-free volume. This nano-free volume is mainly affected by the size of the CNT and more specifically by the external radius and the number of walls. Specific distributions of CNT radius and walls incorporated into a polymeric matrix can reduce the polymer weight. This behavior is also related to the CNT volume fraction within the polymer nano-composite, resulting logically to the conclusion that the higher the volume fraction is, the lower the PNC density. At this point, it should be mentioned that currently there are CNT providers that can supply MWNT in high volumes and in low cost. As a result, using a high volume fraction of CNT in a composite may not be prohibitive as it used to be in the past in terms of cost.

Furthermore, in this section the effect of this CNT structure approach on the modulus of the overall CNT structure is investigated. Examining the literature and comparing several approaches and attempts for describing the properties of a CNT itself, as well as the PNC modulus, this work demonstrates a modulus calculation approach taking into account the volume of the actual carbon atom hexagonal sheets over the total CNT volume. The influence of the external radius and the number of walls on the CNT modulus is of significant importance as well. Finally, using simple rules of mixtures, the polymer nano-composite modulus is calculated (141; 142).

4.4.1 CNT Density and Modulus Approach

4.4.1.1 CNT Density Approach

The nano-free volume within a CNT is the hollow part of the nanotube and is dependent on the CNT external radius and number of walls. In order to accurately measure the nano-free volume enclosed in a CNT, the problem must be approached from a molecular point of view. Thus, at first the mass of carbon atoms composing the hexagonal CNT sheets is calculated by equation 47.

Mass of Carbon Atom (M_A) = (Molecular Weight (MB)) / (Avogadro Number (N_A))

$$M_A = \frac{MB}{N_A} = \frac{12.0108 \cdot \frac{g}{mol}}{6.022 \cdot 10^{23} \cdot \frac{1}{mol}} = 1.9945 \cdot 10^{-23} g ; 2 \cdot 10^{-23} g \quad 47$$

This is verified from the periodic table $\rightarrow M_A = 2.0088 \times 10^{-23}$.

The next step is to calculate the number of atoms in a hexagonal sheet. A scheme of a carbon atom hexagonal sheet is presented in Figure 4.34.

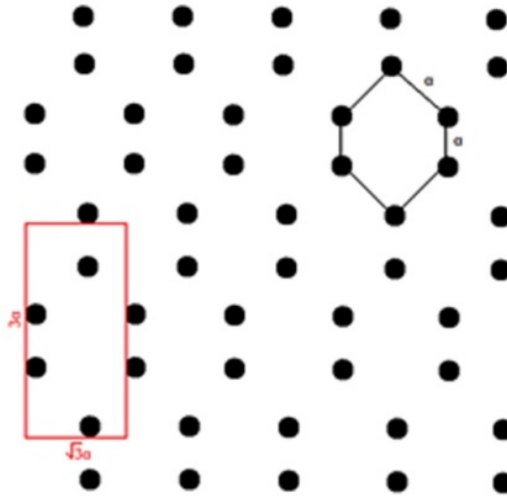


Figure 4.34 Carbon Atoms in a Hexagonal CNT Sheet

The distance between two carbon atoms has the value of the theoretical carbon atom diameter (128) $\alpha = 0.14 - 0.5$ nm. The area that is enclosed in the red area (A_1) is a repeatable area on the sheet and it always contains 4 atoms. In this work, the low value (0.14) is used for α when it comes to carbon atoms within the same graphene sheet, first because this is the one used mostly in the literature, and second because this is the most conservative scenario for density savings calculations. Also, the areal density of the carbon atom hexagonal sheet itself can be calculated within the repeated area through equation 48:

$$\rho_A = \frac{(\text{Number of Atoms within } A_1) \cdot M_A}{(\text{Area of } A_1)} = \frac{4 \cdot (2 \cdot 10^{-23})}{3 \cdot \sqrt{3} \cdot \alpha^2} = 0.79 \cdot 10^{-21} \left(\frac{g}{nm^2}\right) \quad 48$$

Figure 4.35 shows a section of a multiwall nano-tube and how this is taken into account in the calculations.

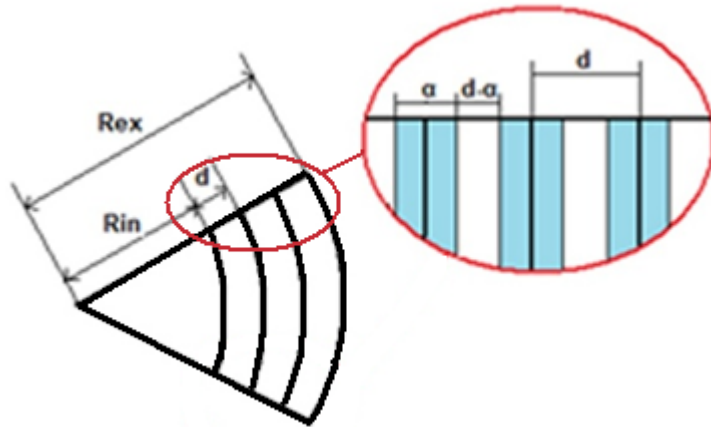


Figure 4.35 Section of Carbon Nanotube (Parallel to Base)

Where:

R_{in} = CNT internal radius (nm)

R_{ex} =CNT external radius (nm)

d = distance between walls, however not always uniform (nm)

α = hexagonal CNT sheet thickness, again it is considered same as the theoretical carbon atom diameter (nm)

Following to the data given above, the total area of the number of hexagonal sheets participating in a CNT is given by equation 49:

$$A_h = 2 \cdot \pi \cdot l \cdot (x \cdot R_m + d \sum_{i=1}^{x-1} (i)) \quad 49$$

Where:

A_h = total area of hexagonal sheets (nm²)

l = CNT length (nm)

x = number of walls

R_m = CNT internal radius (nm)

d = distance between walls (0.34 nm) (Considered as an average value)

Thus, the number of atoms in a CNT is given by equation 50:

$$N_{CNT-A} = 4 \cdot \frac{A_h}{3 \cdot \sqrt{3} \cdot a^2} \quad 50$$

Where:

N_{CNT-A} = Number of atoms in a CNT

a = Distance between atoms on the hexagonal sheet

Moreover, for calculating solely the volume of carbon atom hexagonal sheets in the CNT, the sheets are considered as separate rectangular sheets with length (l), width ($2\pi R$), and thickness ($t=a$). The average distance between two successive walls is d . If an average distance d among the walls is considered from the CNT internal radius to its external periphery, then the external radius can be written as in equation 51:

$$R_{e,x} = R_m + (x-1) \cdot d \quad 51$$

Having calculated the total area of carbon atom hexagonal sheets in the CNT, the total volume of the CNT is calculated by equation 52:

$$V_{CNT} = \pi \cdot R_{ex}^2 \cdot l = \pi \cdot (R_m + (x-1) \cdot d)^2 \cdot l \quad 52$$

Thus, the equivalent density of the CNT can be calculated by multiplying the area of carbon atom hexagonal sheets within the CNT [(A_h) – Equation 49] with the carbon atom hexagonal areal density [(ρ_A) – Equation 48], and then divided by the CNT volume [(V_{CNT}) – Equation 52]. This is given by equation 53:

$$\rho_{h \rightarrow CNT} = \frac{A_h \cdot \rho_A}{V_{CNT}} = \frac{[(x \cdot R_m + d \sum_{i=1}^{x-1} (i))] \cdot (1.58 \cdot 10^{-21})}{(R_m + (x-1) \cdot d)^2} \quad 53$$

4.4.1.2 CNT Modulus Approach

Summarizing the approaches of calculating the CNT and the PNC modulus, it is of high interest to investigate how the CNT modulus would behave considering the real geometry of the CNT, meaning the carbon atom hexagonal sheets participating in the overall CNT volume. For this reason, the model that is proposed has a strong relation with the CNT density approach described in section 4.4.1.1. Considering the CNT in Figure 4.34, the modulus of the CNT could be derived from equation 54:

$$E_{NT} = E_{gr} \cdot \frac{\sum_{i=1}^x (2 \cdot \pi \cdot r_i \cdot l)}{\pi \cdot R_{ex}^2 \cdot l} = 2 \cdot E_{gr} \cdot \frac{x \cdot R_m + d \sum_{i=1}^x (i)}{R_{ex}^2} \quad 54$$

Where, E_{gr} = Graphene Sheet Modulus (GPa) → (~1000GPa) (143; 144; 145).

It is assumed that the CNT layers are modeled as concentric parallel springs with simply added stiffnesses. Focusing on low cost manufacturing, low cost CNT are utilized

assuming non-functionalized external surfaces and no connection of length to potential benefits to load transfer (128).

In order to have the nanotube modulus as a function of external radius and number of walls, equation 54 due to 51 and 53 can be also written:

$$E_{NT} = 2 \cdot E_{gr} \cdot \frac{x \cdot (R_{ex} - (x-1) \cdot d) + d \cdot \sum_{i=1}^x (i)}{R_{ex}^2}$$

Where:

E_{NT} = Nanotube Modulus (GPa)

E_{gr} = Graphene Sheet Modulus (GPa) → (~1000GPa) (143; 144; 145).

l = CNT length (nm)

x = number of walls

R_{ex} = CNT external radius (nm)

R_{in} = CNT internal radius (nm)

r_i = Hexagonal sheet radius (nm) → ($R_{in} + i \cdot d$)

d = average distance between walls based on TEM graphs (142; 143) → (0.34 nm)

As it can be clearly seen, the modulus of the nanotube is calculated after multiplying the graphene modulus with the ratio of the hexagonal sheets volume over the total CNT volume.

4.4.2 Interlayer Zoom in – PNC

Considering a featherweight composite as a multilayer structure and by zooming in to the interlayer region, the area within two carbon fiber layers can be considered as a polymer nanocomposite (PNC).

4.4.2.1 PNC Density Approach

The density of a polymeric nano-composite reinforced with CNT is calculated through the rule of mixtures for a given value of epoxy density (1.2 – 1.4 g/cm³). The epoxy density

value can vary according to the matrix desired. Several combinations of CNT external radius and number of walls have been tried for different CNT densities incorporated in the PNC density calculation through the rule of mixtures.

4.4.2.2 PNC Modulus Approach

Having calculated the CNT modulus through the model according to the given number of walls and external radius, the rule of mixtures modified with certain parameters depending on the CNT orientation (129) is used for the PNC modulus calculation. Using this method for short fibers with length smaller than the critical (length where the stress transferred is large enough to break the fiber), the PNC modulus can be calculated through equation 55 (130):

$$E_{comp} = n \cdot z \cdot E_{NT} \cdot v_{CNT} + E_m \cdot (1 - v_{CNT}) \quad 55$$

Where:

E_{comp} : Modulus of the composite (GPa)

E_{NT} : Nanotube modulus (GPa)

E_m : Matrix modulus (GPa)

v_{CNT} : CNT volume fraction

$n = \mathbf{1/5}$ for randomly oriented CNT,

$\mathbf{3/8}$ for aligned in plane CNT, and

$\mathbf{1}$ for aligned CNT (Modulus is determined along the direction of CNT)

$$z = 1 - \frac{\tanh(\beta \cdot \frac{l}{2})}{(\beta \cdot \frac{l}{2})}$$

Where:

l : CNT average length (nm) \rightarrow (~1000)

$$\beta = \sqrt{\frac{H}{E_{NT} \cdot A}}$$

Where $H = \frac{2 \cdot \pi \cdot E_m}{\ln v_{CNT}}$ And $A = \pi \cdot R_{ex}^2$

Thus, $\beta = \sqrt{\frac{2 \cdot E_m}{E_{NT} \cdot R_{ex}^2 \cdot \ln v_{CNT}}}$

The η factor has to do with the interfacial stress transfer of the CNT within the polymeric matrix taking into account the aspect ratio (l/D) of the CNT. In all calculations of the presented model, it is assumed good dispersion and good interfacial shear strength of the CNT within the polymeric matrix.

4.4.3 Modelling and Experimentation Results

4.4.3.1 Modelling Results

CNT Density

By plotting equation 53, the density of a CNT as a function of the external radius and the number of walls is presented in a three dimensional graph (Figure 4.36). The pure carbon atom hexagonal sheets density in this model can be seen in a theoretical single wall CNT with 0.75 nm external radius. Furthermore, three different CNT cases of radius and number of walls combinations observed in lab are presented in the graph.

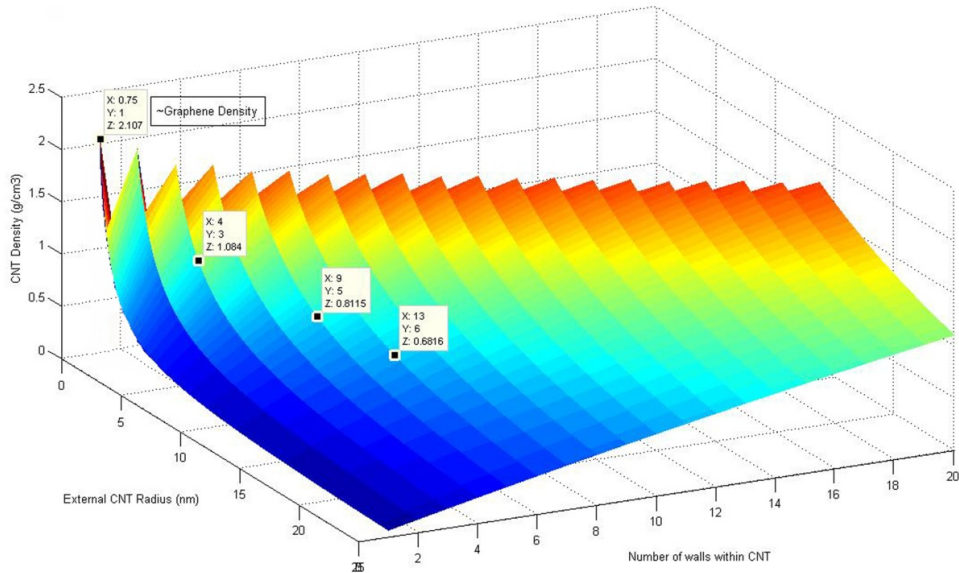


Figure 4.36 CNT Density vs. CNT External Radius and Number of Walls

Figure 4.36 shows how the CNT density varies as a function of the external radius and the number of the walls. In general, the higher the radius the lower the CNT density is; however, as the number of the hexagonal CNT sheets increases the density shows a slight increase as well. Using the three dimensional graph in order to define the CNT that is used or the desired CNT density, the polymer nano-composite density can then easily be calculated through the rule of mixtures.

PNC Density

Using the rule of mixtures for incorporating the CNT and the matrix densities, the PNC density is given for the desired CNT radius and number of external walls that is used. Figure 4.37 shows the PNC density as a function of CNT volume fraction for different CNT distributions.

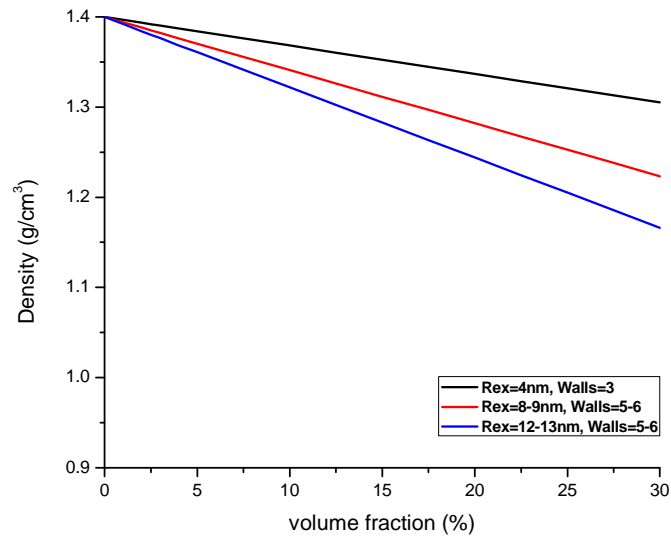


Figure 4.37 PNC Density as a function of CNT volume fraction for different CNT

CNT volume fractions utilized for PNC need to be lower than 30% otherwise they may be impractical for PNC in terms of maintaining matrix cohesion. Carbon nanotubes consist of a costly material; however, there are new methods of CNT manufacturing, which can be proved of significantly low cost. Such techniques are utilized by Rosseter Holdings Ltd, who provided CNT for the scope of this study. This way, volume fractions up to 30% can be economically feasible.

CNT Modulus

As described in section 4.4.1.2 the modulus of the CNT can be given as a function of its external radius and number of walls. This is given by plotting the result of equation 54 (Figure 4.38).

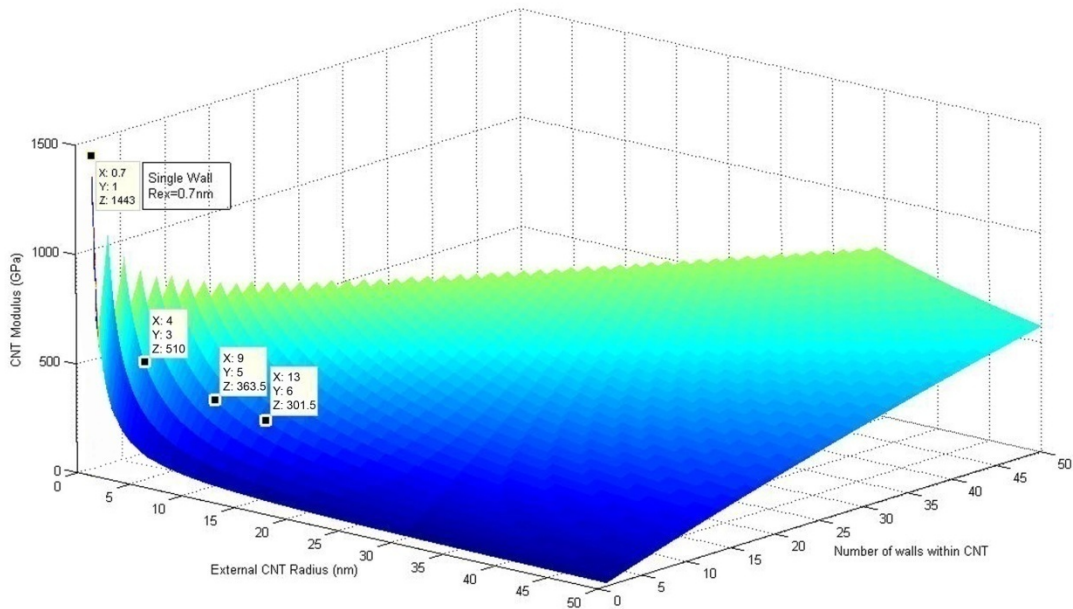


Figure 4.38 CNT Modulus vs. CNT External Radius and Number of Walls

Figure 4.38 shows that the CNT modulus decreases as its radius increases, which is what mostly can be found in literature and it increases as the CNT walls increase. The different CNT distributions that were taken in the density calculations are examined here as well.

PNC Modulus

Figure 4.39, and Figure 4.40 present how the modulus of a PNC for two different CNT ($R_{ex}=4\text{nm}$, 3Walls and $R_{ex}=9\text{nm}$, 6Walls) changes as CNT volume fraction increases. The result of equation 55 is plotted for getting those figures for aligned ($\eta_0=1$), aligned in plane ($\eta_0=3/8$), and randomly oriented CNT ($\eta_0=1/5$).

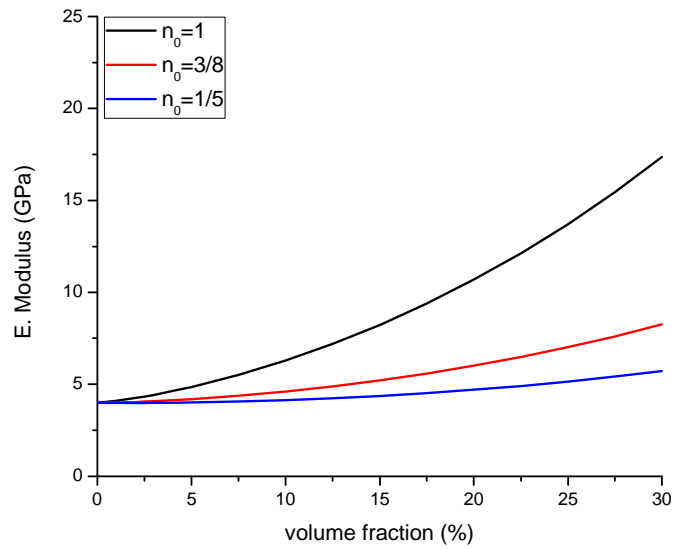


Figure 4.39 PNC Modulus for Aligned, Aligned in Plane, and Randomly Oriented CNT of $R_{ex}=4\text{nm}$ and 3 Walls

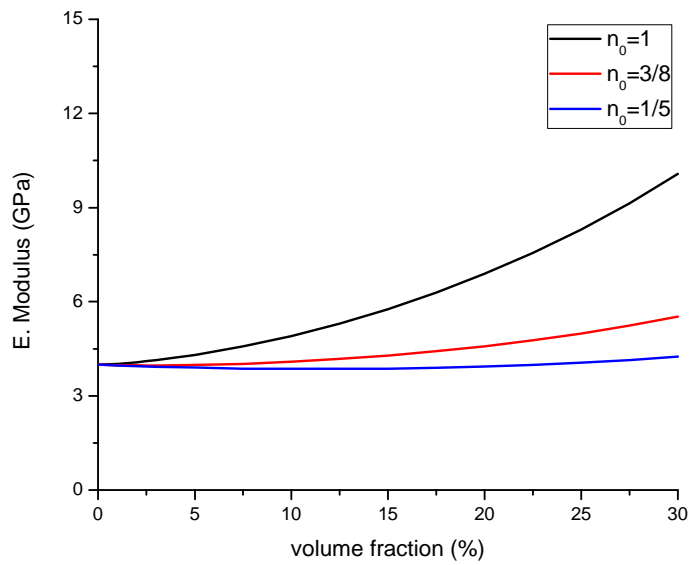


Figure 4.40 PNC Modulus for Aligned, Aligned in Plane, and Randomly Oriented CNT of $R_{ex}=8-9\text{nm}$ and 5-6 Walls

Figure 4.41, presents the theoretical PNC modulus as a function of the CNT volume fraction for aligned CNT, and for three different combinations of CNT external radius and number of walls.

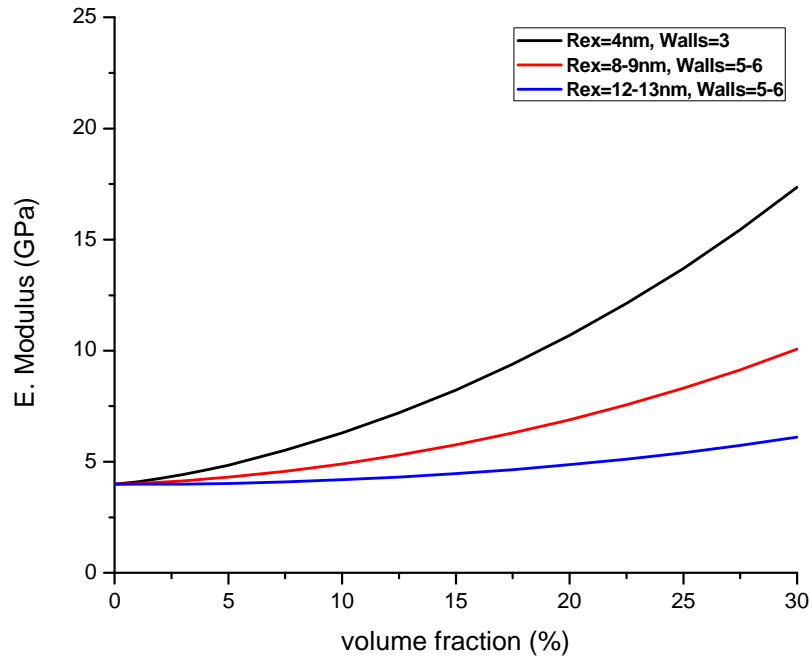


Figure 4.41 PNC Modulus for Aligned CNT of Rex=4, 8, and 12nm and 3, 6, and 6 Walls Respectively

It seems through Figure 4.41 for the large diameter nanotubes that although they increase the weight reduction they do not contribute in modulus enhancement.

Figure 4.42 shows a comparison of the PNC modulus through the CNT approaches found in literature review with the approach investigated in the present model.

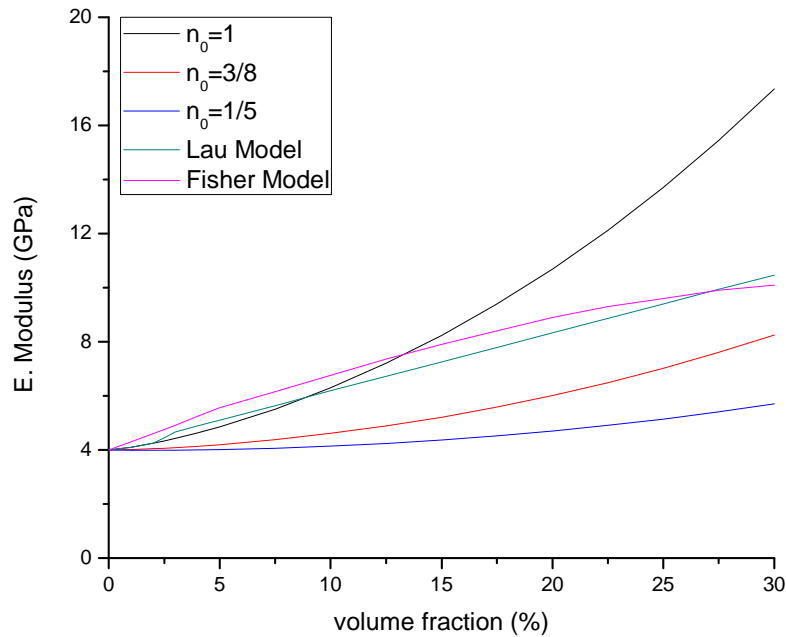


Figure 4.42 PNC Modulus Comparison according to the Different Theories of CNT Modulus Described in Background

Finally, Figure 4.43 presents how the modulus changes with the density variation. It can be seen that in classic materials such as metals, ceramics, FRPs, and polymers, the higher the density gets the higher the modulus. However, in polymer nano-composites this behavior is different since when increasing the CNT volume fraction, even though the modulus increases up to a certain point, the density decreases again up to a certain point. This is in accordance with Figure 2.29 for analyzing the effects of nanopores. Subsequently, the modulus-density relation presented in Figure 4.43 of the investigated PNC cases verifies the theory for nanocomposites to have increased properties due to the extremely high interaction surface area of the nano-inclusion.

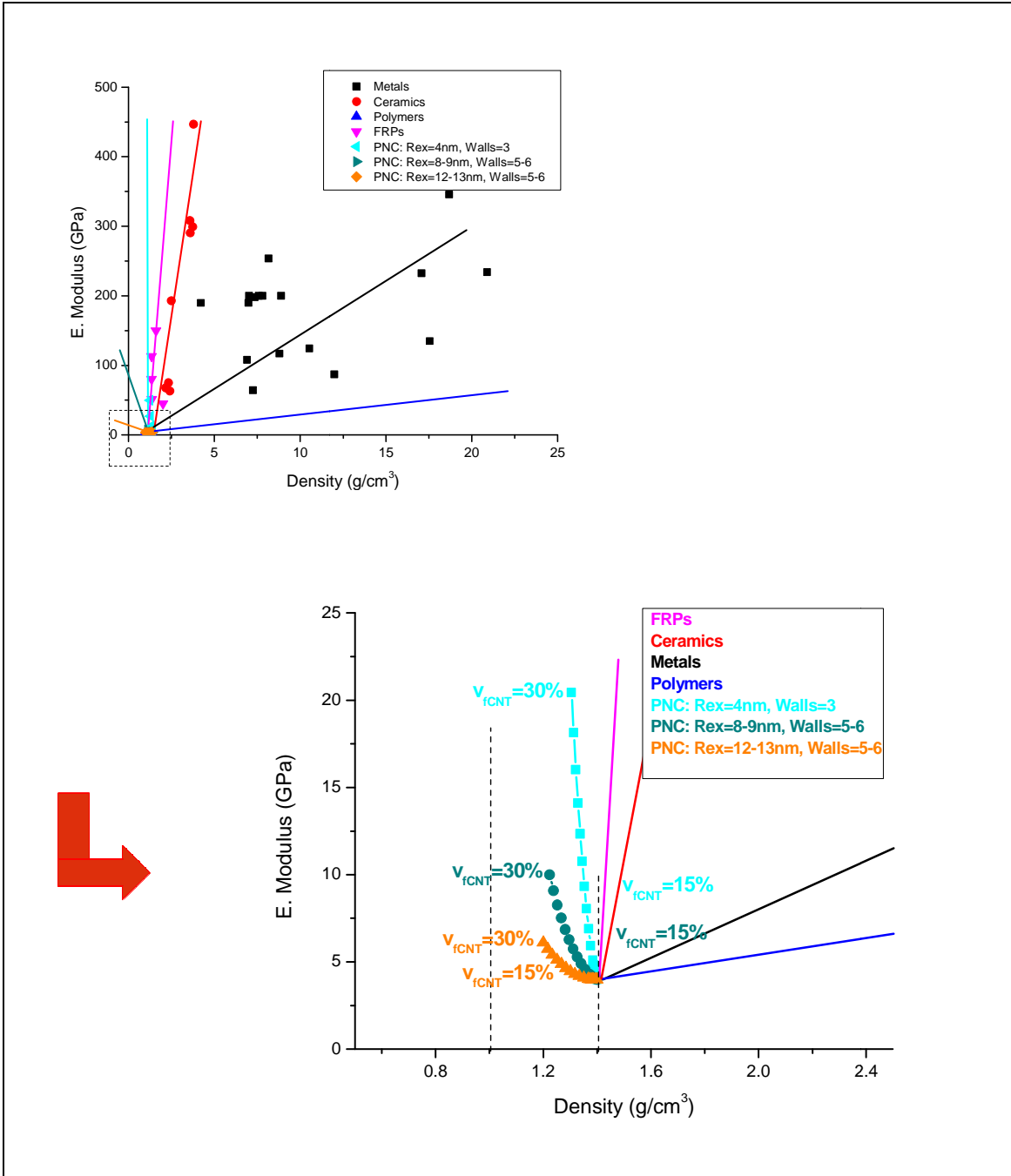


Figure 4.43 Material Modulus vs. Density

4.4.3.2 Experimental Results

Figure 4.44 demonstrates the elastic modulus results measured by the nano-indentation for aligned CNT PNC for ~ 1, 8, and 20 % volume fractions. There is a significant increase of the elastic modulus compared to the randomly oriented CNT in literature PNC.

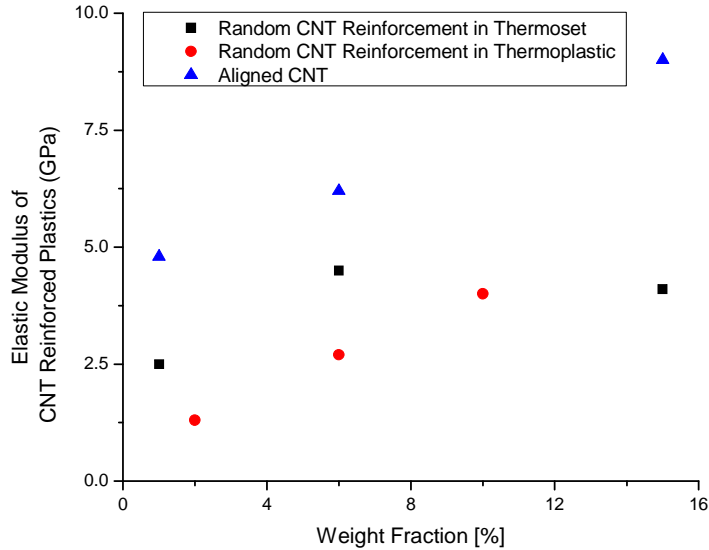


Figure 4.44 Comparison of Aligned CNT PNC (A-PNC) Results to Extant elastic modulus data of random CNT PNC (R-PNC) (88; 134)

Following the theoretical model for the elastic modulus described by equations 53 through 55, there is a good agreement between the experimental findings and the model. This agreement is well presented in Figure 4.45 for CNT with average dimensions of 4nm external radius and 3 walls. A significant, however expected, increase of the modulus is observed.

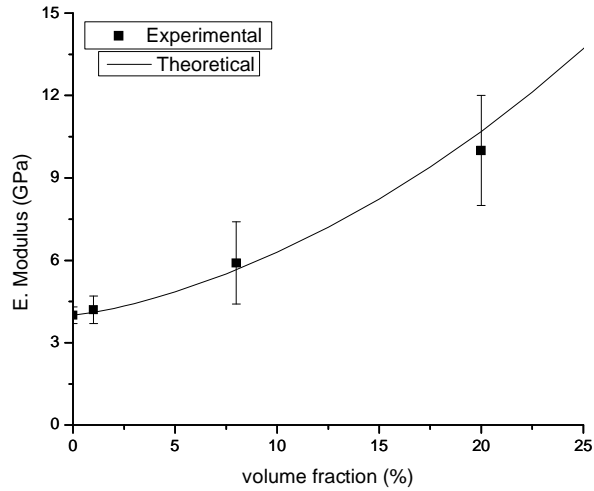


Figure 4.45 PNC Modulus vs. CNT Volume Fraction; Correlation of Experimental Findings with Theoretical Model

Pearson correlation for experimental and theoretical results from Figure 4.45 gives the value of **0.992**, which is important for the good agreement between the theoretical and experimental results and as a result the verification of the theoretical model.

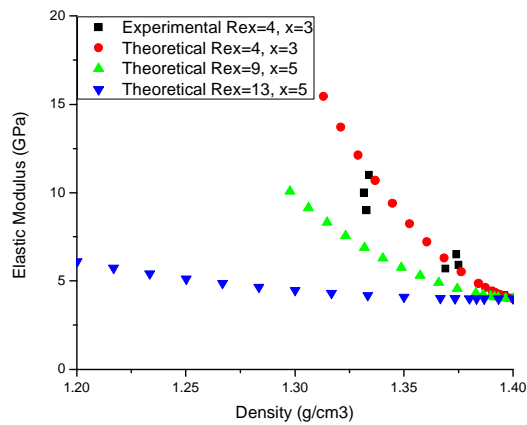


Figure 4.46 PNC Modulus vs. Density. Theoretical Results for Different Types of CNT and Experimental Results for CNT with 4nm External Radius and 3 Walls.

Having in mind the fact that CNT matrix doping reduces the weight as theoretically described in Figure 4.43, and taking a closer look to the polymer nanocomposites, Figure 4.46 is presented. In this figure, the theoretical PNC modulus as a function of density is presented. The experimental modulus and density measurements from nano-indentation and TGA testing respectively, for CNT with 4nm of external radius and 3walls are also presented in Figure 4.46, having a good agreement with the theoretical model.

For having a better understanding and a more clear view of the experimental correlation of the model, Figure 4.47 presents theoretical and experimental results for CNT distribution of 4nm external radius and 3 walls alone.

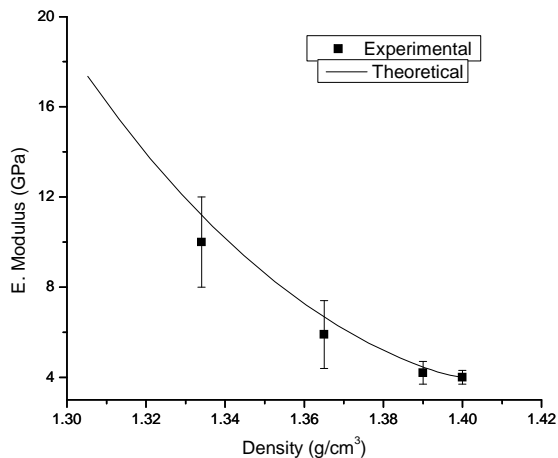


Figure 4.47 Experimental and Theoretical PNC Modulus vs. Density for CNT of 4m External Radius and 3 Walls

Figure 4.47 shows that the PNC density varies within a very small range (comparable to measurement error). However, this reduction is consistent to all specimen measurements. This means that CNT of this particular distribution make the PNC stiffer but not significantly lighter. Following the model previously described, it can be seen that if other CNT distributions with higher radius and less walls are used doping the PNC matrix, then the weight savings are

expected to be more significant for similar volume fractions, however, sacrifices in modulus will have to be accepted.

Furthermore, an extended experimentation took place in order to describe how the CNT are actually reducing the overall weight of the matrix when used as a nano-reinforcement. As it has already been described in methodology section 3.4, the experimentation took place through two approaches:

Experimental Approach 1: Thermogravimetric analysis (TGA) of PNC samples.

Experimental Approach 2: Carbon nanotubes and resin system samples separately analyzed in TGA. Then, the results were combined in the rule of mixtures and re-calculate the PNC density, correlating the Approach 1 TGA measurements

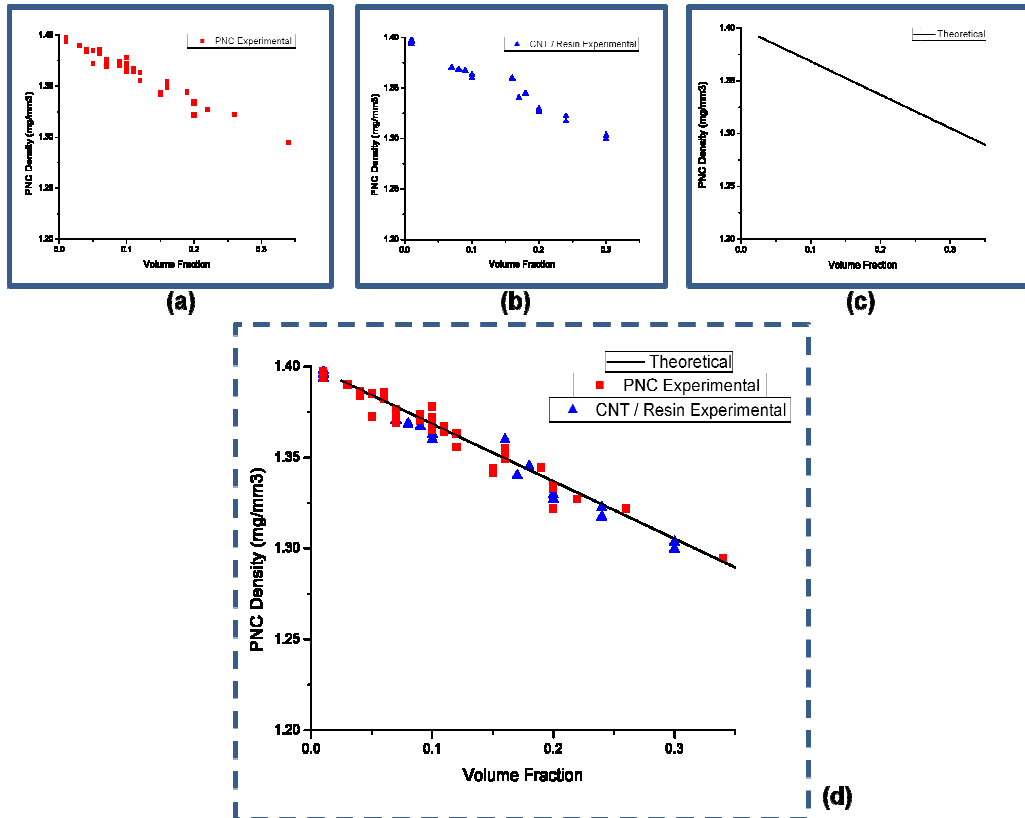


Figure 4.48 PNC Density vs. CNT Volume Fraction: (a) experimental approach 1, (b) experimental approach 2, (c) theoretical approach, (d) merge of a, b, and c graphs

Figure 4.48 presents the density of the PNC as a function of the CNT volume fraction for the theoretical model, the first and the second experimentation approaches (TGA for 1) PNC and 2) Resin + CNT combined in the rule of mixtures)

The good agreement of the density model and experimental results is also verified by Pearson correlation as shown in Table 4.22.

Table 4.22 PNC Theoretical and Experimental Approaches Correlation

	Theoretical Approach	Experimental Approach 1	Experimental Approach 2
Theoretical Approach	1	0.988812	0.990047
Experimental Approach 1	0.988812	1	0.99055
Experimental Approach 2	0.990047	0.99055	1

As it can be observed all correlations are above 0.95 which is important for the theoretical and experimental results agreement.

4.5 Results for Specific Objective #5: Porosity in Epoxy Matrix Systems

4.5.1 CNT Fraction for Pore Surface Reinforcement

A first effort was made in Polymeric Composites Laboratory to incorporate epoxy foam agent with epoxy matrix system and examine the coexistence of both the epoxy foam and resin system into the interlayer of prepreg systems. T300YC carbon fibers were used for fiber reinforcements. The epoxy resins were mixed in a 60:40 weight ratio of MY 9655: EPON 828 and stirred until they were completely mixed. 45 weight ratio Diaminodiphenyl Sulfone (DDS) was melted and added to the epoxy system as the curing agent. 10 weight ratio of Celogen® AZ 120 (Azodicarbonamide) was incorporated into the epoxy and DDS mixture as a foaming agent. Furthermore, styrene oxide was added. Then, Pluronic L-64 that was a block copolymer surfactant was added. After the impregnation by a hot-melt prepreg machine, prepreg sheets were cut and autoclaved.

Table 4.23 Preliminary Foam System Morphology

Sample	Pressure (kPa)	Stir Time Hour	Foam Size
Control	310	0	No foam
1	310	1.0	5 – 50 μm
2	552	1.0	Below 10 μm

Density of the control sample was 1.5g/cm³, while the density of sample 2 was 1.4g/cm³ and the density of sample 1 was 1.3g/cm³. From these numbers, the void content was calculated by the equation (99):

$$\text{Void Content} = \frac{D_c - D_f}{D_c} \cdot 100 \quad 56$$

In equation 56, D_c is the average density of control samples and D_f is the average density of CFRP foam samples. The CFRP foam samples (sample 2 and sample 1) reduced about 7% and 13% in weight, respectively, compared to the control sample. However, this technique was not efficient enough to formulate the desired foaming within the CFRP interlayers as first the pressure was not capable for restraining bubble size to nano-scale and second the curing process forced most of the pores to collapse. This is given by SEM characterization in (99), but also is explained by the fact that very low density reduction was achieved. The absence of CNT or other pore surface reinforcement was the main reason for pores to collapse.

As presented in the background, when a nano-reinforcement is added to a resin which contains an agent and is made to form foamed resin, the nano-reinforcements tend to reinforce the pores surfaces due to electrostatic forces. Figure 4.49 illustrates the pore nano-reinforcement mechanism.

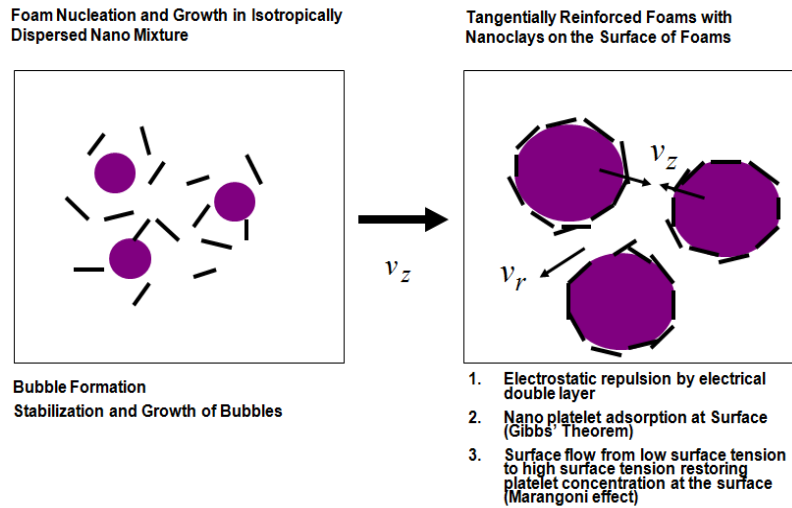


Figure 4.49 Pore Tangential Nano-Reinforcement Mechanism

In order to determine the desired CNT volume fraction for reinforcing the pores surface, formula 63 was developed through the following steps.

The void (bubble) content is calculated through equation 56. However, it is also given by definition through the volume equation 57.

$$v_{fb} = \frac{V_{bubble-total}}{V_{Composite}} \quad 57$$

Where,

v_{fb} = Bubble Volume Fraction

$V_{bubble-total}$ = Total Bubbles Volume (m^3)

$V_{Composite}$ = Composite Volume (m^3)

Following the CNT volume fraction is given by equation 58:

$$v_{fCNT} = \frac{V_{CNT-total}}{V_{Composite}} \quad 58$$

Where,

$V_{f_{CNT}}$ = CNT Volume Fraction

$V_{CNT-total}$ = Total CNT Volume (m^3)

Thus, through equations 56 to 58 the CNT volume fraction can be written:

$$V_{f_{CNT}} = \frac{V_{CNT-total}}{V_{bubble-total}} \cdot V_{fb} \quad 59$$

At this point the calculations can focus on one bubble. So the CNT volume fraction for reinforcing the surface of one average bubble is the same with the volume fraction of the CNT reinforcing all bubbles. Thus, the total volume of the CNT reinforcing one average diameter bubble is given by equation 60:

$$V_{CNT-total} = N_{CNT} \cdot V_{CNT} = \left(\frac{A_{Bubble}}{2 \cdot R_{CNT} \cdot L_{CNT}} \right) \cdot V_{CNT} = \left(\frac{A_{Bubble}}{2} \right) \cdot \pi \cdot R_{CNT} \quad 60$$

Where:

N_{CNT} = Number of CNT

V_{CNT} = Average Volume of one CNT (nm^3)

R_{CNT} = Average External Radius of CNT (nm)

L_{CNT} = Average CNT length (nm)

$A_{Bubble} = 4 \cdot \pi \cdot R_B^2 \rightarrow$ Average Surface of One Bubble (nm^2)

R_B = Bubble Radius (nm)

$V_{Bubble} = \frac{4}{3} \cdot \pi \cdot R_B^3 \rightarrow$ Average Volume of One Bubble (nm^3)

Thus, by assuming that the entire CNT length participates in covering the pore surface, the $V_{f_{CNT}}$ can be written:

$$v_{fCNT} = \frac{3}{2} \cdot \pi \cdot \frac{R_{CNT}}{R_B} \cdot v_{fb} \quad 61$$

Now, by calculating the entire number of bubbles within the composite, the CNT equation fraction equation remains the same.

The assumption that the entire CNT length participates in covering the Bubble Surface is not realistic. In reality, only a part of the CNT is tangentially attached to the bubble surface as CNT are highly stiff and extremely difficult to bend. As a result, taking into account that only a part of the CNT participates in the surface reinforcement due to CNT stiffness, and that this part forms a chord to the bubble geometry with length assumed equal to bubble radius, then the number of the CNT participating in bubble reinforcement changes to:

$$N_{CNT} = \left(\frac{A_{Bubble}}{2 \cdot R_{CNT} \cdot (L_{CNT} - (L_{CNT} - R_B))} \right) = \frac{2 \cdot \pi \cdot R_B}{R_{CNT}} \quad 62$$

And thus, equation of the desired v_{fCNT} for reinforcing pore surface can be written as following:

$$v_{fCNT} = \frac{3}{2} \cdot \pi \cdot \frac{R_{CNT} \cdot L_{CNT}}{R_B^2} \cdot v_{fb} \quad 63$$

4.5.2 Montmorillonite Nanoclay Reinforced Polyurethane

Further towards nano-cellular structure investigation, the first step was to incorporate nano clays of montmorillonite into the polyurethane matrix system, in order to experimentally observe the ability of nano-sized particles to develop on the pore surface, and to control the pore so that it does not collapse while processing. Polyurethane foam is easier to handle both while processing and in observation after manufacturing than epoxy foam. Materials used in matrix system are described below:

-Polyol + MMT: 105 (g)

- Foaming agent: water 1.75 (g),
- Cyclopentane 16.5 (g)
- Catalyst: 2.6 (g)
- Silicone surfactant: 2.5 (g)
- Nucleating agent (PFA): 1.0 (g)

The above mixture is blended in MDI (4,4'-diphenyl methane) 148.75g at 20°C for 5 sec. Finally the specimens are cut at 12cm x 12cm x 12cm, to measure density and weight.

Figure 4.50 presents SEM graphs of examination of polyurethane reinforced with two different types of nanoclays of montmorillonite (30A and 20A) in three different nanoclays weight content of 1, 3, and 5% with and without nucleating agent.

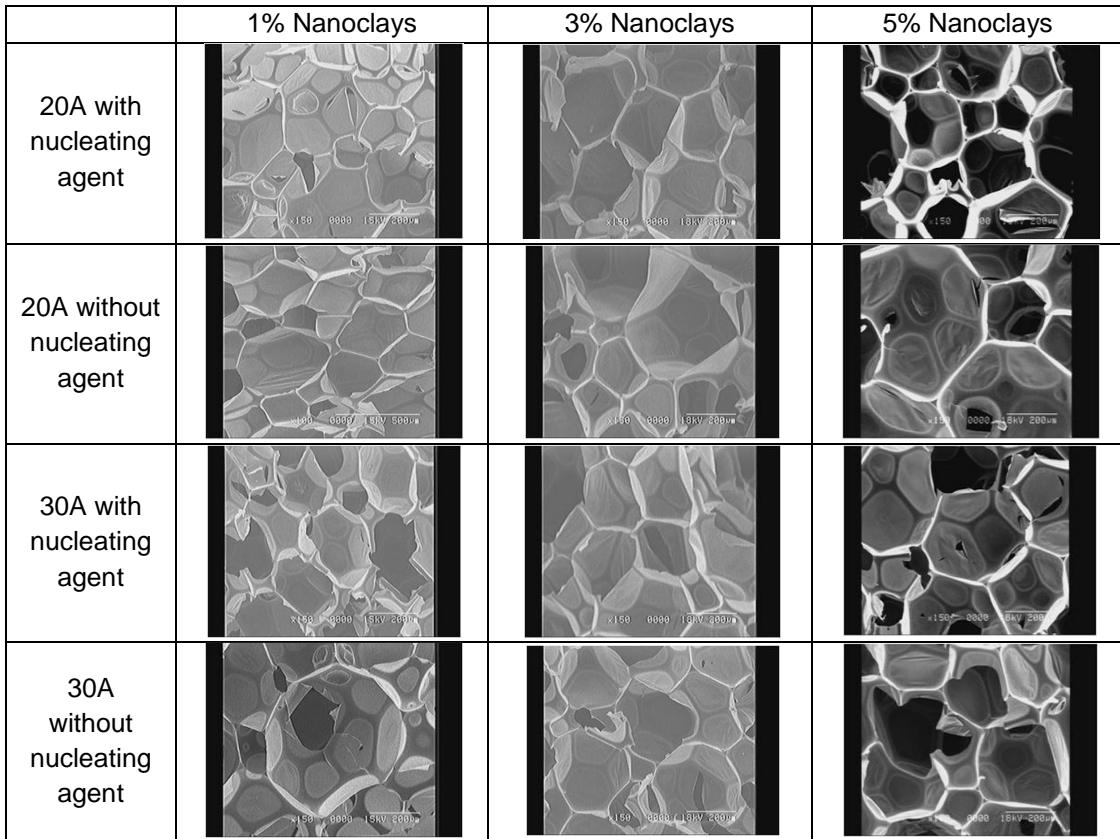


Figure 4.50 Polyurethane Reinforced with Montmorillonite Nano-Clays in Different Weight Fractions (101)

The examination shows a general trend of greater quantity, smaller size, and more intensive surface reinforced pores, as weight content increases. It is clear that nanoclays are developed on pores surface as foaming occurs. From a size point of view, the nucleating agent does not really affect the two different systems, as there are no significant changes in pores size (approximately 200-500 μm) with respect to foam morphology, with and without nucleating agent. However, it is obvious from line 1 and 3 of Figure 4.50 that nucleating agent assists the pores in accumulating more nano-clays on their surface.

4.5.3 CNT Reinforced Epoxy Foam Interlayered CFRP

Having observed the development of nanoclays on polyurethane pores surface, epoxy foamed interlayer was manufactured as a second step by adding the appropriate amount of epoxy foam to the interlayer through a simple lay-up method. At this step the improvement of the material by having such an interlayer is investigated under several testing procedures. Normal epoxy system was utilized within the fiber bed; however, an epoxy foam system was added to the interlayer. As it has already been mentioned in chapter 4, three different samples were manufactured to better evaluate the foaming and CNT reinforcement effect (Control, Carbon Fiber with Epoxy Foamed interlayer, and Carbon Fiber with CNT Epoxy Foamed interlayer).

Materials used in matrix system are described below:

Provided by "Fibermax Composites"

Epoxy System: Resin 921 & Hardener 475524 **Volume Fraction:** 32%

Epoxy Foam System: Foam system F250 & Slow Hardener H02 **Volume Fraction:** 8%

(Final Density: 250 kg/m³)

Carbon Fibers: C160P (160 g/m²), E=235 GPa **Volume Fraction:** 60%

Provided by "Rosseter Holdings Ltd"

Carbon Nanotubes: Distribution Characteristics:

Outer diameter: 8.2 \pm 3.0nm

Inner diameter: $3.1 \pm 0.9 \text{ nm}$

Number of walls: 8 ± 4 layers

Length: 250-300 nm

Volume Fraction: 1.36% (calculated through equation 63)

CNT were stirred within the epoxy foam catalyst over night in a magnetic stirrer so better distribution is achieved. Figure 4.51 illustrates how the lay-up of the three different samples is.

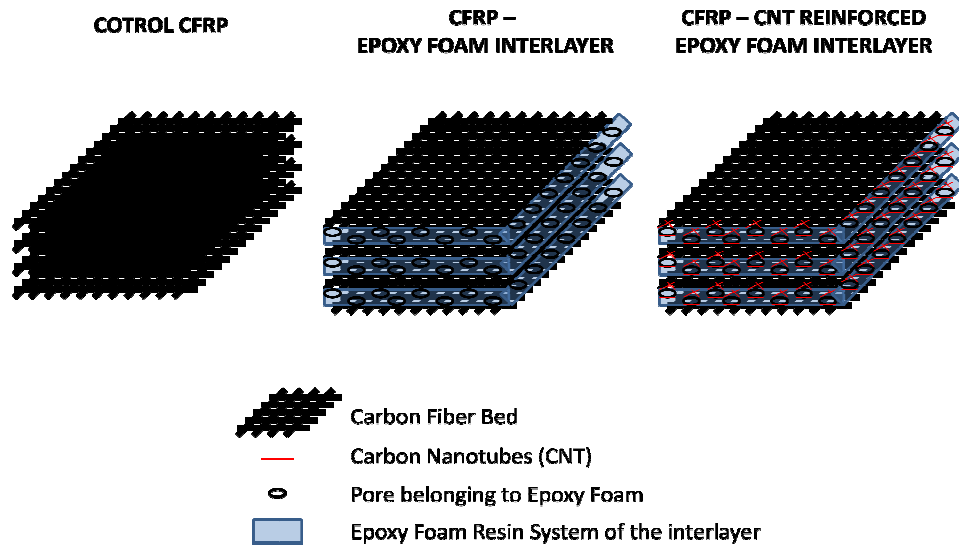


Figure 4.51 Epoxy Foamed Interlayer System Scheme within CFRP

4.5.4 DMA for Viscoelastic Behaviour Evaluation

Table 4.24 presents the results from the DMA flexural experiments. More than three experiments were conducted for each kind of sample. Storage flexural modulus values at 30°C are presented together with glass transition temperature based on storage modulus and $\tan\delta$.

Table 4.24 Epoxy Foamed Interlayered CFRP DMA Characterization

Samples	Storage Modulus at 30 °C	Glass Transition T Based on Storage Modulus (GPa)	Tan δ Peak	T at tan δ peak (Glass Transition T Based on tan δ) (°C)
Control CFRP	235.6±3.9	48.8±2	0.2621± 0.047	55.4±2.1
CFRP with Epoxy Foamed Interlayer	293.7±25.5	49.2±8.4	0.3999±0.064	57.3±5.9
CFRP with CNT Reinforced Epoxy Foamed Interlayer	373.7±14.6	47.2±5.6	0.5067±0.146	53.2±5.49

It can be seen that there is a significant increase of the modulus from the control samples to the epoxy foamed interlayer and even higher to the CNT epoxy foamed interlayer. This finding is of particular importance, since it shows that CNT developed on and reinforcing the pores surfaces of the interlayer increase the stiffness of the overall material. However, the slight changes on the overall samples thickness (0.98 ± 0.25 mm) can justify such differences in modulus calculations and since the geometrical characteristics of the samples slightly vary, the modulus results can be influenced as well. Thus, in order to get a better view of the flexural behaviour of the material stiffness, calculations for each type of samples are given in section 4.5.5.

Additionally, there is a difference between the two methods through which the glass transition temperature (T_g) is measured. This happens because storage modulus and tan δ are different properties, so the latter always gives a little higher values of T_g than the former. Within each method though, there are no significant alterations of the T_g measurements. This means that the interlayer does not affect the glass transition of the material. The tan δ peak values are shown in order to give an idea of the loss modulus values at that point (δ is the damping ratio and tan δ represents the loss over the storage modulus).

4.5.5 Mechanical Testing for Interlayer Evaluation

4.5.5.1 Flexural Testing

The flexural experiments were performed under the following parameters:

Data Rate: 1 point/sec

Crosshead Speed: 5.00000 mm/min

Temperature: 23 °C

Humidity: 50%

Span: 130mm

Figure 4.52 - Figure 4.54, present some of the several samples that were tested in 3 point bending for control, CFRP with epoxy foamed interlayer, and CFRP with CNT epoxy foamed interlayer.

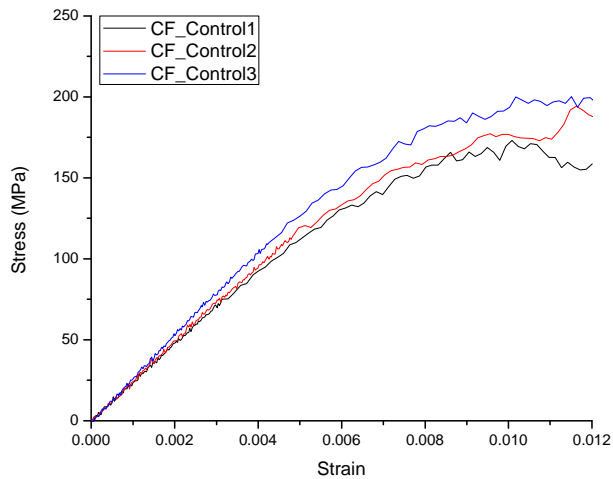


Figure 4.52 Control CFRP Flexural Testing

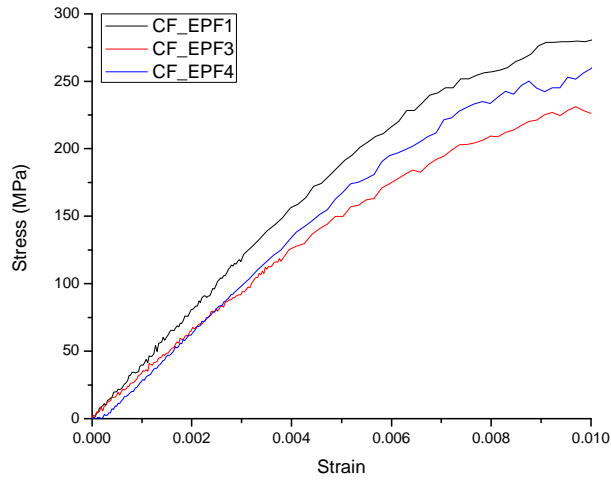


Figure 4.53 CFRP with Epoxy Foamed Interlayer Flexural Testing

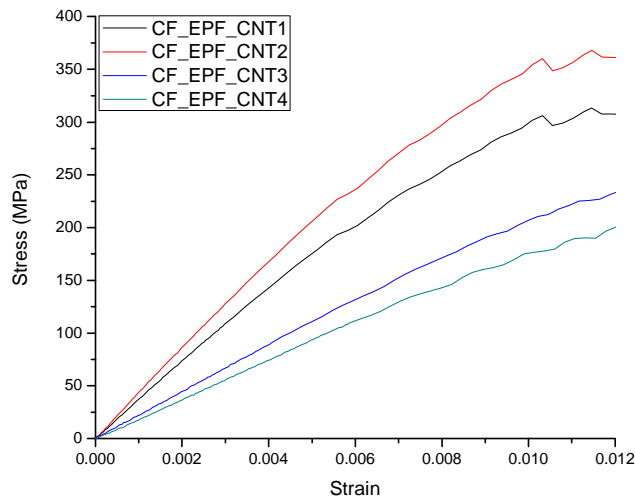


Figure 4.54 CNT Reinforced Epoxy Foamed Interlayer CFRP Flexural Testing

There is a significant flexural strength increase from the control to CFRP with epoxy foamed interlayer, and to CFRP with CNT epoxy foamed interlayer. The following Table 4.25

summarizes the values deriving for the epoxy foamed samples when tested in flexural experiments. The material stiffness improvement is presented later on as well.

Table 4.25 Epoxy Foamed Interlayer CFRP Flexural Testing Summary

	Flexural Strength (MPa)	Flexural Modulus (GPa)
Control CFRP	196.1±24.05	24.67±2.1
CFRP+EP.FOAM	276.81±18.14	38.5±6.81
CFRP+EP.FOAM+CNT	322.4±40.69	38.33±5.13

It can be seen that there is a significant increase of flexural strength from control to epoxy foamed samples of around 48%. This indicates that the foamed interlayer due to its high stiffness plays a key role in the flexural strength enhancement. There is an additional 16.5% flexural strength enhancement from the epoxy foamed interlayer to the CNT reinforced epoxy foamed interlayer and this is due to the CNT existence. However, CNT reinforcement does not change the flexural modulus as although it presents a high increase of around 56% from control to epoxy foamed interlayer samples, it does not change when CNT are added. This was expected as nanotubes do not reinforce the main matrix system through which the load transfer occurs. As a result, the CNT reinforcement contributes to the flexural strength, stiffness, and Mode II fracture toughness improvement but not to a higher flexural modulus. This is explained by simple solid mechanics as modulus is a property of the material, whereas stiffness is a property of the structure. The latter indicates that stiffness and strength depend not only on the material, but on the sample geometry and boundary conditions as well (128; 143). CNT although they can reinforce the resin as it has been proven in section 4.4, at this level they are within the pore surfaces and do not participate in the load transfer within the material entirety.

4.5.5.2 Tensile Testing

The tensile experiments were performed under the following parameters:

Data Rate: 10 point/sec

Crosshead Speed: 1.00000 mm/min

Temperature: 23 °C

Humidity: 50%

Gauge Length: ~80 mm

Figure 4.55 - Figure 4.57, present some of the several samples that were tested in tensile test for control CFRP, CFRP with epoxy foamed interlayer, and CFRP with CNT epoxy foamed interlayer.

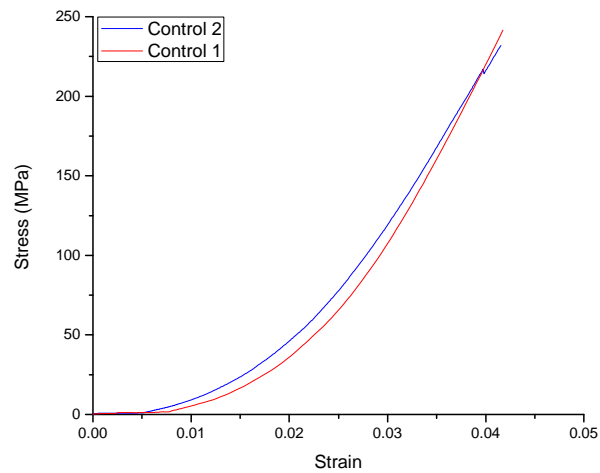


Figure 4.55 Control CFRP Tensile Testing

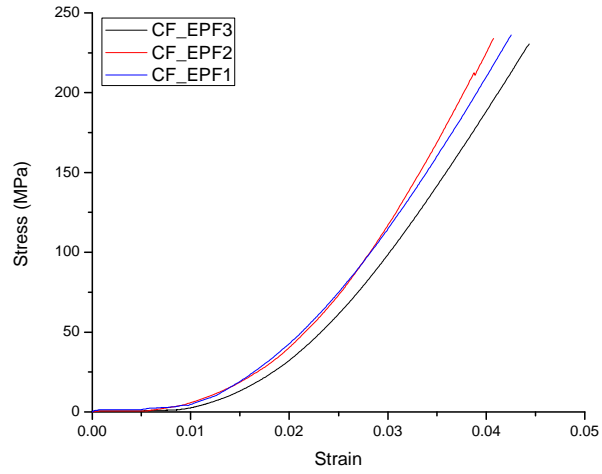


Figure 4.56 CFRP with Epoxy Foamed Interlayer Tensile Testing

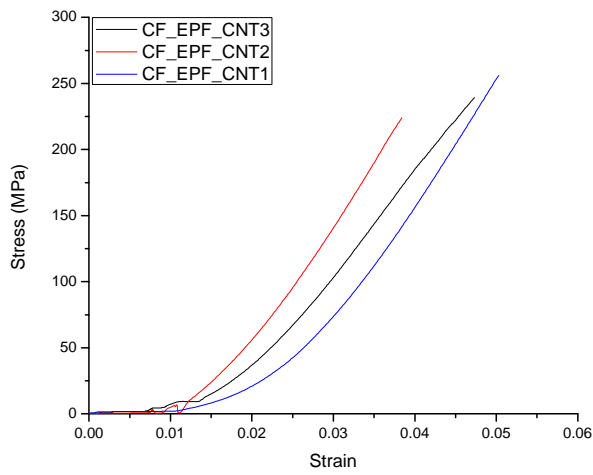


Figure 4.57 CNT Reinforced Epoxy Foamed Interlayer CFRP Tensile Testing

There is no significant tensile strength increase from the control to the CFRP with epoxy foamed interlayer and to the CFRP with CNT epoxy foamed interlayer. The following Table 4.26

summarizes the values deriving for the epoxy foamed samples when tested in tensile testing experiments.

Table 4.26 Epoxy Foamed Interlayer CFRP Tensile Testing Summary

	Tensile Strength (MPa)	Tensile Modulus (GPa)
Control CFRP	238±5.3	9.83±2.6
CFRP+EP.FOAM	233.6±2.8	10.1±1.2
CFRP+EP.FOAM+CNT	233.3±8.2	8.83±0.8

It can be seen that there is no significant increase of tensile strength from control to epoxy foamed samples as the values of the tensile strength remain constant or slightly drop. However, the drop is within the standard deviation limit. This indicates that the foamed interlayer does not contribute; nevertheless, it does not deteriorate as well to the tensile improvement. Similar is the behavior of the tensile strength from the epoxy foamed to the CNT epoxy foamed samples, where there is almost no change at all. As a result the CNT reinforcement contributes to the, flexural strength, stiffness, and Mode II fracture toughness improvement but not to higher tensile strength. This is quite explainable by the fact that fibers are dominant in the axial load transfer mechanisms, which are present in tensile testing.

4.5.5.3 Fracture Toughness

At this point, working on the same way that Mode II flexural testing was performed in section 4.3.2 for the micro-spheres reinforced interlayer, Mode II fracture toughness is calculated and compared for the three kinds of samples in order to evaluate Mode II fracture toughness improvement of the CNT reinforced epoxy foamed interlayer system. The Mode II fracture toughness evaluation is done through equation 41 for calculating G_{IIC} (energy release rate) and is presented in Table 4.27.

Table 4.27 Mode II Fracture Toughness Evaluation of Epoxy Foamed Interlayer CFRP

	Control CFRP (C1)	CFRP with Epoxy Foamed Interlayer (C2)	CFRP with CNT reinforced Epoxy Foamed Interlayer (C3)
Elasticity Modulus (GPa)	9.8	10	8.8
Moment of Inertia (m ⁴)	$1.43 \cdot 10^{-12} \pm 1.24 \cdot 10^{-13}$	$1.99 \cdot 10^{-12} \pm 4.62 \cdot 10^{-14}$	$7.3 \cdot 10^{-12} \pm 5.81 \cdot 10^{-13}$
Stiffness (N*m)	0.1±0.01	0.153±0.004	0.494 ±0.04
Compliance (1/S)	9.34±0.84	6.54±0.153	2.03±0.16
Flex Max Load (N)	16.13±2.0133	31.5±2.413	84.075±14.776
G_{IIC} (J/m ²)	334±55	747.24±134.72	1629.52±588.6

Complementary to Table 4.27, Figure 4.58 and Figure 4.59 present the stiffness and the Mode II energy release rate respectively.

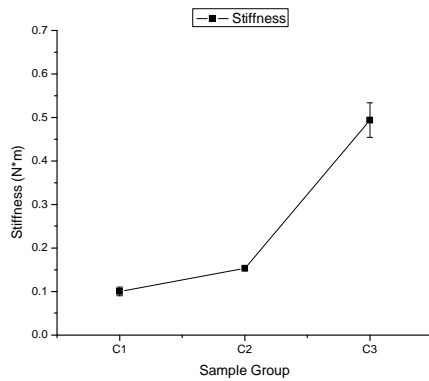


Figure 4.58 Stiffness Improvement of Epoxy Foamed Interlayer

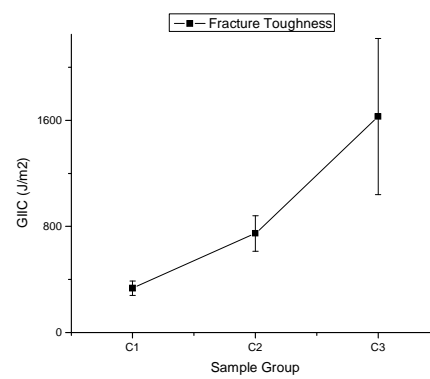


Figure 4.59 Mode II Fracture Toughness Improvement of Epoxy Foamed Interlayer

4.5.6 SEM for Interlayer Micro-Characterization

Figure 4.60 presents the fracture surface of control CFRP samples after a flexural test was performed.

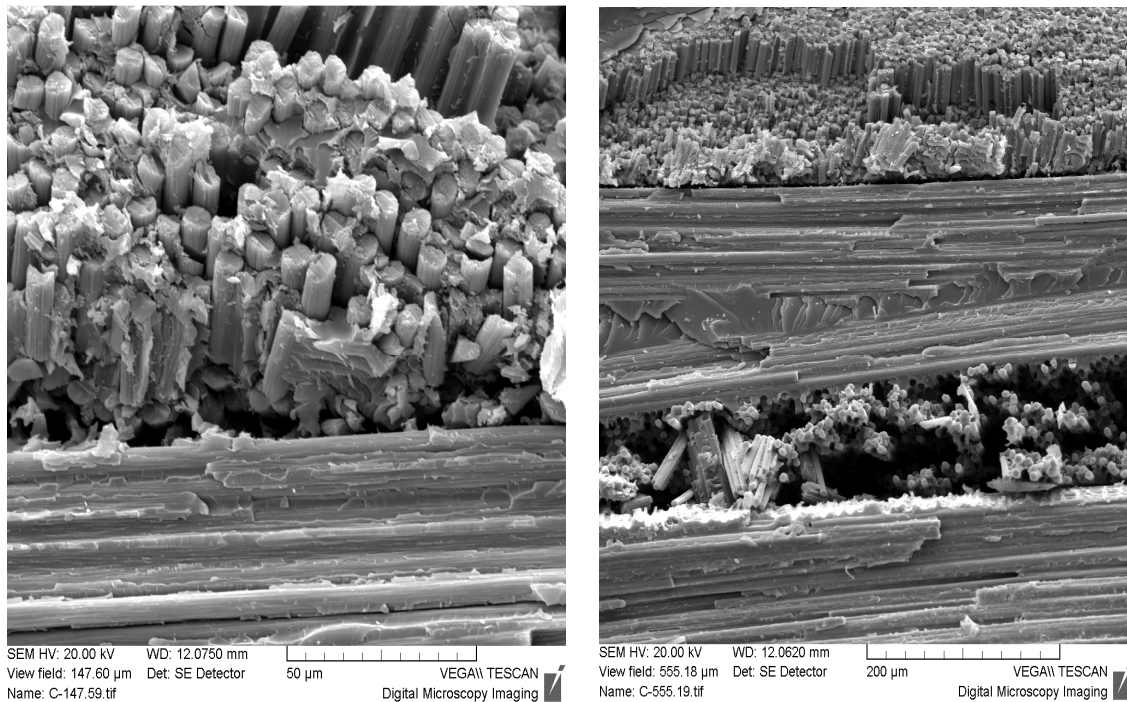
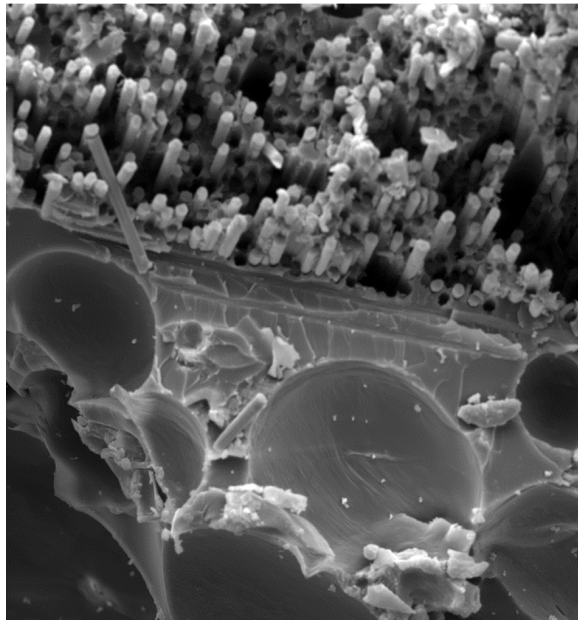


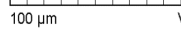
Figure 4.60 (SEM) Control CFRP Fracture Surface at SEM

Next, epoxy foam interlayers are seen distinctly between the CFRP layers in Figure 4.61. The epoxy foamed interlayer is nicely fitted within the CFRP layers. The interlayer width does not exceed the 200µm.

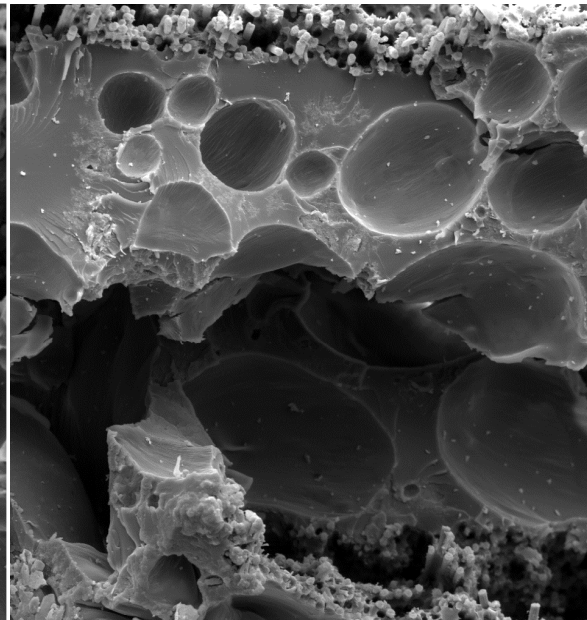
In Figure 4.62, up and left is a picture of a sample that has been delaminated after fracture. Thus the interlayer plane is seen. Within the pores, there are some spots – not the dust – within the epoxy foam voids which are observed only in samples that contain CNT, and they potentially are CNT agglomerates (Up-Right and Down-Left pictures). CNT themselves cannot be clearly seen as the SEM utilized for the characterization of this material is not capable of going to magnifications below few µm.



SEM HV: 20.00 kV WD: 14.1280 mm
View field: 357.97 μ m Det: SE Detector
Name: CF-357.96.tif



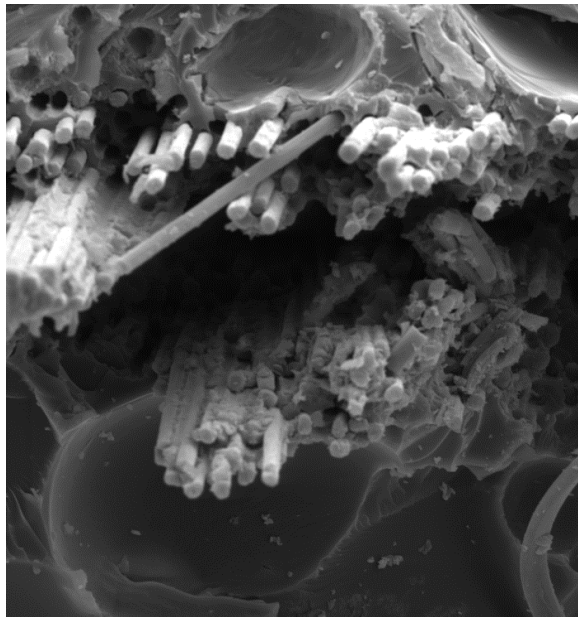
VEGA\\ TESCAN
Digital Microscopy Imaging



SEM HV: 20.00 kV WD: 14.0960 mm
View field: 528.94 μ m Det: SE Detector
Name: CF-528.94.tif



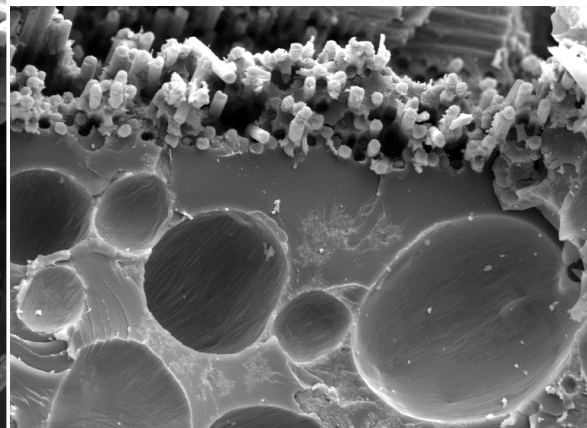
VEGA\\ TESCAN
Digital Microscopy Imaging



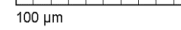
SEM HV: 20.00 kV WD: 15.7040 mm
View field: 243.51 μ m Det: SE Detector
Name: CF-243.51.tif



VEGA\\ TESCAN
Digital Microscopy Imaging



SEM HV: 20.00 kV WD: 14.0960 mm
View field: 349.58 μ m Det: SE Detector
Name: CF-349.6.tif



VEGA\\ TESCAN
Digital Microscopy Imaging

Figure 4.61 (SEM) Epoxy Foamed Interlayer within Carbon Fiber Plies

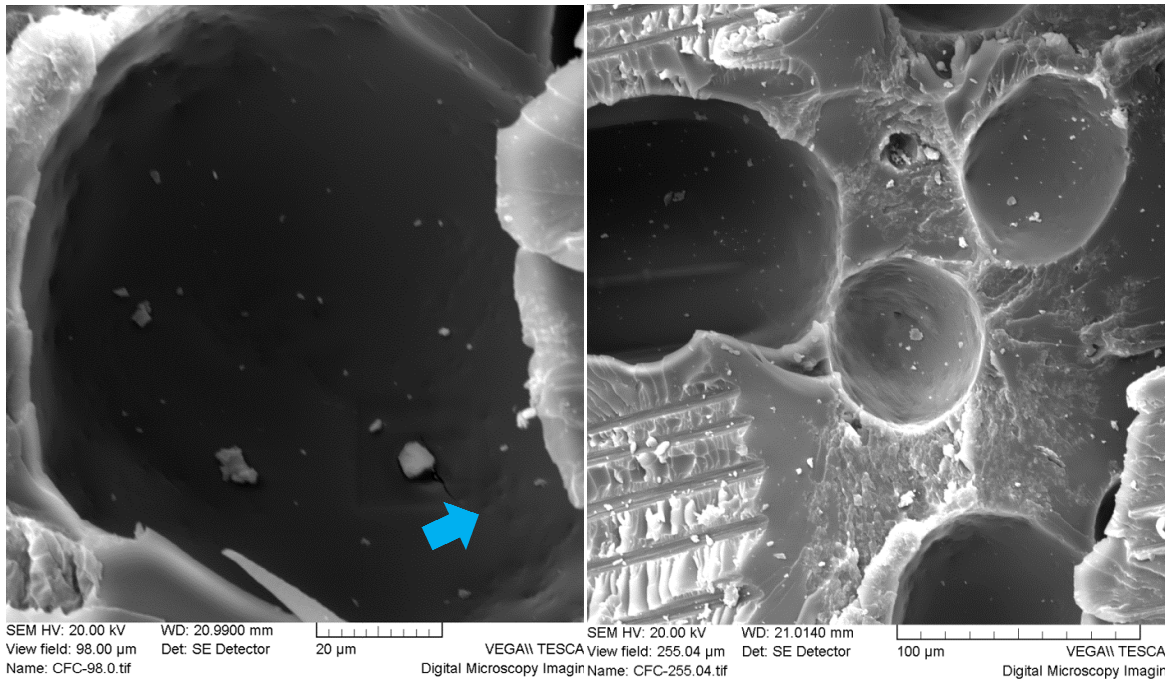
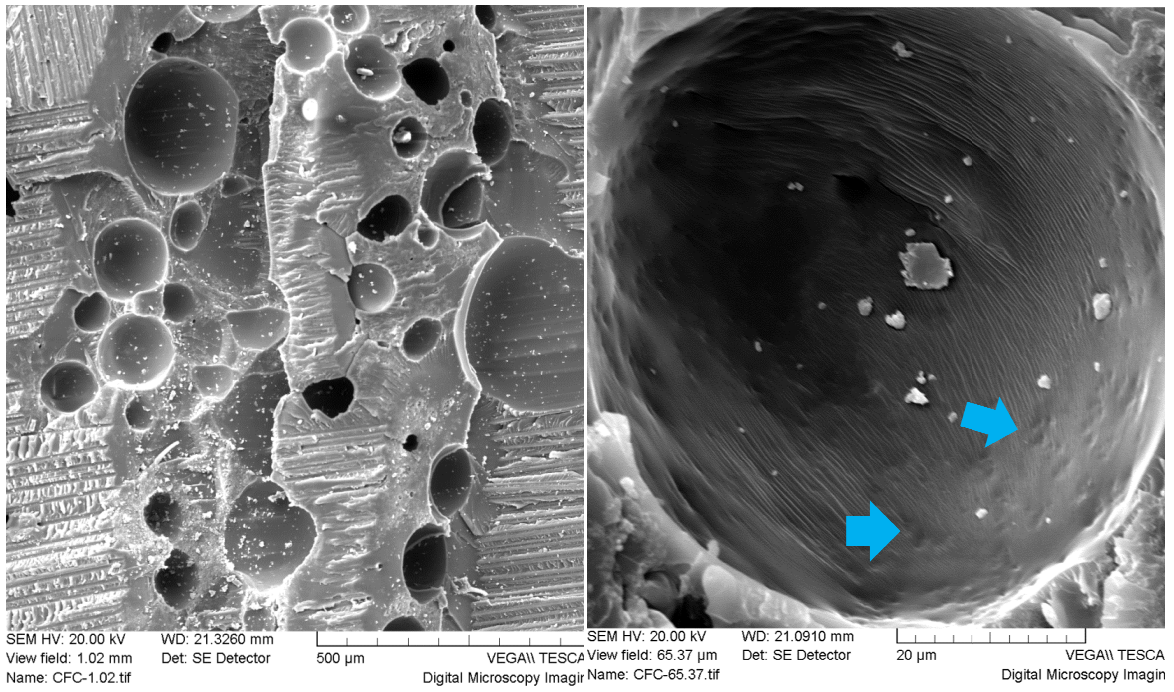


Figure 4.62 (SEM) CNT Reinforced Epoxy Foamed Interlayer within Carbon Fiber Plies

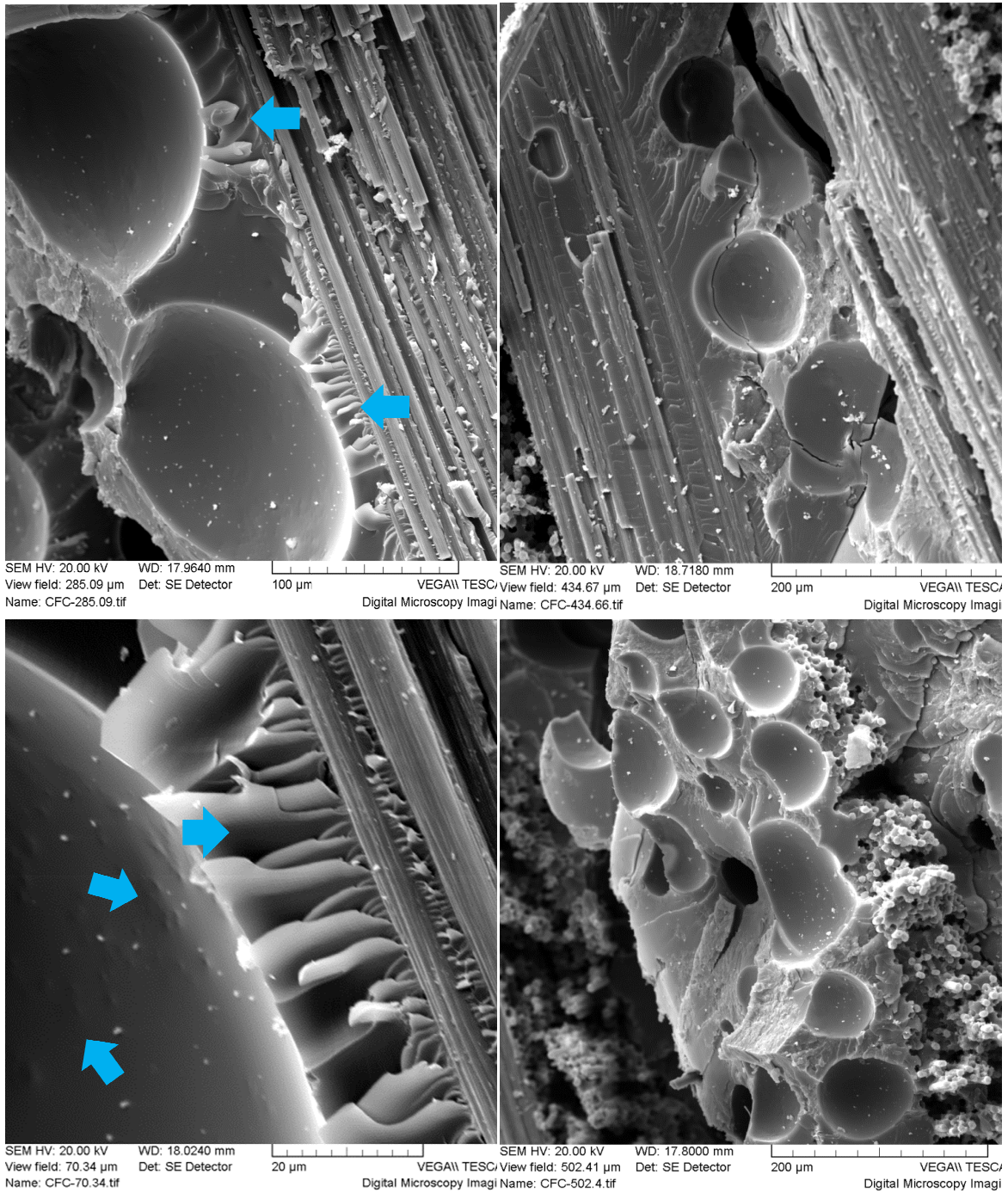


Figure 4.63 (SEM) CNT Reinforced Epoxy Foamed Interlayer within Carbon Fiber Plies

Figure 4.63 presents the CNT reinforced epoxy foamed interlayer from a lower magnification, thus the interlayer region is clearly observed on the right pictures of Figure 4.63.

As in Figure 4.62, the pores observed in the interlayer, which contains CNT, present high concentration of some spots, which probably are CNT agglomerates. Additionally, to the left of Figure 4.63, there is low and high magnification of the area which seems to be the interface between the epoxy foam interlayer and the carbon fiber bed. Hackle formation as described in section 2.5 is seen in both left pictures of Figure 4.63 in low and high magnification.

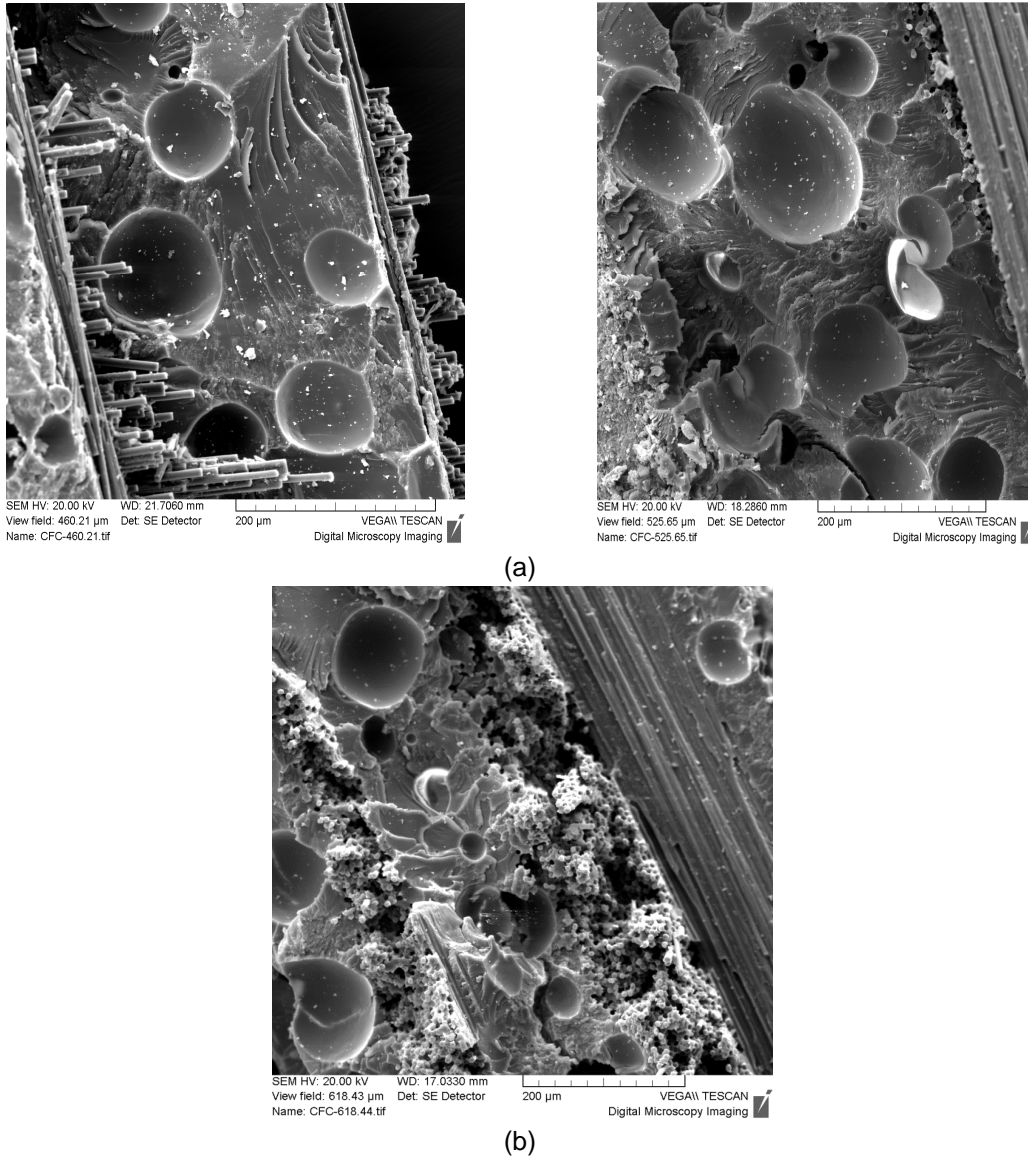


Figure 4.64 (SEM) (a) and (b): CNT Reinforced Epoxy Foamed Interlayer within Carbon Fiber Plies

Finally, by examining the plane of the multilayer structure (Figure 4.64), the fiber beds and the foamed interlayers can be seen. The high concentration of the previously mentioned spots is again observed. This behavior is in agreement with the theory that CNT while foaming tends to develop on the pores surface.

4.5.7 Parametrical Prediction of Strength

In this section an effort is made to predict the material flexural strength through given properties of the material such as flexural modulus and glass transition temperature, through the tension strength which can be easily measured and through the interlayer improvement. The latter can be translated as Mode II fracture toughness energy release rate. As a result a linear regression model will be constructed with its variable presented in Table 4.28.

Table 4.28 Variables – Epoxy Foamed Interlayer CFRP for Regression Analysis

Response Variable (y)	Flexural Strength (MPa)
Predictor Variable (x1)	Flexural Modulus (GPa)
Predictor Variable (x2)	Tension Strength (MPa)
Predictor Variable (x3)	Glass Transition Temperature ($^{\circ}$ C), through $\tan\delta$
Predictor Variable (x4)	Mode II energy-release rate (J/m^2) [Interlayer Improvement]

Next, the Pearson pairwise correlations followed by a scatter plot matrix of the variables from Table 4.28 are presented (Table 4.29, and Figure 4.65)

Table 4.29 Pearson Correlation Matrix – Epoxy Foamed Interlayer CFRP

	Flexural Strength (MPa)	Flexural Modulus (GPa)	Tension Strength (MPa)	Glass Transition Temperature ($^{\circ}$ C)	Mode II energy-release rate (J/m^2) [Interlayer Improvement]
Flexural Strength	1	0.89413	0.26501	-0.21767	0.91499
Flexural Modulus (GPa)	0.89413	1	0.16	-0.08788	0.68853
Tension Strength (MPa)	0.26501	0.16	1	-0.07607	0.36428
Glass Transition Temperature ($^{\circ}$ C)	-0.21767	-0.08788	-0.07607	1	-0.36107

Mode II energy-release rate (J/m ²) [Interlayer Improvement]	0.91499	0.68853	0.36428	-0.36107	1
--	---------	---------	---------	----------	---

In Table 4.29 and Figure 4.65, it can be seen that there is good correlation between the flexural strength with flexural modulus and interlayer improvement as expected. Regarding the other two predictor variables, first it has not been investigated how the glass transition temperature (T_g) behaves with the flexural modulus. Nevertheless, depending on the manufacturing process and the material physics, T_g was expected to increase when constant pressure is applied, to decrease when pressure is increased due to the residual internal stresses, and again to decrease when an interlayer of lower crosslinking content is added within the plies. Specifically in this material with the epoxy foamed interlayer, although the pressure is constant while manufacturing, it is expected to have the T_g decreasing, while the flexural strength is increasing. Apparently, flexural strength increase means larger amount of epoxy foam into the interlayer, which has a much lower content of crosslinking, and less epoxy resin into the entire composite. The value of -0.21767 demonstrates a small drop of T_g as flexural strength is increased, however this is not highly correlated. Moreover, tensile strength is expected to have an increase with the flexural strength increase; however this increase is not too high as their correlation is only 0.26501.

Furthermore, the nonzero correlations between the predictor variables indicate the presence of multicollinearity. However, concern would have been raised only for high correlations (above 0.7). High multicollinearity can result in high variance (low precision) in the estimated coefficients. There are no such high values of correlation that could have possibly demonstrated high multicollinearity. However, this matter will be examined later through the variance inflation diagnostics.

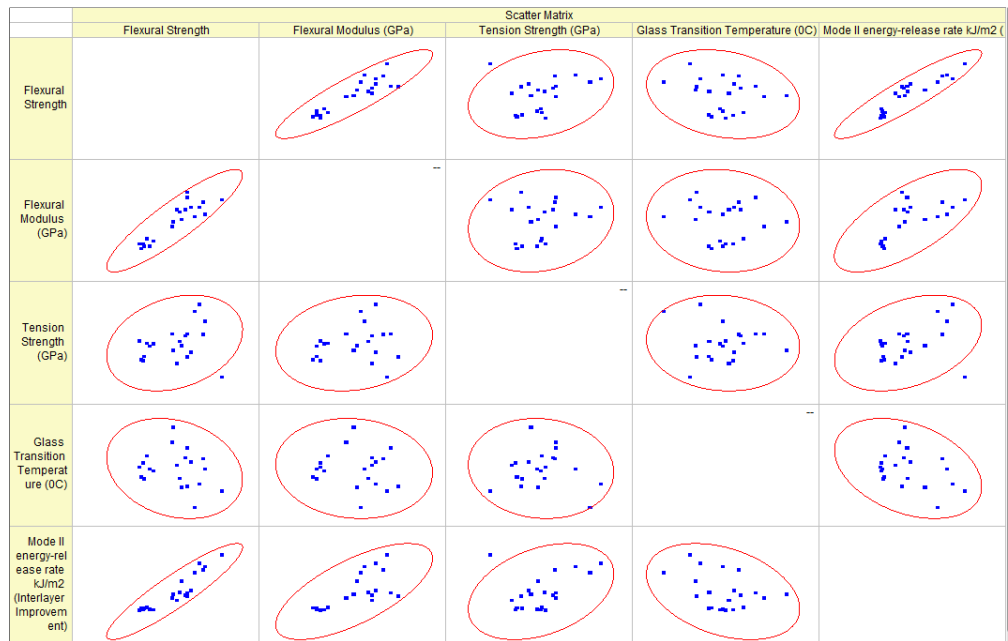


Figure 4.65 Scatter Plot of Epoxy Foamed Interlayer CFRP

Table 4.30i Flexural Strength Model Data of Epoxy Foamed Interlayer CFRP

Flexural Strength (MPa)	Flexural Modulus (GPa)	Tension Strength (MPa)	Glass Transition Temperature (°C)	Mode II energy-release rate (J/m ²) [Interlayer Improvement]
190.5	26	241.6	55.4	292.4
198.3	26	231.9	56.1	300.2
207.6	28	240.5	57.2	389.3
201.2	25	234.1	53.6	344.6
194.3	24	232.5	53.9	361.4
220.95	27	240.1	54.8	313.2
212.4	25	239	55.1	321.7
302	41	236.2	56.2	929.5
292.6	47	233.9	52.4	756.7
271.2	40	230.7	55.7	614.4
260.55	33	245	59.3	688.3
263.1	35	237	61.6	811.4
288.6	40	244.2	56.9	783.1
294.2	45	245	58.4	861.2

Table 4.31ii Flexural Strength Model Data (Continuation) of Epoxy Foamed Interlayer CFRP

Flexural Strength (MPa)	Flexural Modulus (GPa)	Tension Strength (MPa)	Glass Transition Temperature (°C)	Mode II energy-release rate (J/m ²) [Interlayer Improvement]
308.6	37	256	49.1	1521.3
368.2	44	224	51.7	2100.3
281.6	36	239.4	52.3	1243.3
277	39	241.3	53.7	871
319	41	259.5	52.8	1834.6
331	38	251.2	55.1	1721.2
328.1	43	244.7	56.7	1610.4

Table 4.30 presents the data used for the preliminary fitted model. Utilizing origin lab software, version 8, (138) the linear regression analysis is done. Following, Table 4.32 gives the parameters and Table 4.33 the ANOVA Table of the preliminary fitted model. Table 4.34 gives additional information for the regression of the preliminary fitted model.

Table 4.32 Parameters of the Preliminary Fitted Model – Epoxy Foam Interlayer CFRP

	Value	Standard Error	t-Value	Prob> t	Variance Inflation
Flexural Strength	101.72656	79.65767	1.27705	0.21981	0
X1-Flexural Modulus (GPa)	3.35608	0.41745	8.03949	5.20193E-7	2.064836
X2-Tension Strength (GPa)	-0.19147	0.28406	-0.67406	0.5099	1.185958
X3-Glass Transition Temperature (°C)	0.78578	0.86763	0.90566	0.37855	1.230951
X4-Mode II energy-release rate (J/m ²) [Interlayer Improvement]	0.05612	0.00629	8.92065	1.31293E-7	2.646903

Table 4.33 ANOVA Table – Epoxy Foam Interlayer CFRP

	DF	Sum of Squares	Mean Square	F Value	Prob>F
Model	4	53256.37305	13314.09326	138.37856	3.4055E-12
Error	16	1539.44004	96.215		
Total	20	54795.8131			

Table 4.34 Other Parameters of the Preliminary Model Regression – Epoxy Foam Interlayer CFRP

Number of Points	21
Degrees of Freedom	16
Residual Sum of Squares	1539.44004
R Square	0.97191
Adj. R Square	0.96488
Root MSE	9.80892

Through the analysis, it can be seen that the regression is significant since the p-value for the F-test on the regression is much smaller than a significance level of $\alpha = 0.1$. Furthermore, the high R^2 value shows that 97% of the variability in flexural strength is explained by this current model. Finally, the calculated variance inflation gives acceptable values for all predictor variables, which means that there is no high multicollinearity. However, alternative models will be explored as some of the current predictor variables may not be needed to the analysis.

Additional to the above tables, Figure 4.66 contains several figures with information about the residuals of the model. Residuals are plotted versus each predictor variable and versus the fitted values obtained from the current model. A normal probability plot of the residuals is presented to assess the probability distribution of the residuals. Finally, in the bottom plot the residuals over the time order are plotted.

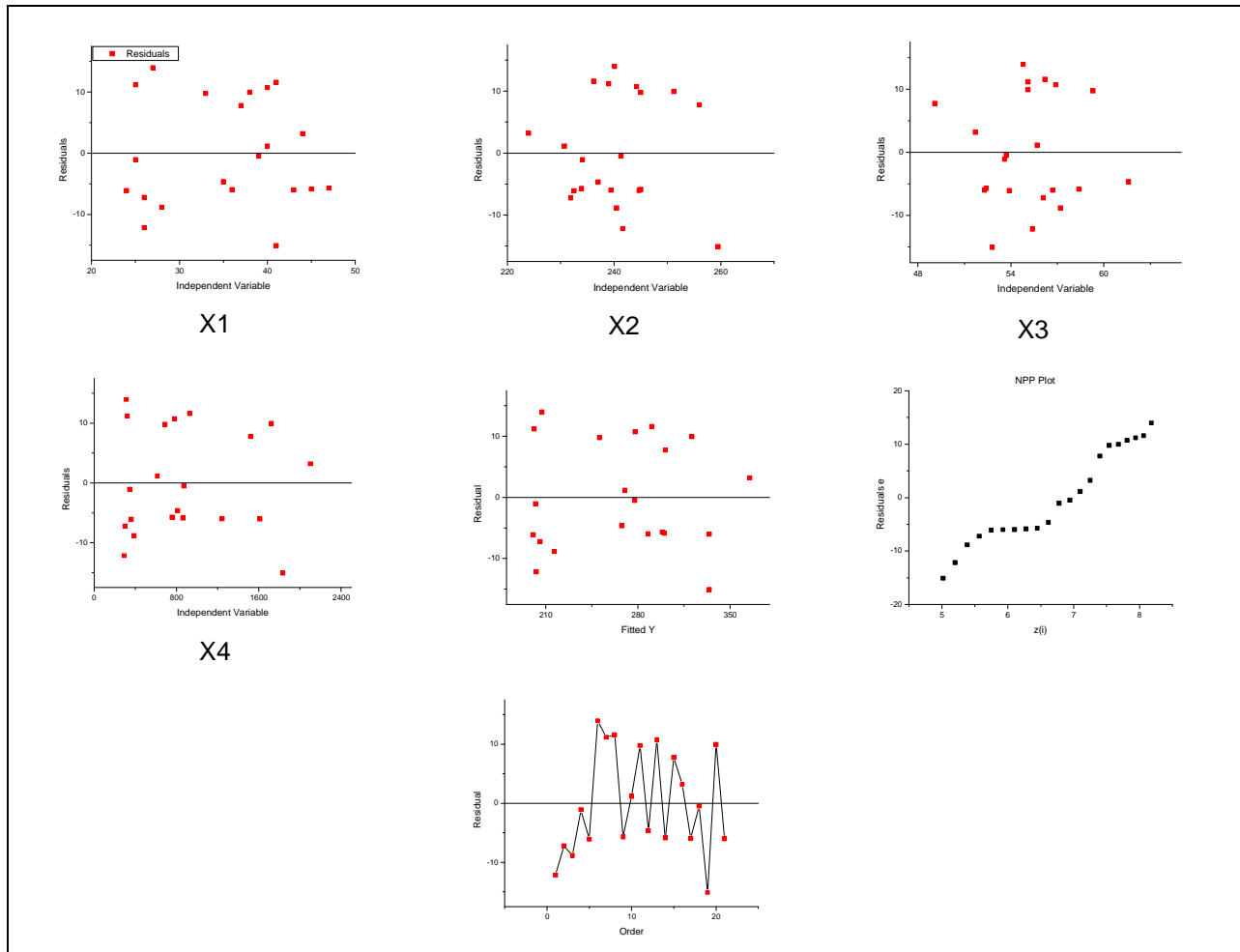


Figure 4.66 Residuals Analysis for Epoxy Foamed Interlayer CFRP Model

Before going into the interpretation of the residual analysis, the model assumptions have to be clearly stated.

Assumptions:

Model Assumptions:

1. *MLR model form is reasonable.*
2. *Residuals have constant variance.*
3. *Residuals are normally distributed.*
4. *Residuals are uncorrelated.*

Based on the analysis so far, the preliminary current model is:

$$\hat{y} = 101.72656 + 3.35608 \cdot x_1 - 0.19147 \cdot x_2 + 0.78578 \cdot x_3 + 0.05612 \cdot x_4$$

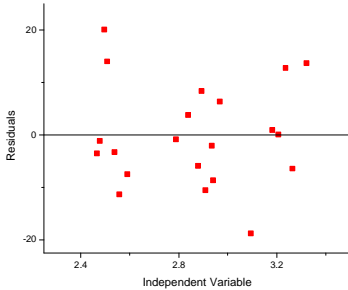
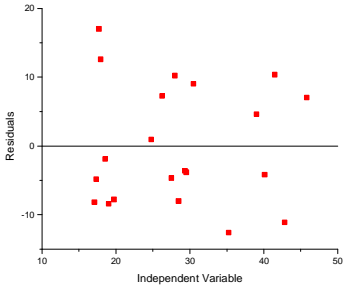
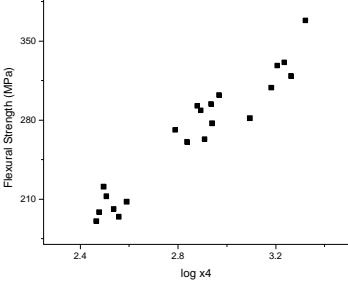
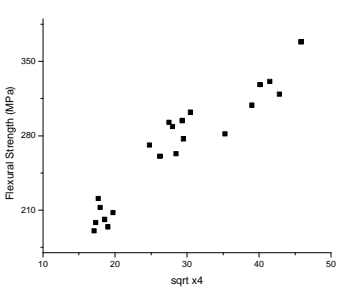
Where variable \hat{y} , is the fitted flexural modulus, and x_1, x_2, x_3, x_4 are defined in Table 4.28.

Regarding the first model assumption, the graphs of Figure 4.66 plotting the residuals over the predictor variables should not present curvature. As it can be seen within Figure 4.66 there is no curvature within most of the plots of residuals over the predictor variables apart from the residuals vs. interlayer improvement (x_4), where a curvature can be seen. As a result, an action of transformation has to be taken. Taking a closer look to the flexural strength vs. interlayer improvement curve from Figure 4.65, a compression of high interlayer improvement values is advisable and this can be achieved through transforming x_4 to square root of x_4 or to logarithm of x_4 . Both transformations are evaluated in Table 4.35. Evaluation is done on a comparison between models a, and b:

Model a: $y, x_1, x_2, x_3, \log(x_4)$

Model b: $y, x_1, x_2, x_3, \text{sqrt}(x_4)$

Table 4.35 Transformations Evaluations for Interlayer Improvement (x4 of the preliminary fitted model)

Model	a	b
Transformation	Logarithm of x4	Square Root of x4
R^2	0.965	0.973
r_{yx}	0.96	0.94
r_{xx}	X1: -0.82657 X2: -0.44217 X3: 0.32697	X1: -0.77356 X2: -0.40972 X3: 0.38792
e vs. transformed (x4)		
y vs. transformed (x4)		

The use of either transformation in the preliminary model does not affect the percentage of variability explanation in flexural strength. P-values of both transformations when used in the preliminary model are significant for $\alpha = 0.1$. Furthermore, both transformations present a high correlation with response variable, flexural strength. However, they also present a high correlation with flexural modulus predictor variable and as a result there may be a high multicollinearity issue. The logarithm transformation presents higher correlation with flexural modulus than the square root. In addition, by comparing the residuals vs. the transformed interlayer improvement each time, both transformations present no curvature, however, when

the flexural strength (y) vs. the transformed interlayer improvement is compared, the square root presents a curvature, thus the logarithmic transformation, which does not present such a curvature in the y vs. $\log(x^4)$ curve, is preferred over the square root transformation of the interlayer improvement predictor variable

Having replaced the x4 column from Table 4.30 with the logarithmic transformation of x4 and utilizing origin lab software, version 8, (138) the linear regression analysis is done. Following, Table 4.36 gives the parameters and Table 4.37 the ANOVA Table of the updated preliminary fitted model. Table 4.38 gives additional information for the regression of the updated preliminary fitted model.

Table 4.36 Parameters of Preliminary Fitted Model Using Transformation

	Value	Standard Error	t-Value	Prob> t	Variance Inflation
Flexural Strength	-83.73584	88.93436	-0.94155	0.36042	
X1-Flexural Modulus (GPa)	2.21481	0.5833	3.79706	0.00158	3.259
X2-Tension Strength (GPa)	-0.4099	0.32828	-1.24863	0.22976	1.281
X3-Glass Transition Temperature ($^{\circ}$ C)	-0.11052	0.92567	-0.11939	0.90645	1.133
Log(X4)-[Interlayer Improvement]	131.93013	16.85316	7.82821	7.34083E-7	3.955

Table 4.37 ANOVA Table of Preliminary Fitted Model Using Transformation

	DF	Sum of Squares	Mean Square	F Value	Prob>F
Model	4	52891.89408	13222.97352	111.12215	1.8528E-11
Error	16	1903.91901	118.99494		
Total	20	54795.8131			

Table 4.38 Other Parameters of Preliminary Fitted Model Using Transformation

Number of Points	21
Degrees of Freedom	16
Residual Sum of Squares	1903.91901
R Square	0.96525
Adj. R Square	0.95657
Root MSE	10.90848

Through the analysis, it can be seen that the regression is significant since the p-value for the F-test on the regression is much smaller than a significance level of $\alpha = 0.1$. Furthermore, the high R^2 value shows that 96.5% of the variability in flexural strength is explained by this current model. Finally, the calculated variance inflation gives acceptable values for all predictor variables, which means that there is no high multicollinearity. However, alternative models will be explored as some of the current predictor variables may not be needed to the analysis. This can be seen by the fact that not all p-values are significant for $\alpha = 0.1$.

Additional to the above tables, Figure 4.67 contains several figures with information about the residuals of the model. Residuals are plotted versus each predictor variable and versus the fitted values obtained from the current model. A normal probability plot of the residuals is presented to assess the probability distribution of the residuals. Finally, in the bottom plot the residuals over the time order are plotted.

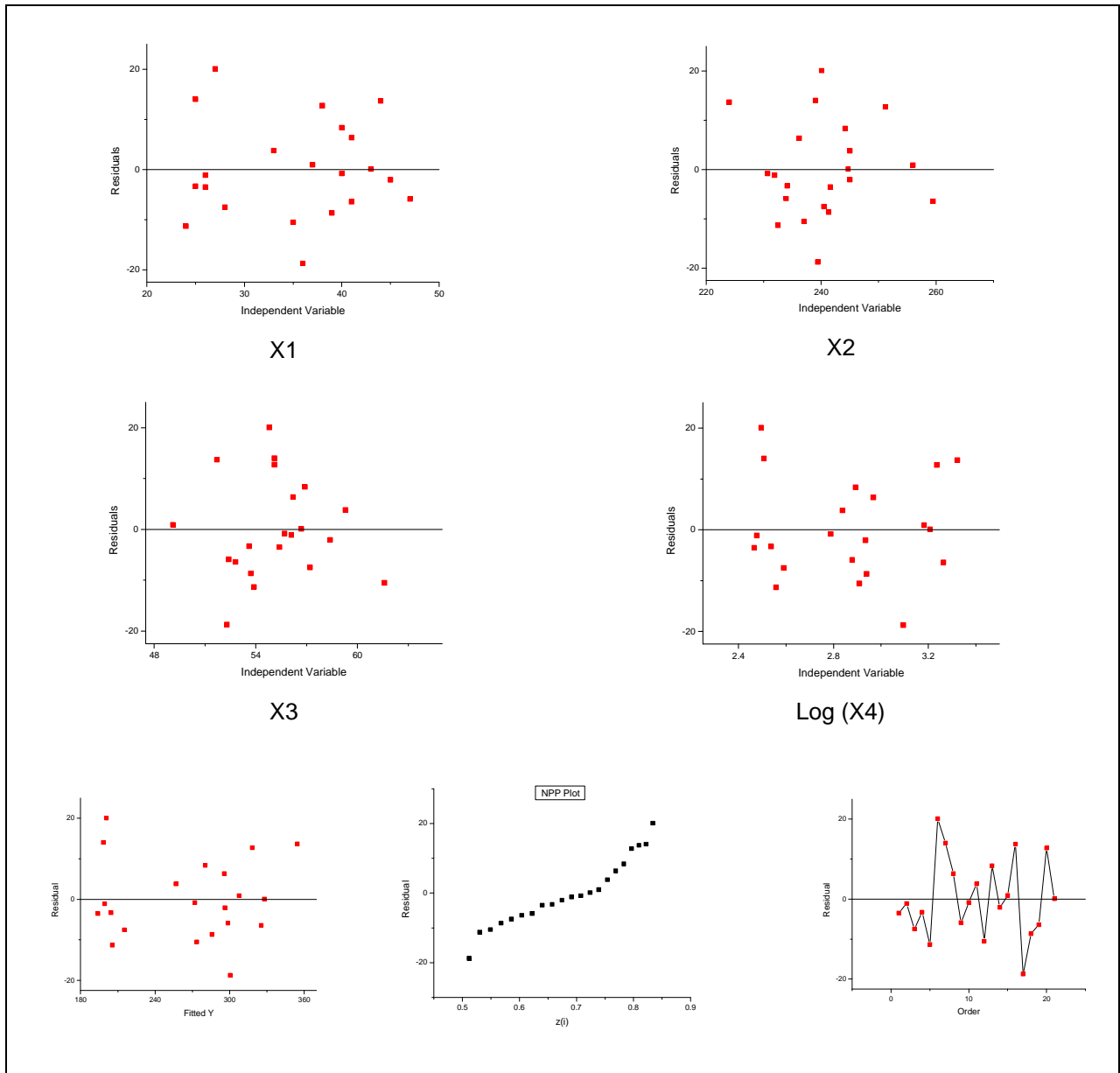


Figure 4.67 Residuals Analysis for Epoxy Foamed Interlayer CFRP Model with transformation

The next step is to check if the assumptions for the model are fulfilled. Regarding the first model assumption, the graphs of Figure 4.67 plotting the residuals over the predictor variables should not present curvature. As it can be seen within Figure 4.67 there is no

curvature within the plots of residuals over the predictor variables, as a result the first assumption is reasonable.

The second assumption is that the residuals have constant variance. This can be seen from the residuals versus the fitted values. In this case there is no funnel shape so the residuals must have constant variance. However, there is a constant variance test (Levene's test Figure 4.68) that will be performed to assure the constant variance of residuals.

Yhat	ei	Rank	e1i	e2i	d1i	d2i	
194.03092	-3.53092	8	-18.75449	-0.81704	11.55397455	8.737607	
199.43801	-1.13801	11	-11.33618	0.07722	4.135664545	7.843347	
215.11235	-7.51235	5	-10.54358	0.91921	3.343064545	7.001357	
204.50093	-3.30093	9	-8.67455	3.78842	1.474034545	4.132147	
205.63618	-11.33618	2	-7.51235	6.35708	0.311834545	1.563487	
200.86427	20.08573	21	-6.42588	8.34831	0.774634545	0.427743	
198.38664	14.01336	20	-5.90977	12.72634	1.290745455	4.805773	
295.64292	6.35708	16	-3.53092	13.70704	3.669595455	5.786473	
298.50977	-5.90977	7	-3.30093	14.01336	3.899585455	6.092793	
272.01704	-0.81704	12	-2.07901	20.08573	5.121505455	12.165163	
256.76158	3.78842	15	-1.13801		6.062505455		
273.64358	-10.54358	3					
280.25169	8.34831	17					
296.27901	-2.07901	10					
307.68079	0.91921	14					
354.49296	13.70704	19					
300.35449	-18.75449	1					
285.67455	-8.67455	4					
325.42588	-6.42588	6					
318.27366	12.72634	18					
328.02278	0.07722	13					
			Avg	Avg	Avg	Avg	
			-7.200515455	7.920567	3.785195041	5.855589	
					(d1i-d(avg)1)^2	(d2i-d(avg)2)^2	
					60.35393498	8.306027752	
					0.122828873	3.951181867	
					0.195479375	1.31278431	
					5.341462838	2.970252327	
					12.06423313	18.42213958	
					9.063469026	29.4615122	
					6.222278741	1.102113634	
					0.013363264	0.004777021	
					0.013085167	0.056265738	
					1.78572552	39.81072406	
					5.186142718		
					Sum	100.3620036	105.3977785
						s^2	9.798084863
						t*	1.478997349

Figure 4.68 Microsoft XL(139) Algorithm for Levene's Test

Hypothesis:

H_0 : Error Variance is Constant ($H_0 : \sigma_{d1} = \sigma_{d2}$)

H_1 : Error Variance is Not Constant ($H_1 : \sigma_{d1} \neq \sigma_{d2}$)

$$t^* = 1.479 < t(0.95;15) = 1.753$$

The t-test conducted with the t-value derived from Levene's test (Figure 4.68) fails to reject H_0 for $\alpha = 0.1$, thus, constant error variance is verified to be a reasonable assumption for $\alpha = 0.1$.

The normal probability plot within Figure 4.67 exhibits a mostly straight line with a curve at the left. This indicates that the distribution of the residuals is similar to a normal distribution, except that it has a longer left tail. However, normality is not a required assumption. A normality test will be performed to assess if normality is violated.

Hypothesis:

H_0 : Normality Reasonable

H_1 : Normality Violated

$$\rho = 0.965 > C(0.1, 21) = 0.9607$$

The test fails to reject H_0 , thus normality is not violated and assumption 3 is fulfilled as well.

Finally, the time plot in Figure 4.67 appears to show a random jagged pattern. This indicates that correlation over time is not a problem.

Diagnostics:

The variance inflation factors are kept in low values for all the predictor variables. More specifically, VIF_1 through VIF_4 do not inflate variance more than around 3.5 times and VIF_2 and VIF_3 more than 1.2. As a result, there is no significant issue of variance inflation and thus, high

multicollinearity. Following, Figure 4.69 and Figure 4.70 show the results from the outlier analysis as well as their influences. In Figure 4.69, the Bonferroni outlier test does not detect any y-outliers. However, observation 16 is detected as an x-outlier with not significant influence to both the fitted line and some of the parameters.

ihat	e	Standardized	Studentized	cookdi	hii	ti	dfitsi	x-outlier - hii	Bonferromi - ti	DFFITs	COOKDi
								2'p/n	t(1-.1/2(21),n-p-1)		
								0.476190476	3.4279		1
194.03092	-3.53092	-0.266312036	-0.292916	-0.1585	0.1734	-0.284380242	-0.13025	ok	ok	ok	ok
199.43801	-1.13801	-0.085831953	-0.093650339	-0.048119	0.16	-0.090702058	-0.03959	ok	ok	ok	ok
215.11235	-7.51235	-0.566602818	-0.603657744	-0.26553	0.119	-0.591265212	-0.2173	ok	ok	ok	ok
204.50093	-3.30093	-0.248965536	-0.274768949	-0.15153	0.179	-0.266675707	-0.12452	ok	ok	ok	ok
205.63618	-11.33618	-0.85500696	-0.963177971	-0.61577	0.212	-0.9608727	-0.49839	ok	ok	ok	ok
200.86427	20.08573	1.514922924	1.646169197	0.95119	0.1531	1.748876948	0.743585	ok	ok	ok	ok
198.38664	14.01336	1.056927495	1.14438111	0.59509	0.147	1.15638642	0.480051	ok	ok	ok	ok
295.64292	6.35708	0.479469067	0.506814552	0.20634	0.105	0.494711697	0.169448	ok	ok	ok	ok
298.50977	-5.90977	-0.445731674	-0.628477166	-0.7486	0.497	-0.616177994	-0.61249	x-outlier	ok	ok	ok
272.01704	-0.81704	-0.061623482	-0.068093285	-0.03774	0.181	-0.065941064	-0.031	ok	ok	ok	ok
256.76158	3.78842	0.285733419	0.318862367	0.1866	0.197	0.309725022	0.153409	ok	ok	ok	ok
273.64358	-10.54358	-0.795226812	-1.037939319	-1.0782	0.413	-1.040632686	-0.87288	ok	ok	ok	y-outlier
280.25169	8.34831	0.629653301	0.673512667	0.30662	0.126	0.661576282	0.251194	ok	ok	ok	ok
296.27901	-2.07901	-0.156804851	-0.188770858	-0.14721	0.31	-0.182981778	-0.12265	ok	ok	ok	ok
307.68079	0.91921	0.069329434	0.091668398	0.09348	0.428	0.088781493	0.076797	ok	ok	ok	ok
354.49296	13.70704	1.033823969	1.696709599	3.0327	0.62874	1.814138846	2.360842	x-outlier	ok	y-outlier	y-outlier
300.35449	-18.75449	-1.414517014	-1.551699655	-0.93334	0.169	-1.630090064	-0.73511	ok	ok	ok	ok
285.67455	-8.67455	-0.65425925	-0.682483437	-0.24312	0.081	-0.670650498	-0.1991	ok	ok	ok	ok
325.42588	-6.42588	-0.484658159	-0.595221711	-0.50765	0.337	-0.582813896	-0.41552	ok	ok	ok	ok
318.27366	12.72634	0.958856784	1.093858324	0.74362	0.23	1.101103698	0.601793	ok	ok	ok	ok
328.02278	0.07722	0.006824152	0.006354671	3.29E-03	0.16	0.006152935	0.002685	ok	ok	ok	ok

Figure 4.69 Outliers and Influence on Preliminary Model of Epoxy Foamed Interlayer CFRP

DFBETAS						Flag influence				
						1				
Intercept	Flexural Mod	Tension Str	Glass Tra	Mode II energy-release rate	x0	x1	x2	x3	x4	
-0.004265	-0.0063174	-0.062071	0.0259	0.080628	ok	ok	ok	ok	ok	
-0.019857	0.011494	0.017089	-0.003	0.0054901	ok	ok	ok	ok	ok	
0.061071	0.061389	-0.047632	-0.097	0.033548	ok	ok	ok	ok	ok	
-0.083702	0.056536	0.040417	0.0544	0.0026965	ok	ok	ok	ok	ok	
-0.32087	0.34391	0.25761	0.1327	-0.13123	ok	ok	ok	ok	ok	
0.17201	0.07453	0.28576	-0.272	-0.50222	ok	ok	ok	ok	ok	
0.099951	-0.16554	0.067499	-0.083	-0.12009	ok	ok	ok	ok	ok	
0.024337	0.073325	-0.075333	0.0539	-0.0030185	ok	ok	ok	ok	ok	
-0.35397	-0.64139	0.00496	0.3721	0.51271	ok	ok	ok	ok	ok	
-0.01857	-0.022439	0.015268	0.0019	0.015861	ok	ok	ok	ok	ok	
-0.13038	-0.054838	0.037379	0.1496	0.048873	ok	ok	ok	ok	ok	
0.46557	3.84E-01	0.31514	-0.981	-0.51781	ok	ok	ok	ok	ok	
-0.12635	0.18363	0.13217	0.0836	-0.1407	ok	ok	ok	ok	ok	
0.05985	-0.10769	-0.056932	-0.048	0.076882	ok	ok	ok	ok	ok	
-0.0075118	-0.0089451	0.046417	-0.059	0.0060208	ok	ok	ok	ok	ok	
1.7276	-0.74472	-2.4714	-0.466	1.7101	FLAG	ok	FLAG	ok	FLAG	
-0.28422	0.47723	0.35166	0.2955	-0.59197	ok	ok	ok	ok	ok	
-0.054762	-0.11717	-0.03701	0.1125	0.083198	ok	ok	ok	ok	ok	
0.27509	-0.0049652	-0.35653	0.1039	-0.041193	ok	ok	ok	ok	ok	
-0.43266	-0.36654	0.17537	0.1895	0.48338	ok	ok	ok	ok	ok	
-0.0016542	-0.0001566	1.25E-05	0.0016	0.0014493	ok	ok	ok	ok	ok	

Figure 4.70 Influence on parameters of on Preliminary Model of Epoxy Foamed Interlayer CFRP

5.5.7.1 Interactions Analysis and Best Model Exploration

Interactions between the predictor variables are investigated to allow for modeling more complex relationships. Following, interactions x_1x_2 , $x_1\log(x_4)$, and $x_2\log(x_4)$ are presented in Figure 4.71 as they are the ones that they present some trend which can possibly benefit the model. For each interaction the residuals are plotted against the interactions, the standardized interactions and the residuals of the interaction when regressed on all predictor variables in order to demonstrate the slight trends.

In Figure 4.71, residuals are also plotted against the standardized forms of the interactions. These standardized variables are calculated by first centering the mean of predictor variables to zero and then by scaling the variance to one. Now the values approximately lie in $(-1, 1)$. Centering the predictor variables is of significant importance for multiplying them afterwards as interactions. Scaling the variance is important as well, for numerical stability. As a result, the standardized forms assist in overcoming high multicollinearity that the non standardized interactions present.

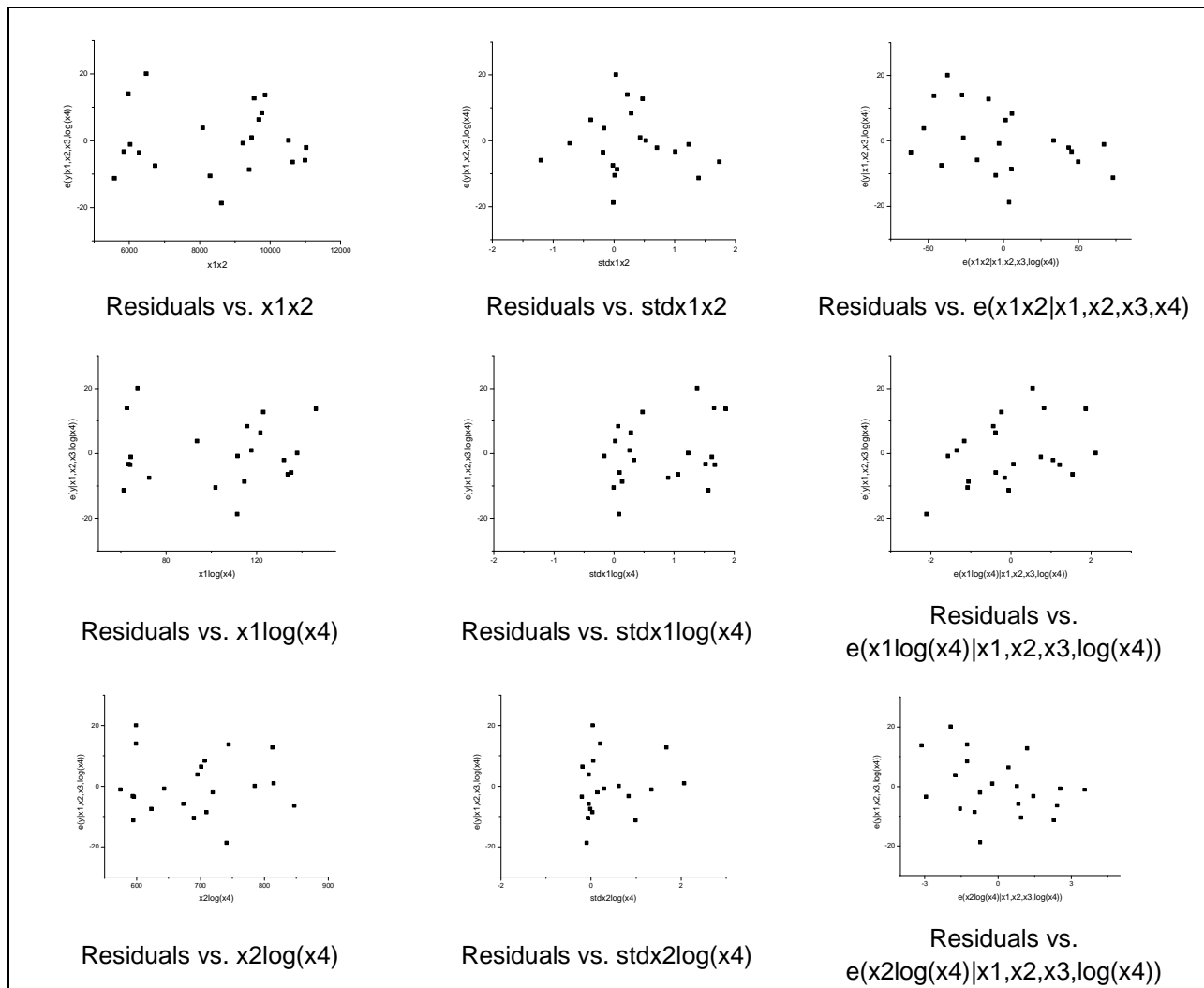


Figure 4.71 Interactions of Epoxy Foamed Interlayer CFRP Preliminary Model

Complementing the interactions graphs is the correlation matrix in Figure 4.72, which includes all variables and interactions. It seems that the interactions are highly correlated (above 0.7) with two of the predictor variables and all the other interactions. This is a common phenomenon because interaction terms are composed from the original predictors. To overcome this high multicollinearity, the standardized form is employed. Figure 4.73 shows the correlation with the standardized interactions, where it can be seen that standardized interactions overall have lower correlation with the other predictor variables.

	y	x1	x2	x3	log(x4)	x1x2	x1log(x4)	x2log(x4)
y	1	0.89413	0.26501	-0.21767	0.95911	0.8995	0.96113	0.88047
x1	0.89413	1	0.16	-0.08788	0.80598	0.98451	0.97699	0.71957
x2	0.26501	0.16	1	-0.07607	0.385	0.32929	0.23555	0.64081
x3	-0.21767	-0.08788	-0.07607	1	-0.26008	-0.09476	-0.16469	-0.24599
log(x4)	0.95911	0.80598	0.385	-0.26008	1	0.83759	0.91108	0.95491
x1x2	0.8995	0.98451	0.32929	-0.09476	0.83759	1	0.97555	0.80058
x1log(x4)	0.96113	0.97699	0.23555	-0.16469	0.91108	0.97555	1	0.83173
x2log(x4)	0.88047	0.71957	0.64081	-0.24599	0.95491	0.80058	0.83173	1

Figure 4.72 Pearson Correlation with Predictor Variables and Interactions – Epoxy Foamed Interlayer CFRP

	y	x1	x2	x3	log(x4)	x1x2	x1log(x4)	x2log(x4)
y	1	0.89413	0.26501	-0.21767	0.95911	-0.35698	-0.37923	-0.1114
x1	0.89413	1	0.16	-0.08788	0.80598	-0.3949	-0.55048	-0.15008
x2	0.26501	0.16	1	-0.07607	0.385	0.5121	0.25086	0.69754
x3	-0.21767	-0.08788	-0.07607	1	-0.26008	0.08774	-0.22021	-0.14157
log(x4)	0.95911	0.80598	0.385	-0.26008	1	-0.20169	-0.3745	0.03002
x1x2	-0.35698	-0.3949	0.5121	0.08774	-0.20169	1	0.1742	0.8294
x1log(x4)	-0.37923	-0.55048	0.25086	-0.22021	-0.3745	0.1742	1	-0.07157
x2log(x4)	-0.1114	-0.15008	0.69754	-0.14157	0.03002	0.8294	-0.07157	1

Figure 4.73 Pearson Correlation with Predictor Variables and Standardized Interactions – Epoxy Foamed Interlayer CFRP

At this point, a search for the best model that explains flexural strength will be performed. Figure 4.73 shows that there is high correlation between the standardized interaction $stdx2log(x4)$ and $stdx1x2$. As a result, these should not be included together in the same model. Two different model searches will be performed which will include the four main predictor variables and each time one a pair of uncorrelated interactions. The first step is to do the two best subset regressions, which include all predictor variables plus the standardized interactions $stdx1x2$, and $stdx1log(x4)$ – Case 1, and then all predictor variables plus the standardized interactions $stdx1log(x4)$, and $stdx2log(x4)$ – Case 2 (Figure 4.74). The best

subset regression analyses are performed with the Minitab software (140). Backward elimination and stepwise methods are also performed to compare with the best subset results and are also presented in Figure 4.75.

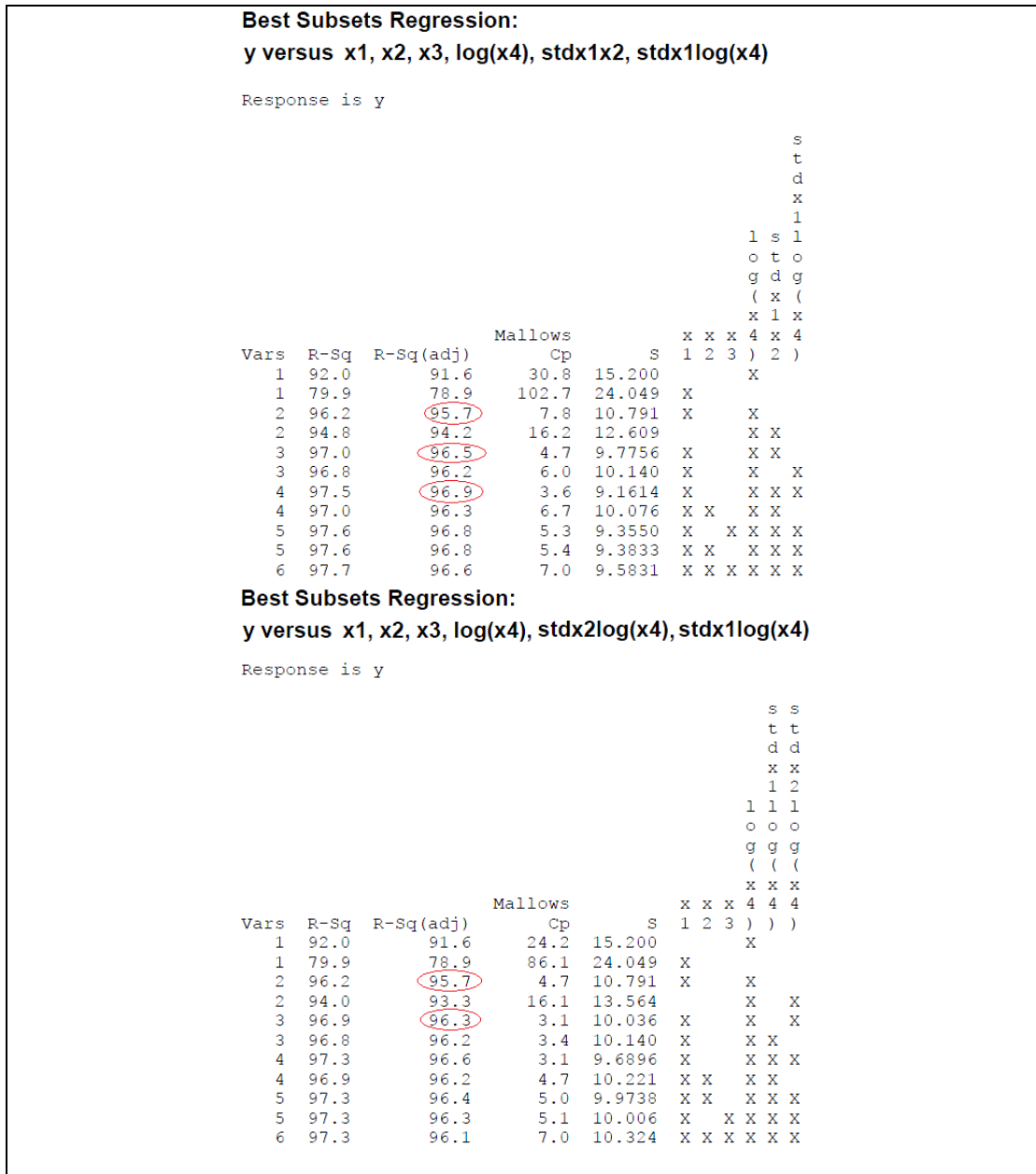


Figure 4.74 Best Subsets Regression of all Predictor Variables and Interactions for Both Cases for Epoxy Foamed Interlayer CFRP

Forward Selection	Backward Elimination																																																																																																																																																																																										
Case 1																																																																																																																																																																																											
<p>Stepwise Regression: y versus x1, x2, x3, log(x4), stdx1x2, stdx1log(x4)</p> <p>Forward selection. Alpha-to-Enter: 0.1</p> <p>Response is y on 6 predictors, with N = 21</p> <table border="1"> <thead> <tr> <th>Step</th> <th>1</th> <th>2</th> <th>3</th> <th>4</th> </tr> </thead> <tbody> <tr> <td>Constant</td> <td>-231.9</td> <td>-171.4</td> <td>-171.6</td> <td>-182.7</td> </tr> <tr> <td>log(x4)</td> <td>174</td> <td>124</td> <td>130</td> <td>126</td> </tr> <tr> <td>T-Value</td> <td>14.77</td> <td>8.74</td> <td>9.90</td> <td>10.15</td> </tr> <tr> <td>P-Value</td> <td>0.000</td> <td>0.000</td> <td>0.000</td> <td>0.000</td> </tr> <tr> <td>x1</td> <td></td> <td>2.40</td> <td>1.92</td> <td>2.38</td> </tr> <tr> <td>T-Value</td> <td></td> <td>4.44</td> <td>3.60</td> <td>4.25</td> </tr> <tr> <td>P-Value</td> <td></td> <td>0.000</td> <td>0.002</td> <td>0.001</td> </tr> <tr> <td>stdx1x2</td> <td></td> <td></td> <td>-6.1</td> <td>-5.7</td> </tr> <tr> <td>T-Value</td> <td></td> <td></td> <td>-2.22</td> <td>-2.20</td> </tr> <tr> <td>P-Value</td> <td></td> <td></td> <td>0.040</td> <td>0.043</td> </tr> <tr> <td>stdx1log(x4)</td> <td></td> <td></td> <td></td> <td>6.4</td> </tr> <tr> <td>T-Value</td> <td></td> <td></td> <td></td> <td>1.83</td> </tr> <tr> <td>P-Value</td> <td></td> <td></td> <td></td> <td>0.086</td> </tr> <tr> <td>S</td> <td>15.2</td> <td>10.8</td> <td>9.78</td> <td>9.16</td> </tr> <tr> <td>R-Sq</td> <td>91.99</td> <td>96.17</td> <td>97.04</td> <td>97.55</td> </tr> <tr> <td>R-Sq(adj)</td> <td>91.57</td> <td>95.75</td> <td>96.51</td> <td>96.94</td> </tr> <tr> <td>Mallows Cp</td> <td>30.8</td> <td>7.8</td> <td>4.7</td> <td>3.6</td> </tr> </tbody> </table>	Step	1	2	3	4	Constant	-231.9	-171.4	-171.6	-182.7	log(x4)	174	124	130	126	T-Value	14.77	8.74	9.90	10.15	P-Value	0.000	0.000	0.000	0.000	x1		2.40	1.92	2.38	T-Value		4.44	3.60	4.25	P-Value		0.000	0.002	0.001	stdx1x2			-6.1	-5.7	T-Value			-2.22	-2.20	P-Value			0.040	0.043	stdx1log(x4)				6.4	T-Value				1.83	P-Value				0.086	S	15.2	10.8	9.78	9.16	R-Sq	91.99	96.17	97.04	97.55	R-Sq(adj)	91.57	95.75	96.51	96.94	Mallows Cp	30.8	7.8	4.7	3.6	<p>Stepwise Regression: y versus x1, x2, x3, log(x4), stdx1x2, stdx1log(x4)</p> <p>Backward elimination. Alpha-to-Remove: 0.1</p> <p>Response is y on 6 predictors, with N = 21</p> <table border="1"> <thead> <tr> <th>Step</th> <th>1</th> <th>2</th> <th>3</th> </tr> </thead> <tbody> <tr> <td>Constant</td> <td>-260.5</td> <td>-215.9</td> <td>-182.7</td> </tr> <tr> <td>x1</td> <td>2.40</td> <td>2.35</td> <td>2.38</td> </tr> <tr> <td>T-Value</td> <td>4.02</td> <td>4.08</td> <td>4.25</td> </tr> <tr> <td>P-Value</td> <td>0.001</td> <td>0.001</td> <td>0.001</td> </tr> <tr> <td>x2</td> <td>0.21</td> <td></td> <td></td> </tr> <tr> <td>T-Value</td> <td>0.54</td> <td></td> <td></td> </tr> <tr> <td>P-Value</td> <td>0.596</td> <td></td> <td></td> </tr> <tr> <td>x3</td> <td>0.53</td> <td>0.49</td> <td></td> </tr> <tr> <td>T-Value</td> <td>0.62</td> <td>0.59</td> <td></td> </tr> <tr> <td>P-Value</td> <td>0.547</td> <td>0.566</td> <td></td> </tr> <tr> <td>log(x4)</td> <td>126</td> <td>129</td> <td>126</td> </tr> <tr> <td>T-Value</td> <td>8.34</td> <td>9.62</td> <td>10.15</td> </tr> <tr> <td>P-Value</td> <td>0.000</td> <td>0.000</td> <td>0.000</td> </tr> <tr> <td>stdx1x2</td> <td>-7.1</td> <td>-5.9</td> <td>-5.7</td> </tr> <tr> <td>T-Value</td> <td>-2.02</td> <td>-2.21</td> <td>-2.20</td> </tr> <tr> <td>P-Value</td> <td>0.063</td> <td>0.043</td> <td>0.043</td> </tr> <tr> <td>stdx1log(x4)</td> <td>7.7</td> <td>7.0</td> <td>6.4</td> </tr> <tr> <td>T-Value</td> <td>1.92</td> <td>1.89</td> <td>1.83</td> </tr> <tr> <td>P-Value</td> <td>0.076</td> <td>0.079</td> <td>0.086</td> </tr> <tr> <td>S</td> <td>9.58</td> <td>9.35</td> <td>9.16</td> </tr> <tr> <td>R-Sq</td> <td>97.65</td> <td>97.60</td> <td>97.55</td> </tr> <tr> <td>R-Sq(adj)</td> <td>96.65</td> <td>96.81</td> <td>96.94</td> </tr> <tr> <td>Mallows Cp</td> <td>7.0</td> <td>5.3</td> <td>3.6</td> </tr> </tbody> </table>	Step	1	2	3	Constant	-260.5	-215.9	-182.7	x1	2.40	2.35	2.38	T-Value	4.02	4.08	4.25	P-Value	0.001	0.001	0.001	x2	0.21			T-Value	0.54			P-Value	0.596			x3	0.53	0.49		T-Value	0.62	0.59		P-Value	0.547	0.566		log(x4)	126	129	126	T-Value	8.34	9.62	10.15	P-Value	0.000	0.000	0.000	stdx1x2	-7.1	-5.9	-5.7	T-Value	-2.02	-2.21	-2.20	P-Value	0.063	0.043	0.043	stdx1log(x4)	7.7	7.0	6.4	T-Value	1.92	1.89	1.83	P-Value	0.076	0.079	0.086	S	9.58	9.35	9.16	R-Sq	97.65	97.60	97.55	R-Sq(adj)	96.65	96.81	96.94	Mallows Cp	7.0	5.3	3.6
Step	1	2	3	4																																																																																																																																																																																							
Constant	-231.9	-171.4	-171.6	-182.7																																																																																																																																																																																							
log(x4)	174	124	130	126																																																																																																																																																																																							
T-Value	14.77	8.74	9.90	10.15																																																																																																																																																																																							
P-Value	0.000	0.000	0.000	0.000																																																																																																																																																																																							
x1		2.40	1.92	2.38																																																																																																																																																																																							
T-Value		4.44	3.60	4.25																																																																																																																																																																																							
P-Value		0.000	0.002	0.001																																																																																																																																																																																							
stdx1x2			-6.1	-5.7																																																																																																																																																																																							
T-Value			-2.22	-2.20																																																																																																																																																																																							
P-Value			0.040	0.043																																																																																																																																																																																							
stdx1log(x4)				6.4																																																																																																																																																																																							
T-Value				1.83																																																																																																																																																																																							
P-Value				0.086																																																																																																																																																																																							
S	15.2	10.8	9.78	9.16																																																																																																																																																																																							
R-Sq	91.99	96.17	97.04	97.55																																																																																																																																																																																							
R-Sq(adj)	91.57	95.75	96.51	96.94																																																																																																																																																																																							
Mallows Cp	30.8	7.8	4.7	3.6																																																																																																																																																																																							
Step	1	2	3																																																																																																																																																																																								
Constant	-260.5	-215.9	-182.7																																																																																																																																																																																								
x1	2.40	2.35	2.38																																																																																																																																																																																								
T-Value	4.02	4.08	4.25																																																																																																																																																																																								
P-Value	0.001	0.001	0.001																																																																																																																																																																																								
x2	0.21																																																																																																																																																																																										
T-Value	0.54																																																																																																																																																																																										
P-Value	0.596																																																																																																																																																																																										
x3	0.53	0.49																																																																																																																																																																																									
T-Value	0.62	0.59																																																																																																																																																																																									
P-Value	0.547	0.566																																																																																																																																																																																									
log(x4)	126	129	126																																																																																																																																																																																								
T-Value	8.34	9.62	10.15																																																																																																																																																																																								
P-Value	0.000	0.000	0.000																																																																																																																																																																																								
stdx1x2	-7.1	-5.9	-5.7																																																																																																																																																																																								
T-Value	-2.02	-2.21	-2.20																																																																																																																																																																																								
P-Value	0.063	0.043	0.043																																																																																																																																																																																								
stdx1log(x4)	7.7	7.0	6.4																																																																																																																																																																																								
T-Value	1.92	1.89	1.83																																																																																																																																																																																								
P-Value	0.076	0.079	0.086																																																																																																																																																																																								
S	9.58	9.35	9.16																																																																																																																																																																																								
R-Sq	97.65	97.60	97.55																																																																																																																																																																																								
R-Sq(adj)	96.65	96.81	96.94																																																																																																																																																																																								
Mallows Cp	7.0	5.3	3.6																																																																																																																																																																																								
Case 2																																																																																																																																																																																											
<p>Stepwise Regression: y versus x1, x2, x3, log(x4), stdx2log(x4), stdx1log(x4)</p> <p>Forward selection. Alpha-to-Enter: 0.1</p> <p>Response is y on 6 predictors, with N = 21</p> <table border="1"> <thead> <tr> <th>Step</th> <th>1</th> <th>2</th> <th>3</th> </tr> </thead> <tbody> <tr> <td>Constant</td> <td>-231.9</td> <td>-171.4</td> <td>-179.0</td> </tr> <tr> <td>log(x4)</td> <td>174</td> <td>124</td> <td>131</td> </tr> <tr> <td>T-Value</td> <td>14.77</td> <td>8.74</td> <td>9.58</td> </tr> <tr> <td>P-Value</td> <td>0.000</td> <td>0.000</td> <td>0.000</td> </tr> <tr> <td>x1</td> <td></td> <td>2.40</td> <td>2.09</td> </tr> <tr> <td>T-Value</td> <td></td> <td>4.44</td> <td>3.99</td> </tr> <tr> <td>P-Value</td> <td></td> <td>0.000</td> <td>0.001</td> </tr> <tr> <td>stdx2log(x4)</td> <td></td> <td></td> <td>-3.9</td> </tr> <tr> <td>T-Value</td> <td></td> <td></td> <td>-1.95</td> </tr> <tr> <td>P-Value</td> <td></td> <td></td> <td>0.068</td> </tr> <tr> <td>S</td> <td>15.2</td> <td>10.8</td> <td>10.0</td> </tr> <tr> <td>R-Sq</td> <td>91.99</td> <td>96.17</td> <td>96.88</td> </tr> <tr> <td>R-Sq(adj)</td> <td>91.57</td> <td>95.75</td> <td>96.32</td> </tr> <tr> <td>Mallows Cp</td> <td>24.2</td> <td>4.7</td> <td>3.1</td> </tr> </tbody> </table>	Step	1	2	3	Constant	-231.9	-171.4	-179.0	log(x4)	174	124	131	T-Value	14.77	8.74	9.58	P-Value	0.000	0.000	0.000	x1		2.40	2.09	T-Value		4.44	3.99	P-Value		0.000	0.001	stdx2log(x4)			-3.9	T-Value			-1.95	P-Value			0.068	S	15.2	10.8	10.0	R-Sq	91.99	96.17	96.88	R-Sq(adj)	91.57	95.75	96.32	Mallows Cp	24.2	4.7	3.1	<p>Stepwise Regression: y versus x1, x2, x3, log(x4), stdx2log(x4), stdx1log(x4)</p> <p>Backward elimination. Alpha-to-Remove: 0.1</p> <p>Response is y on 6 predictors, with N = 21</p> <table border="1"> <thead> <tr> <th>Step</th> <th>1</th> <th>2</th> <th>3</th> <th>4</th> </tr> </thead> <tbody> <tr> <td>Constant</td> <td>-216.7</td> <td>-216.4</td> <td>-187.4</td> <td>-179.0</td> </tr> <tr> <td>x1</td> <td>2.56</td> <td>2.56</td> <td>2.53</td> <td>2.09</td> </tr> <tr> <td>T-Value</td> <td>4.05</td> <td>4.20</td> <td>4.33</td> <td>3.99</td> </tr> <tr> <td>P-Value</td> <td>0.001</td> <td>0.001</td> <td>0.001</td> <td>0.001</td> </tr> <tr> <td>x2</td> <td>0.14</td> <td>0.14</td> <td></td> <td></td> </tr> <tr> <td>T-Value</td> <td>0.30</td> <td>0.32</td> <td></td> <td></td> </tr> <tr> <td>P-Value</td> <td>0.767</td> <td>0.755</td> <td></td> <td></td> </tr> <tr> <td>x3</td> <td>0.00</td> <td></td> <td></td> <td></td> </tr> <tr> <td>T-Value</td> <td>0.00</td> <td></td> <td></td> <td></td> </tr> <tr> <td>P-Value</td> <td>0.996</td> <td></td> <td></td> <td></td> </tr> <tr> <td>log(x4)</td> <td>125</td> <td>125</td> <td>127</td> <td>131</td> </tr> <tr> <td>T-Value</td> <td>7.62</td> <td>8.24</td> <td>9.43</td> <td>9.58</td> </tr> <tr> <td>P-Value</td> <td>0.000</td> <td>0.000</td> <td>0.000</td> <td>0.000</td> </tr> <tr> <td>stdx1log(x4)</td> <td>5.9</td> <td>5.9</td> <td>5.7</td> <td></td> </tr> <tr> <td>T-Value</td> <td>1.37</td> <td>1.49</td> <td>1.50</td> <td></td> </tr> <tr> <td>P-Value</td> <td>0.192</td> <td>0.158</td> <td>0.154</td> <td></td> </tr> <tr> <td>stdx2log(x4)</td> <td>-3.8</td> <td>-3.8</td> <td>-3.2</td> <td>-3.9</td> </tr> <tr> <td>T-Value</td> <td>-1.26</td> <td>-1.34</td> <td>-1.62</td> <td>-1.95</td> </tr> <tr> <td>P-Value</td> <td>0.228</td> <td>0.199</td> <td>0.125</td> <td>0.068</td> </tr> <tr> <td>S</td> <td>10.3</td> <td>9.97</td> <td>9.69</td> <td>10.0</td> </tr> <tr> <td>R-Sq</td> <td>97.28</td> <td>97.28</td> <td>97.26</td> <td>96.88</td> </tr> <tr> <td>R-Sq(adj)</td> <td>96.11</td> <td>96.37</td> <td>96.57</td> <td>96.32</td> </tr> <tr> <td>Mallows Cp</td> <td>7.0</td> <td>5.0</td> <td>3.1</td> <td>3.1</td> </tr> </tbody> </table>	Step	1	2	3	4	Constant	-216.7	-216.4	-187.4	-179.0	x1	2.56	2.56	2.53	2.09	T-Value	4.05	4.20	4.33	3.99	P-Value	0.001	0.001	0.001	0.001	x2	0.14	0.14			T-Value	0.30	0.32			P-Value	0.767	0.755			x3	0.00				T-Value	0.00				P-Value	0.996				log(x4)	125	125	127	131	T-Value	7.62	8.24	9.43	9.58	P-Value	0.000	0.000	0.000	0.000	stdx1log(x4)	5.9	5.9	5.7		T-Value	1.37	1.49	1.50		P-Value	0.192	0.158	0.154		stdx2log(x4)	-3.8	-3.8	-3.2	-3.9	T-Value	-1.26	-1.34	-1.62	-1.95	P-Value	0.228	0.199	0.125	0.068	S	10.3	9.97	9.69	10.0	R-Sq	97.28	97.28	97.26	96.88	R-Sq(adj)	96.11	96.37	96.57	96.32	Mallows Cp	7.0	5.0	3.1	3.1						
Step	1	2	3																																																																																																																																																																																								
Constant	-231.9	-171.4	-179.0																																																																																																																																																																																								
log(x4)	174	124	131																																																																																																																																																																																								
T-Value	14.77	8.74	9.58																																																																																																																																																																																								
P-Value	0.000	0.000	0.000																																																																																																																																																																																								
x1		2.40	2.09																																																																																																																																																																																								
T-Value		4.44	3.99																																																																																																																																																																																								
P-Value		0.000	0.001																																																																																																																																																																																								
stdx2log(x4)			-3.9																																																																																																																																																																																								
T-Value			-1.95																																																																																																																																																																																								
P-Value			0.068																																																																																																																																																																																								
S	15.2	10.8	10.0																																																																																																																																																																																								
R-Sq	91.99	96.17	96.88																																																																																																																																																																																								
R-Sq(adj)	91.57	95.75	96.32																																																																																																																																																																																								
Mallows Cp	24.2	4.7	3.1																																																																																																																																																																																								
Step	1	2	3	4																																																																																																																																																																																							
Constant	-216.7	-216.4	-187.4	-179.0																																																																																																																																																																																							
x1	2.56	2.56	2.53	2.09																																																																																																																																																																																							
T-Value	4.05	4.20	4.33	3.99																																																																																																																																																																																							
P-Value	0.001	0.001	0.001	0.001																																																																																																																																																																																							
x2	0.14	0.14																																																																																																																																																																																									
T-Value	0.30	0.32																																																																																																																																																																																									
P-Value	0.767	0.755																																																																																																																																																																																									
x3	0.00																																																																																																																																																																																										
T-Value	0.00																																																																																																																																																																																										
P-Value	0.996																																																																																																																																																																																										
log(x4)	125	125	127	131																																																																																																																																																																																							
T-Value	7.62	8.24	9.43	9.58																																																																																																																																																																																							
P-Value	0.000	0.000	0.000	0.000																																																																																																																																																																																							
stdx1log(x4)	5.9	5.9	5.7																																																																																																																																																																																								
T-Value	1.37	1.49	1.50																																																																																																																																																																																								
P-Value	0.192	0.158	0.154																																																																																																																																																																																								
stdx2log(x4)	-3.8	-3.8	-3.2	-3.9																																																																																																																																																																																							
T-Value	-1.26	-1.34	-1.62	-1.95																																																																																																																																																																																							
P-Value	0.228	0.199	0.125	0.068																																																																																																																																																																																							
S	10.3	9.97	9.69	10.0																																																																																																																																																																																							
R-Sq	97.28	97.28	97.26	96.88																																																																																																																																																																																							
R-Sq(adj)	96.11	96.37	96.57	96.32																																																																																																																																																																																							
Mallows Cp	7.0	5.0	3.1	3.1																																																																																																																																																																																							

Figure 4.75 Backward Elimination and Forward Stepwise Methods for evaluating all Predictor Variables and Interactions for Both Cases for Epoxy Foamed Interlayer CFRP

The best model ($\alpha = 0.1$) deriving from stepwise forward selection method (Figure 4.75) in case 1 includes flexural modulus and logarithm of interlayer improvement, the standard interaction of those two, and the standard interaction of flexural modulus with tensile strength. In case 2, stepwise forward selection gives as best model the one which includes flexural modulus, logarithm of interlayer improvement, and the standard interaction of the latter with tensile strength. The same models are given as best models for each case with the backward elimination method. However, having a closer look at the best subset regression analyses, there is a better model than the one with four predictor variables in case 1. More specifically, the model with flexural modulus, logarithm of interlayer improvement, and standard interaction of flexural modulus and tensile strength has a low C_p as well as a high adjusted R^2 . Relatively low and high are the C_p and the adjusted R^2 respectively of the model with only two predictor variables, however, the C_p in this case is almost double compared to the C_p of the three predictor variables model. In case 2 of best subsets, the best models seem to be first the two predictor variable model (flexural modulus and interlayer improvement) and the three predictor variable one (the two of the first model plus the standardized interaction of tensile strength and logarithmic interlayer improvement). Concluding on best model search three models seems to be the best for predicting flexural strength. Furthermore, the analysis in Figure 4.75 shows that all the p-values for all these three best models (with two predictor variables (x_1, x_4), with three predictor variables ($x_1, x_4, \text{std}x_1x_2$), and ($x_1, x_4, \text{std}x_2\log(x_4)$)) are significant for $\alpha = 0.1$. The variance inflations are also measured for the two models and they are:

- For the two predictor variable model: $VIF_1=2.854, VIF_4=2.854$
- For the first three predictor variable model: $VIF_1=3.34, VIF_4=2.99, VIF_{\text{std}12}=1.242$
- For the second three predictor variable model: $VIF_1=3.125, VIF_4=3.06, VIF_{\text{std}24}=1.096$

Variance inflations are relatively low, so they do not indicate high multicollinearity. As a result, the best two models selected (from all the ways of regression analyses) are:

Model 1: Variables= $x_1, \log(x_4) / R(\text{adj})^2 = 95.7 / C_p = 4.7$ (Case 2)

Model 2: Variables= $x_1, \log(x_4), \text{std}x_1x_2 / R(\text{adj})^2 = 96.3 / C_p = 4.7$ (Case 1)

Model 3: Variables= $x_1, \log(x_4), \text{std}x_2\log(x_4) / R(\text{adj})^2 = 96.3 / C_p = 3.1$ (Case 2)

The next step will be to evaluate and compare the three selected models and choose the best one to keep for predicting the flexural strength of the epoxy foamed featherweights.

Model 1:

Parameters, ANOVA Table and other information on Model 1 are presented from Table 4.39 to Table 4.41.

Table 4.39 Model 1 Parameters – Epoxy Foamed Interlayer CFRP

	Value	Standard Error	t-Value	Prob> t
Intercept	-171.4	27.692	-6.189	0.000
X1-Flexural Modulus	2.4	0.54	4.44	0.000
Log(X4)-Interlayer Improvement	123.76	14.162	8.74	0.000

Table 4.40 Model 1 ANOVA Table – Epoxy Foamed Interlayer CFRP

	DF	Sum of Squares	Mean Square	F Value	Prob>F
Model	2	52699.8	26349.9	226.29	1.21347E-13
Error	18	2096	116.4		
Total	20	54795.8			

Table 4.41 Other Information of Model 1 – Epoxy Foamed Interlayer CFRP

Number of Points	21
Degrees of Freedom	18
Residual Sum of Squares	2096
R Square	0.9617
Adj. R Square	0.9575
Root MSE	10.79

Thus, model 1 can be written as:

$$\hat{y} = -171.383 + 2.39638 \cdot x_1 + 123.761 \cdot \log(x_4)$$

Figure 4.76 presents the analysis of the residuals over the predictor variables, the fitted values, the time order, and the NPP plot for model 1.

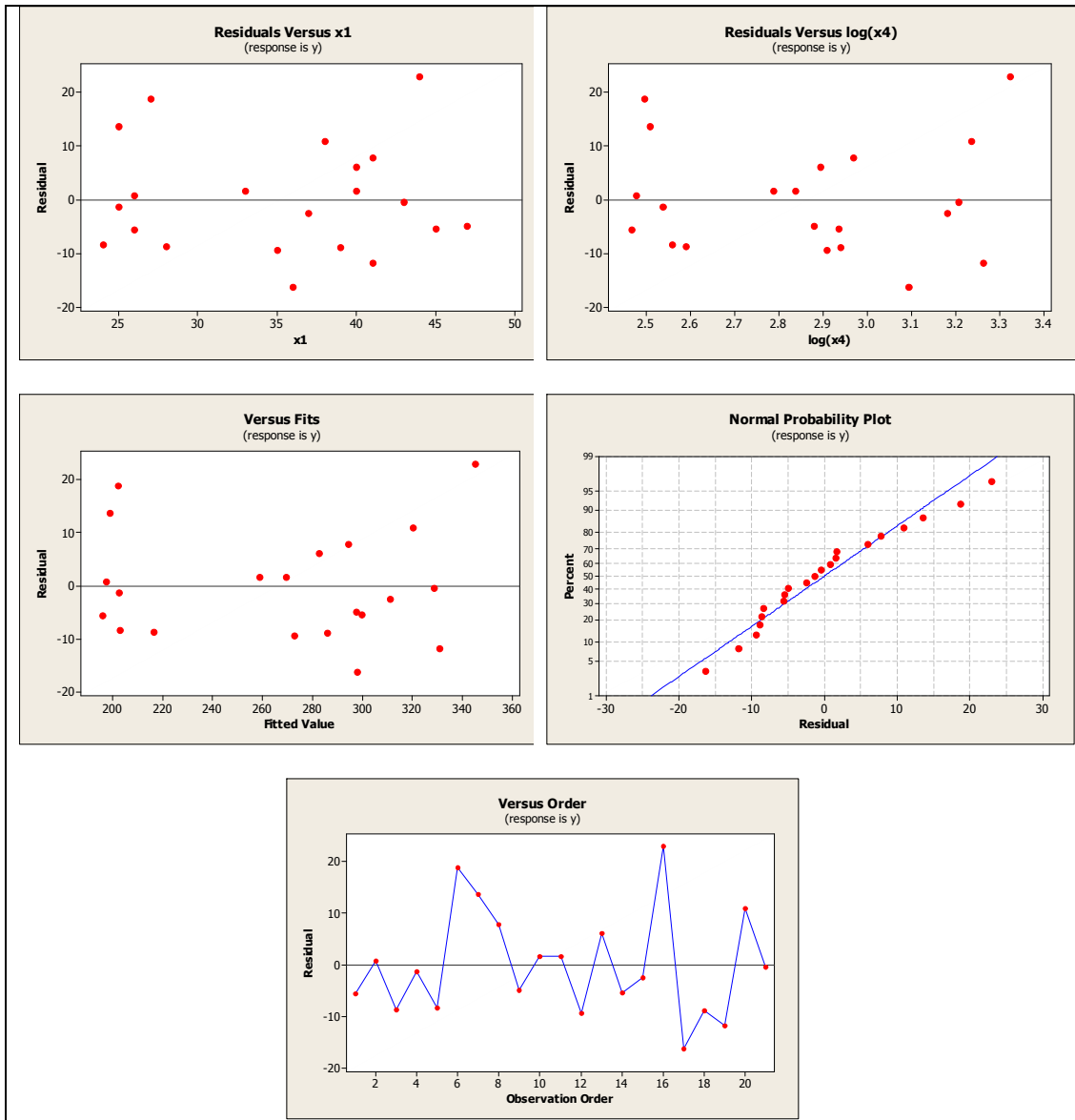


Figure 4.76 Model 1 Residuals Graphs – Epoxy Foamed Interlayer CFRP

Model 2:

Parameters, ANOVA Table and other information on Model 2 are presented from Table 4.42 to Table 4.44.

Table 4.42 Model 2 Parameters – Epoxy Foamed Interlayer CFRP

	Value	Standard Error	t-Value	Prob> t
Intercept	-171.6	25.0864	-6.84	4.5595E-8
X1-Flexural Modulus	1.92	0.534	3.598	0.002
X4-Interlayer Improvement	130.016	13.135	9.898	5.74209E-9
stdx1x2	-6.123	2.757	-2.221	0.04

Thus, model 2 can be written as:

$$\hat{y} = -171.601 + 1.92119 \cdot x_1 + 130.016 \cdot \log(x_4) - 6.12257 \cdot \text{std}x_1x_2$$

Table 4.43 Model 2 ANOVA Table – Epoxy Foamed Interlayer CFRP

	DF	Sum of Squares	Mean Square	F Value	Prob>F
Model	4	53171.3	17723.8	185.47	4.23439E-13
Error	16	1624.6	95.6		
Total	20	54795.8			

Table 4.44 Other information of Model 2 – Epoxy Foamed Interlayer CFRP

Number of Points	21
Degrees of Freedom	16
Residual Sum of Squares	1624.6
R Square	0.9704
Adj. R Square	0.965
Root MSE	9.78

Figure 4.77 presents the analysis of the residuals over the predictor variables, the fitted values, the time order, and the NPP plot for model 2.

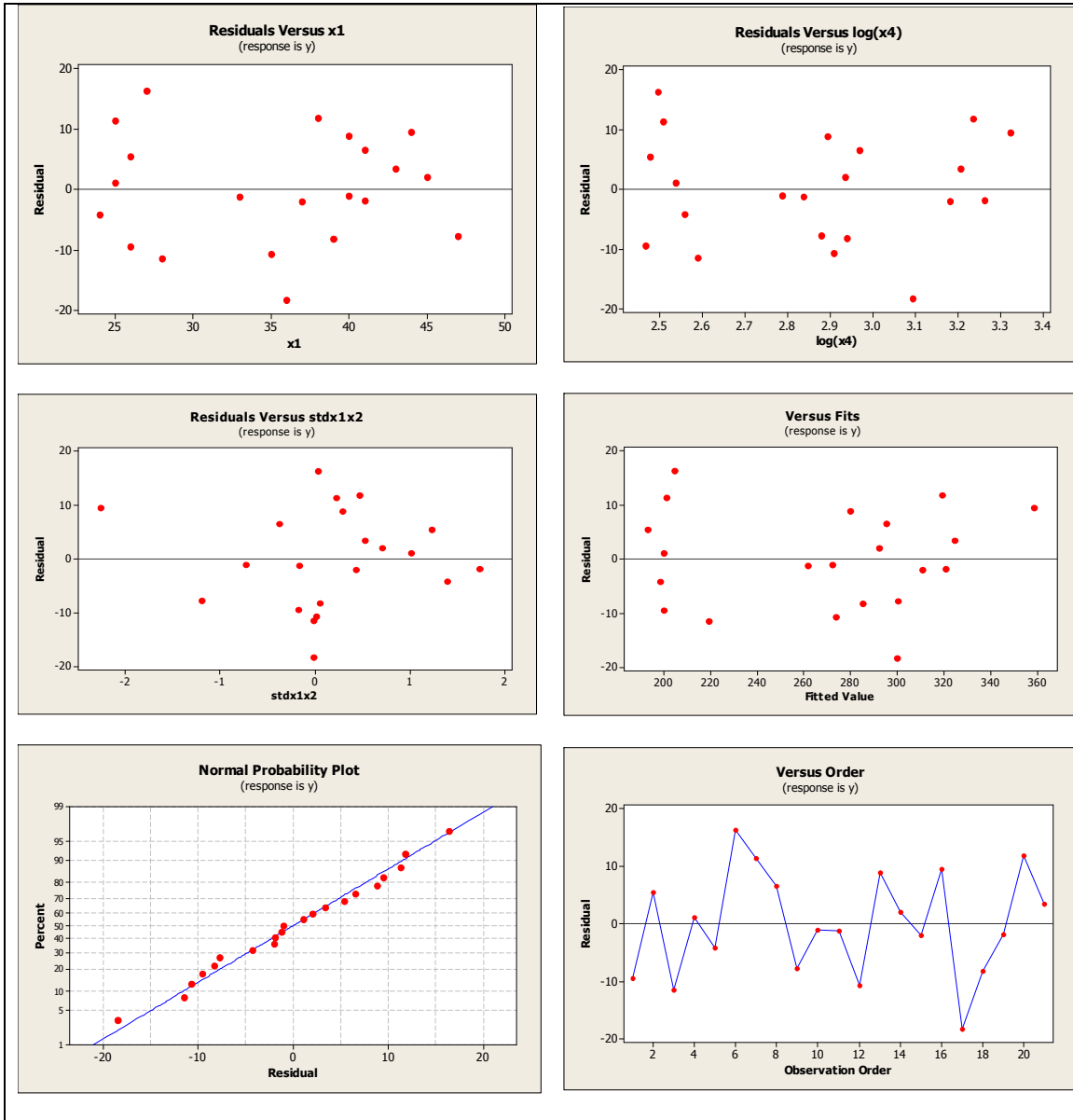


Figure 4.77 Model 2 Residuals Graphs – Epoxy Foamed Interlayer CFRP

Model 3:

Parameters, ANOVA Table and other information on Model 3 are presented from Table 4.45 to Table 4.47.

Table 4.45 Model 3 Parameters – Epoxy Foamed Interlayer CFRP

	Value	Standard Error	t-Value	Prob> t
Intercept	-178.97	26.0445	-6.872	0.000
X1-Flexural Modulus	2.094	0.526	3.985	0.001
X4-Interlayer Improvement	130.63	13.632	9.5823	0.000
Std _x 2log(x ₄)	-3.862	1.9783	-1.9523	0.068

Thus, model 3 can be written as:

$$\hat{y} = -178.965 + 2.09423 \cdot x_1 + 130.627 \cdot \log(x_4) - 3.86215 \cdot \text{std}_x 2\log(x_4)$$

Table 4.46 Model 3 ANOVA Table – Epoxy Foamed Interlayer CFRP

	DF	Sum of Squares	Mean Square	F Value	Prob>F
Model	4	53083.7	17694.6	175.7	4.23439E-13
Error	16	1712.1	100.7		
Total	20	54795.8			

Table 4.47 Other information of Model 3 – Epoxy Foamed Interlayer CFRP

Number of Points	21
Degrees of Freedom	16
Residual Sum of Squares	1712.1
R Square	0.9688
Adj. R Square	0.9632
Root MSE	10.035

Figure 4.78 presents the analysis of the residuals over the predictor variables, the fitted values, the time order, and the NPP plot for model 3.

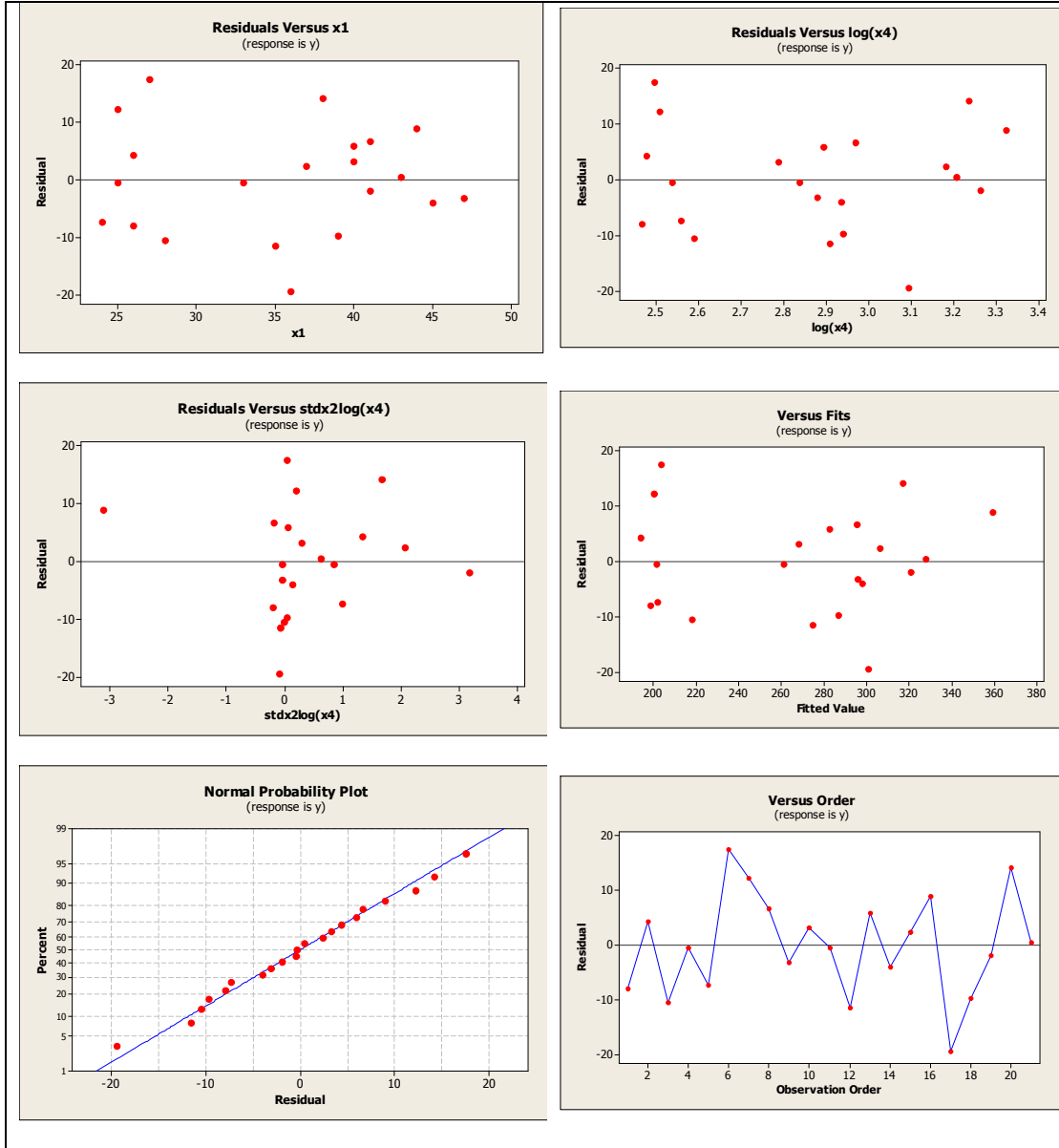


Figure 4.78 Model 3 Residuals Graphs – Epoxy Foamed Interlayer CFRP

Having presented the parameters and the analysis of each of the three best models then a comparison among their assumptions is performed (Table 4.48)

Table 4.48 Model Assumptions Comparison – Epoxy Foamed Interlayer CFRP

ASSUM.	Model1	Model 2	Model 3
1	Slight curvature on residuals vs. Log(x4) → Model Form Not Reasonable	No curvature → Model Form Reasonable	Slight curvature on residuals vs. Log(x4) → Model Form Not Reasonable
2	No Funnel Shape → Constant Error Variance is Reasonable	No Funnel Shape → Constant Error Variance is Reasonable	No Funnel Shape → Constant Error Variance is Reasonable
3	NPP Plot - slight curvature, however normality can be considered reasonable → Normality not violated	NPP Plot looks reasonable → Normality not violated	NPP Plot looks reasonable → Normality not violated
4	No trend - No serial correlation	No trend - No serial correlation	No trend - No serial correlation
Adj. R ² Cp Case 1	Adjusted R ² = 95.7% Cp = 7.8	Adjusted R ² = 96.5% Cp = 4.7	-
Adj. R ² Cp Case 2	Adjusted R ² = 95.7% Cp = 4.7	-	Adjusted R ² = 96.3% Cp = 3.1

The first and third models fail to fulfill the first assumption, so the model forms are not reasonable due to the curvatures presented in the plots of residuals versus the logarithm of interlayer improvement. As a consequence, model 1 and 3 are not considered capable to predict flexural strength and they are not included in the model comparison in Table 4.49, and Table 4.50.

Variance inflations are considered low as variance is inflated around three times for flexural modulus and the logarithm of interlayer improvement predictor variables, while it is near to 1 for the standardized interaction of tensile strength and logarithm of interlayer improvement.

Table 4.49 presents the x and y outliers along with their influence to the fitted model for model 3. The model has neither x nor y outliers according to the leverage test and to the Bonferroni test, respectively. Concluding, there are no y outliers that influence model 3. Observation 16 is seen as an x-outlier with no significant influence to the model though.

Table 4.49 Outliers and Influence - Epoxy Foamed Interlayer CFRP

	Model 2
X - Outlier	Observations 16
Y - Outlier through Bonferonni test	0
Y - Outlier through DFFITS	Observations 16
Y - Outlier through COOKDi	0

Finally, the parameters influence of model 3 is presented in Table 4.50.

Table 4.50 Observation Influence on Parameters - Epoxy Foamed Interlayer CFRP

Influence On	Model 2
Intercept	0
x1	0
Log(x4)	0
Std _{x1x2}	0

Model Selection:

Model 2 is selected over model 1 and 3 for the main reason that assumption 1 is not fulfilled for model forms 1 and 3 and thus the latter are not reasonable. Furthermore, model 2 has diagnostics capable for reasonably predicting the flexural strength.

The ANOVA Table as well as certain parameters of the selected model is presented in Table 4.51, and Table 4.52 respectively.

Table 4.51 Selected Model ANOVA Table – Epoxy Foamed Interlayer CFRP

	DF	Sum of Squares	Mean Square	F Value	Prob>F
Model	4	53171.3	17723.8	185.47	4.23439E-13
Error	16	1624.6	95.6		
Total	20	54795.8			

Table 4.52 Other Information on Selected Model – Epoxy Foamed Interlayer CFRP

Number of Points	21
Degrees of Freedom	16
Residual Sum of Squares	1624.6
R Square	0.9704
Adj. R Square	0.965
Root MSE	9.78

Thus, the model selected is:

$$\hat{y} = -171.601 + 1.92119 \cdot x_1 + 130.016 \cdot \log(x_4) - 6.12257 \cdot \text{std}x_1x_2$$

Parameters Interpretation:

- 1) Regarding β_0 , for $x_1 = \log(x_4) = \text{std}x_1x_2 = 0$, the value of $y_{\text{hat}} = -171.6$ Nevertheless, the point $[0, 0, 0]$ is not included in all x ranges.
- 2) The estimator for β_1 is $b_1 = 1.92$ and it means that the estimated change of the flexural strength when the flexural modulus increases by 1 is 1.92 MPa, assuming that the logarithm of Mode II Energy Release Rate (Interlayer Improvement) and the interaction of flexural modulus and tensile strength remain constant.
- 3) The estimator for β_2 is $b_2 = 130.016$ and it means that the estimated change of the flexural strength when the logarithm of Mode II Energy Release Rate (Interlayer Improvement) increases by 1 is 130.016 MPa, assuming that the flexural modulus and the interaction of flexural modulus and tensile strength remain constant.
- 4) The estimator for β_3 is $b_3 = -6.123$ and it means that the estimated change of the flexural strength when the interaction of flexural modulus and tensile strength

increases by 1 is -6.123 MPa, assuming that the flexural modulus and the interlayer improvement remain constant.

Inferences for the selected model parameters are presented through Bonferroni joint t-interval.

Table 4.53 Selected Model Parameters and Covariance Table – Epoxy Foamed Interlayer CFRP

S(b) ²				b
629.46	6.0632	-293.08	0.26583	-171.61
6.0632	0.28506	-5.6609	0.58976	1.9215
-293.08	-5.6609	172.55	-7.7605	130.02
0.26583	0.58976	-7.7605	7.5998	-6.1205

The Bonferroni joint t-interval is performed for significance level of $\alpha = 0.03$ as following:

$$B = t\left(1 - \frac{\alpha}{2 \cdot g}; n - p\right) = t(1 - 0.005; 17) = t(0.995; 17) = 2.898$$

$$S\{b_1\} = \sqrt{0.28506} = 0.534 \rightarrow \text{Interval} : \beta_1 = 1.9215 \pm 2.898 \cdot 0.534 \Rightarrow \beta_1 : (-0.626, 2.47)$$

$$S\{b_2\} = \sqrt{172.55} = 13.136 \rightarrow \text{Interval} : \beta_2 = 130.02 \pm 2.898 \cdot 13.136 \Rightarrow \beta_2 : (91.952, 168.09)$$

$$S\{b_3\} = \sqrt{7.6} = 2.757 \rightarrow \text{Interval} : \beta_3 = -6.121 \pm 2.898 \cdot 2.757 \Rightarrow \beta_3 : (-14.111, 1.869)$$

We are 97% confident that β_1 is contained in (-0.626, 2.47), β_2 is contained in (91.952, 168.09), and β_3 is contained in (-14.111, 1.869) simultaneously.

Individually for each parameter:

For β_1 , we are 99% confident that β_1 is contained in (-0.626, 2.47).

For β_2 , we are 99% confident that β_2 is contained in (91.952, 168.09).

For β_3 , we are 99% confident that β_2 is contained in (-14.111, 1.869).

Summarizing, the best model for predicting flexural strength of composites when the interlayer is enhanced with foaming resins is:

$$\hat{y} = -171.601 + 1.92119 \cdot x_1 + 130.016 \cdot \log(x_4) - 6.12257 \cdot \text{std}x_1x_2$$

The model uses as predictor variables flexural modulus (x_1), mode II fracture toughness energy release rate (interlayer improvement) (x_4), and the standardized interaction of flexural modulus with tensile strength. Mode II is analogous to the interlayer improvement, and flexural modulus is given material property. As a result, the developed statistical model assists the engineer to design an epoxy foamed interlayered composite with a desired flexural strength by introducing to the model, the flexural modulus, the interlayer toughness improvement and the interaction of flexural modulus with tensile strength. This helps the engineer to avoid performing time-consuming experimental mechanical testing. Finally, it can be seen through the model equation that higher flexural modulus contributes to a higher flexural strength as it is expected due to stiffness enhancement. This is correlated by the experimental results where an approximate 50% flexural modulus increase corresponds to an almost same flexural strength increase. Similar is the behaviour of the interlayer improvement-fracture toughness-which is represented in the model through a logarithm, so higher interlayer improvement corresponds to higher flexural strength. However, the rate of this change is different. The last variable, the interaction of flexural modulus with tensile strength, shows that its increase basically decreases the flexural strength. This happens because tensile strength increase means more carbon fiber within the material, as a result less epoxy foamed interlayer and thus lower flexural strength.

4.6 Results for Specific Objective #6: CNT Electrospun Fiber Interlayer

4.6.1 CNT Reinforced Electrospun Fiber CFRP

Three types of samples were manufactured in order to investigate the role of electrospun interlayer within the CFRP plies. The samples include four plies of (0, 90) carbon fibers. The fiber bed is cut in dimensions of 200x400 mm² due to electrospinning configuration size restrictions. Each of the first three plies is placed within the electrospinning configuration,

before resin is applied and the polymeric solution is electrospun in nano-fibers onto the fiber bed. This is done on the one side of each of the three plies, and during the lay-up the electrospun sides of the three fiber beds are placed in such a way that the three interlayers include one electrospun sheet. After that, the normal manufacturing process for resin application within the fiber bed is performed. In the case of the CNT reinforced electrospun interlayer, CNT solution is stirred with the polymer solution and the entire mix is electrospun onto the fiber bed which has been placed in the electrospinning configuration.

The electrospun fibers are manufactured as follows through the configuration described in Figure 4.79

Cellulose acetate (CA) polymer is stirred with acetone in a fraction of 5% w/v. In the CA solution, CNT (within butanole solution) of fraction 2%w/v are added for forming the third type of samples, for the second type, simply CNT are not added. CA, CNT and acetone are stirred overnight. A needle of 160 μm is used, the distance between the tip of the needle and the target is 25 cm and the voltage is 25 V. 10 ml of CA+CNT solution is utilized to cover the surface of each carbon fiber bed, which for this work was also 200x400 cm^2 .

Nanotubes are mixed within butanol solution. CNT are manufactured in an innovative inexpensive method. The CNT fraction within butanole solution is 50% w/v.

Normal epoxy system was utilized within the fiber bed. As it has already been mentioned three different types of samples were manufactured to better evaluate the electrospun and CNT reinforcement effect (Control, Carbon Fiber with Electrospun interlayer, and Carbon Fiber with CNT Electrospun interlayer).

Materials used in matrix system are described below:

Interlayer Polymer Solution: Cellulose Acetate (CA) 5% w/v in acetone solution **Volume**

Fraction: 6.65%

(Final Density: $\sim 0.81 \text{ g/cm}^3$)

Provided by "Fibermax Composites"

Epoxy System: Resin 921 & Hardener 475524 **Volume Fraction:** 32%

Carbon Fibers: C160P (160 g/m²), E=235 GPa **Volume Fraction:** 60%

Provided by "Rosseter Holdings Ltd"

Carbon Nanotubes: Distribution Characteristics:

Outer diameter: 8.2±3.0nm

Inner diameter: 3.1±0.9nm

Number of walls: 8±4 layers

Length:: 250-300 nm

Volume Fraction: 1.36%

CNT are stirred within the cellulose acetate solution over night in a magnetic stirrer so better distribution is achieved before electrospinning takes place. Figure 4.79 illustrates how the lay-up of the three different samples is.

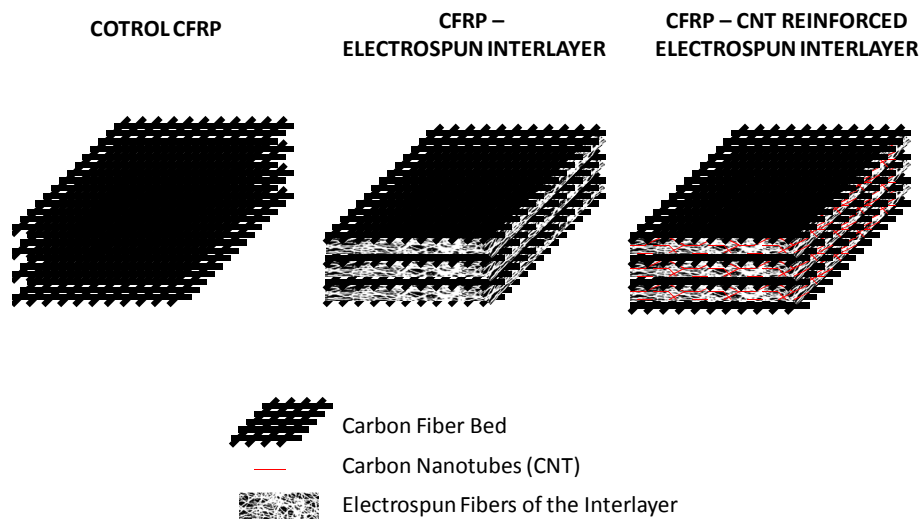


Figure 4.79 Scheme of Electrospun Fiber Interlayer within CFRP Plies

4.6.2 DMA Viscoelastic Behaviour Evaluation

Table 4.54 presents the results from the DMA flexural experiments. More than three experiments were conducted for each type of samples. Storage flexural modulus values at 30 °C are presented together with glass transition temperature based on storage modulus and $\tan\delta$.

Table 4.54 Dynamic Mechanical Analysis of Electrospun Fiber Interlayer CFRP

Samples	Storage Modulus at 30 °C	Glass Transition T Based on Storage Modulus (GPa)	Tan δ Peak	T at tan δ peak (Glass Transition T Based on tan δ) °C
Control CFRP	235.6±3.9	48.8±2	0.2621± 0.047	55.4±2.1
CFRP with ELSP Interlayer	313.33±4.73	47±6.14	0.3757±0.058	54.1±1.75
CFRP with CNT Reinforced ELSP Interlayer	436.33±62.52	49±0.87	0.2927±0.0164	54.03±0.81

It can be seen that there is a significant increase of the storage modulus under flexural load from the control samples to the electrospun interlayer and even higher to the CNT electrospun interlayer. This finding is of particular importance, since it shows that CNT reinforcing the electrospun fibers of the interlayer increase even more the stiffness of the overall material. However, in order to get a better view of the flexural behaviour of the material, flexural mechanical testing is performed and presented for each group of samples in section 4.6.3.

Additionally, there is a difference between the two methods through which the glass transition temperature (T_g) is measured. This happens because storage modulus and $\tan\delta$ are different properties, so the latter always gives little higher values of T_g than the former. Within each method though, there are no significant alterations of the T_g measurements. This means that the interlayer does not affect the glass transition of the material. The $\tan\delta$ peak values are

shown in order to give an idea of the loss modulus values at that point (δ is the damping ratio and $\tan\delta$ represents the loss over the storage modulus).

4.6.3 Mechanical Testing Interlayer Evaluation

4.6.3.1 Flexural Testing

The flexural experiments were performed under the following parameters:

Data Rate: 1 point/sec

Crosshead Speed: 5.00000 mm/min

Temperature: 23 °C

Humidity: 50%

Span: 130mm

Figure 4.80, and Figure 4.82, present some of the several samples that were tested in 3 point bending for control, CFRP with electrospun interlayer, and CFRP with CNT electrospun interlayer.

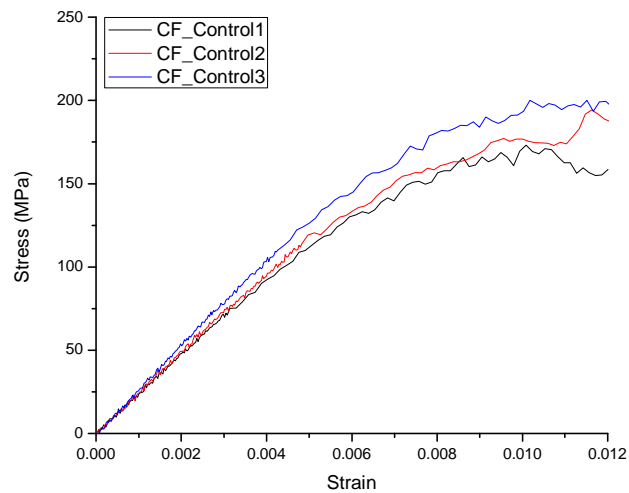


Figure 4.80 Control CFRP Flexural Testing

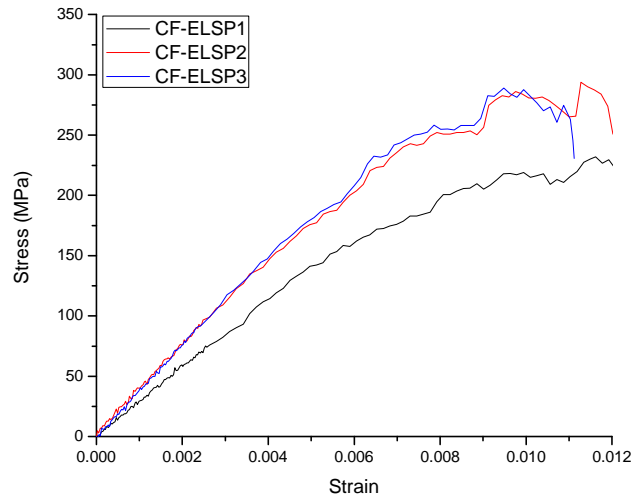


Figure 4.81 CFRP with Electrospun Fiber Interlayer Flexural Testing

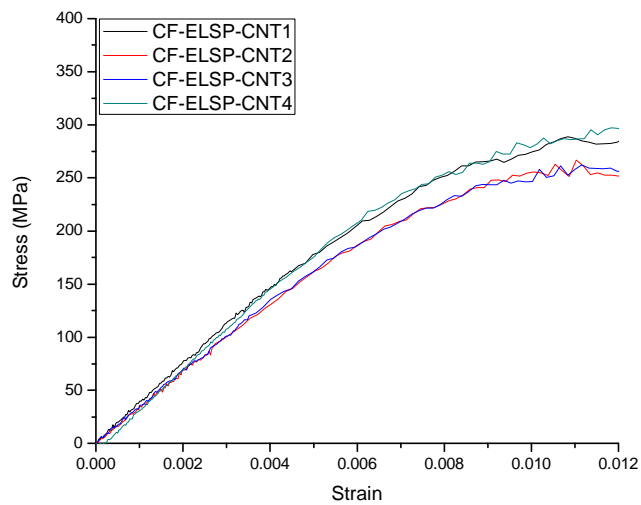


Figure 4.82 CFRP with CNT Reinforced Electrospun Fiber Interlayer Flexural Testing

There is a significant flexural strength increase from the control to CFRP with electrospun interlayer and to CFRP with CNT electrospun interlayer. Table 4.55 summarizes the

values deriving for the electrospun interlayered samples when tested in flexural experiments. The material stiffness improvement is presented later on as well.

Table 4.55 Flexural Testing Summary of CFRP Composites with CNT Electrospun Fibers

	Flexural Strength (MPa)	Flexural Modulus (GPa)
Control CFRP	196.1±24.05	24.67±2.1
CFRP+ELSP Fibers	271.7±34.43	35.33 ±5.5
CFRP+ELSP Fibers+CNT	307±31.6	38±2

It can be seen that there is a significant increase of flexural strength from control to electrospun samples of around 38.5%. This indicates that the electrospun interlayer due to its high stiffness plays a key role in the flexural strength enhancement. There is an additional 13.24% flexural strength enhancement from the electrospun interlayer to the CNT reinforced electrospun interlayer and this is due to the CNT existence. As it can be seen, the electrospun interlayer not only enhances the flexural modulus of the composite around 43% when added to the interlayer by itself, but it looks like the extra CNT reinforcement in the third sample type does influence the flexural modulus too as it presents a slight increase of around 7.6% from electrospun interlayer to CNT electrospun interlayer samples. Contrarily to the epoxy foamed interlayer system, it seems that CNT participates to the load transfer as part of the electrospun fibers. As a result, the CNT reinforcement contributes to the, flexural strength, stiffness, and Mode II fracture toughness improvement as well as to flexural modulus slight enhancement.

4.6.3.2 Tension Testing

The tensile experiments were performed under the following parameters:

Data Rate: 10 point/sec

Crosshead Speed: 1.00000 mm/min

Temperature: 23 °C

Humidity: 50%

Gauge Length: ~80 mm

Figure 4.83 to Figure 4.85 present some of the several samples that were tested in tensile test for control CFRP, CFRP with electrospun interlayer, and CFRP with CNT electrospun interlayer.

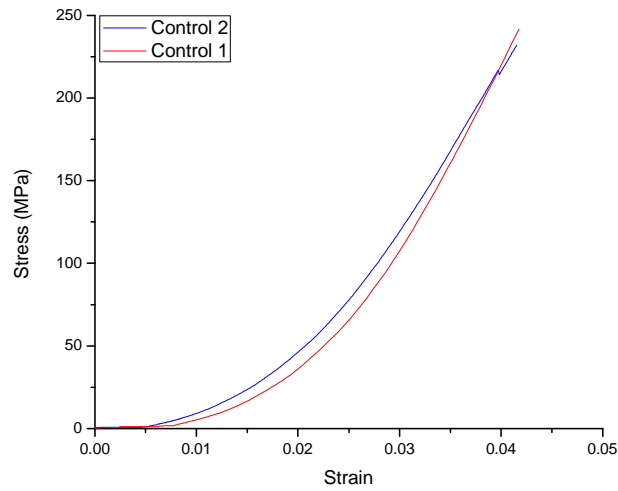


Figure 4.83 Control CFRP Tensile Testing

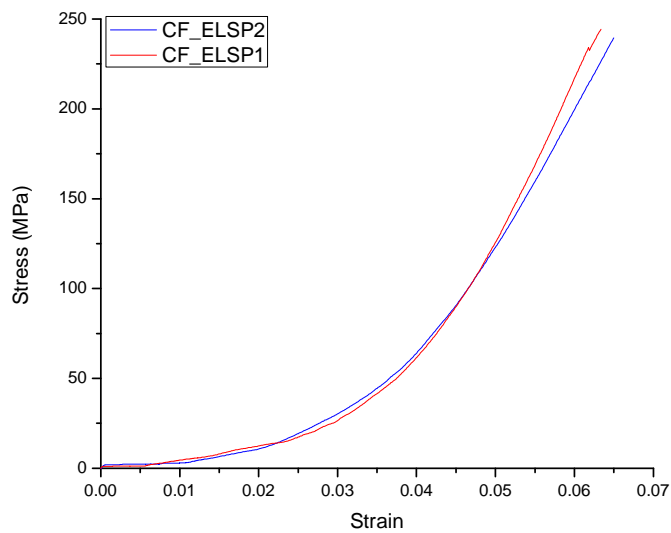


Figure 4.84 CFRP with Electrospun Fiber Interlayer Tensile Testing

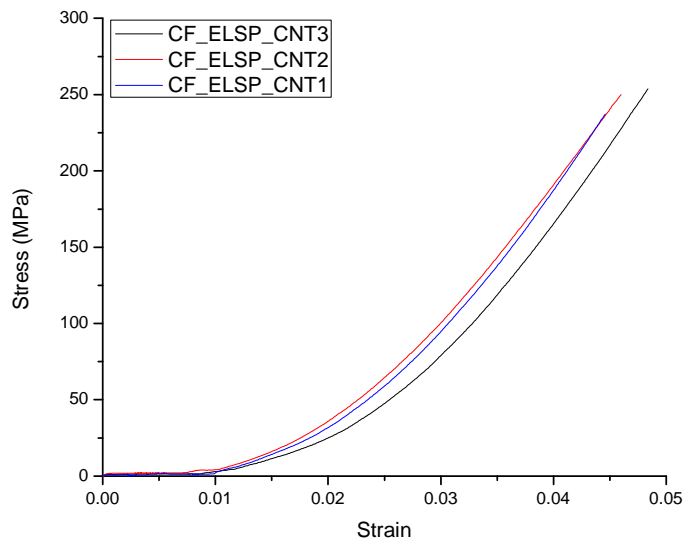


Figure 4.85 CFRP with CNT Reinforced Electrospun Fiber Interlayer Tensile Testing

There is no significant tensile strength increase from the control to the CFRP with epoxy foamed interlayer and to the CFRP with CNT epoxy foamed interlayer. The following Table 4.56 summarizes the values deriving for the electrospun interlayer samples when tested in tensile testing experiments.

Table 4.56 Tensile Testing Summary of CFRP Composites with CNT Electrospun Fibers

	Tensile Strength (MPa)	Tensile Modulus (GPa)
Control CFRP	238±5.3	9.83±2.6
CFRP+ELSP	244±4.25	8.43±0.6
CFRP+ ELSP +CNT	247±8.64	9.27±0.3

It can be seen that there is no significant increase of tensile strength from control to electrospun samples. A slight increase, which is however within the standard deviation limits, can be observed. This indicates that the electrospun interlayer does not really contribute;

nevertheless, it does not deteriorate as well the tensile strength. Similar is the behavior of the tensile strength from the electrospun to the CNT electrospun CFRP samples, where there is almost no change at all. As a result the CNT reinforcement contributes to the, flexural strength, stiffness, and Mode II fracture toughness improvement but not to higher tensile strength. This is quite explainable by the fact that fibers are dominant in the axial load transfer mechanisms which are present in tensile testing.

4.6.3.3 Fracture Toughness

At this point, working on the same way that Mode II flexural testing was performed in section 4.3.2 for the micro-spheres reinforced interlayer, Mode II fracture toughness is calculated and compared for the three types of samples in order to evaluate Mode II fracture toughness of the CNT reinforced electrospun interlayer system. The Mode II fracture toughness evaluation is done through equation 41 for calculating G_{IIC} (energy release rate) and is presented in Table 4.57.

Table 4.57 Mode II Fracture Toughness Improvement of CFRP with Electrospun Fiber Interlayer

	Control CFRP (C1)	CFRP with ELSP Interlayer (C2)	CFRP with CNT reinforced ELSP Interlayer (C3)
Modulus of Elasticity (GPa)	9.8	8.43	9.3
Moment of Inertia (m^4)	$1.43 \cdot 10^{-12} \pm 1.24 \cdot 10^{-13}$	$1.85 \cdot 10^{-12} \pm 2.8 \cdot 10^{-14}$	$2.3 \cdot 10^{-12} \pm 9.6 \cdot 10^{-14}$
Stiffness (N*m)	0.1 ± 0.01	0.12 ± 0.002	0.17 ± 0.007
Compliance (1/S)	9.34 ± 0.84	8.34 ± 0.125	$2.06.08 \pm 0.25$
Flex Max Load (N)	16.13 ± 2.0133	27.6 ± 1.2	35.9 ± 2.093
G_{IIC} (J/m ²)	334 ± 55	780 ± 55.73	892 ± 89.6

Complementary to Table 4.57, Figure 4.86, and Figure 4.87 present the stiffness and the Mode II energy release rate respectively.

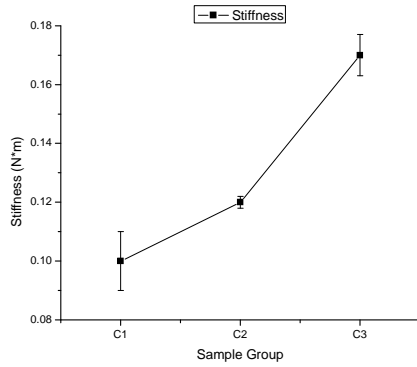


Figure 4.86 Stiffness Improvement of Electrospun Fiber Interlayer

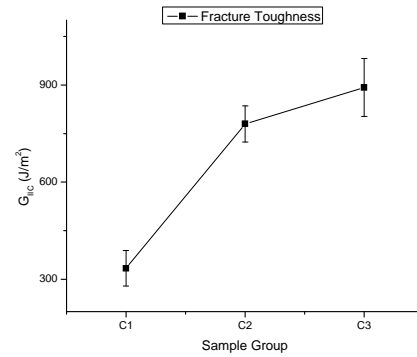


Figure 4.87 Mode II Fracture Toughness Improvement of Electrospun Fiber Interlayer

4.6.4 SEM Interlayer Micro-Characterization

The different layers of carbon fibers have already been observed on control CFRP samples fracture surfaces from flexural mechanical testing Figure 4.60.

Following, Figure 4.88 shows failure surface from flexural testing of the electrospun microfiber interlayer within the CFRP layers.

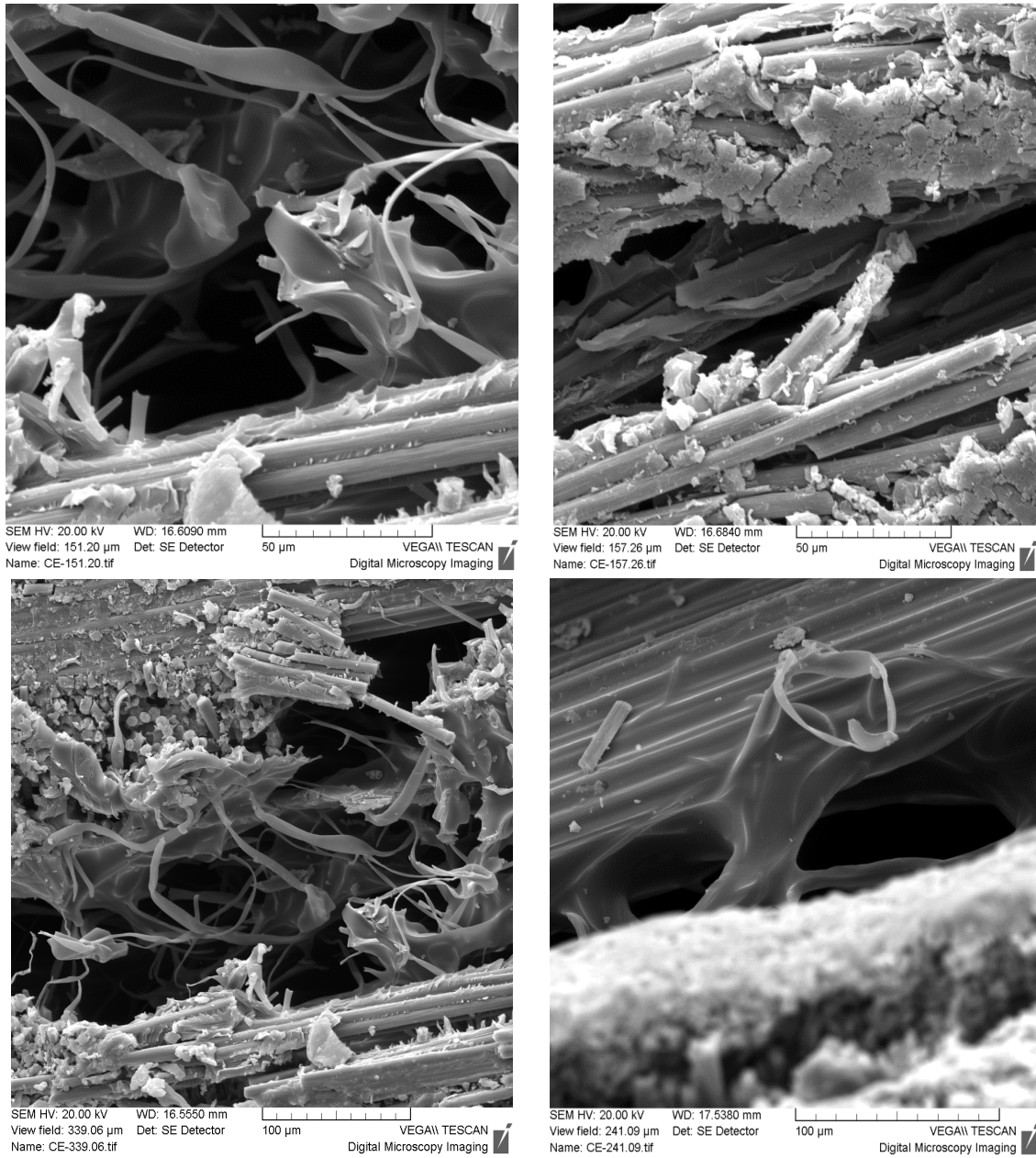


Figure 4.88 (SEM) Electrospun Fiber Interlayer within CFRP Plies

Figure 4.89 presents electrospun fibers on CFRP layer without presence of resin, exactly as they come out of the electrospinning configuration.

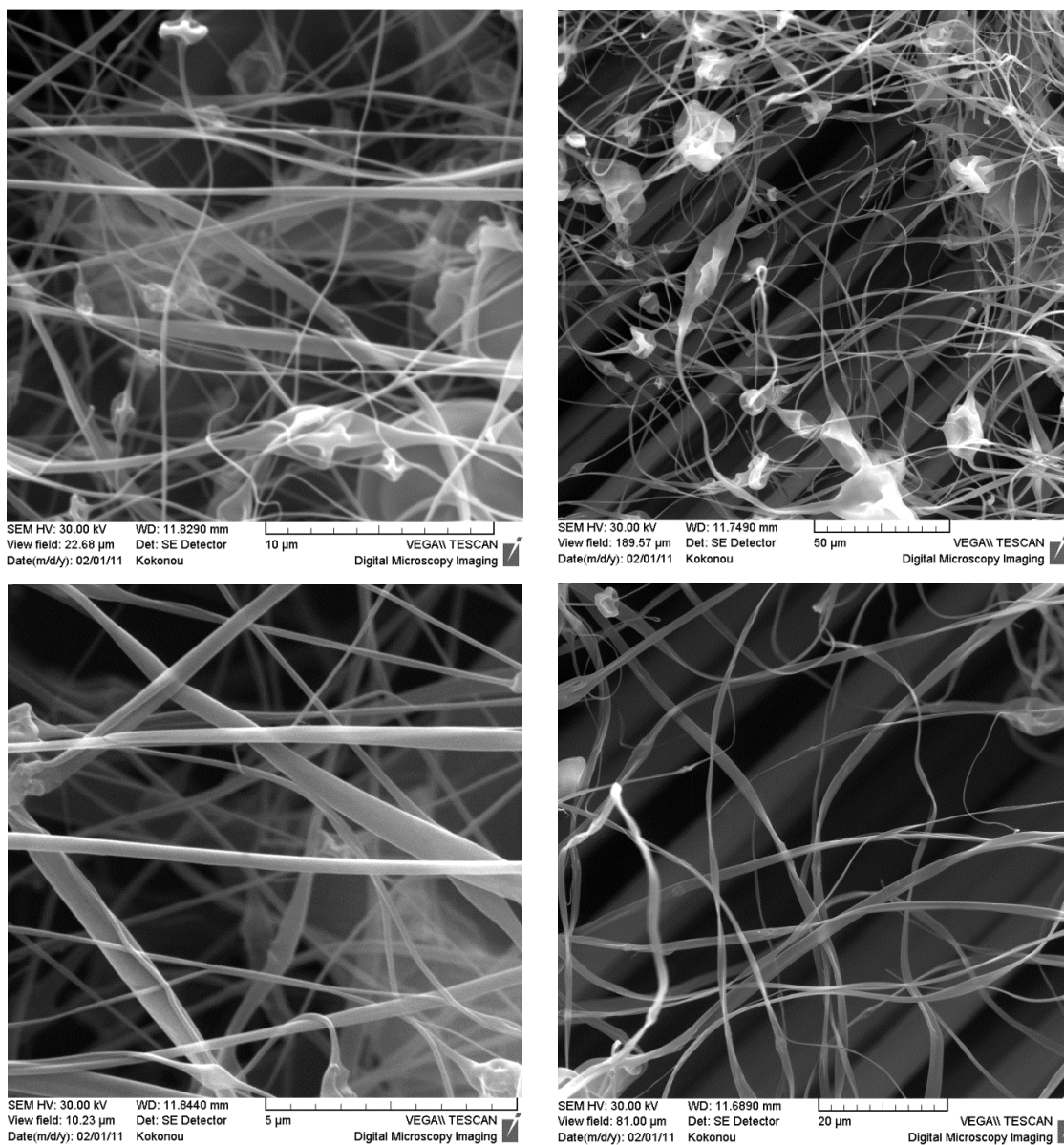


Figure 4.89 (SEM) Electrospun Fibers on Top of Fiber Bed prior to Polymerization

The graphs presented in Figure 4.90 show electrospun fibers that include CNT. CNT agglomerates are probably shown on the surface. These small spots, which are thought to be CNT agglomerates, are not present in the figures of the electrospun fibers that do not contain CNT.

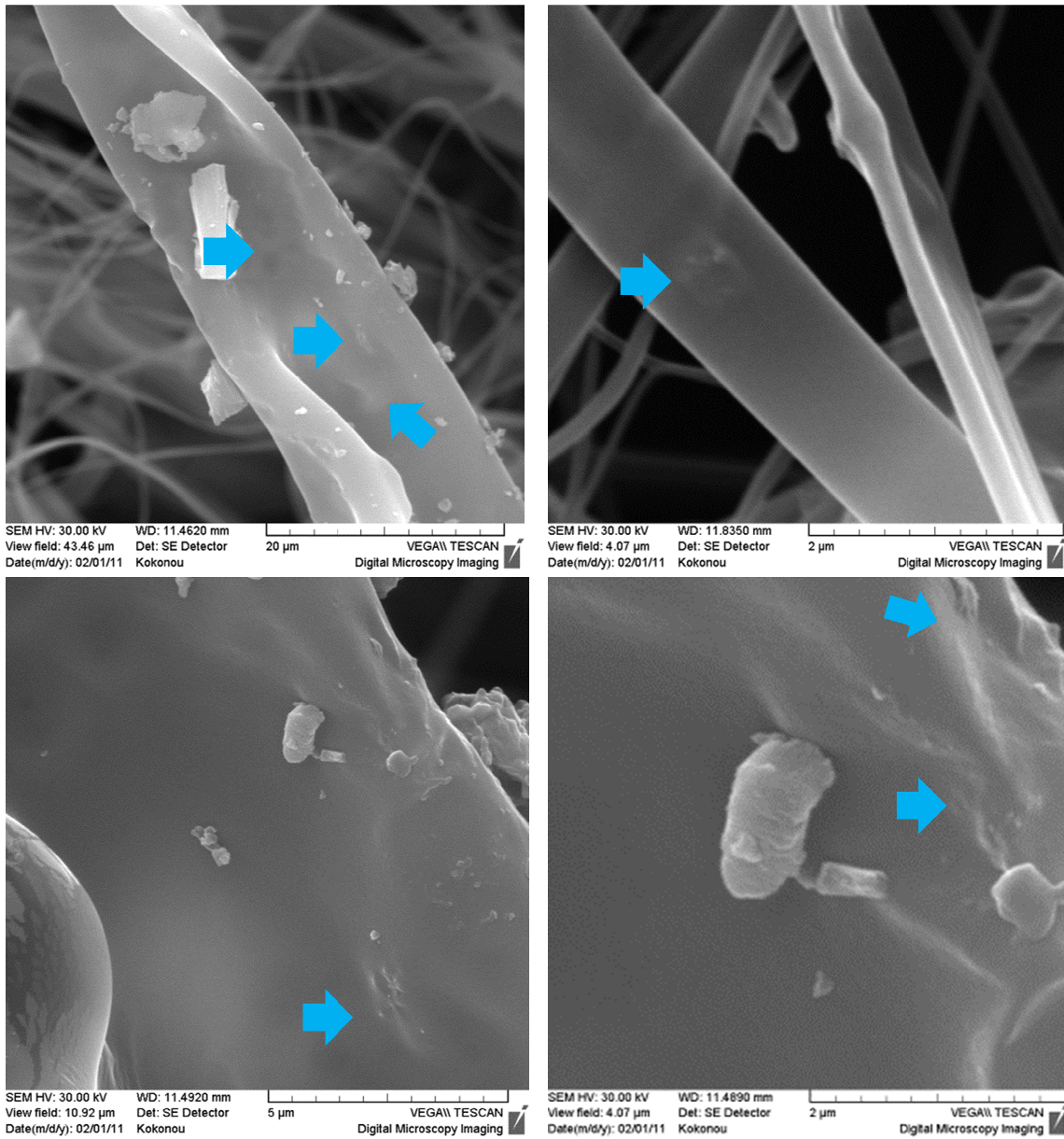


Figure 4.90 (SEM) Electrospun Fibers including CNT

In Figure 4.91, CNT reinforced electrospun microfiber interlayer is clearly observed (right pictures in Figure 4.91). The CNT in this case are not clearly observed. Additionally, the interface between fiber bed and interlayer includes hackle formation as this was presented in section 2.5 (left pictures in Figure 4.91). At this point, it must be noted that due to the exothermic reaction of polymerization the electrospun microfibers in some areas of the sample

may have been melted and thus agglomerated to bigger masses of the polymer that is used for electrospinning, thus the agglomerates of CNT shown before in samples prior to polymerization, cannot be seen in all the polymerized samples. However, melting of the electrospun fibers, especially at junction points, may yield a connected network which can transfer stress better than unconnected fibers. It may also yield anchoring nodes with the matrix polymer, also improving stress transfer.

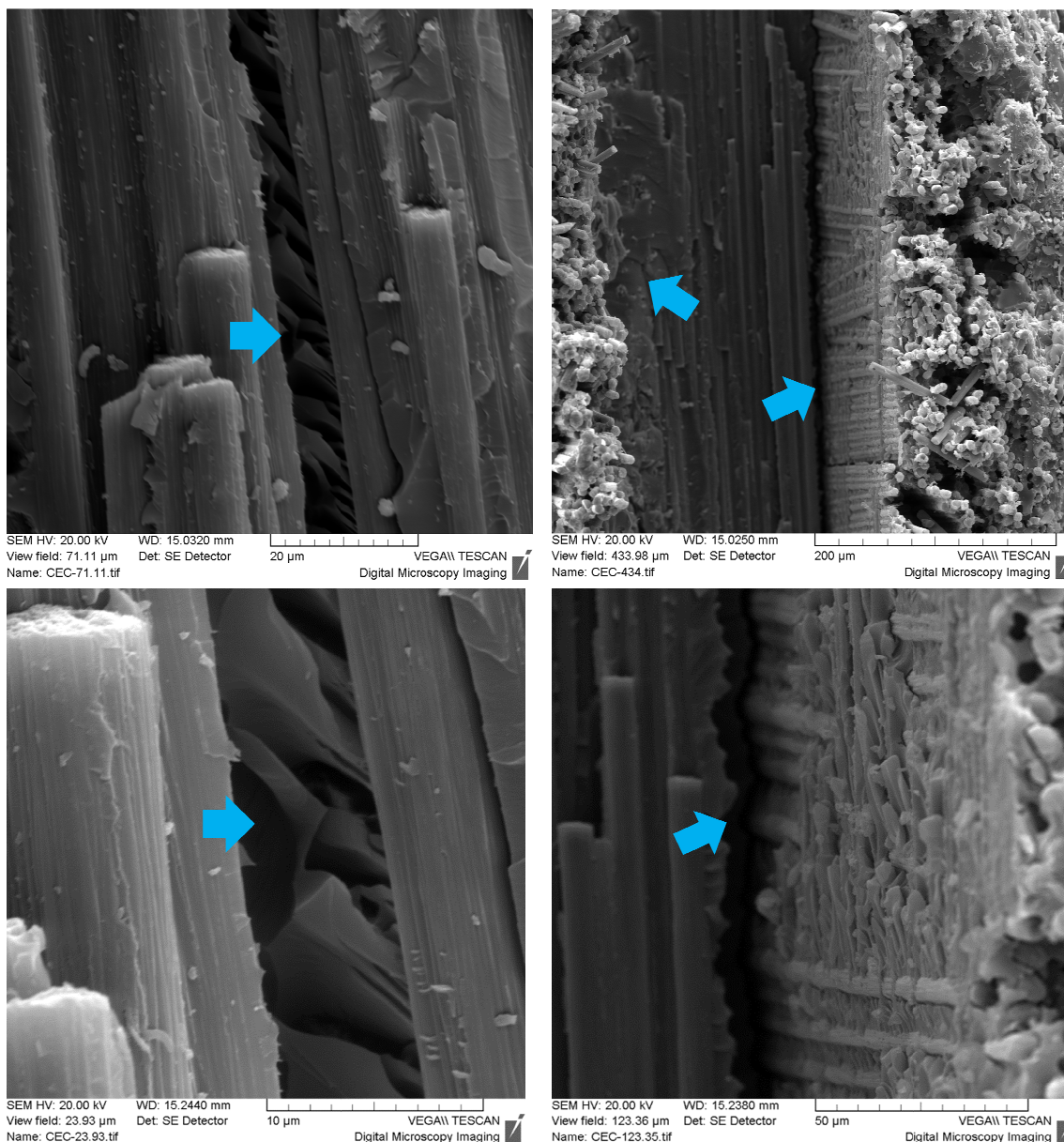


Figure 4.91 (SEM) CNT Reinforced Electrospun Fiber Interlayer within CFRP Plies

Finally, Figure 4.92 presents lower magnification of the CNT reinforced electrospun interlayered CFRP layers. The electrospun microfiber interlayers are well observed and identified within the CFRP layers.

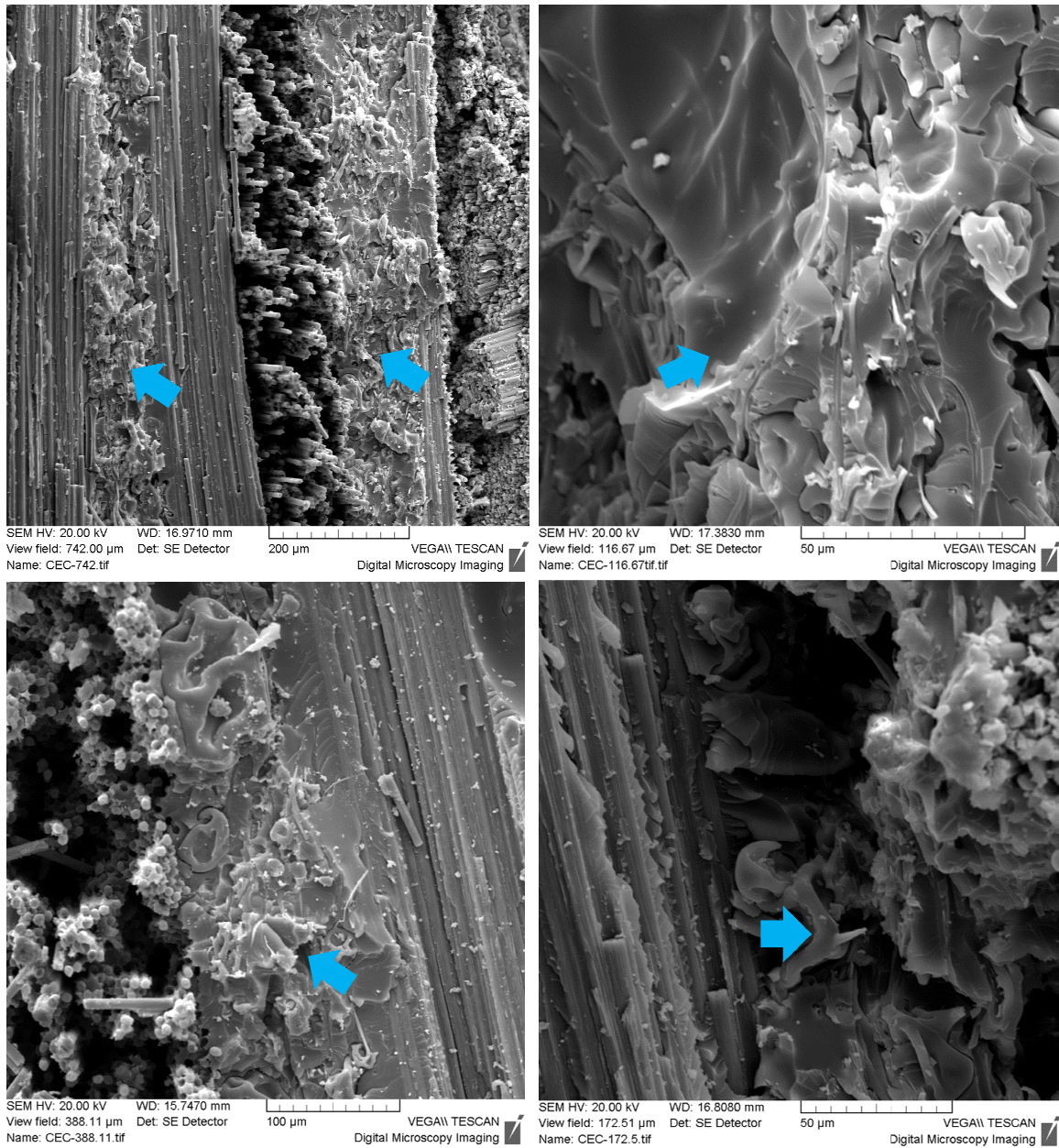


Figure 4.92 (SEM) CNT Reinforced Electrospun Fiber Interlayer within CFRP Plies

4.6.5 Parametrical Prediction of Strength

In this section an effort is made to predict the material flexural strength through given properties of the material such as flexural modulus and glass transition temperature, through the tension strength which can be easily measured and through the interlayer improvement. The latter can be translated as Mode II fracture toughness energy release rate. As a result a linear regression model will be constructed with its variable presented in Table 4.58.

Table 4.58 Preliminary Model Variables – Electrospun Fiber Interlayer CFRP

Response Variable (y)	Flexural Strength (MPa)
Predictor Variable (x1)	Flexural Modulus (GPa)
Predictor Variable (x2)	Tension Strength (MPa)
Predictor Variable (x3)	Glass Transition Temperature ($^{\circ}\text{C}$), through $\tan\delta$
Predictor Variable (x4)	Mode II energy-release rate (kJ/m^2) [Interlayer Improvement]

Next, the Pearson pairwise correlations followed by a scatter plot matrix of the variables from Table 4.58 are presented (Table 4.59, and Figure 4.93).

Table 4.59 Pearson Correlation Matrix – Electrospun Fiber Interlayer CFRP

	Y	X1	X2	X3	X4
Y	1	0.948335	0.674807	-0.40438	0.907305
X1	0.948335	1	0.667254	-0.34779	0.8841
X2	0.674807	0.667254	1	-0.34483	0.66368
X3	-0.40438	-0.34779	-0.34483	1	-0.44844
X4	0.907305	0.8841	0.66368	-0.44844	1

In Table 4.59 and Figure 4.93, it can be seen that there is good correlation between the Flexural Strength and both flexural modulus and interlayer improvement. Tension strength presents a correlation close to 0.7, which can be considered good as well, as tensile strength

was expected to increase with flexural strength. The glass transition temperature however, presents a low correlation at 0.4. It has not been investigated how the glass transition temperature (T_g) behaves with the flexural modulus. Nevertheless, depending on the manufacturing process and the material physics, T_g was expected to increase when constant pressure is applied, to decrease when pressure is increased due to the residual internal stresses, and again to decrease when an interlayer of lower crosslinking or crystalline content is added within the plies. Specifically in this material with the electrospun fiber interlayer, although the pressure is constant while manufacturing, it was expected to have T_g decreasing while flexural strength is increasing. Apparently, flexural strength increase means larger amount of electrospun fibers into the interlayer, with the latter being amorphous or semi-crystalline and thus having much lower T_g than the epoxy resin of the fiber bed. The value of -0.4 demonstrates a decrease of T_g as flexural strength is increased, however this is not highly correlated. The nonzero correlations between the predictor variables indicate the presence of multicollinearity. Nevertheless, concern is raised for high correlations (above 0.7) of interlayer improvement with flexural modulus. High multicollinearity can result in high variance (low precision) in the estimated coefficients. However, this matter will be examined later through the variance inflation diagnostics.



Figure 4.93 Scatter Plot – Electrospun Fiber Interlayer CFRP

Table 4.60i Model Data – Electrospun Fiber Interlayer CFRP

Flexural Strength (MPa)	Flexural Modulus (GPa)	Tension Strength (MPa)	Glass Transition Temperature (°C)	Mode II energy-release rate (J/m ²) [Interlayer Improvement]
190.5	26	241.6	55.4	292.4
198.3	26	231.9	56.1	300.2
207.6	28	240.5	57.2	389.3
173.2	23	234.1	53.6	344.6
194.3	24	232.5	53.9	361.4
220.95	27	240.1	54.8	313.2
212.4	25	239	55.1	321.7
232	29	244.3	54.6	604.5
294	39	239.4	54.9	693.8
289	38	248	53.2	674.3
273.4	37	247.1	52.8	627.8
267.8	36	240.5	55.6	632.1
251.4	35	242	55.1	681.4
258.3	37	245	53.8	669.8

Table 4.61ii Model Data – Electrospun Fiber Interlayer CFRP

Flexural Strength (MPa)	Flexural Modulus (GPa)	Tension Strength (MPa)	Glass Transition Temperature (°C)	Mode II energy-release rate (J/m ²) [Interlayer Improvement]
298	38	237.27	53.7	945
266.7	34	250	53.4	757.3
279.6	40	253.6	54.7	833.8
299	36	249.1	54.3	782
273	37	244.6	54.1	893.1
288	35	251.6	53.9	903.4
293	39	248	54.2	819.6

Table 4.60 presents the data used for the preliminary fitted model. Utilizing origin lab software, version 8 (138), the linear regression analysis is done. Following, Table 4.62 gives the parameters and Table 4.63 the ANOVA Table of the preliminary fitted model. Table 4.64 gives additional information for the regression of the preliminary fitted model.

Table 4.62 Parameters of the Preliminary Fitted Model – Electrospun Fiber Interlayer CFRP

	Value	Standard Error	t-Value	Prob> t	Variance Inflation
Flexural Strength	89.28356	235.70655	0.37879	0.70982	0
X1-Flexural Modulus (GPa)	4.73729	1.09747	4.31655	5.31995E-4	4.92805
X2-Tension Strength (MPa)	0.20846	0.64483	0.32328	0.75067	1.906687
X3-Glass Transition Temperature (°C)	-1.40528	3.10427	-0.45269	0.65685	1.281986
X4-Mode II energy-release rate (kJ/m ²) [Interlayer Improvement]	0.05191	0.02935	1.76863	0.09601	5.262327

Table 4.63 ANOVA Table – Electrospun Fiber Interlayer CFRP

	DF	Sum of Squares	Mean Square	F Value	Prob>F
Model	4	31061.0239	7765.25597	47.76105	1.06608E-8
Error	16	2601.36849	162.58553		
Total	20	33662.39238			

Table 4.64 Other Parameters of the Preliminary Model Regression – Electrospun Fiber Interlayer CFRP

Number of Points	21
Degrees of Freedom	16
Residual Sum of Squares	2601.36849
R Value	0.96058
R Square	0.92272
Adj. R Square	0.9034
Root MSE	12.7509

Through the analysis, it can be seen that the regression is significant since the p-value for the F-test on the regression is much smaller than a significance level of $\alpha = 0.1$. Furthermore, the high R^2 value shows that 92% of the variability in flexural strength is explained by this current model. With regard to multicollinearity, one variance inflation factor is above 5.0, and one is near 5.0. This indicates an inflation of the variance for these estimated coefficients is about a factor of 5, which is considered to be too high. Alternative models will have to be explored.

Additional to the above tables, Figure 4.94 contains several figures with information about the residuals of the model. Residuals are plotted versus each predictor variable and versus the fitted values obtained from the current model. A normal probability plot of the residuals is presented to assess the probability distribution of the residuals. Finally, in the bottom plot the residuals over the time order are plotted.

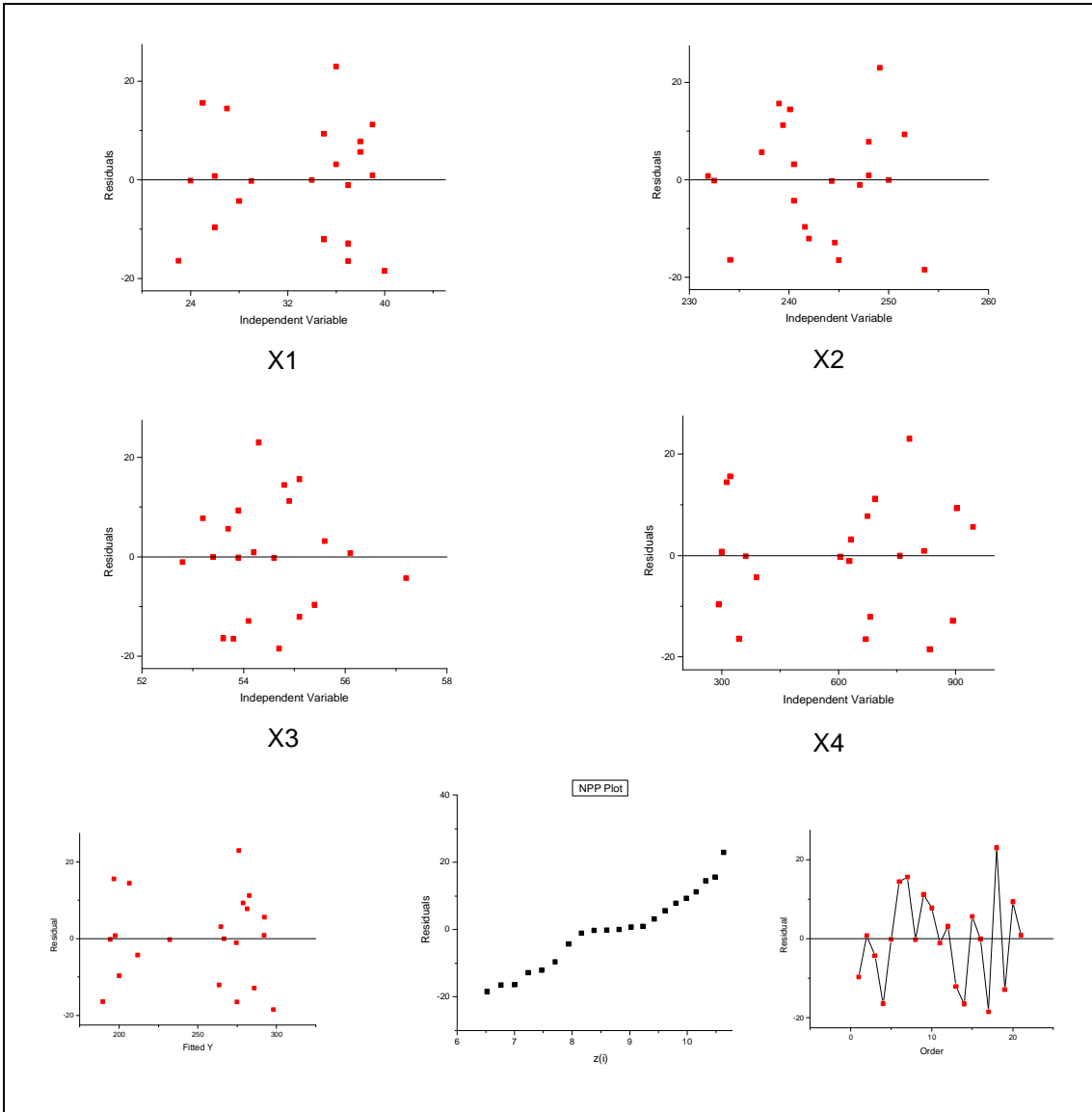


Figure 4.94 Residuals Analysis of the Preliminary Fitted Model – Electrospun Fiber Interlayer CFRP

Before going into the interpretation of the residual analysis, the model assumptions have to be clearly stated.

Assumptions:

Model Assumptions:

1. *MLR model form is reasonable.*
2. *Residuals have constant variance.*
3. *Residuals are normally distributed.*
4. *Residuals are uncorrelated.*

Based on the analysis so far, the preliminary current model is:

$$\hat{y} = 89.284 + 4.74 \cdot x_1 + 0.2085 \cdot x_2 - 1.4053 \cdot x_3 + 0.0519 \cdot x_4$$

Where variable \hat{y} , is the fitted flexural modulus, and x_1, x_2, x_3, x_4 are defined in Table 4.58.

Regarding the first model assumption, the graphs of Figure 4.94 plotting the residuals over the predictor variables have to present no curvature. As it can be seen within Figure 4.94 there is no curvature within the plots of residuals over the predictor variables and as a result it can concluded that the model form is reasonable.

Yhat	ei	Rank	e1i	e2i	d1i	d2i
200.14254	-9.64254	6	-18.45171	0.75839	10.11130273	8.416056
197.54161	0.75839	12	-16.49925	0.8874	8.158842727	8.287046
211.88798	-4.28798	7	-16.40618	3.16249	8.065772727	6.011956
189.60618	-16.40618	3	-12.88484	5.64988	4.544432727	3.524566
194.46036	-0.16036	10	-12.07451	7.76132	3.734102727	1.413126
206.48995	14.46005	19	-9.64254	9.31481	1.302132727	0.140364
196.80567	15.59433	20	-4.28798	11.19363	4.052427273	2.019184
232.2413	-0.2413	9	-1.06226	14.46005	7.278147273	5.285604
282.80637	11.19363	18	-0.2413	15.59433	8.099107273	6.419884
281.23868	7.76132	16	-0.16036	22.96216	8.180047273	13.787714
274.46226	-1.06226	8	-0.03355		8.306857273	
264.63751	3.16249	14				
263.47451	-12.07451	5				
274.79925	-16.49925	2				
292.35012	5.64988	15				
266.73355	-0.03355	11				
298.05171	-18.45171	1				
276.03784	22.96216	21				
285.88484	-12.88484	4				
278.68519	9.31481	17				
292.1126	0.8874	13				
			Avg	Avg	Avg	Avg
			-8.340407273	9.174446	6.53028843	5.53055
					(d1i-d(avg)1)^2	(d2i-d(avg)2)^2
					12.8236634	8.326144876
					2.6521891	7.598270198
					2.357712028	0.231751737
					3.943622871	4.023971808
					7.818654483	16.9531804
					27.33361205	29.05410511
					6.139795913	12.32969119
					0.559292849	0.059998543
					2.461192562	0.790914964
					2.72170424	68.18075732
					3.156196854	
			Sum		71.96763635	147.5487861
					s^2	10.45316298
					t*	-0.6914289

Figure 4.95 Microsoft XL (139) Algorithm for Levene's Test – Electrospun Fiber Interlayer CFRP

The second assumption is that the residuals have constant variance. This can be seen from the residuals versus the fitted values. In this case there is no funnel shape so the residuals must have constant variance. However, there is a constant variance test (Levene's test Figure 4.95) that will be performed to assure the constant variance of residuals.

Hypothesis:

$$H_0: \text{Error Variance is Constant } (H_0 : \sigma_{d1} = \sigma_{d2})$$

$$H_1: \text{Error Variance is Not Constant } (H_1 : \sigma_{d1} \neq \sigma_{d2})$$

$$t^* = 0.69 < t(0.95;15) = 1.753$$

The t-test conducted with the t-value derived from Levene's test (Figure 4.95) fails to reject H_0 , thus, constant error variance is verified to be a reasonable assumption.

The normal probability plot within Figure 4.94 exhibits a mostly straight line with a curve at the left. This indicates that the distribution of the residuals is overall similar to a normal distribution, except that it has a longer left tail. However, normality is not a required assumption. A normality test will be performed to assess if normality is violated.

Hypothesis:

$$H_0: \text{Normality Reasonable}$$

$$H_1: \text{Normality Violated}$$

$$\rho = 0.9784 > C(0.1, 21) = 0.9607$$

The test fails to reject H_0 , thus normality is not violated and assumption 3 is fulfilled as well.

Finally, the time plot in Figure 4.94 appears to show a random jagged pattern. This indicates that correlation over time is not a problem.

Diagnostics:

The variance inflation factors are quite high compared to the desired values for flexural modulus and interlayer improvement. More specifically, VIF_1 and VIF_4 are close to 5 and above 5 respectively, thus for those predictor variables variance is inflated almost 5 times. As a result, the issue of variance inflation will continue to be monitored, due to multicollinearity. Following, Figure 4.96, and Figure 4.97 show the results from the outlier analysis as well as their influences. In Figure 4.96, the Bonferroni outlier test and the x-outlier diagnostic do not detect any outliers.

yhat	e	Standardized	Studentized	cookdi	hii	ti	Studentized Deleted	dffitsi	x-outlier - hii 2*p/n	Bonferonni - ti t[1-.1/2(21);n-p-1]	DFFITs	COOKDi
layer Improvement)									0.476190476	3.4579	1	1
200.14254	-9.64254	-0.756222989	-0.8482443	0.037153	0.2052	-0.840419183	-0.427	ok	ok	ok	ok	ok
197.54161	0.75839	0.05947727	0.06918769	0.000338	0.261	0.067000403	0.03982	ok	ok	ok	ok	ok
211.88798	-4.28798	-0.336287851	-0.4367743	0.026209	0.4072	-0.425446885	-0.3526	ok	ok	ok	ok	ok
189.60618	-16.40618	-1.286666219	-1.5816213	0.256671	0.3382	-1.667260405	-1.1919	ok	ok	y-outlier	ok	ok
194.46036	-0.16036	-0.012576346	-0.0150391	1.95E-05	0.3007	-0.014561611	-0.0095	ok	ok	ok	ok	ok
206.48995	14.46005	1.134039603	1.23955412	0.059844	0.163	1.262327728	0.55706	ok	ok	ok	ok	ok
196.80567	15.59433	1.222996311	1.32722858	0.062611	0.1509	1.362252237	0.57428	ok	ok	ok	ok	ok
232.2413	-0.2413	-0.018924122	-0.0207382	1.73E-05	0.1673	-0.020079872	-0.009	ok	ok	ok	ok	ok
282.80637	11.19363	0.877868315	1.0477576	0.093203	0.298	1.051184732	0.68489	ok	ok	ok	ok	ok
281.23868	7.76132	0.608686986	0.70715435	0.034976	0.2591	0.695653339	0.41138	ok	ok	ok	ok	ok
274.46226	-1.06226	-0.083308488	-0.1031412	0.001134	0.3476	-0.099898815	-0.0729	ok	ok	ok	ok	ok
264.63751	3.16249	0.248020505	0.27557834	0.003563	0.19	0.267461847	0.12954	ok	ok	ok	ok	ok
263.47451	-12.07451	-0.946951949	-0.9961846	0.021174	0.0964	-0.99592691	-0.3253	ok	ok	ok	ok	ok
274.79925	-16.49925	-1.293965299	-1.3915214	0.060596	0.1353	-1.437089931	-0.5685	ok	ok	ok	ok	ok
292.35012	5.64988	0.443095817	0.62278276	0.075671	0.4938	0.610448337	0.60293	x-outlier	ok	ok	ok	ok
266.73355	-0.03355	-0.002631182	-0.0029293	4.11E-07	0.1932	-0.002836297	-0.0014	ok	ok	ok	ok	ok
298.05171	-18.45171	-1.44708835	-1.6653013	0.179887	0.2449	-1.77340974	-1.01	ok	ok	y-outlier	ok	ok
276.03784	22.96216	1.800823567	1.91306531	0.094087	0.1139	2.109172316	0.75619	ok	ok	ok	ok	ok
285.88484	-12.88484	-1.01050265	-1.1169356	0.055328	0.1815	-1.126261978	-0.5304	ok	ok	ok	ok	ok
278.68519	9.31481	0.730520533	0.9029789	0.086084	0.3455	0.897468112	0.65206	ok	ok	ok	ok	ok
292.1126	0.8874	0.06959497	0.07366713	0.000131	0.1075	0.07133966	0.02476	ok	ok	ok	ok	ok

Figure 4.96 Outliers and Influence – Electrospun Fiber Interlayer CFRP

DFBETAS						Flag influence				
Intercept	Flexural Modt	Tension Stri	Glass Tra	Mode II energy-release rate		x0	x1	x2	x3	x4
0.17232	0.019728	-0.21214	-0.071	0.18375		ok	ok	ok	ok	ok
0.0014927	0.0046509	-0.019591	0.0157	-0.0032883		ok	ok	ok	ok	ok
0.26148	0.039491	-0.074038	-0.304	-0.017863		ok	ok	ok	ok	ok
-0.76447	0.45654	0.32143	0.6769	-0.12997		ok	ok	ok	ok	ok
-0.0066727	0.0027463	0.004487	0.0046	-0.0012143		ok	ok	ok	ok	ok
-0.0058279	0.090493	0.14563	-0.105	-0.33885		ok	ok	ok	ok	ok
-0.078403	-0.17535	0.14101	0.0306	-0.086915		ok	ok	ok	ok	ok
0.0026559	0.0073975	-0.003451	-0.002	-0.0052386		ok	ok	ok	ok	ok
0.15442	0.51674	-0.40903	0.0809	-0.21561		ok	ok	ok	ok	ok
0.11159	0.25308	0.07723	-0.248	-0.28011		ok	ok	ok	ok	ok
-0.029393	-0.041543	-0.009805	0.0531	0.050326		ok	ok	ok	ok	ok
-0.02496	0.068084	-0.049552	0.0694	-0.020413		ok	ok	ok	ok	ok
0.063831	-0.054282	0.10671	-0.173	-0.066501		ok	ok	ok	ok	ok
-0.17579	-0.38916	0.029252	0.2592	0.33919		ok	ok	ok	ok	ok
0.32637	-0.055646	-0.46456	-0.047	0.34803		ok	ok	ok	ok	ok
0.00011786	0.00067263	-0.000795	0.0005	-0.00035843		ok	ok	ok	ok	ok
0.68496	-0.15768	-0.63526	-0.352	0.11233		ok	ok	ok	ok	ok
-0.34295	-0.23472	0.39704	0.1427	0.24092		ok	ok	ok	ok	ok
-0.051749	0.19814	0.14912	-0.07	-0.39802		ok	ok	ok	ok	ok
-0.21425	-0.47545	0.29585	0.0822	0.44843		ok	ok	ok	ok	ok
-0.0043634	0.0076899	0.003182	0.0018	-0.00057143		ok	ok	ok	ok	ok

Figure 4.97 Influence on Parameters – Electrospun Fiber Interlayer CFRP

4.6.5.1 Interactions Analysis and Best Model Exploration

Interactions between the predictor variables are investigated to allow for modeling more complex relationships. Following, interactions x_1x_2 , x_2x_3 , and x_2x_4 are presented in Figure 4.98 as they are the ones that they present some trend which can possibly benefit the model. For each interaction the residuals are plotted against the interaction, the standardized interaction and the interaction regression on all predictor variables.

In Figure 4.98, residuals are also plotted against the standardized forms of the interactions. These standardized variables are calculated by first centering the mean of predictor variables to zero and then by scaling the variance to one. Now the values approximately lie in $(-1, 1)$. Centering the predictor variables is of significant importance for multiplying them afterwards as interactions. Scaling the variance is important as well, for numerical stability. As a result, the standardized forms assist in overcoming high multicollinearity that the non standardized interactions present.

Complementing the interactions graphs is the correlation matrix in Figure 4.99, which includes all variables and interactions. It seems that the interactions are highly correlated (above 0.7). This is a common phenomenon because interaction terms are composed from the original predictors. To overcome this high multicollinearity, the standardized form is employed. Figure 4.100 shows the correlation with the standardized interactions, where it can be seen that standardized interactions have overall lower correlation with the other predictor variables.

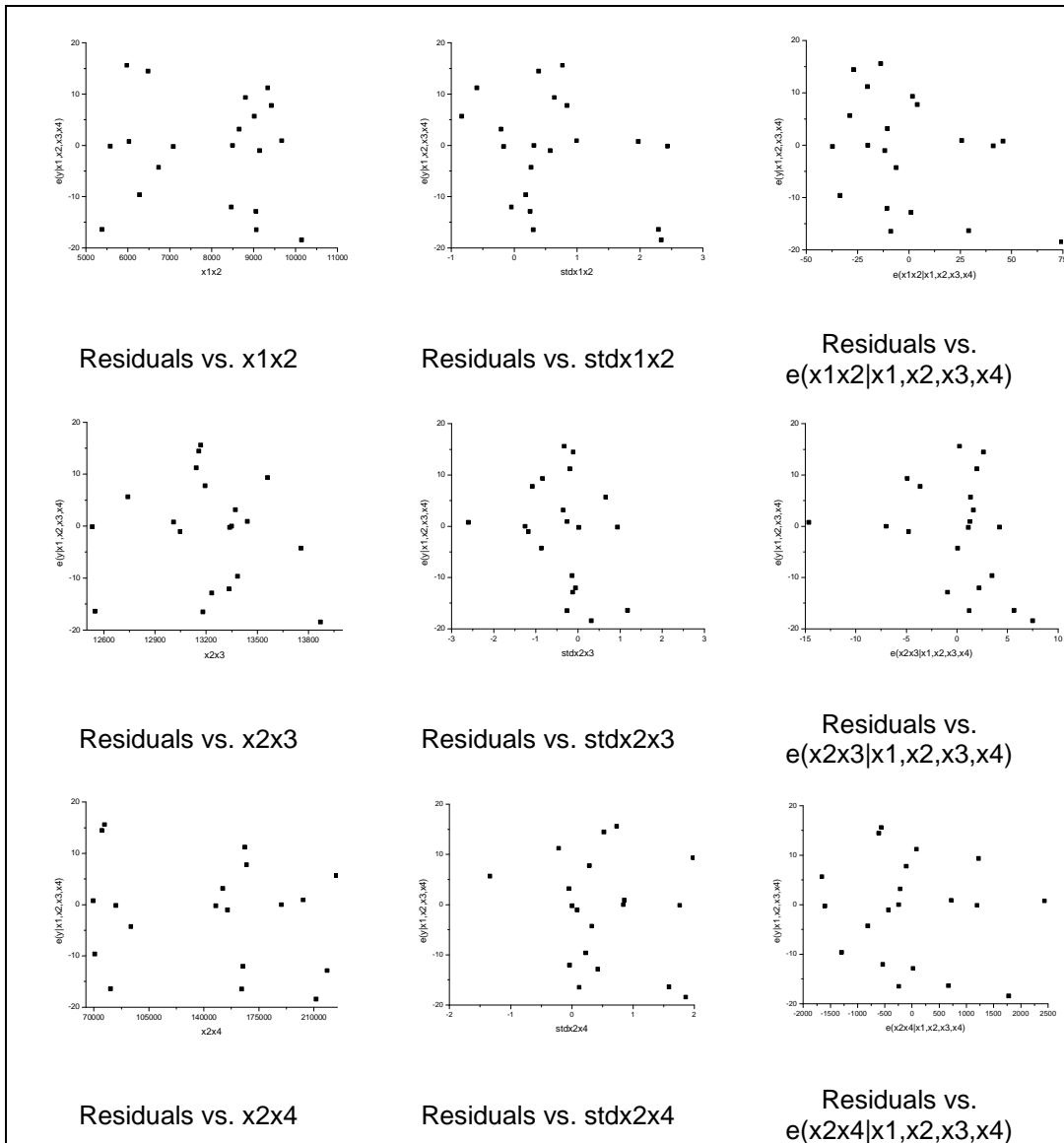


Figure 4.98 Interactions – Electrospun Fiber Interlayer CFRP

	y	x1	x2	x3	x4	x1x2	x2x4	x2x3
y - Flexural Strenght (MPa)	1	0.948335	0.674807	-0.40438	0.907305	0.947445	0.908159	0.359294
x1 - Flexural Modulus (GPa)	0.948335	1	0.667254	-0.34779	0.8841	0.994777	0.88494	0.39412
x2 - Tension Strength (MPa)	0.674807	0.667254	1	-0.34483	0.66368	0.738403	0.702854	0.72118
x3 - Glass Transition Temperature (0 C)	-0.40438	-0.34779	-0.34483	1	-0.44844	-0.36538	-0.45207	0.40142
x4 - Mode II - Fracture Energy Release rate (kJ/m2) [Interlayer Improvement]	0.907305	0.8841	0.66368	-0.44844	1	0.888936	0.998346	0.318254
x1x2	0.947445	0.994777	0.738403	-0.36538	0.888936	1	0.895293	0.450578
x2x4	0.908159	0.88494	0.702854	-0.45207	0.998346	0.895293	1	0.353671
x2x3	0.359294	0.39412	0.72118	0.40142	0.318254	0.450578	0.353671	1

Figure 4.99 Pearson Correlation (predictor variables & interactions) – Electrospun Fiber Interlayer CFRP

	y - Flexural	x1 - Flexu	x2 - Tensi	x3 - Glass	x4 - Mode	stdx1x2	stdx2x4	stdx2x3
y - Flexural Strenght (MPa)	1	0.948335	0.674807	-0.40438	0.907305	-0.42482	-0.34012	-0.10034
x1 - Flexural Modulus (GPa)	0.948335	1	0.667254	-0.34779	0.8841	-0.37899	-0.36047	-0.08852
x2 - Tension Strength (MPa)	0.674807	0.667254	1	-0.34483	0.66368	-0.13326	0.008948	-0.16612
x3 - Glass Transition Temperature (0 C)	-0.40438	-0.34779	-0.34483	1	-0.44844	-0.09074	0.053126	-0.2249
x4 - Mode II - Fracture Energy Release rate (kJ/m2) - [Interlayer Improvement]	0.907305	0.8841	0.66368	-0.44844	1	-0.34113	-0.25267	0.063616
stdx1x2	-0.42482	-0.37899	-0.13326	-0.09074	-0.34113	1	0.862109	0.063312
stdx2x4	-0.34012	-0.36047	0.008948	0.053126	-0.25267	0.862109	1	-0.19317
stdx2x3	-0.10034	-0.08852	-0.16612	-0.2249	0.063616	0.063312	-0.19317	1

Figure 4.100 Pearson Correlation (predictor variables & standardized interactions) – Electrospun Fiber Interlayer CFRP

At this point, a search for the best model that explains flexural strength will be performed. Figure 4.100 shows that there is high correlation between stdx1x2 and stdx2x4 standardized interactions. As a result, these should not be included together in the same model. Two different model searches will be performed which will include the four main predictor variables and each time one a pair of uncorrelated interactions. The first step is to do the two best subset regressions, which include all predictor variables plus the standardized interactions stdx1x2, and stdx2x3, and then all predictor variables plus the standardized interactions stdx2x4, and stdx2x3 (Figure 4.101). The best subset regression is performed with the Minitab software (140). Backward elimination and stepwise methods are also performed to compare with the best subset results and are also presented in Figure 4.102.

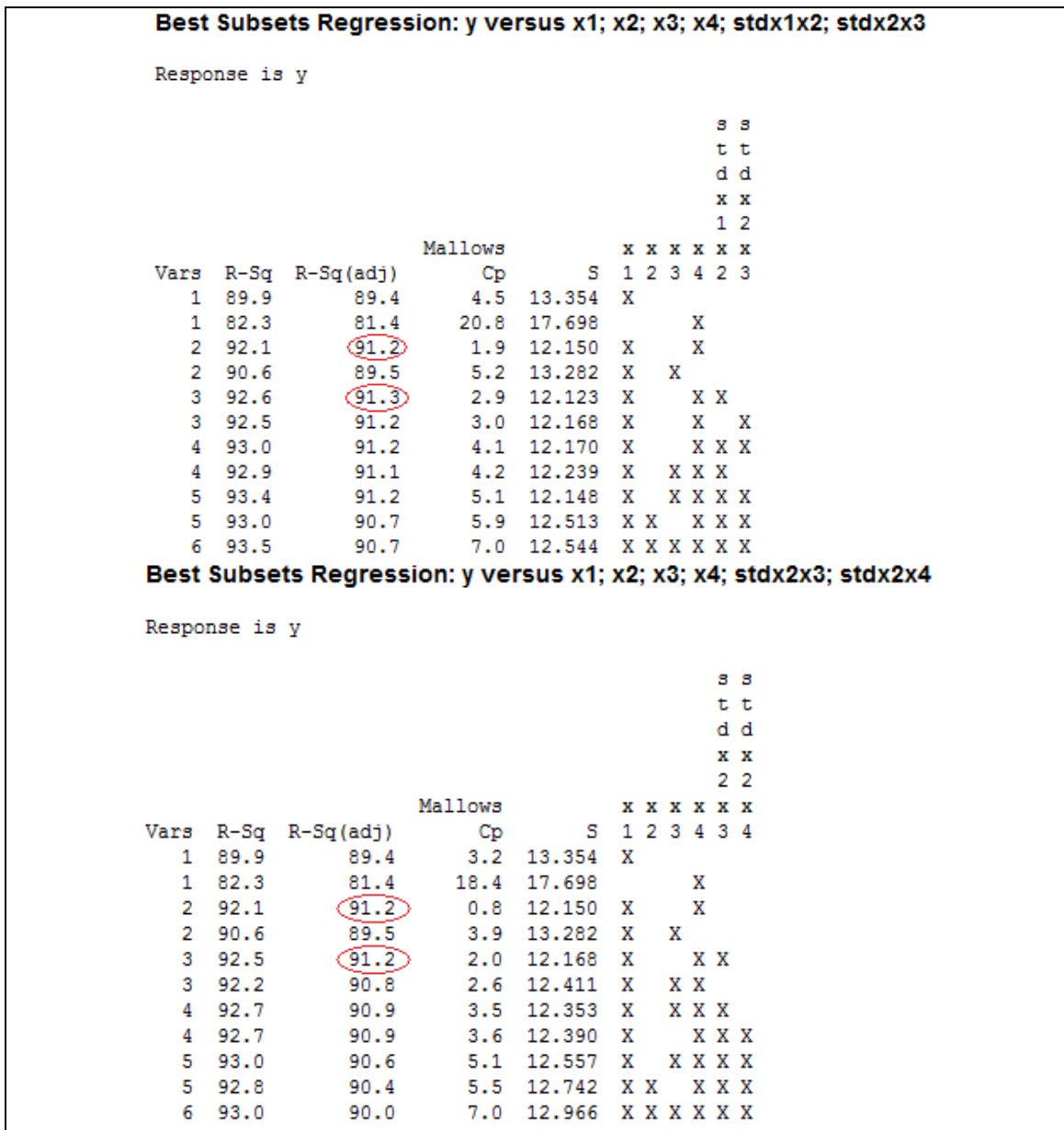


Figure 4.101 Best Subsets Regression for Evaluating All Predictor Variables in the Two Cases for Electrospun Fiber Interlayered Composite

<i>Forward Selection</i>	<i>Backward Elimination</i>																																																																																																																																																																																																																								
<p>Stepwise Regression: y versus x1; x2; x3; x4; stdx1x2; stdx2x3</p> <p>Forward selection. Alpha-to-Enter: 0.1</p> <p>Response is y on 6 predictors, with N = 21</p> <table style="width: 100%; border-collapse: collapse;"> <tr> <td style="width: 10%;">Step</td> <td style="width: 10%;">1</td> <td style="width: 10%;">2</td> <td colspan="3"></td> </tr> <tr> <td>Constant</td> <td>29.16</td> <td>58.75</td> <td colspan="3"></td> </tr> <tr> <td>x1</td> <td>6.75</td> <td>4.76</td> <td colspan="3"></td> </tr> <tr> <td>T-Value</td> <td>13.03</td> <td>4.72</td> <td colspan="3"></td> </tr> <tr> <td>P-Value</td> <td>0.000</td> <td>0.000</td> <td colspan="3"></td> </tr> <tr> <td>x4</td> <td></td> <td>0.058</td> <td colspan="3"></td> </tr> <tr> <td>T-Value</td> <td></td> <td>2.23</td> <td colspan="3"></td> </tr> <tr> <td>P-Value</td> <td></td> <td>0.039</td> <td colspan="3"></td> </tr> <tr> <td>S</td> <td>13.4</td> <td>12.1</td> <td colspan="3"></td> </tr> <tr> <td>R-Sq</td> <td>89.93</td> <td>92.11</td> <td colspan="3"></td> </tr> <tr> <td>R-Sq(adj)</td> <td>89.40</td> <td>91.23</td> <td colspan="3"></td> </tr> <tr> <td>Mallows Cp</td> <td>4.5</td> <td>1.9</td> <td colspan="3"></td> </tr> </table>	Step	1	2				Constant	29.16	58.75				x1	6.75	4.76				T-Value	13.03	4.72				P-Value	0.000	0.000				x4		0.058				T-Value		2.23				P-Value		0.039				S	13.4	12.1				R-Sq	89.93	92.11				R-Sq(adj)	89.40	91.23				Mallows Cp	4.5	1.9				<p>Stepwise Regression: y versus x1; x2; x3; x4; stdx1x2; stdx2x3</p> <p>Backward elimination. Alpha-to-Remove: 0.1</p> <p>Response is y on 6 predictors, with N = 21</p> <table style="width: 100%; border-collapse: collapse;"> <tr> <td style="width: 10%;">Step</td> <td style="width: 10%;">1</td> <td style="width: 10%;">2</td> <td style="width: 10%;">3</td> <td style="width: 10%;">4</td> <td style="width: 10%;">5</td> </tr> <tr> <td>Constant</td> <td>207.00</td> <td>250.97</td> <td>71.20</td> <td>67.21</td> <td>58.75</td> </tr> <tr> <td>x1</td> <td>4.2</td> <td>4.3</td> <td>4.3</td> <td>4.6</td> <td>4.8</td> </tr> <tr> <td>T-Value</td> <td>3.74</td> <td>3.99</td> <td>3.97</td> <td>4.48</td> <td>4.72</td> </tr> <tr> <td>P-Value</td> <td>0.002</td> <td>0.001</td> <td>0.001</td> <td>0.000</td> <td>0.000</td> </tr> <tr> <td>x2</td> <td>0.17</td> <td></td> <td></td> <td></td> <td></td> </tr> <tr> <td>T-Value</td> <td>0.26</td> <td></td> <td></td> <td></td> <td></td> </tr> <tr> <td>P-Value</td> <td>0.797</td> <td></td> <td></td> <td></td> <td></td> </tr> <tr> <td>x3</td> <td>-3.1</td> <td>-3.2</td> <td></td> <td></td> <td></td> </tr> <tr> <td>T-Value</td> <td>-0.96</td> <td>-1.03</td> <td></td> <td></td> <td></td> </tr> <tr> <td>P-Value</td> <td>0.352</td> <td>0.320</td> <td></td> <td></td> <td></td> </tr> <tr> <td>x4</td> <td>0.055</td> <td>0.057</td> <td>0.066</td> <td>0.058</td> <td>0.058</td> </tr> <tr> <td>T-Value</td> <td>1.83</td> <td>2.01</td> <td>2.39</td> <td>2.22</td> <td>2.23</td> </tr> <tr> <td>P-Value</td> <td>0.089</td> <td>0.062</td> <td>0.030</td> <td>0.041</td> <td>0.039</td> </tr> <tr> <td>stdx1x2</td> <td>-4.3</td> <td>-4.1</td> <td>-3.2</td> <td>-3.3</td> <td></td> </tr> <tr> <td>T-Value</td> <td>-1.23</td> <td>-1.24</td> <td>-1.00</td> <td>-1.04</td> <td></td> </tr> <tr> <td>P-Value</td> <td>0.239</td> <td>0.233</td> <td>0.333</td> <td>0.314</td> <td></td> </tr> <tr> <td>stdx2x3</td> <td>-3.7</td> <td>-4.0</td> <td>-3.3</td> <td></td> <td></td> </tr> <tr> <td>T-Value</td> <td>-0.98</td> <td>-1.11</td> <td>-0.93</td> <td></td> <td></td> </tr> <tr> <td>P-Value</td> <td>0.344</td> <td>0.283</td> <td>0.365</td> <td></td> <td></td> </tr> <tr> <td>S</td> <td>12.5</td> <td>12.1</td> <td>12.2</td> <td>12.1</td> <td>12.1</td> </tr> <tr> <td>R-Sq</td> <td>93.46</td> <td>93.42</td> <td>92.96</td> <td>92.58</td> <td>92.11</td> </tr> <tr> <td>R-Sq(adj)</td> <td>90.65</td> <td>91.23</td> <td>91.20</td> <td>91.27</td> <td>91.23</td> </tr> <tr> <td>Mallows Cp</td> <td>7.0</td> <td>5.1</td> <td>4.1</td> <td>2.9</td> <td>1.9</td> </tr> </table>	Step	1	2	3	4	5	Constant	207.00	250.97	71.20	67.21	58.75	x1	4.2	4.3	4.3	4.6	4.8	T-Value	3.74	3.99	3.97	4.48	4.72	P-Value	0.002	0.001	0.001	0.000	0.000	x2	0.17					T-Value	0.26					P-Value	0.797					x3	-3.1	-3.2				T-Value	-0.96	-1.03				P-Value	0.352	0.320				x4	0.055	0.057	0.066	0.058	0.058	T-Value	1.83	2.01	2.39	2.22	2.23	P-Value	0.089	0.062	0.030	0.041	0.039	stdx1x2	-4.3	-4.1	-3.2	-3.3		T-Value	-1.23	-1.24	-1.00	-1.04		P-Value	0.239	0.233	0.333	0.314		stdx2x3	-3.7	-4.0	-3.3			T-Value	-0.98	-1.11	-0.93			P-Value	0.344	0.283	0.365			S	12.5	12.1	12.2	12.1	12.1	R-Sq	93.46	93.42	92.96	92.58	92.11	R-Sq(adj)	90.65	91.23	91.20	91.27	91.23	Mallows Cp	7.0	5.1	4.1	2.9	1.9
Step	1	2																																																																																																																																																																																																																							
Constant	29.16	58.75																																																																																																																																																																																																																							
x1	6.75	4.76																																																																																																																																																																																																																							
T-Value	13.03	4.72																																																																																																																																																																																																																							
P-Value	0.000	0.000																																																																																																																																																																																																																							
x4		0.058																																																																																																																																																																																																																							
T-Value		2.23																																																																																																																																																																																																																							
P-Value		0.039																																																																																																																																																																																																																							
S	13.4	12.1																																																																																																																																																																																																																							
R-Sq	89.93	92.11																																																																																																																																																																																																																							
R-Sq(adj)	89.40	91.23																																																																																																																																																																																																																							
Mallows Cp	4.5	1.9																																																																																																																																																																																																																							
Step	1	2	3	4	5																																																																																																																																																																																																																				
Constant	207.00	250.97	71.20	67.21	58.75																																																																																																																																																																																																																				
x1	4.2	4.3	4.3	4.6	4.8																																																																																																																																																																																																																				
T-Value	3.74	3.99	3.97	4.48	4.72																																																																																																																																																																																																																				
P-Value	0.002	0.001	0.001	0.000	0.000																																																																																																																																																																																																																				
x2	0.17																																																																																																																																																																																																																								
T-Value	0.26																																																																																																																																																																																																																								
P-Value	0.797																																																																																																																																																																																																																								
x3	-3.1	-3.2																																																																																																																																																																																																																							
T-Value	-0.96	-1.03																																																																																																																																																																																																																							
P-Value	0.352	0.320																																																																																																																																																																																																																							
x4	0.055	0.057	0.066	0.058	0.058																																																																																																																																																																																																																				
T-Value	1.83	2.01	2.39	2.22	2.23																																																																																																																																																																																																																				
P-Value	0.089	0.062	0.030	0.041	0.039																																																																																																																																																																																																																				
stdx1x2	-4.3	-4.1	-3.2	-3.3																																																																																																																																																																																																																					
T-Value	-1.23	-1.24	-1.00	-1.04																																																																																																																																																																																																																					
P-Value	0.239	0.233	0.333	0.314																																																																																																																																																																																																																					
stdx2x3	-3.7	-4.0	-3.3																																																																																																																																																																																																																						
T-Value	-0.98	-1.11	-0.93																																																																																																																																																																																																																						
P-Value	0.344	0.283	0.365																																																																																																																																																																																																																						
S	12.5	12.1	12.2	12.1	12.1																																																																																																																																																																																																																				
R-Sq	93.46	93.42	92.96	92.58	92.11																																																																																																																																																																																																																				
R-Sq(adj)	90.65	91.23	91.20	91.27	91.23																																																																																																																																																																																																																				
Mallows Cp	7.0	5.1	4.1	2.9	1.9																																																																																																																																																																																																																				
<p>Stepwise Regression: y versus x1; x2; x3; x4; stdx2x3; stdx2x4</p> <p>Forward selection. Alpha-to-Enter: 0.1</p> <p>Response is y on 6 predictors, with N = 21</p> <table style="width: 100%; border-collapse: collapse;"> <tr> <td style="width: 10%;">Step</td> <td style="width: 10%;">1</td> <td style="width: 10%;">2</td> <td colspan="3"></td> </tr> <tr> <td>Constant</td> <td>29.16</td> <td>58.75</td> <td colspan="3"></td> </tr> <tr> <td>x1</td> <td>6.75</td> <td>4.76</td> <td colspan="3"></td> </tr> <tr> <td>T-Value</td> <td>13.03</td> <td>4.72</td> <td colspan="3"></td> </tr> <tr> <td>P-Value</td> <td>0.000</td> <td>0.000</td> <td colspan="3"></td> </tr> <tr> <td>x4</td> <td></td> <td>0.058</td> <td colspan="3"></td> </tr> <tr> <td>T-Value</td> <td></td> <td>2.23</td> <td colspan="3"></td> </tr> <tr> <td>P-Value</td> <td></td> <td>0.039</td> <td colspan="3"></td> </tr> <tr> <td>S</td> <td>13.4</td> <td>12.1</td> <td colspan="3"></td> </tr> <tr> <td>R-Sq</td> <td>89.93</td> <td>92.11</td> <td colspan="3"></td> </tr> <tr> <td>R-Sq(adj)</td> <td>89.40</td> <td>91.23</td> <td colspan="3"></td> </tr> <tr> <td>Mallows Cp</td> <td>3.2</td> <td>0.8</td> <td colspan="3"></td> </tr> </table>	Step	1	2				Constant	29.16	58.75				x1	6.75	4.76				T-Value	13.03	4.72				P-Value	0.000	0.000				x4		0.058				T-Value		2.23				P-Value		0.039				S	13.4	12.1				R-Sq	89.93	92.11				R-Sq(adj)	89.40	91.23				Mallows Cp	3.2	0.8				<p>Stepwise Regression: y versus x1; x2; x3; x4; stdx2x3; stdx2x4</p> <p>Backward elimination. Alpha-to-Remove: 0.1</p> <p>Response is y on 6 predictors, with N = 21</p> <table style="width: 100%; border-collapse: collapse;"> <tr> <td style="width: 10%;">Step</td> <td style="width: 10%;">1</td> <td style="width: 10%;">2</td> <td style="width: 10%;">3</td> <td style="width: 10%;">4</td> <td style="width: 10%;">5</td> </tr> <tr> <td>Constant</td> <td>156.15</td> <td>203.06</td> <td>181.93</td> <td>63.21</td> <td>58.75</td> </tr> <tr> <td>x1</td> <td>4.1</td> <td>4.2</td> <td>4.5</td> <td>4.4</td> <td>4.8</td> </tr> <tr> <td>T-Value</td> <td>3.21</td> <td>3.51</td> <td>4.15</td> <td>4.18</td> <td>4.72</td> </tr> <tr> <td>P-Value</td> <td>0.006</td> <td>0.003</td> <td>0.001</td> <td>0.001</td> <td>0.000</td> </tr> <tr> <td>x2</td> <td>0.19</td> <td></td> <td></td> <td></td> <td></td> </tr> <tr> <td>T-Value</td> <td>0.26</td> <td></td> <td></td> <td></td> <td></td> </tr> <tr> <td>P-Value</td> <td>0.797</td> <td></td> <td></td> <td></td> <td></td> </tr> <tr> <td>x3</td> <td>-2.3</td> <td>-2.4</td> <td>-2.1</td> <td></td> <td></td> </tr> <tr> <td>T-Value</td> <td>-0.70</td> <td>-0.76</td> <td>-0.70</td> <td></td> <td></td> </tr> <tr> <td>P-Value</td> <td>0.498</td> <td>0.459</td> <td>0.492</td> <td></td> <td></td> </tr> <tr> <td>x4</td> <td>0.064</td> <td>0.065</td> <td>0.061</td> <td>0.066</td> <td>0.058</td> </tr> <tr> <td>T-Value</td> <td>2.03</td> <td>2.18</td> <td>2.11</td> <td>2.41</td> <td>2.23</td> </tr> <tr> <td>P-Value</td> <td>0.062</td> <td>0.046</td> <td>0.051</td> <td>0.027</td> <td>0.039</td> </tr> <tr> <td>stdx2x3</td> <td>-4.6</td> <td>-4.7</td> <td>-3.9</td> <td>-3.4</td> <td></td> </tr> <tr> <td>T-Value</td> <td>-1.13</td> <td>-1.23</td> <td>-1.08</td> <td>-0.97</td> <td></td> </tr> <tr> <td>P-Value</td> <td>0.278</td> <td>0.239</td> <td>0.298</td> <td>0.345</td> <td></td> </tr> <tr> <td>stdx2x4</td> <td>-2.8</td> <td>-2.5</td> <td></td> <td></td> <td></td> </tr> <tr> <td>T-Value</td> <td>-0.72</td> <td>-0.70</td> <td></td> <td></td> <td></td> </tr> <tr> <td>P-Value</td> <td>0.483</td> <td>0.497</td> <td></td> <td></td> <td></td> </tr> <tr> <td>S</td> <td>13.0</td> <td>12.6</td> <td>12.4</td> <td>12.2</td> <td>12.1</td> </tr> <tr> <td>R-Sq</td> <td>93.01</td> <td>92.97</td> <td>92.75</td> <td>92.52</td> <td>92.11</td> </tr> <tr> <td>R-Sq(adj)</td> <td>90.01</td> <td>90.63</td> <td>90.93</td> <td>91.20</td> <td>91.23</td> </tr> <tr> <td>Mallows Cp</td> <td>7.0</td> <td>5.1</td> <td>3.5</td> <td>2.0</td> <td>0.8</td> </tr> </table>	Step	1	2	3	4	5	Constant	156.15	203.06	181.93	63.21	58.75	x1	4.1	4.2	4.5	4.4	4.8	T-Value	3.21	3.51	4.15	4.18	4.72	P-Value	0.006	0.003	0.001	0.001	0.000	x2	0.19					T-Value	0.26					P-Value	0.797					x3	-2.3	-2.4	-2.1			T-Value	-0.70	-0.76	-0.70			P-Value	0.498	0.459	0.492			x4	0.064	0.065	0.061	0.066	0.058	T-Value	2.03	2.18	2.11	2.41	2.23	P-Value	0.062	0.046	0.051	0.027	0.039	stdx2x3	-4.6	-4.7	-3.9	-3.4		T-Value	-1.13	-1.23	-1.08	-0.97		P-Value	0.278	0.239	0.298	0.345		stdx2x4	-2.8	-2.5				T-Value	-0.72	-0.70				P-Value	0.483	0.497				S	13.0	12.6	12.4	12.2	12.1	R-Sq	93.01	92.97	92.75	92.52	92.11	R-Sq(adj)	90.01	90.63	90.93	91.20	91.23	Mallows Cp	7.0	5.1	3.5	2.0	0.8
Step	1	2																																																																																																																																																																																																																							
Constant	29.16	58.75																																																																																																																																																																																																																							
x1	6.75	4.76																																																																																																																																																																																																																							
T-Value	13.03	4.72																																																																																																																																																																																																																							
P-Value	0.000	0.000																																																																																																																																																																																																																							
x4		0.058																																																																																																																																																																																																																							
T-Value		2.23																																																																																																																																																																																																																							
P-Value		0.039																																																																																																																																																																																																																							
S	13.4	12.1																																																																																																																																																																																																																							
R-Sq	89.93	92.11																																																																																																																																																																																																																							
R-Sq(adj)	89.40	91.23																																																																																																																																																																																																																							
Mallows Cp	3.2	0.8																																																																																																																																																																																																																							
Step	1	2	3	4	5																																																																																																																																																																																																																				
Constant	156.15	203.06	181.93	63.21	58.75																																																																																																																																																																																																																				
x1	4.1	4.2	4.5	4.4	4.8																																																																																																																																																																																																																				
T-Value	3.21	3.51	4.15	4.18	4.72																																																																																																																																																																																																																				
P-Value	0.006	0.003	0.001	0.001	0.000																																																																																																																																																																																																																				
x2	0.19																																																																																																																																																																																																																								
T-Value	0.26																																																																																																																																																																																																																								
P-Value	0.797																																																																																																																																																																																																																								
x3	-2.3	-2.4	-2.1																																																																																																																																																																																																																						
T-Value	-0.70	-0.76	-0.70																																																																																																																																																																																																																						
P-Value	0.498	0.459	0.492																																																																																																																																																																																																																						
x4	0.064	0.065	0.061	0.066	0.058																																																																																																																																																																																																																				
T-Value	2.03	2.18	2.11	2.41	2.23																																																																																																																																																																																																																				
P-Value	0.062	0.046	0.051	0.027	0.039																																																																																																																																																																																																																				
stdx2x3	-4.6	-4.7	-3.9	-3.4																																																																																																																																																																																																																					
T-Value	-1.13	-1.23	-1.08	-0.97																																																																																																																																																																																																																					
P-Value	0.278	0.239	0.298	0.345																																																																																																																																																																																																																					
stdx2x4	-2.8	-2.5																																																																																																																																																																																																																							
T-Value	-0.72	-0.70																																																																																																																																																																																																																							
P-Value	0.483	0.497																																																																																																																																																																																																																							
S	13.0	12.6	12.4	12.2	12.1																																																																																																																																																																																																																				
R-Sq	93.01	92.97	92.75	92.52	92.11																																																																																																																																																																																																																				
R-Sq(adj)	90.01	90.63	90.93	91.20	91.23																																																																																																																																																																																																																				
Mallows Cp	7.0	5.1	3.5	2.0	0.8																																																																																																																																																																																																																				

Figure 4.102 Backward Elimination and Forward Stepwise Methods for Evaluating All Predictor Variables in the Two Cases for Electrospun Fiber Interlayered Composite

The best model ($\alpha=0.1$) deriving from stepwise forward selection method (Figure 4.102) in both cases - first using stdx1x2 and then stdx2x4 - includes flexural modulus and interlayer improvement. The same model derives as the best one ($\alpha=0.1$) in both cases from the backward elimination method. In best subsets regression of both cases this model has the lowest Cp and one of the highest adjusted R^2 . As a result, the model that contains flexural modulus and interlayer improvement can be considered as one of the two best models. Furthermore, best subsets regression indicates that there are two more very good models. In the case that stdx2x4 is not considered in the model, the second best model is the one using flexural modulus and interlayer improvement together with a standardized interaction of flexural modulus and tensile strength. In the case that stdx1x2 is not considered in the model, the second best model is the one using flexural modulus and interlayer improvement together with a standardized interaction of tensile strength and glass transition temperature. However, by having a closer look to Figure 4.102, the p-values for the two model with the three predictor variables (x1, x4, stdx1x2 and x1, x4, stdx2x3) are not all below the significance level of ($\alpha=0.1$). More specifically, the standardized interactions stdx1x2 and stdx2x3 present p-values above 0.3. In conclusion, the best model that will be evaluated, as soon as the variance inflation is reasonable, is the one with flexural modulus (x1) and interlayer improvement (x4) as predictor variables. Variance inflation of the model with x1 and x4 is:

$$\mathbf{VIF_1 = VIF_4 = 4.58}$$

Although, the VIF is quite high as it indicates that variance is inflated by 4.5 times and it would be definitely desired to have a value as closer to 1 as possible, the model is accepted mainly because the same predictor variables were selected for predicting the flexural strength of the epoxy foamed interlayer composite. Thus, it seems that there is a continuation here on how the flexural strength of the interlayered materials is predicted through flexural modulus and interlayer improvement. Also, it seems that the next good model and significant for $\alpha=0.1$ has only one predictor variable. As a matter of fact, it is less accurate to predict flexural strength

based only on flexural modulus, because the interlayer improvement plays a key role in material properties as it can be seen through the experimental results. Consequently, the one predictor variable model for predicting flexural strength is not preferred.

Model 1: Variables=x1, x4 / $R(\text{adj})^2 = 91.2$ in both cases /

Cp = 1.9 (case 1, stdx1x2 is included) - Cp = 0.8 (case 2, stdx2x4 is included)

The next step will be to evaluate the selected model for predicting the flexural strength of the featherweights.

Parameters, ANOVA Table and other information on Model 1 are presented from Table 4.65 to Table 4.67.

Table 4.65 Model 1 Parameters – Electrospun Fiber Interlayer CFRP

	Value	Standard Error	t-Value	Prob> t
Intercept	58.75	20.555	3.86	0.01
X1-Flexural Modulus	4.7622	1.0080	4.724	3.31393E-4
X4-Interlayer Improvement	0.0581	0.0261	2.226	0.039

Thus, model 1 can be written as:

$$\hat{y} = 58.75 + 4.762 \cdot x_1 + 0.0581 \cdot x_4$$

Table 4.66 Model 1 ANOVA Table – Electrospun Fiber Interlayer CFRP

	DF	Sum of Squares	Mean Square	F Value	Prob>F
Model	3	31005.3	15502.7	105.022	8.322E-10
Error	18	2657	147.6		
Total	20	33662.4			

Table 4.67 Other information of Model 1 – Electrospun Fiber Interlayer CFRP

Number of Points	21
Degrees of Freedom	18
Residual Sum of Squares	2657
R Square	0.9211
Adj. R Square	0.9123
Root MSE	12.15

Figure 4.103 presents the analysis of the residuals over the predictor variables, the fitted values, the time order, and the NPP plot for model 1.

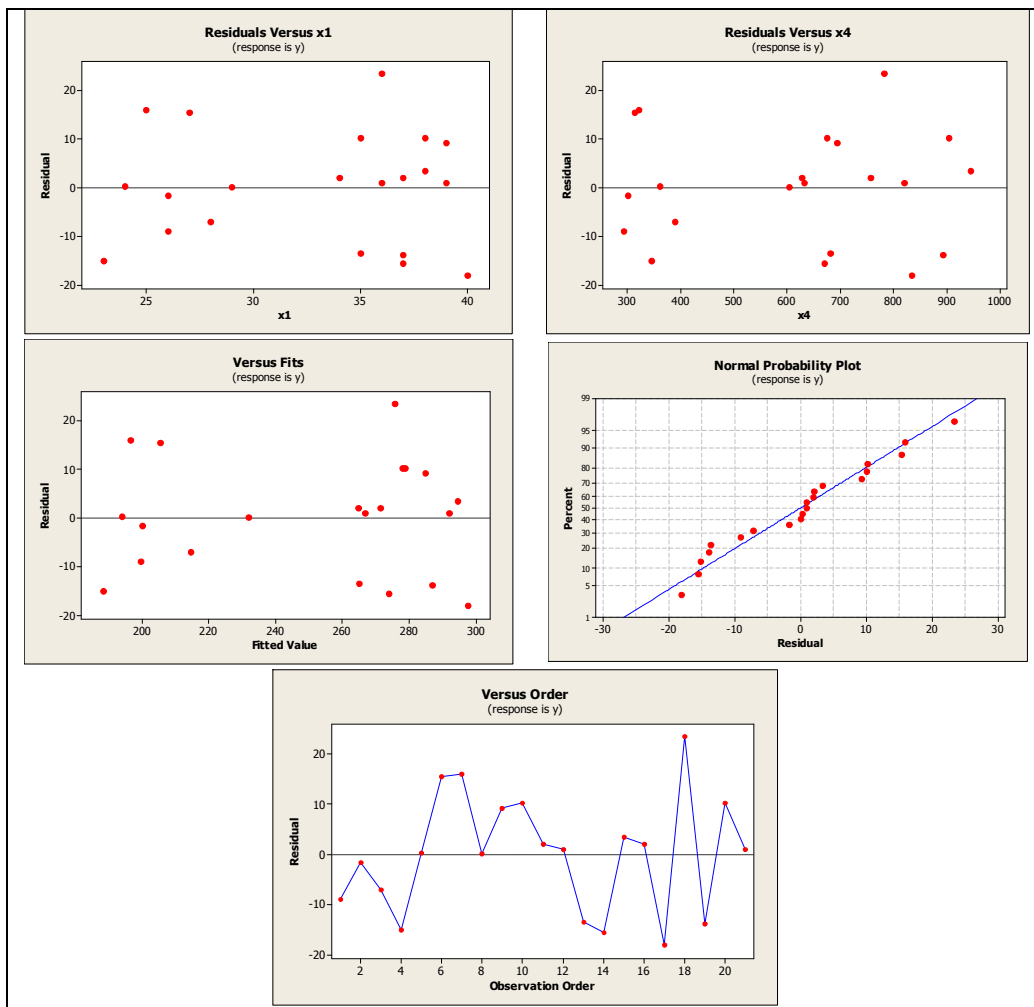


Figure 4.103 Model Residuals graphs – Electrospun Fiber Interlayer CFRP

Having presented the parameters and the analysis of the best model, the fulfillment of assumptions has to be tested in order to decide if another model approach must be made (Table 4.68).

Table 4.68 Model Assumptions Fulfillment – Electrospun Fiber Interlayer CFRP

	Model1
ASSUMPTION 1	No curvature → Model Form Reasonable
ASSUMPTION 2	No Funnel Shape → Const Error Variance
ASSUMPTION 3	Normal Probability Plot → Normality Reasonable
ASSUMPTION 4	No trend – No serial correlation
Adjusted R ² / Mallow Cp Case 1	Adjusted R ² = 91.2% Cp = 1.9
Adjusted R ² / Mallow Cp Case 2	Adjusted R ² = 91.2% Cp = 0.8

Models assumptions evaluation shows that model 1 fulfills all the requirements for being adequate. Furthermore, a diagnostics evaluation is performed in Table 4.69 and Table 4.70 in order to get a better idea on the selected model description for flexural strength.

Table 4.69 Variance Inflation – Electrospun Fiber Interlayer CFRP

	VIF Model 1
Intercept	0
X1	4.58
X4	4.58

Table 4.69 presents a variance inflation of the model which has already been discussed and is quite high (~4.5 times inflated). However, the model is selected for the previously described reasons.

Table 4.70 presents the x and y outliers along with their influence to the fitted model for model 1. The model has no y outliers according to the Bonferroni test; however, it presents a x outlier in observation 17. This outlier is influential on y_{hat} and this can be seen from the DFFITS, where observation 17 is influential to the model.

Table 4.70 Outliers and Influence– Electrospun Fiber Interlayer CFRP

	Model 1
X – Outlier	Observation 17
Y - Outlier through Bonferonni test	0
Y - Outlier through DFFITS	Observation 17
Y - Outlier through COOKDi	0

Finally, the parameters influence is presented in Table 4.71, which shows that there is no significant influence of any observation to any of the parameters for the model.

Table 4.71 Observation Influence on Parameters – DFBETAS – Electrospun Fiber Interlayer CFRP

Influence On	Model 1
Intercept	0
X1	0
X4	0

Model Selection:

Again, the model is selected mainly because the same predictor variables were selected for predicting the flexural strength of the epoxy foamed interlayer composite. Thus, it seems that there is a continuity here on how the flexural strength of interlayered materials is predicted through flexural modulus and interlayer improvement. Furthermore, due to the fact that the next good model and significant for $\alpha=0.1$ has only one predictor variable, which makes it less accurate to predict flexural strength based only on flexural modulus as the interlayer improvement plays a key role in material properties as it can be seen through the experimental results, it is not selected.

The selected model is:

$$\hat{y} = 58.75 + 4.762 \cdot x_1 + 0.0581 \cdot x_4$$

Parameters Interpretation

- 1) Regarding β_0 , for $x_1 = x_4 = 0$, the value of $y_{\text{hat}} = 58.75$. Nevertheless, the point $[0, 0]$ is not included in all x ranges.
- 2) The estimator for β_1 is $b_1 = 4.762$ and it means that the estimated change of the flexural strength when the flexural modulus increases by 1 is 4.762 MPa, assuming that the Mode II Energy Release Rate (Interlayer Improvement) remains constant.
- 3) The estimator for β_2 is $b_2 = 0.0581$ and it means that the estimated change of the flexural strength when the Mode II Energy Release Rate (Interlayer Improvement) increases by 1 is 0.05769 MPa, assuming that the flexural modulus remains constant.

Inferences for the selected model parameters are presented through Bonferroni joint t-interval.

Table 4.72 Selected Model Parameters and Covariance Table – Epoxy Foamed Interlayer CFRP

$S(b)^2$			b
422.5	-19.124	0.34668	58.75
-19.124	1.0162	-0.023249	4.762
0.34668	-0.023249	0.0006805	0.0581

The Bonferroni joint t-interval is performed for significance level of $\alpha = 0.02$ as following:

$$B = t\left(1 - \frac{\alpha}{2 \cdot g}; n - p\right) = t(1 - 0.005; 18) = t(0.995; 18) = 2.878$$

$$S\{b_1\} = \sqrt{1.0441} = 1.022 \rightarrow \text{Interval} : \beta_1 = 4.5752 \pm 2.878 \cdot 1.022 \Rightarrow \beta_1 : (1.634, 7.52)$$

$$S\{b_2\} = \sqrt{0.000678} = 0.026 \rightarrow \text{Interval} : \beta_2 = 0.057688 \pm 2.878 \cdot 0.026 \Rightarrow \beta_2 : (-0.01714, 0.13252)$$

We are 98% confident that β_1 is contained in (1.634, 7.52), and β_2 is contained in (-0.01714, 0.13252) simultaneously.

Individually for each parameter:

For β_1 , we are 99% confident that β_1 is contained in (1.634, 7.52).

For β_2 , we are 99% confident that β_2 is contained in (-0.01714, 0.13252).

Summarizing, the best model for predicting flexural strength of composites when the interlayer is enhanced with electrospun fibers is:

$$\hat{y}=58.75+4.762 \cdot x_1+0.0581 \cdot x_4$$

The model uses as predictor variables flexural modulus (x_1), and mode II fracture toughness energy release rate (interlayer improvement) (x_4). Mode II is analogous to the interlayer improvement, tension strength is easily measured, and flexural modulus is given material property. Additionally, the regression model selected for the epoxy foamed interlayered composite contains the two predictor variables that the best model of this section for the electrospun fiber interlayered composite revealed. Concluding, the developed statistical model assists the engineer to design an electrospun fiber interlayered composite with a desired flexural strength by introducing to the model the flexural modulus and the interlayer toughness improvement. This helps the engineer to avoid performing time-consuming experimental mechanical testing. Finally, it can be seen through the model equation that higher flexural modulus contributes to a higher flexural strength as it is expected due to stiffness enhancement. This is correlated by the experimental results where specific flexural modulus increase corresponds to an almost same flexural strength increase. Similar is the behaviour of the interlayer improvement-fracture toughness-as higher interlayer improvement corresponds to higher flexural strength due to crack propagation inhibit. The rate of this change is different though. The interlayer improvement can be interpreted as flexural modulus improvement resulting in multicollinearity of the two predictor variables; however, this is not definite as the modulus may not increase when the interlayer is improved (e.g. fracture toughness from Epoxy Foamed to CNT Epoxy Foamed interlayer CFRP-Table 4.25)

4.7 Comparison of the Three Different Interlayer Enabling Systems

The main goal of the present work was to examine several interlayer systems focusing on reduced weight and enhanced strength. Two main interlayer systems were investigated in order to examine the potential of weight savings and strength improvement. Based on the

multilayer structure theory, a nylon micro-spherical reinforcement within the interlayer was investigated. This reinforcement examination was of specific interest as the nylon micro-spherical reinforced CFRP is utilized in main aerospace applications such as the 737 tail Fin and the 787. The acceptance of the multilayer structured material by the aerospace industry establishes the background for further investigating the nature and design of interlayer systems in order to contribute in even higher material properties. The first interlayer system beyond the existent multilayer structure consists of epoxy foam reinforced with carbon nanotubes. This interlayer reinforcement presents great interest because of the potential high weight reduction, but also the increased stiffness that adds to the composite. Finally, the third interlayer is the electrospun nanofibers which are placed in the interlayer containing CNT. This last reinforcement is of specific interest due to the highly fractal structure of the interlayer, which combines weight reduction together with stiffness and strength improvement. The three types of interlayer are categorized and listed as following:

Table 4.73 List of Interlayer Types

Symbol	Interlayer System within CFRP Laminates
I1A	Nylon Micro-Spherical Interlayer (Micro-Sphere volume fraction – 25%)
I1B	Nylon Micro-Spherical Interlayer (Micro-Sphere volume fraction – 36%)
I1C	Nylon Micro-Spherical Interlayer (Micro-Sphere volume fraction – 44%)
I2A	Epoxy Foamed Interlayer
I2B	CNT Reinforced Epoxy Foamed Interlayer
I3A	Electrospun Fiber Interlayer
I3B	CNT Reinforced Electrospun Fiber Interlayer

The three main interlayers are then compared in Figure 4.104 in terms of flexural strength improvement and in Figure 4.105 in terms of Mode II fracture toughness improvement.

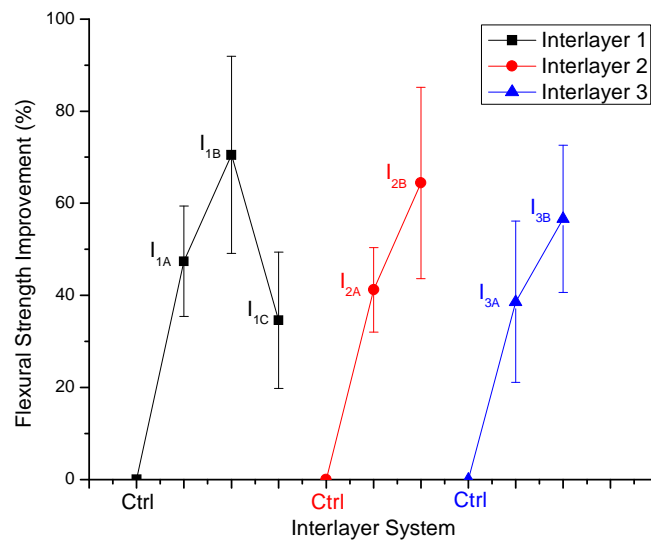


Figure 4.104 Flexural Strength Improvement Comparison between the Three Different Interlayer Systems

In Figure 4.104 it can be seen that all interlayer systems present flexural strength improvement of similar level. Interlayer 1 presents the highest flexural strength improvement when the micro-spheres fraction is 36% (70%), this is the highest flexural strength of all interlayer systems. CNT reinforced epoxy foamed interlayer presents similar flexural strength enhancement which is around 65%. Lastly, the CNT reinforced electrospun interlayer presents the lowest improvement, however close to the rest interlayer systems, which is around 57%.

Additionally, Figure 4.105 presents the fracture toughness (Mode II) improvement for all the interlayer systems. Again, as for interlayer 1 the highest Mode II fracture toughness improvement occurs at 36% and is 118%. Similar value for interlayer 2 has the epoxy foamed interlayer which presents improvement of around 120%. However, when the CNT are added to the interlayer, because of the foam surface reinforcement, the fracture toughness enhancement reaches the number of 390%. Finally, the third interlayer presents significant fracture toughness

improvement (130%) when plain electrospun fibers are added. When CNT are contained within the electrospun fibers there is an additional improvement which can totally go up to 165%.

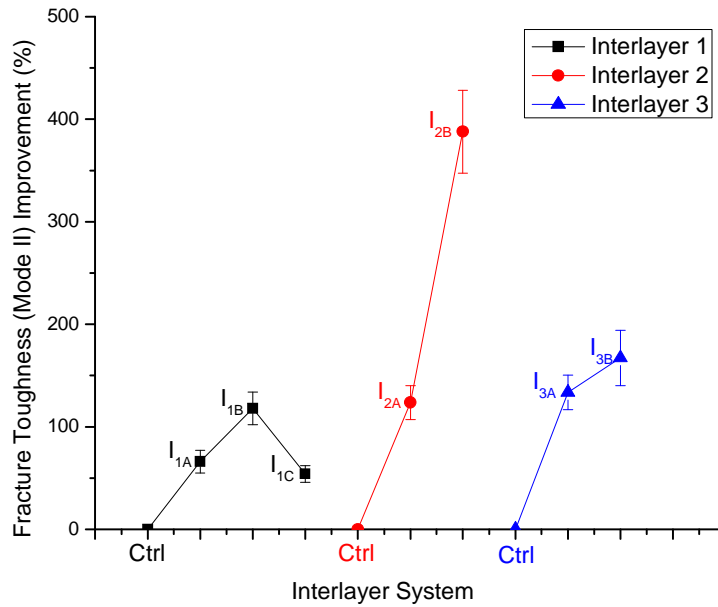


Figure 4.105 Mode II Fracture Toughness Improvement Comparison between the Three Different Interlayer Systems

Finally, the weight savings that each of the interlayer type contributes to the CFRP are presented in Table 4.74. Weight reduction is calculated through thermogravimetric analysis for measuring the densities of the specimens which contain the different interlayer types.

Table 4.74 Average Densities of CFRP with All Interlayer Cases

Control CFRP Density (g/cm³)		1.69 ± 0.01	
	v_f=25% (g/cm³)	v_f=36% (g/cm³)	v_f=44% (g/cm³)
Nylon Micro-Spherical Interlayer (1)	1.66 ± 0.01	1.65 ± 0.011	1.645 ± 0.01
	Epoxy Foam (g/cm³)	CNT Reinforced Epoxy Foam (g/cm³)	
Epoxy Foamed Interlayer (2)	1.544 ± 0.034	1.561 ± 0.03	
	Electrospun Fibers (g/cm³)	CNT Reinforced Electrospun Fibers (g/cm³)	
Electrospun Fibers Interlayer (3)	1.6015 ± 0.02	1.615 ± 0.018	

As it can be seen in Table 4.74, all interlayer systems offer some weight reduction when compared to the conventional CFRP. This reduction although it can be observed in all measurements, it is not highly significant as it is still within the error limits. Weight reduction is highest in the case of the plain epoxy foamed interlayer (8.5%) and lowest in the case of 25% nylon micro-spherical interlayer (1.8%). These reductions happen because the overall volume fraction of fibers does not change within the CFRP and thus, the interlayer inclusion material density in all cases is always smaller than the epoxy system density. In interlayer systems 2 and 3, the CNT do not offer extra weight reduction as it has been predicted in section 4.4 model, because the CNT distribution utilized is not of the same distribution presented in section 4.4. This happens because the supplier could not provide the desired CNT distribution (in terms of radius and number of walls) for the next step of this work. However, the CNT distribution used still follows the model as according to it, the CNT should slightly add weight to the CFRP compared to the plain interlayer reinforcement, but still increase its strength.

CHAPTER 5

CONCLUSIONS

Summarizing, this work focuses on improving the conventional carbon fiber reinforced composites by reducing the weight and at the same time maintaining if not increasing the strength. The key towards achieving this goal is to introduce a new phase in composites, the interlayer, which basically is the area between two successive plies. In order to achieve this goal first, the matrix system process evaluation together with the manufacturing process were extensively described and analyzed. Following, based on the design and process of micro-spherical interlayer structures, two interlayer systems that could potentially add to the CFRP properties were investigated through theoretical analysis and tested in a series of experiments as mentioned in the methodology section. The interlayer systems under examination exhibited significant increase in mechanical properties (Around MIN 15 to 25 %) and high weight reduction (Around MIN 15 to 25 %).

5.1 Conclusions for Objective #1

A DMA time - temperature multiplexing technique from 100 to 400⁰C in a nitrogen atmosphere was used to analyze phenolic resin/carbon fiber composites. The glass transition and degradation processes were clearly detected by the changing DMA modulus with respect to temperature. In addition to the typical glass transition exhibited by the model system, during the degradation stage, the storage modulus initially increased and then passed through a maximum value, followed by a decrease.

The DMA results exhibit a good agreement with the general standard linear solid model which has been established for the dynamic and viscoelastic behaviour of composite materials. The correlation of experimental results with theoretical model is more than 99% in storage modulus and more than 95% in $\tan\delta$. This agreement of the experimental results with the GSLS

model reveals the validation of DMA technique for evaluating the viscoelastic characteristics and coupling relaxation phenomena to cure and degradation processes in composites.

5.2 Conclusions for Objective #2

Towards the evaluation of Repair Clave innovative manufacturing, the DSC results were not conclusive with respect to expected percentages of curing. It could not be concluded that the percentage of cure would be higher with a higher pressure, and also it was noticed that the differences from one pressure to another were quite small. These small differences could appear also because of the way the lay-up is done or the way the vacuum was maintained through the curing process. It is also possible that the differences are so small because of the small number of plies subjected to the experiments. An increased number of plies could offer more definitive answers with respect to the influence of pressure on the manufacturing process of composite parts.

Furthermore, the dynamic mechanical analysis DMA gives the expected results regarding the storage modulus reaction with the manufacturing pressure increase. The higher the manufacturing pressure the higher the modulus. However, there is a significant decrease in glass transition temperature as the manufacturing pressure increases. This happens due to internal stresses formed in the materials when pressure is higher. Then, these internal stresses are relieved during heating and soften the material, resulting in a reduced T_g . Scanning electron microscope observation was performed for samples from all pressures. The results verified the storage modulus increase, as the higher the pressure, the less void formation.

In addition, starting from specimens manufactured in 0 psi and going to specimens manufactured in 70 psi the flexural testing totally presents a 40% improvement in both flexural modulus and flexural strength, while there are no improvements in compression modulus and strength which are maintained in similar levels. This in relation to the SEM characterization means that the higher pressure during manufacturing impedes the void formation within the matrix system and as a result the flexural modulus and strength are significantly improved.

Moreover, specimens of the same number of plies manufactured through autoclave in 85 psi, present similar properties to the specimens manufactured under 70 psi. Flexural modulus and strength are slightly higher at 2.4% and 0.8% respectively, while compression modulus and strength present an improvement of 11% and 3.5% respectively. The autoclave manufactured specimens present similar mechanical properties to the 70 psi samples manufactured at the press clave and as a result it can be concluded that press clave is a low cost alternative for manufacturing carbon fiber reinforced composites.

Additionally, a multi-linear regression analysis was performed to explore how the flexural strength can be modeled and predicted from other predictor variables such as flexural modulus, manufacturing pressure, compression modulus and glass transition temperature. The best resulting model for predicting flexural strength through the analysis uses as predictor variables flexural modulus (x1), manufacturing pressure (x2), and compression modulus (x3). Finally, it can be seen through the model equation that higher flexural and compression moduli contribute to a higher flexural strength as expected since material stiffness is enhanced. This is correlated by the experimental results where a 40% flexural modulus increase corresponds to an almost same (37%) flexural strength increase. Similar is the behaviour of the pressure while manufacturing. However, the rate of this change is different as the pressure has a smaller multiplier factor within the model. Thus, much bigger pressure is needed for similar (37%) flexural strength improvement. In fact the pressure increase is 500% (0 to 485 kPa).

To sum up, the well cured specimens manufactured through the press clave, the acceptable surface that they present in SEM characterization and most importantly the slight differences in flexural strength and modulus at high pressure manufacturing when compared with autoclaved samples demonstrate that the press clave can be utilized as a descent low cost alternative manufacturing process of the extremely expensive autoclave.

5.3 Conclusions for Objective #3

The toughness of heterogeneous multilayer laminates is strongly dependent on the host resin matrix resin. Nevertheless, the percentage increase of G_{IIC} due to the creation of the multilayer structure is independent of the base resin toughness. The maximum toughness improvements from all different microsphere volume fractions examined was approximately 100%.

Furthermore, the observed toughness improvements correlate directly to the location of crack propagation during testing. If crack propagation occurs in the interlaminar region, toughness improvements can be expected. But if the crack moves into the intralaminar region, toughness degrades. Consequently, the amount of toughness improvement must be balanced between interlaminar and intralaminar fracture-toughness.

Finally, this section demonstrated that even though the multilayer structured laminates provide Mode II interlaminar fracture-toughness improvements, their mechanical testing behavior is extremely different than conventional composite structures. Understanding the multilayer system and more specifically the fundamental differences in process, structure and properties between multilayer and conventional prepregs is essential for the introduction of new interlayer systems and their utilization in load-bearing structural applications.

5.4 Conclusions for Objective #4

CNT were investigated as the smallest part of the fractal structure the featherweight composites comprise. Detail analysis of CNT properties was performed. More specifically, a new approach for calculating the density and the modulus of the carbon nanotubes was investigated. The volume estimation of the graphene sheets participating in the CNT over the total CNT volume was the key approach of the model for calculating the density and modulus as a function of CNT external radius and the number of walls. Based on the nano-hollowness of carbon nanotubes, the model tried to give an estimate of the weight reduction of a polymer

nanocomposite reinforced with CNT and to describe the nanotube modulus depending on the radius and the number of walls.

Furthermore, the density and the modulus of the polymer nano-composites were calculated for specific CNT cases of radius and walls combinations and for several scenarios such as aligned, aligned in plane and randomly oriented CNT. The model seems to follow several applications, theoretical and experimental, within the literature, and it is also comparable with other models that were reviewed in background.

Additionally, the modulus was plotted as a function of density. Traditional materials such as metals, ceramics, fiber reinforced composites, and polymers, have a specific behaviour in the relation between modulus and density. As the density increases, the modulus increases, as well. On the contrary, PNC demonstrated a different behavior due to the low density of the incorporated CNT. For their case, when CNT volume fraction was higher, modulus was higher, but density was lower.

The theoretical models for PNC density and PNC modulus as functions of CNT volume fraction present good agreement (Pearson Correlation more than 95%) with the experimental measurements through nano-indentation and TGA measurements for PNC manufactured with the CNT of 4nm external radius and 3 walls. Of significant importance is the PNC density reduction over the CNT volume fraction increase, which is also presenting an increase of the PNC modulus. The CNT distribution used for this work may give small PNC density reduction; however, if different CNT distributions (larger diameters and fewer walls) are incorporated within the matrix, higher density reduction will be achieved.

5.5 Conclusions for Objective #5

The porous interlayer is based on the concept of reinforcing the pores surfaces with nano-inclusions so the crack initiation can be avoided and the crack propagation can be prevented and as a result, the fracture toughness is enhanced. The porosity volume fraction is

defined through density calculations and following the desired carbon nanotubes amount can be determined as well.

To observe more easily the distribution of the nano-inclusion within the pore surface, polyurethane samples are prepared reinforced with montmorillonite nanoclays. The SEM characterization confirms the neat distribution of the clays on the polyurethane pores surface. Following, CFRP composites were manufactured first with plain epoxy foamed interlayer and then with CNT reinforced epoxy foamed interlayer. The specimens were tested in dynamic mechanical analysis and were compared with control samples. The flexural storage modulus exhibits significant increase from the control samples to the epoxy foamed interlayer and even higher to the CNT epoxy foamed interlayer. This finding although it shows that CNT reinforced pores within the interlayer increase the stiffness of the overall material, it may be subjected to specimens geometry changes, which can justify such improvements/alterations in modulus calculations. As a result, in order to get a better view of the flexural behaviour of the material stiffness, mechanical flexural testing for each type of samples was performed.

In mechanical testing, flexural and tensile experiments were performed. Flexural tests present a significant increase of flexural strength from control to epoxy foamed interlayer samples of around 48%. This enhancement indicates that epoxy foam provides higher stiffness which plays a key role in the flexural strength enhancement. There is an additional 16.5% flexural strength improvement from the epoxy foamed interlayer to the CNT reinforced epoxy foamed interlayer and this is due to the nanotubes existence. However, CNT reinforcement does not affect the flexural modulus as although it presents a high increase of around 56% from control to epoxy foamed interlayer samples, it does not change when CNT are added. This was expected as the CNT do not reinforce the main matrix system through which the load transfer occurs. CNT at this structure are within the pore surfaces and do not participate in the load transfer within the material entirety. As a result the CNT reinforcement contributes to the, flexural strength, stiffness, and Mode II fracture toughness improvement but not to a higher

flexural modulus. Moreover, there is significant improvement to both stiffness and Mode II fracture toughness from control to epoxy foamed and from the epoxy foamed to the CNT epoxy foamed specimens with the ultimate enhancement being in both properties in the order of 400%.

Furthermore, in tensile testing, it can be seen that there is no significant increase of tensile strength from control to epoxy foamed and from the epoxy foamed to the CNT epoxy foamed samples. As a result, the foamed interlayer does not improve, but it does not either deteriorate the tensile strength improvement. Consequently, the CNT reinforcement contributes to the, flexural strength, stiffness, and Mode II fracture toughness improvement but not to higher tensile strength. This is quite explainable by the fact that fibers are dominant in the axial load transfer mechanisms, which are present in tensile testing.

In addition, scanning electron microscope observation presents the distinct interlayer region placed within the plies. CNT epoxy foamed specimens present some spots within the pores surfaces – not the dust – which are observed only in samples that contain CNT and they potentially are CNT agglomerates. CNT themselves cannot be clearly seen as the SEM utilized for the characterization of this material is not capable of magnifications below few μm . As a result, although it can be concluded that CNT reinforce the pores surface, the fact that CNT are randomly distributed in other places rather than the pores of the interlayer system as well cannot be excluded. Hackle formation due to the crack yielding mechanism within the interlayer while fracture is also observed in SEM pictures.

Finally, a multi-linear regression analysis was performed to explore how the flexural strength can be modeled and predicted from other predictor variables such as flexural modulus, tensile strength, Mode II fracture toughness (Interlayer Improvement), and glass transition temperature. The best model uses as predictor variables flexural modulus (x1), mode II fracture toughness energy release rate (interlayer improvement) (x4), and the standardized interaction of flexural modulus with tensile strength. The developed statistical model assists the engineer to design an epoxy foamed interlayered composite with a desired flexural strength by introducing

to the model, the flexural modulus, the interlayer toughness improvement and the interaction of flexural modulus with tensile strength. It can be seen through the model equation that higher flexural modulus contributes to a higher flexural strength as it is expected due to stiffness enhancement. This is correlated by the experimental results where an approximate 50% flexural modulus increase corresponds to an almost same flexural strength increase. Similar is the behaviour of the interlayer improvement-fracture toughness-which is represented in the model through a logarithm, so higher interlayer improvement corresponds to higher flexural strength as well. However, the rate of this change is different. The last variable, the interaction of flexural modulus with tensile strength, shows that its increase basically decreases the flexural strength. This happens because tensile strength increase means more carbon fiber within the material, as a result less epoxy foamed interlayer, and thus, lower flexural strength.

5.6 Conclusions for Objective #6

CFRP composites were manufactured first with electrospun fiber interlayer and then with CNT reinforced electrospun fiber interlayer. In dynamic mechanical analysis, specimens present a significant increase of the storage modulus under flexural load from the control samples to the electrospun interlayer and even higher to the CNT electrospun interlayer. This finding is of particular importance, since it demonstrates that CNT reinforcing the electrospun fibers of the interlayer increase even more the stiffness of the overall material. However, in order to get a better view of the flexural behaviour of the material, flexural mechanical testing was performed as well.

Flexural testing presents a significant increase of flexural strength from control to electrospun samples of around 38.5%. This indicates that the electrospun interlayer plays a key role in the flexural strength enhancement. There is an additional 13% flexural strength enhancement from the electrospun interlayer to the CNT reinforced electrospun interlayer and this is due to the CNT existence. As it can be seen, the electrospun interlayer not only enhances the flexural modulus of the composite around 43% when added to the interlayer by

itself, but it looks like the extra CNT reinforcement in the third sample group (CNT electrospun CFRP) does influence the flexural modulus too as it presents a slight increase of around 7.6%. Contrarily to the epoxy foamed interlayer system, it seems that CNT participates to the load transfer as part of the electrospun fibers. As a result, the CNT reinforcement contributes to the, flexural strength, stiffness, and Mode II fracture toughness improvement as well as to flexural modulus slight enhancement. Stiffness and Mode II fracture toughness are also enhanced from control to electrospun interlayer and even more to the CNT electrospun interlayer with ultimate improvement around 80% and 165% respectively.

Additionally, tensile testing demonstrates that there is no significant increase of tensile strength from control to electrospun samples. Thus, it is concluded that the electrospun interlayer does not really improve, but it does not either deteriorate the tensile strength improvement. Similarly, the tensile strength from the electrospun to the CNT electrospun CFRP samples presents almost no change at all. As a result the CNT reinforcement contributes to the flexural strength, stiffness, and Mode II fracture toughness improvement but not to higher tensile strength. This is quite explainable by the fact that fibers are dominant in the axial load transfer mechanisms which are present in tensile testing.

Furthermore, the SEM characterization presents first electrospun fibers on CFRP layer without presence of resin, exactly as they come out of the electrospinning configuration. Homogeneous electrospun fiber dispersion over the fiber bed area can be observed. CNT agglomerates are probably shown on the electrospun fibers as small spots, as such spots cannot be found in the figures of the electrospun fibers that do not include CNT. Also, the CNT reinforced electrospun fiber interlayer is clearly observed; however, CNT in this case are not clearly observed even in agglomerate form. This is explained by the fact that due to the exothermic reaction of polymerization the electrospun microfibers in some areas of the sample may have been melted and thus aggregated to bigger masses of cellulose acetate, thus, the CNT agglomerates demonstrated in samples prior to polymerization, cannot be seen in all the

polymerized samples. Nevertheless, melting of the electrospun fibers, especially at junction points may yield a connected network which can transfer stress better than unconnected fibers. It may also yield anchoring nodes with the matrix polymer, also improving stress transfer. Hackle formation due to the crack yielding mechanism within the interlayer while fracture is also observed in SEM pictures.

Finally, a multi-linear regression analysis was performed to explore how the flexural strength can be modeled and predicted from other predictor variables such as flexural modulus, tensile strength, Mode II fracture toughness (Interlayer Improvement), and glass transition temperature. The best resulting model through the analysis uses as predictor variables flexural modulus (x1), and mode II fracture toughness energy release rate (interlayer improvement) (x4). It can be seen through the model equation that higher flexural modulus contributes to a higher flexural strength as it is expected due to stiffness enhancement. This is correlated by the experimental results where specific flexural modulus increase corresponds to an almost same flexural strength increase. Similar is the behaviour of the interlayer improvement-fracture toughness-as higher interlayer improvement corresponds to higher flexural strength due to crack propagation inhibit. The rate of this change is different though. The interlayer improvement can be interpreted as flexural modulus improvement resulting in multicollinearity of the two variables; however, this is not definite as the modulus may not increase when the interlayer is improved (e.g. fracture toughness from Epoxy Foamed to CNT Epoxy Foamed interlayer CFRP-Table 4.25)

5.7 Summary and Future Work

Overall, the three interlayer systems (nylon micro-spheres, CNT epoxy foam, and CNT electrospun fibers) that were tested demonstrate significant flexural strength enhancement, which ultimately is between 55 and 70%. The strongest interlayer is the nylon micro-spheres with a 70% improvement, followed by the CNT epoxy foamed interlayer with a 65% improvement and the CNT electrospun fiber interlayer coming last with a 57% improvement.

Mode II fracture toughness demonstrates dramatic improvements as well. Ultimately, nylon micro-spheres interlayer has a 118% maximum improvement for the epoxy system, CNT epoxy foamed interlayer has a tremendous improvement of 390%, and CNT electrospun fiber interlayer an improvement of 130%. Finally, there is a slight weight reduction in all interlayer systems. The highest weight reduction occurs in the plain epoxy foamed interlayer system (8.5%) and the lowest in the 25% nylon micro-spherical interlayer (1.8%). These reductions occur because the overall volume fraction of fibers does not change within the CFRP and thus, the interlayer inclusion material density in all cases is always smaller than the epoxy system density. In interlayer systems 2 and 3, the CNT do not offer extra weight reduction as it has been predicted in section 4.4 model for CNT distributions of specific diameter and number of walls. However, the CNT distribution used still follows the model as according to it, the CNT utilized should slightly add weight to the CFRP compared to the plain interlayer reinforcement, but still increase its strength.

In the future, potentially combining the three different technologies in interlayer systems could be investigated. Micro-particle reinforced epoxy foam and micro-particle electrospun fibers could be tried as interlayers. The replacement of nanotubes with micro-particles could possibly result in less strength and weight reduction, but much higher fracture toughness. Moreover, further analysis of the overall manufacturing process can be performed based on the results of this work. Inventory and quality controls can be investigated for improving and scaling up a continuous low cost manufacturing process. Finally, the research of other properties while experimentation, as potential predictor variables for optimizing current or creating new linear or non-linear models can be conducted.

REFERENCES

1. *Kinetic Viscoelasticity Applied to Degradation During Carbon Carbon Composite Processing*. **Drakonakis, V. M., et al.** 2010, Acta Astronautica 66, (7-8), pp. 1189 - 1200.
2. *Analysis of Carbon Carbon Pyrolytic Processes through Viscoelastic Modeling*. **Drakonakis, V. M., et al.** 2011, Journal of Advanced Materials 43, (1), pp. 65 - 85.
3. **Seferis, J. C., Velisaris, C. N. and Drakonakis, V. M.,.** Prepreg Manufacturing. [book auth.] L., Borzacchiello, A., Lee, S. M. Luigi Nicolais. *Encyclopedia of Composites*. New Jersey : Wiley & Sons, 2012.
4. *Effects of Curing Pressure on Structural Polymeric Composites for Commercial Aviation Cured Without Autoclave*. **Drakonakis, V. M., et al.** Tarbes, France : ICSAAM, 2009. International Conference on Structural Analysis of Advanced Materials.
5. *Matrix Hybridization in the Interlayer for Carbon Fiber Reinforced Composites*. **Drakonakis, V. M., et al.** 2010, Polymer Composites 31, (11), pp. 1965 - 1976.
6. *Feather Weight Composites: Development of Controlled free Volume in CNT Reinforced Polymeric Matrix Systems*. **Drakonakis, V. M., et al.** Dayton, OH : American Society of Composites, 2010. American Society of Composites.
7. *Nanobridization in Carbon Fiber Polymeric Matrix Nanocomposite Systems*. **Drakonakis, V. M., et al.** Jeju, S. Korea : ICCM, 2011. 18th International Conference on Composite Materials.
8. *Kinetic Viscoelasticity for the Dynamic Mechanical Properties of Polymeric Systems*. **Dillman, S. H. and Seferis, J. C.** 1989, Journal of Macromolecules Science and Chemistry 26, (1), pp. 227 - 247.

9. *Viscoelastic Characterization of the Phenolic Resin-Carbon Fiber Composite Degradation Process*. **Nam, J. D. and Seferis, J. C.** 1999, Journal of Polymer Science Part B: Polymer Physics 37, (9), pp. 907 - 918.
10. *Dynamic mechanical analysis of fiber reinforced composites*. **Reed, K.E.** 1980, Polymer Composites 1, (1), pp. 44 - 49.
11. *Investigation of composite interphase using dynamic mechanical analysis: artifacts and reality*. **Thomason, J.L.** 1990, Polymer Composites 11, (2), pp. 105 - 113.
12. **Milovic, J. and Lin, K. F.** Polymer Blends and Composites in Multiphase Systems. [book auth.] C. D. Han. *Advanced Chemical Series No 206*. Washington D. C. : American Chemical Society, 1984.
13. **Sternsein, S. S. and Yang, P.** [book auth.] J. C., Nicolais, L. Seferis. *The Role of the Polymeric Matrix in the Processing and Structural Properties of Composite Materials*. New York : Plenum Press, 1983.
14. *Error analysis and modelling of non-linear stress strain behaviour in measuring mechanical properties of polymers with the Rehovibron*. **Wedgewood, A. R. and Seferis, J. C.** 1981, Polymer 22, (7), pp. 966 - 991.
15. *Characterization of Cure of Carbon/Epoxy Prepreg used in the Aerospace Field*. **Costa, M. L., et al.** 2005, Journal of Material Research 8, (3), pp. 317 - 322.
16. *Evaluation of Thermal Degradation on Carbon Fiber/Cyamate Ester Composites*. **Chung, K. and Seferis, J. C.** 2001, Polymer Degradation and Stability 71, (3), pp. 425 - 434.
17. **Nam, J. D.** *Polymer Matrix Degradation: Characterization and Manufacturing Process for High Temperature Composites*. Seattle : University of Washington, 1991. PhD Thesis.
18. **Bartenev, G. M. and Zelenev, Yu. V.** *Relaxation Phenomena in Polymers*. New York : John Willey & Sons, 1974.
19. **Ferry, J. D.** *Viscoelastic Properties of Polymers*. New York : John Willey, 1980, pp. 264 - 320.

20. *The Temperature Dependence of Relaxation Mechanisms in Amorphous Polymers and Other Glase-forming Liquids.* **Williams, M. L., Landal, R. F. and Ferry, J. D.** 1955, Journal of American Chemistry Society 77, (14), p. 3701.
21. **Dusi, M. R., May, C. A. and Seferis, J. C.** Predictive Models as Aids to Thermoset Resin Processing. [book auth.] C. A. May. *Chemorheology of Thermosetting Polymers.* s.l. : American Chemical Society Symposium Series 227, 1983, pp. 301 - 318.
22. **Dillman, S. H.** *Kinetic Viscoelasticity of Reacting Polymer Systems.* Seattle : University of Washington, 1988. PhD Thesis.
23. **Ward, I. M.** *Mechanical Properties of Solid Polymer.* New York : Wiley, 1983.
24. *Dielectric Studies of the Cure of Epoxy Matrix Systems.* **Lane, J. W., Seferis, J. C. and Bachmann, M. A.** 1986, Journal of Applied Polymer Science 31, (5), pp. 1155 - 1167.
25. *Relaxation processes in crystalline polymers: molecular interpretation — a review.* **Boyd, R. H.** 1985, Polymer 26, (8), pp. 1123 - 1133.
26. *A complex plane representation of dielectric and mechanical relaxation processes in some polymers.* **Havriliak, S. and Negami, S.** 1967, Polymer 8, pp. 161 - 210.
27. **Brinson, H. F. and Brinson, L. C.** *Polymer Engineering Science and Viscoelasticity, An Introduction.* New York : Springer, 2008.
28. **Hohne, G. W. H., Heminger, W. F. and Flammersheim, H. -J.** Theoretical Fundamentals of Differential Scanning Calorimeters. [book auth.] G. W. H., Heminger, W. F., Flammersheim, H. -J., Hohne. *Differential Scanning Calorimetry.* s.l. : Springer, 2003, pp. 31 - 63.
29. —. Applications of Differential Scanning Calorimetry. [book auth.] G. W. H., Heminger, W. F., Flammersheim, H. -J., Hohne. *Differential Scanning Calorimetry.* s.l. : Springer, 2003, pp. 200 - 241.
30. *Powder Curtain Prepreg Process.* **Baucom, R. M. and Marchello, J. M.** 1994, Journal of Advnaced Materials 25, (4), pp. 31 - 35.

31. **Hayes, B. S.** *Simulation Engineering of Polymeric Prepreg Composite Systems*. Seattle : University of Washington, 1997. PhD Thesis.
32. *Scale-Up for Hot Melt Prepreg Manufacturing*. **Hoisington, M. A., Seferis, J. C. and Thompson, D.** Anaheim, CA; Covina, CA : SAMPE, 1992. 37th International SAMPE Symposium and Exhibition. pp. 264 - 277.
33. *Prepreg Manufacturing under Constant Pressure of Deformation*. **Buehler, F. U. and Seferis, J. C.** 1998, Journal of Advanced Materials 30, (1), pp. 3 - 9.
34. *Prepreg Processing Science and Analysis*. **Seferis, J. C. and Ahn, K. J.** Reno, NV; Covina, CA : SAMPE, 1989. 34th International SAMPE Symposium and Exhibition. pp. 63 - 68.
35. *Prepreg processing science and engineering*. **Ahn, K. J. and Seferis, J. C.** 1993, Polymer Engineering and Science 33, (18), pp. 1177 - 1188.
36. *Cracks and Microcracks in Stitched Structural Composites Manufactured with Resin Film Infusion Process*. **Shim, S. B., et al.** 1995, Journal of Advanced Materials 26, (4), pp. 48 - 62.
37. *Void control for polymer-matrix composites (2): Experimental evaluation of a diffusion model for the growth and collapse of gas bubbles*. **Bader, M. G. and Wood, J. R.,.** 1994, Composites Manufacturing 5, (3), pp. 149 - 158.
38. *Optimized curing process for an autoclave cured fibre reinforced composite*. **Boey, F. Y. C. and Lye, S. W.** 1990, Journal of Material Processing Technology 23, (2), pp. 121 - 132.
39. *Void growth and resin transport during processing of thermosetting matrix composites*. **Kardos, J. L., Dudokovic, M. P. and Dave, R.** 1980, Advances in Polymer Science 80, pp. 101 - 123.
40. *Processing Science: An Approach for Prepreg Composite Systems*. **Halpin, J. C., Kardos, J. L. and Dudukovic, M.P.** Athens : Editors Seferis, J. C. and Theocaris, P. C. - Elsevier, 1982. Proceedings of the IUPAC International Symposium on the Interrelations between Processing Structure and Properties of Polymeric Materials. pp. 893 - 906.

41. *Fundamentals of Breather Technology in Prepreg Consolidation*. **Shafizadeh, J. E., et al.** 1997, *Journal of Advanced Materials* 28, (3), pp. 42 - 49.
42. *The Effect of Fabric Tension and the Number of Impregnation Rollers on Woven Fabric Prepreg Quality and Cured Laminates*. **Hayes, B. S. and Seferis, J. C.** 1997, *Composites Part A* 28, (9-10), pp. 791 - 799.
43. **Strong, A. B.** *Fundamentals of Composites Manufacturing (2nd Edition)*. Dearborn, MI : Society of Manufacturing Engineering, 2008.
44. *Gas Permeation and Viscoelastic Deformation of Prepregs in Composite Manufacturing Processes*. **Nam, J. D., et al.** 1995, *SOC PLASTICS ENG INC* 16, (5), pp. 370-379.
45. *Process Induced Void Formation in a High Performance Structural Composite System Manufactured by Autoclave Lay –Up*. **Shim, S. B., Seferis, J. C. and Hudson, W.** 1997, *Journal of Advanced Materials* 28, (4), pp. 26 - 36.
46. **Heatcon Composite Systems, Inc.** www.heatcon.com. [Online] 2012. [Cited: June 07, 2012.] <http://www.heatcon.com/aerospace-rotor-wing/equipment/portable-autoclave>.
47. **TEC.** Thermal Equipment Corporation. [Online] 2012. [Cited: June 07, 2012.] <http://www.thermalequipment.com/>.
48. **Hoisington, M. A.** *Process/property interrelations of layered structured composites*. Seattle : University of Washington, 1992.
49. **Miracle, D. B. and Donaldson, S.L.** *ASM Handbook Volume 21: Composites*. Materials Park, OH : ASM International, 2001.
50. **Boyd, J. D.** *Toughened Thermosetting Structural Materials*. 5037689 U.S.A, 1991.
51. **Folda, T., et al.** *Toughened thermosetting structural materials*. 5242748 U.S.A., 1993.
52. *An Improved 270 0C Performance Interleaf System Having Extremely High Impact Resistance*. **Hirschbuehler, K. R.** 1985, *SAMPE Q.* 17, (1), pp. 46 - 49.
53. *Model Multilayer Structured Composites*. **Hoisington, M. A. and Seferis, J. C.** 1993, *SAMPE Q.* 24, (2), pp. 10 - 20.

54. *Interlayer Toughened Unidirectional Carbon Prepreg Systems: Effect of Preformed Particle Morphology*. **Gilbert, E. N., Hayes, B. S. and Seferis, J. C.** 2002, Composites Part A: Applied science and Manufacturing 34, (3), p. 245.
55. **Odagiri, N., et al.** *Highly tough composite materials*. 0274899 (A2) European, 1988.
56. **Odagiri, N., et al.** *Fiber Reinforced Composite Materials*. 5789073 U.S.A., 1998.
57. **Brown, J. E., et al.** *Epoxy Resin for Fiber Reinforced Composite Materials*. 7208228 U.S.A., 2007.
58. *Process-Structure-Property Relationships for Layered Structured Composites*. **Hoisington, M. A. and Seferis, J. C.** Albany, NY : ASC, 1991. Proceedings of 6th Technical Conference of American Society for Composites. pp. 53 - 62.
59. *Novel Elastomeric Modification of Epoxy/Carbon Fiber Composite Systems*. **Hayes, B. S., et al.** 1997, Journal of Advanced Materials 28, (4), pp. 20 - 25.
60. *Particulate Interlayer Toughening of Dicyanate Matrix Composites*. **Zeng, S., Hoisington, M. A. and Seferis, J.C.** 1993, Polymer Composites 14, (6), pp. 458 - 466.
61. *Prepreg Process-Structure-Property Analysis and Scale-Up for Manufacturing and Performance*. **Putnam, J. W., Hayes, B. S. and Seferis, J. C.** 1996, Journal of Advanced Materials, pp. 47 - 57.
62. *Microstructure of Two-Phase Polymers*. **Sultan, J. N., Laible, R. C. and McGarry, F. J.** 1971, Applied Polymer Symposium 16, pp. 127 - 136.
63. *Tensile crazing and shear banding of styrene A: Temperature and rate effects*. **Sultan, J. N. and McGarry, F. N.** 1974, Polymer Engineering and Science 14, (4), pp. 282 - 287.
64. *Toughening mechanisms in elastomer-modified epoxies Part 1 Mechanical studies*. **Yee, A. F. and Pearson, R. A.** 1986, Journal of Materials Science 21, (7), pp. 2462-2474.
65. *Toughening mechanisms in elastomer-modified epoxies Part 2 Microscopy studies*. **Pearson, R. A and Yee, A. F.** 1986, Journal of Materials Science 21, (7) , pp. 2475 - 2488.

66. *Failure mechanisms in toughened epoxy resins - A review.* **Garg, A. C. and Mai, Y. W.** 1988, *Composites Science and Technology* 31, (3), pp. 179 - 223.
67. *Toughening mechanisms in elastomer-modified epoxies.* **Pearson, R. A. and Yee, A. F.** 1989, *Journal of Materials Science* 24, (7), pp. 2571 - 2580.
68. *Ternary blends of epoxy, rubber and polycarbonate: phase behaviour, mechanical properties and chemical interactions.* **Jayle, L., et al.** 1996, *Polymer* 37, (10), pp. 1897 - 1905.
69. *Influence of Particle Size Distribution of Preformed Rubber on the Structure and Properties of Composite Systems.* **Hayes, B. S. and Seferis, J. C.** 2002, *Journal of Composite Materials* 36, (3), pp. 299 - 312.
70. *Interlayer Toughening of Resin Transfer Molding Composites.* **Hillermeier, R. W. and Seferis, J. C.** 2001, *Composites Part A: Applied Science and Manufacturing* 32, (5), pp. 721 - 729.
71. *Toughening tetrafunctional epoxy resins using polyetherimide.* **Bucknall, C. B. and Gilbert, A. H.** 1989, *Polymer* 30, (2), pp. 213 - 217.
72. *Mode II fracture of composites interlayered with nylon particles.* **Groleau, M.R., et al.** 1996, *Composites Science and Technology* 56, (11), pp. 1223 - 1240.
73. *Mode I and mode II delamination properties of glass/vinyl-ester composite toughened by particulate modified interlayers.* **Stevanovic, D., et al.** 2003, *Composites Science and Technology* 63, (13), pp. 1949 - 1964.
74. *Improving the fatigue resistance of carbon/ epoxy laminates with dispersed-particle interlayers.* **Tanimoto, T.** 1998, *Acta Materialia* 46, (7), pp. 2455 - 2460.
75. *Reinforcement effects of MWCNT and VGCF in bulk composites and interlayer of CFRP laminates.* **Hu, N., et al.** 2012, *Composites Part B: Engineering* 43, (1), pp. 3 - 9.

76. *Improvement of interlaminar mechanical properties of CFRP laminates using VGCF.* **Li, Y., et al.** 2009, Composites Part A: Applied Science and Manufacturing 40, (12), pp. 2004 - 2012.
77. *Mode I and mode II interlaminar fracture toughness of CFRP laminates toughened by carbon nanofiber interlayer.* **Arai, M., et al.** 2008, Composites Science and Technology 68, (2), pp. 516 - 525.
78. *Influence of electrospun Nylon 6,6 nanofibrous mats on the interlaminar properties of Gr-epoxy composite laminates.* **Palazzetti, R., et al.** 2012, Composite Structures 94, (2), pp. 571 - 579.
79. *Structurally stitched NCF CFRP laminates. Part 1: Experimental characterization of in-plane and out-of-plane properties.* **Heß, H. and Himmel, N.,** 2011, Composites Science and Technology 71, (5), pp. 549 - 568.
80. *Aligned Carbon Nanotube Reinforcement of Ply Interfaces in Woven Composites.* **Garcia, E. J., et al.** Honolulu, HA : AIAA, 2007. 48th AIAA Structures, Dynamics, and Materials Conference. pp. 2007-2037.
81. *Multifunctional Characterization of Aligned CNT-Reinforced Hybrid Composites.* **Yamamoto, N., et al.** Kyoto, Japan : ICCM, 2007. 16th International Conference on Composite Materials (ICCM).
82. *Fatigue damage behaviors of carbon fiber-reinforced epoxy composites containing nanoclay.* **Khan, S. U., et al.** 2010, Composites Science and Technology 70, (14), pp. 2077 - 2085.
83. *Mode I interlaminar fracture behavior and mechanical properties of CFRPs with nanoclay-filled epoxy matrix.* **Siddiqui, N. A., et al.** 2007, Composites Part A: Applied Science and Manufacturing 38, (2), pp. 449 - 460.
84. *On the improvement of toughness of CFRPs with resin doped with CNF and PZT particles.* **Tsantzalidis, S., et al.** 2007, Composites Part A: Applied Science and Manufacturing 38, (4), pp. 1159 - 1162.

85. *A SMA/CFRP hybrid composite with damage suppression effect at ambient temperature*
Original Research Article. **Xu, Y., et al.** 2003, Scripta Materialia 49, (6), pp. 587 - 595.
86. *Fabrication and Nanocompression Testing of Aligned Carbon-Nanotube–Polymer Nanocomposites.* **García, E. J., et al.** 2007, Advanced Material 19, (16), pp. 2151 - 2156.
87. *Multifunctional carbon nanotube yarns and transparent sheets: Fabrication, properties, and applications.* **Atkinsona, K.R., et al.** 2007, Physica B 394, pp. 339 - 343.
88. *Small but strong: A review of the mechanical properties of carbon nanotube–polymer composites.* **Coleman, J.N., et al.** 2006, Carbon 44, (9), pp. 1624 - 1652.
89. *Interfacial bonding characteristics of Nanotube/Polymer Composites.* **Lau, K.-T.** 2003, Chemical Physics Letters 370, pp. 399 - 405.
90. *Effect of CNT length and CNT-matrix interphase in carbon nanotube (CNT) reinforced composites.* **Wan, H., Delale, F. and Shen, L.** 2005, Mechanics Research Communications 32, (5), pp. 481 - 489.
91. *Fiber waviness in nanotube-reinforced polymer composites - I: Modulus predictions using effective nanotube properties.* **Fisher, F.T., Bradshaw, R.D. and Brinson, L.C.** 2003, Composites Science and Technology 63, pp. 1689 - 1703.
92. *Fiber waviness in nanotube-reinforced polymer composites - II: modeling via numerical approximation of the dilute strain concentration tensor.* **Bradshaw, R.D., Fisher, F.T. and Brinson, L.C.** 2003, Composites Science and Technology 63, pp. 1705 - 1722.
93. *Prediction of elastic properties of carbon nanotube reinforced composites.* **Hu, N., et al.** 2005, Proceedings of the Royal Society A 461, pp. 1685 - 1710.
94. *Nanotube Composites.* **Ajayan, P. M. and Tour, J. M.** 2007, Nature 447, pp. 1066 - 1068.
95. *Epoxy Foams for Polynanomeric Reinforced Composites.* **Ishiguro, K., et al.** San Diego, CA : SAMPE, 2004. SAMPE International Symposium and Exhibition.
96. *Polystyrene foams. I: processing-structure relationships.* **Doroudiani, S. and Kortschot, M.T.** 2003, Journal of Applied Polymer Science 90, pp. 1412 - 1420.

97. *Short-fiber-reinforced epoxy foams*. **Auada, M.L. and Nutt, S.** 2006, Composites Part A: Applied Science and Manufacturing 37, (11), pp. 1952 - 1960.
98. *Nanoporous Thermosets via Reactive Encapsulation of a Chemically Inert Solvent Versus Free Radically Polymerized and Phase Separating Systems*. **Raman, V. I. and Palmese, G. R.** s.l.: Material Research Society Proceedings, 2004, Material Research Society Symposium Proceedings 788, Vol. 788, pp. 347 - 352.
99. *Morphological and Mechanical Properties of Epoxy Foam Reinforced Composites*. **Ishiguro, K., et al.** Boston, MA : Society of Plastics Engineers, 2005. SPE ANTEC.
100. *The Influence on Mechanical Properties of Epoxy Foam Matrix Structural Differentiations*. **Ishiguro, K., Sangari, S. S. and Seferis, J. C.** Seattle, WA : SAMPE, 2005. SAMPE International Technical Conference.
101. *The Use of Principal Component Analysis to Classify PDMS Surfactants Used to Make Rigid Polyurethane Foams Based on Their Dynamic Surface Tension Characteristics* . **Biesmans, G., Colman, L. and Vandensande, R.** 1998, Journal of Colloid and Interface Science 199, (2), pp. 140 - 150.
102. **Thomas, P.** *Water & Solvent Based Surface Coating Resins and Their Applications, vol. 3.* London : SITA Technology, 1999.
103. *Hybrid organic-inorganic nanocomposites: Exfoliation of magadiite nanolayers in an elastomeric epoxy polymer*. **Wang, Z. and Pinnavaia, T. J.** 1998, Chemistry of Materials 10, pp. 1820 - 1826.
104. *Generation of microcellular polyurethane foams via polymerization in carbon dioxide. II: Foam formation and characterization*. **Park, K. L. and Beckman, E. J.** 1996, Polymer Engineering and Science 36, (19), pp. 2417 - 2431.
105. *Cyclopentane-Blown Rigid Foams for Refrigerators*. **Volkert, O.** 1995, Journal of Cellular Plastics 31, (3), p. 210.

106. *Kinetics of the hydrolysis and condensation of organofunctional alkoxysilanes: a review.* **Osterholtz, F. D. and Pohl, E. R.** 1992, *Journal of Adhesion Science Technology* 6, (1), pp. 127 - 149.
107. **Oertel, G.** *Polyurethane handbook.* Munich : Carl Hanser, 1985.
108. **Kline, G. M.** Foamed Plastics vol.50. *Modern Plastics Encyclopedia.* Michigan : McGraw-Hill, 1973, p. 125.
109. **Frisch, K. C. and Saunders, J. H.** *Plastic Foam.* New York : Marcel Dekker Inc., 1972.
110. **Saunders, J. H. and Frisch, K.C.** *Polyurethanes Chemistry and Technology.* New York : Interscience, 1962.
111. *Elastomeric nanofibers of styrene-butadiene-styrene triblock copolymer.* **Fong, H. and Reneker, D.H.** 1999, *Journal of Polymer Science: Part B: Polymer Physics* 37, (24), pp. 3488 - 3493.
112. *Nanometre diameter fibres of polymer, produced by electrospinning.* **Reneker, D.H. and Chun, I.** 1996, *Nanotechnology* 7, (3), pp. 216 - 223.
113. *Bending instability of electrically charged liquid jets of polymer solutions in electrospinning.* **Reneker, D.H., et al.** 2000, *Journal of Applied Physics* 87, (9), pp. 4531 - 4547.
114. *Bending instability in electrospinning of nanofibers.* **Yarin, A.L., Koombhongse, S. and Reneker, D.H.** 2001, *Journal of Applied Physics* 89, (5), pp. 3018 - 3026.
115. *A review on polymer nanofibers by electrospinning and their applications in nanocomposites.* **Huang, Z.-M., et al.** 2003, *Composites Science and Technology* 63, (15), pp. 2223 - 2253.
116. *Electrospinning of nanofibers: Reinventing the wheel?* **Li, D. and Xia, Y.** 2004, *Advance Materials* 16, (14), pp. 1151 - 1170.
117. *The effect of processing variables on the morphology of electrospun nanofibers and textiles.* **Deitzel, J.M., et al.** 2001, *Polymer* 42, (1), pp. 261 - 272.

118. *Transparent nanocomposites with ultrathin, electrospun nylon-4,6 fiber reinforcement.* **Bergshoef, M.M. and Vancso, G.J.** 1999, *Advanced Materials* 11, (16), pp. 1362 - 1365.
119. *Biodegradable Cellulose Acetate Nanofiber Fabrication via Electrospinning.* **Christoforou, T. and Doumanidis, C.C.** 2009, *Proc. IMechE - Journal of Nanoengineering and Nanosystems* 10, (9), pp. 1 - 8.
120. *Electrospinning process and applications of electrospun fibers.* **Doshi, J. and Reneker, D.H.** 1995, *Journal of Electrostatics* 35, (2-3), pp. 151 - 160.
121. *Experimental characterization of electrospinning: the electrically forced jet and instabilities.* **Shin, Y.M., et al.** 2001, *Polymer* 42, (25), pp. 9955 - 9967.
122. *Electrically driven jets.* **Taylor, G.** 1969, *Proceedings of the Royal Society of London, Series A* 313, (1515), pp. 453 - 475.
123. *Development of electrospinning from molten polymers in vacuum .* **Rangkupan, R. and Reneker, D.H.** s.l. : The Fiber Society, 2001. Book of Abstracts, In: *New frontiers in fiber science.*
124. *Branched and split fiber from electrospinning process.* **Koombhongse, S. and Reneker, D.H.** s.l. : The Fiber Society, 2001. Book of Abstracts, In: *New Frontiers in Fiber Science.*
125. *Electrospinning of Nanofibers.* **Subbiah, T., et al.** 2005, *Journal of Applied Polymer Science* 96, (2), pp. 557 - 569.
126. **Knop, A. and Pilato, L. A.** *Phenolic Resins.* New York : Springer-Verlag, 1985.
127. **McAllister, L. E., Lachman, W. L. and Walter, L.** *Multidirectional Carbon-Carbon Composites.* [book auth.] A. Kelly. *Fabrication of Composites, Handbook of Composites.* New York : Elsevier Science Publishers, 1983, pp. 109 - 175.
128. *Elastic Properties of Carbon Nanotubes and Nanoropes.* **Lu, J. P.** 1997, *Physical Review Letters* 79, (7), pp. 1297 - 1301.
129. *Load transfer in carbon nanotube epoxy composites.* **Schadler, L. S., Giannaris, S. C. and Ajayan, P. M.** 1998, *Applied Physics Letters* 73, (26), pp. 3842 - 3844.

130. *Micromechanics of short-fiber composites*. **Carman, G.P. and Reifsnider, K. L.** 1992, Composite Science and Technology 43, (2), pp. 137–146.
131. *Rapid growth and flow-mediated nucleation of millimeter-scale aligned carbon nanotube structures from a thin-film catalyst*. **Hart, A.J. and Slocum, A.H.** 2006, The Journal of Physical Chemistry B 110, (16), pp. 8250–8257.
132. *Fabrication, characterization of ultrahigh volume-fraction aligned carbon nanotube–polymer composites*. **Wardle, B.L., et al.** 2008, Advanced Materials 20, p. 2707.
133. *Decoupled thermal treatment of precursor and catalyst enables engineering of diameter, structural quality, and growth kinetics of vertically aligned carbon nanotubes*. **Meshot, E.M., et al.** 2009, ACS Nano, p. doi:10.1021/nn9004.
134. *Multifunctional properties of high volume fraction aligned carbon nanotube polymer composites with controlled morphology*. **Cebeci, H., et al.** 2009, Composites Science and Technology 69, pp. 2649 - 2656.
135. *Measurement of hardness and elastic modulus by instrumented indentation: advances in understanding and refinements to methodology*. **Oliver, W.C. and G.M., Pharr.** 2004, Journal of Materials Research 19, (1), pp. 3–20.
136. *Determination of mechanical properties of carbon nanotubes and vertically aligned carbon nanotube forests using nanoindentation*. **Qi, H.J., et al.** 2003, Journal of the Mechanics and Physics of Solids 51, (11-12), pp. 2213 - 2237.
137. *Internal Stress Determination by Process Simulated Laminates*. **Manson, J.-A. and Seferis, J.C.** Los Angeles : SPE, 1987. Proc. SPE ANTEC '87. p. 1446.
138. **OriginLab, Corp.** OriginLab Data Analysis and Graphing Software. [Online] 2012. [Cited: June 18, 2012.] <http://www.originlab.com>.
139. **Microsoft.** Microsoft. *Microsoft*. [Online] Microsoft, 2012. <http://www.microsoft.com>.
140. **Minitab, Inc.** Minitab, Software for Quality Improvement. [Online] 2012. [Cited: June 18, 2012.] <http://www.minitab.com>.

141. *Mechanical properties of carbon nanotubes*. **Salvetat, J.P., et al.** 1999, *Applie Physics A* 69, pp. 255 - 260.
142. *The method and device for producing higher fullerenes and nanotubes*. **Ryzhkov, V.A.** 2000, Int. Publ. Number WO 00/61492 A3, 19 .
143. *Elastic bending modulus of monolayer graphene* . **Lu, Q., Arroyo, M. and Huang, R.** 2009, *Journal of Physics D: Applied Physics* 42, (10), pp. 102002 -102008.
144. *Elastic Properties of Chemically Derived Single Graphene Sheets*. **Gómez-Navarro, C., Burghard, M. and Kern, K.** 2008, *Nano Letters* 8, (7), pp. 2045 - 2049.
145. *Effective elastic mechanical properties of single layer graphene sheets*. **Scarpa, F., Adhikari, S. and S., Phani A.** 2009, *Nanotechnology* 20, (6), pp. 065709 - 065720.
146. **Shimp, D. A.** *Technology Driven Applications for Cyanate Ester Resins*. [book auth.] I. Hamerton. *Chemistry and Technology of Cyanate Ester Resins*. London, UK : Chapman & Hall, 1994, pp. 282 - 327.

BIOGRAPHICAL INFORMATION

Vasileios M. Drakonakis (Dipl. Ing. 2008, Mechanical & Aeronautics Eng; PhD 2012, Industrial & Manufacturing Engineering) has conducted research as an undergrad at the Composite Materials Group (CMG) (10/2006 – 09/2007) and the Applied Mechanics Laboratory (AML) (05/2005 – 12/2006) of University of Patras, under Prof George Papanicolaou and Prof Vassilis Kostopoulos respectively; as a research associate at the Polymeric Composites Laboratory (PCL) under Prof James Seferis from 10/2007 to present; as a PhD Candidate initially at the MME Dept of UCY under Prof Charalambos Doumanidis starting at 06/2008 and continuing at the Industrial & Manufacturing Engineering Dept of University of Texas at Arlington from 01/2011 to 08/2012; and as a visiting graduate student at the Aeronautics and Astronautics Dept of Massachusetts Institute of Technology under Prof Brian Wardle from 12/2008 to 09/2010. He has been a member of European Association of Aerospace Students, an association with presence in more than 31 universities within Europe, and elected at the International Board 2006-07 of the association. He has also been responsible for performing the Young Engineer Satellite 2 (YES2) thermal analysis and design, a project of the European Space Agency (ESA). Furthermore, he was part of the ATLAS team, serving as responsible for the manufacturing of a UAV made by CFRP at University of Patras; The Atlas team was awarded as the winner of the 2009 Young Aerospace Engineer of the Year – “Aerospace Testing, Design and Manufacturing 09”. His current research under Prof Doumanidis and Prof Seferis on the concept of featherweight composites supported by the Air Force Office of Scientific Research (AFOSR) has been awarded as the most innovative AFOSR research project of 2009-10. Finally, his work so far is well documented in over 15 papers in scientific journals and conferences. His research interest and expertise is in applied mechanics, (nano) composite materials processing, (interlayer) toughening mechanisms, and thermal engineering.